MULTI-BEAM-INTERFERENCE-BASED METHODOLOGY FOR THE FABRICATION OF PHOTONIC CRYSTAL STRUCTURES

A Thesis
Presented to
The Academic Faculty

by

Justin L. Stay

In Partial Fulfillment
of the Requirements for the Degree
Doctor of Philosophy in the
School of Electrical and Computer Engineering

Georgia Institute of Technology
December 2009

MULTI-BEAM-INTERFERENCE-BASED METHODOLOGY FOR THE FABRICATION OF PHOTONIC CRYSTAL STRUCTURES

Approved by:

Professor Thomas K. Gaylord,
Committee Chair
School of Electrical and Computer Engineering
Georgia Institute of Technology

Professor Gee-Kung Chang
School of Electrical and Computer Engineering
Georgia Institute of Technology

Professor Phillip N. First
School of Physics
Georgia Institute of Technology

Dr. Muhannad S. Bakir
School of Electrical and Computer Engineering
Georgia Institute of Technology

Dr. Donald D. Davis
School of Electrical and Computer Engineering
Georgia Institute of Technology

Date Approved: October 5, 2009

The most exciting phrase to hear in science, the one that heralds new discoveries, is not "Eureka!" (I found it!) but "That's funny ..."

—Isaac Asimov

To my parents,

Jeffrey and Elizabeth

ACKNOWLEDGEMENTS

It is difficult to begin to thank all of the people who have supported me along the way during my time at Georgia Tech. It is even more difficult to believe that the journey towards earning this degree is almost complete. Throughout the stressful days and sometimes seemingly impossible obstacles, it is these people who, whether they knew it or not, kept me level-headed and optimistic through these difficult moments.

It has been a pleasure and a privilege to have Professor Thomas K. Gaylord as an advisor. He not only shows his students what it means to be a great scientist and engineer, but also how to be a gentleman in any situation. I thank him for all of his encouragement and support and all that I have learned from him over the years.

Thanks also goes to the other members of my thesis committee Dr. Muhannad S. Bakir, Professor Gee-Kung Chang, Dr. Donald D. Davis, and Professor Phillip N. First. Their encouragement, support, and constructive criticism helped me reach my highest potential.

I would also like to thank all of the past and present members of the Georgia Tech Optics group. Specifically, I would like to thank Dr. Brent Bachim, Lieutenant Colonel Matt Burrow, Dr. Yin-Jung Chang, Andy Heidt, Michael Hutsel, Prof. Greg Kilby, Chien-I Lin, Jonathan Maikisch, Dr. Carole Montarou, Dr. Oluwafemi Ogunsola, Dr. Ricardo Villalaz, and Dr. Shun-Der Wu for everything from the insightful discussions at our Friday lunch meetings to the gatherings of the Optics All Stars!!!

A special thanks goes out to the friends I've made throughout the years here in Atlanta. You in particular allowed me to enjoy my life outside of the classroom and helped me relieve the stress that accumulates on the shoulders of a Ph.D. student. I cannot be expected to list everyone that meant so much to me, however, for those who take the time to read this thesis (at least the first page!), this is especially for you. Thank you.

Finally, I want to thank my family: my mother Elizabeth, my father Jeffrey, and my brothers Bryan and Derek. There is nothing I can say that can fully express what your love and support has meant to me, not just during the last decade, but my entire life.

JUSTIN L. STAY

Georgia Institute of Technology

October 2009

This research has been supported in part by the National Science Foundation under grant no. ECCS 0925119.

TABLE OF CONTENTS

LIST OF TABLES

LIST OF FIGURES

LIST OF ABBREVIATIONS

A-to-D Analog to Digital.

BCC Body-Centered Cubic.

BSC Beam Splitter Cube.

CMOS Complementary Metal-Oxide-Semiconductor.

CVD Chemical Vapor Deposition.

DIPCS Dense Integrated Photonic Circuits and Systems.

EBL Electron Beam (E-Beam) Lithography.

FCC Face-Centered Cubic.

FDTD Finite-Difference Time-Domain.

FIB Focused Ion Beam.

FTIR Fourier Transform Infrared Spectrometer.

HWP Half-Wave Plate.

ICP Inductively Coupled Plasma.

IR Infrared.

M Mirror.

MBIL Multi-Beam-Interference Lithography.

MEEP MIT Electromagnetic Equation Propagation Software.

MPB MIT Photonic Bands Software.

PC Photonic Crystal.

RCWA Rigorous Coupled Wave Analysis.

RIE Reactive Ion Etch.

SEM Scanning Electron Microscopy.

TE Transverse Electric.

TM Transverse Magnetic.

UV Ultra Violet.

VCSEL Vertical-Cavity-Surface-Emitting Laser.

VIS Visible.

SUMMARY

Photonic crystal (PC) technology offers the potential of lossless control of the propagation of light at microelectronic and nanoelectronic size scales. Numerous important physical characteristics have already been demonstrated. These phenomena include the photonic bandgap, the superprism effect, negative refraction, and negative diffraction. Individual components that have been demonstrated include waveguides, resonators, filters, waveguide couplers, directional couplers, demultiplexers, antennas, switches, and sensors. The integration of optimized versions of these components would produce the first truly dense integrated photonic circuits and systems (DIPCS) that would perform functions such as interconnection, communication, image acquisition, image processing, image recognition, A-to-D conversion, control, and bio/chem-sensing.

A variety of techniques are available to enable the fabrication of photonic crystal structures. Multi-beam-interference lithography (MBIL) is a relatively new technique which offers many advantages over more traditional means of fabrication. Unlike the more common fabrication methods such as optical and electron-beam lithography, MBIL is a method that can produce both two- and three-dimensional large-area photonic crystal structures for use in the infrared and visible light regimes. While multi-beam-interference lithography represents a promising methodology for the fabrication of PC structures, there has been an incomplete understanding of MBIL itself. The research in this thesis focuses on providing a more complete, systematic description of MBIL in order to demonstrate its full capabilities.

Analysis of both three- and four-beam interference is investigated and described in terms of contrast and crystallography. The concept of a *condition for primitive-lattice-vector-direction equal contrasts* is introduced in this thesis. These conditions are developed

as nonlinear constraints when optimizing absolute contrast for producing lithographically useful interference patterns (meaning high contrast and localized intensity extrema). By understanding the richness of possibilities within MBIL, a number of useful interference patterns are found that can be created in a straightforward manner. These patterns can be both lithographically useful and structurally useful (providing interference contours that can define wide-bandgap photonic crystals). Included within this investigation are theoretical calculations of band structures for photonic crystals that are fabricatable through MBIL. The resulting calculations show that not only do most MBIL-defined structures exhibit similar performance characteristics compared to conventionally designed photonic crystal structures, but in some cases MBIL-defined structures show a significant increase in bandgap size. Using the results from this analysis, a number of hexagonal photonic crystals are fabricated using a variety of process conditions. It is shown that both rod- and hole-type photonic crystal structures can be fabricated using processes based on both positive and negative photoresist. The "light-field" and "dark-field" interference patterns used to define the hexagonal photonic crystal structures are quickly interchanged by the proper adjustment of each beam's intensity and polarization. The resulting structures, including a large area ($\sim$ 1 cm^2, 1×10^9 lattice points) photonic crystal are imaged using a scanning electron microscope.

Multi-beam-interference lithography provides an enabling initial step for the wafer-scale, cost-effective integration of the impressive PC-based devices into manufacturable DIPCS. While multi-beam-interference lithography represents a promising methodology for the fabrication of PC structures, it lacks in the ability to produce PC-based integrated photonic circuits. Future research will target the lack of a large-scale, cost-effective fabrication methodology for photonic crystal devices. By utilizing diffractive elements, a photomask will be able to combine both MBIL and conventional lithography techniques into a single fabrication technology while taking advantage of the inherent positive attributes of both.

CHAPTER 1

INTRODUCTION

Photonic crystal (PC) technology offers the potential of lossless control of the propagation of light at microelectronic and nanoelectronic size scales [1]. This technology may produce the first truly dense integrated photonic circuits and systems (DIPCS). Numerous important physical characteristics have already been demonstrated. These phenomena include the photonic band gap [1], the superprism effect [2–4], negative refraction [5, 6], and negative diffraction [7–9]. Individual components that have been demonstrated include waveguides [10, 11], resonators [12–15], filters [15–17], waveguide couplers [18–21], directional couplers [22], demultiplexers [23], antennas [24], switches [25], and sensors [26]. The integration of optimized versions of these components would produce DIPCS that would perform functions such as interconnection, communication, image acquisition, image processing, image recognition, A-to-D conversion, control, and bio/chem-sensing. Further, the resulting DIPCS would be very compact in size and could be integrated with conventional microelectronics.

Despite the advantages and benefits of using PC technology in devices, there is a major problem: the practical commercial development of PC structures has been extremely slow. This slow development is due, to a large extent, to the lack of a manufacturing methodology for producing integrated PC structures and devices. For these complex structures and devices, there is a lack of fabrication and integration methods available that enable PC-based optoelectronic circuits to be made in parallel over a large area. Ideally, the fabrication and integration of optimized devices over an entire wafer are needed. These hindrances have severely limited the pace of PC technology development.

The objective of this thesis is to develop a multi-beam-interference-based methodology

for the fabrication of photonic crystal structures. This investigation will be an enabling step for the integration of a multiplicity of photonic crystal devices and structures, in parallel, across an entire wafer based on multi-beam-interference lithography (MBIL). This research includes a full treatment of two-, three-, and four-beam interference. Contrast, translational symmetry, and crystallography in two and three dimensions have been examined and quantified within the framework of MBIL. This research has also developed a configurable, tabletop MBIL fabrication facility with real-time monitoring. This facility allows for the experimental verification of MBIL concepts and photonic crystal structure fabrication. Using this facility, both one-dimensional gratings and hexagonal lattice structures have been fabricated using a variety of process conditions. This research also presents band structure modeling and simulation through the eigenmode calculation of Maxwell's equations. The concept of a MBIL-based photo-mask for the wafer scale fabrication of photonic crystal structures and devices is introduced.

1.1 Background

1.1.1 Engineered Materials

For thousands of years, engineers have strived to change and improve the properties of naturally occurring materials. Building materials have evolved from stone to brick and concrete. The need for stronger, lighter materials birthed bronze, iron, and steel. Now, the focus has shifted from controlling the mechanical properties of materials to the electrical and optical properties due in part to The Information Age.

The advent of the modern computer has had a profound impact on the scientific community. We know more about silicon than most, if not all, other elements. Even more impressive is the fact that engineers can precisely change the electrical properties of silicon to fit our ever-changing needs. Historically, silicon is used for its electrical properties. However, it is suggested that electrical-based silicon technologies are quickly approaching the physical limitations of the material system. Paradigm shifts in software and hardware

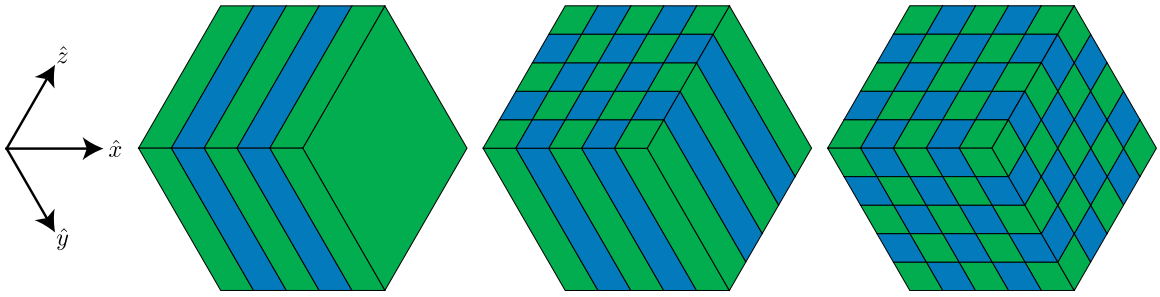

Figure 1.1: Classical examples of one-, two-, and three-dimensional photonic crystal structures [1].

design will be needed to continue fulfilling the goals of companies and expectations of the consumer. One of these hardware design paradigm shifts includes bringing photons closer to the chip. As of today, fiber-to-the-home is a real possibility, albeit at a premium price. However, it is imperative to continue pushing optical components and communications closer and closer to the computer, board, and chip. To fulfill this need, novel and reliable microscale and nanoscale optical components need to be realized. Photonic crystal (PC) technology potentially offers a technology platform to fill this need [1].

1.1.2 Photonic Crystals

In the simplest of terms, a photonic crystal is a structure periodic in one, two, or three dimensions (see Fig. 1.1). This periodicity can have a profound effect on the optical properties of the material, similar to how the periodic potential affects the electrical properties of semiconductors. Much of photonic crystal theory is derived from the macroscopic Maxwell equations given in SI units as

$$\nabla \times \boldsymbol{\mathcal{E}} = -\frac{\partial \boldsymbol{\mathcal{B}}}{\partial t} \tag{1.1}$$

$$\nabla \times \boldsymbol{\mathcal{H}} = \frac{\partial \boldsymbol{\mathcal{D}}}{\partial t} \tag{1.2}$$

$$\nabla \cdot \boldsymbol{\mathcal{D}} = 0 \tag{1.3}$$

$$\nabla \cdot \boldsymbol{\mathcal{B}} = 0 \tag{1.4}$$

for charge free, non-conducting materials. From these four equations, a number of computational techniques have evolved to analyze photonic crystal structures and devices. They can be categorized into frequency-domain responses, time-domain simulations, and frequency-domain eigenproblems. It is the frequency-domain eigenproblem approach that has brought about much of band theory. This approach is based on solving for a decoupled version of Maxwell's equations in terms of the complex magnetic field $\mathbf{H}(\mathbf{r})$ in the form of

$$\nabla \times \left(\frac{1}{\epsilon_r(\mathbf{r})} \nabla \times \mathbf{H}(\mathbf{r}) \right) = \left(\frac{\omega}{c} \right)^2 \mathbf{H}(\mathbf{r}) \, . \tag{1.5}$$

As the name suggests, the problem reduces to an eigenvalue problem, resulting in the allowable electromagnetic modes of the structure defined by the relative permittivity function $\epsilon_r(\mathbf{r})$ corresponding to an eigenvalue of $(\omega/c)^2$. The complex electric field $\mathbf{E}(\mathbf{r})$ is then recovered by

$$\mathbf{E}(\mathbf{r}) = \frac{i}{\omega \epsilon_o \epsilon_r(\mathbf{r})} \nabla \times \mathbf{H}(\mathbf{r}) \, . \tag{1.6}$$

A particularly interesting and useful property of the time harmonic version of Maxwell's equations (and subsequent derivatives) is the absence of a fundamental length scale associated with the constants. Specifically, a change in the dielectric profile by $\epsilon_r'(\mathbf{r}) = \epsilon_r(\mathbf{r}/s)$ results in a magnetic field profile of $\mathbf{H}'(\mathbf{r}) = \mathbf{H}(\mathbf{r}/s)$ and a frequency $\omega' = \omega/s$. This means that, given a dielectric function, the calculated eigenmode profile and corresponding eigenvalue frequency can be rescaled as the dielectric function is scaled spatially. A similar approach can be taken when the dielectric function is scaled in magnitude by $\epsilon_r'(\mathbf{r}) = \epsilon_r(\mathbf{r})/s^2$. The resulting magnetic field $\mathbf{H}(\mathbf{r})$ remains unchanged when the frequency is scaled by $\omega' = s\omega$.

The scaling properties of Maxwell's equations allow research to be conducted at normalized frequencies and arbitrary dielectric values. The resulting theories and concepts can be experimentally evaluated at the microwave, infrared, or visible light regimes. Of course, the structures must be physically possible in both mechanical stability and dielectric value. The technology needed to fabricate nanoscale structures has just recently become available.

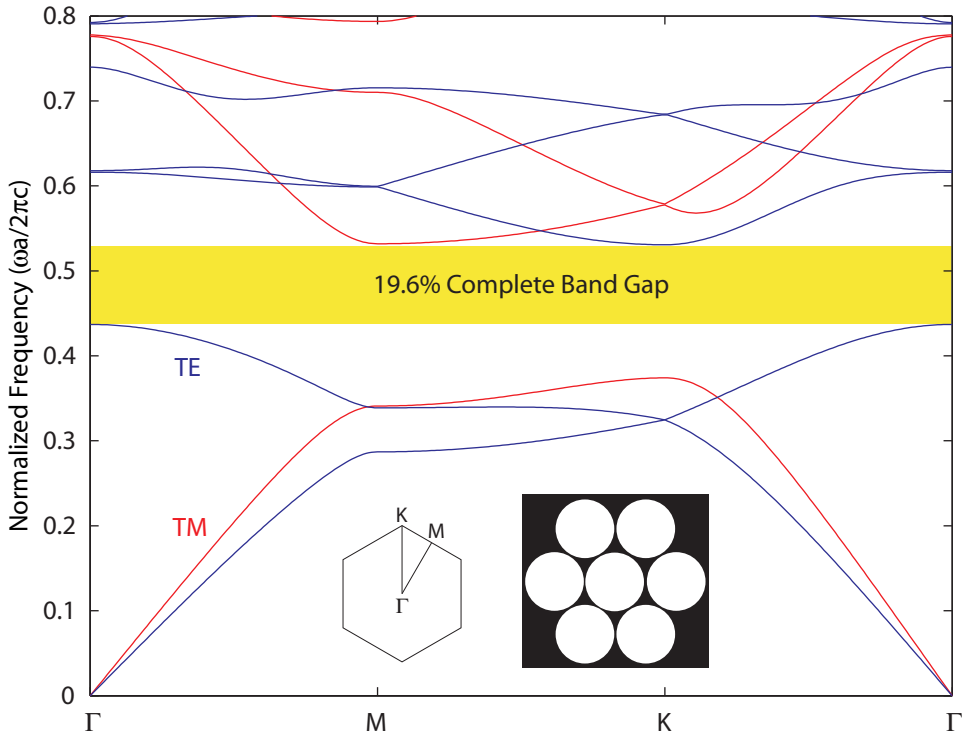

Figure 1.2: Band diagram for a hexagonal lattice of circular holes ($\epsilon_r = 1$, $r/a = 0.482$) in silicon ($\epsilon_r = 13$) exhibiting a complete band gap of 19.6%.

However, an expensive support system is needed to operate and maintain such resources. For this reason, many photonic crystal concepts have been studied and experimentally verified in the microwave [12, 27–37] and long-infrared regimes [38–41]. The photonic band gap has been, and continues to be, the basis of photonic crystal device research. Figures 1.2 and 1.3 illustrate the band diagrams for a hexagonal lattice of circular holes and a diamond square lattice of spherical vacancies respectively. Both of these structures exhibit relatively large band gaps. Figure 1.4 illustrates two experimental configurations used for band gap calculation in the microwave and long-infrared frequency ranges. In addition to the photonic band gap [1], other important physical effects have been demonstrated at microwave, infrared, and telecom wavelengths. These phenomena include the superprism effect [2–4], negative refraction [5, 6], and negative diffraction [7–9, 42]. These phenomena allow for the fabrication of a multitude of photonic crystal-based devices. Individual components that have been demonstrated include waveguides [10, 11], resonators [12–15],

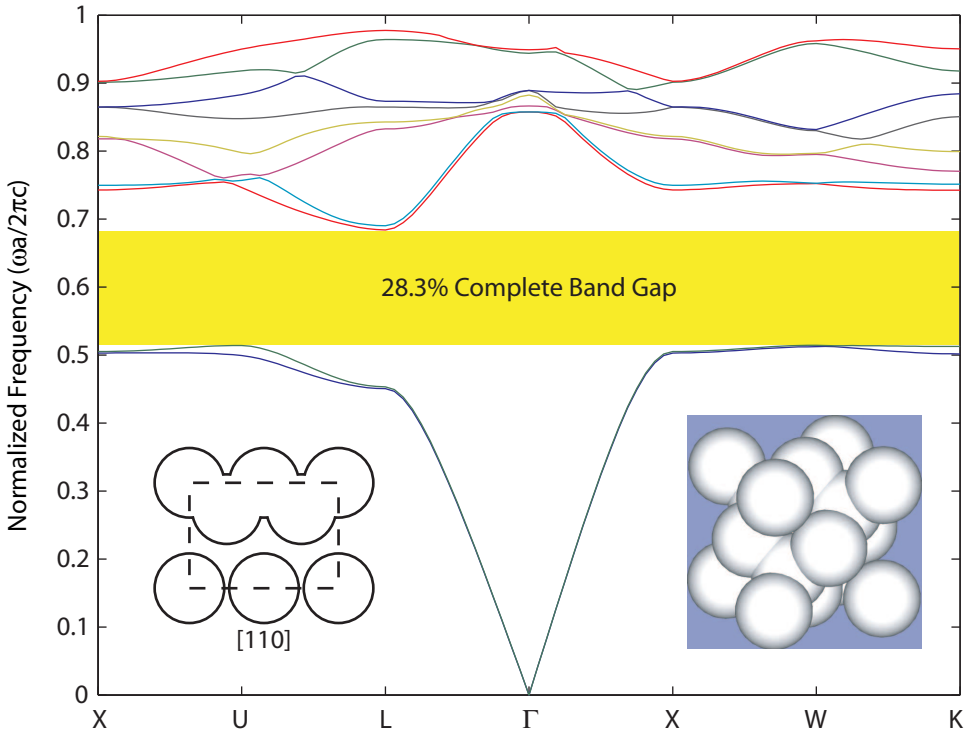

Figure 1.3: Band diagram for a diamond square lattice of (overlapping) spherical vacancies ($\epsilon_r = 1$, $r/a = 0.33$) in silicon ($\epsilon_r = 13$) exhibiting a complete band gap of 28.3%.

filters [15, 17], waveguide couplers [18–21], directional couplers [22], demultiplexers [23], antennas [24], switches [25], and sensors [26].

1.1.3 Fabrication Techniques

A number of techniques are currently used to fabricate photonic crystal structures and devices. In the microwave regime, structures can be constructed "by hand" by systematically drilling into dielectric material [43], arranging dielectric rods [27] or more complicated structures [44, 45] in a two-dimensional lattice, and stacking two-dimensionally periodic etched wafers [29]. Of course these techniques can only be employed when the periodicity of the lattices is on the order of millimeters. For structures and devices designed for operation at infrared wavelengths, more advanced micro- and nano-fabrication technologies must be utilized. Two-photon polymerization is a rapid prototyping technique used to define the polymer templates of microscale structures [46, 47]. Arbitrary two- and

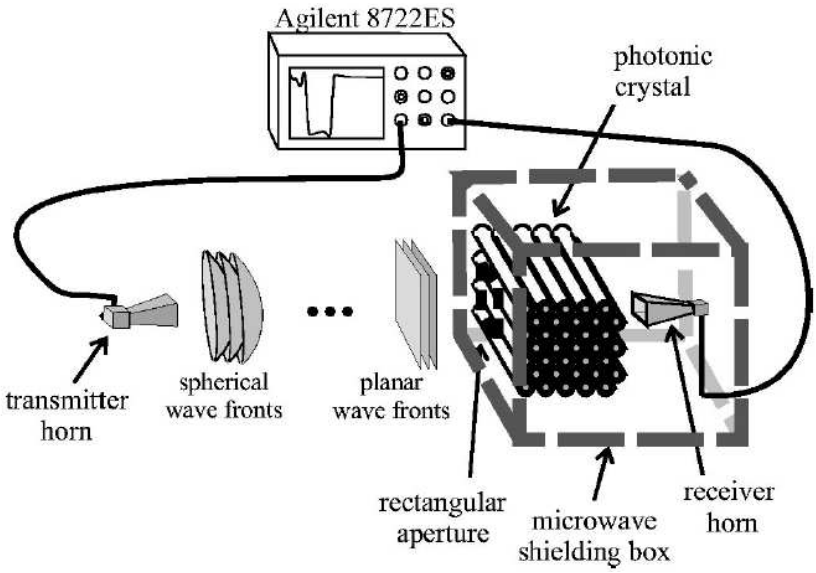

(a)

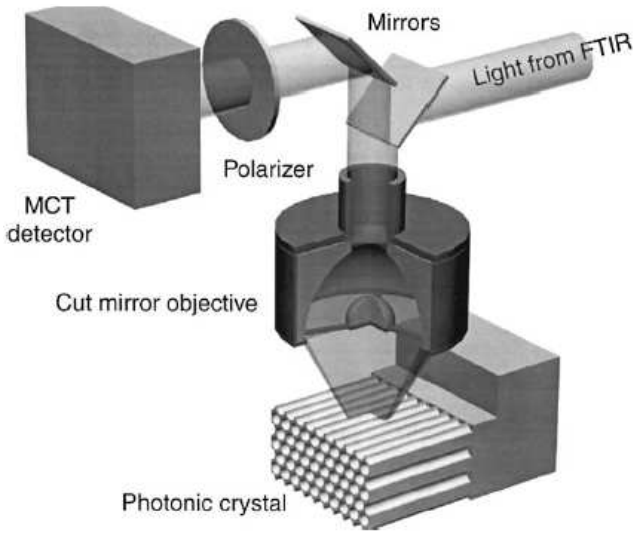

(b)

Figure 1.4: (a) Experimental configuration for measuring the photonic band gap of the photonic crystal slab (microwave regime) [34]. (b) Reflection characterization configuration using a Fourier-transform infrared spectrometer coupled to an achromatic infrared microscope (long-infrared regime) [40].

three-dimensional structures can be fabricated by simply programming the control logic of the piezoelectric stages. Focused-ion-beam (FIB) etching is yet another rapid prototyping technique [48]. FIB differs in that the pattern is machined directly into the substrate instead of a photo-reactive material. While two-photon polymerization and FIB allow for the fabrication of a multitude of complex two- and three-dimensional structures on the same wafer, there is little hope that these techniques could be used in a manufacturing setting. Given the number of components on a DIPCS, the time required to define even a single device is excessive. Self-assembly can also be used to fabricate some three-dimensional photonic crystal structures [49–55]. These techniques require depositing an aqueous colloidal suspension of nanoparticle spheres on a wafer and can result in highly ordered structures. Optical lithography and e-beam lithography are used considerably more often than the previous techniques for devices designed for operation in the long- to mid-infrared regimes (optical lithography) [38, 40, 41, 56] and at telecom wavelengths (e-beam lithography) [40, 57–59]. The resulting photoresist masks are used to pattern the substrate using a number of etching techniques including photo-electrochemical etching [38, 40, 56, 59], reactive-ion etching [60], and inductively-coupled plasma etching [41, 61]. A relatively new technique for defining the photoresist mask and polymer templates used to construct photonic crystal structures uses the interference of light called multi-beam-interference lithography (MBIL) [62–68]. By interfering two or more coherent beams of light, periodic interference patterns can be created and used to expose and define photosensitive materials for use as etching masks or templates.

Many useful photonic crystal devices for telecom wavelengths have been fabricated using e-beam lithography (EBL). The resolution and rapid prototyping capabilities of EBL make it an ideal candidate for testing small-area DIPCS. However, like many of the fabrication techniques described above, there are aspects of the technology that do not lend

Table 1.1: Fabrication Methods of Photonic Crystal Structures and Devices.

Fabrication Method	Characteristics				
	Operating wavelength	Integrated devices	Processing	Wafer scale	2D/3D
"By hand" construction	Microwave	Yes	Slow	N/A	Both
Self-assembly	IR/Vis	No	Slow	Yes	3D
Focused ion beam	IR/Vis	Yes	Slow	No	Both
Two-photon polymerization	IR/Vis	Yes	Slow	No	Both
Conventional lithography	Long-mid IR	Yes	Fast	Yes	2D
E-beam lithography	IR/Vis	Yes	Slow	No	2D
MBIL	IR/Vis	No	Fast	Yes	Both

themselves well to a manufacturing setting. E-beam lithography, like two-photon polymerization and focused ion-beam etching, is capable of creating very complex devices. Process times, however, are excessive and fabricating large-area DIPCS is not feasible. Self-assembly and MBIL are capable of highly ordered, large-area structures, but are limited to a single type of structure per process flow. Three-dimensional integrated designs make the most common lithographic techniques obsolete. For photonic crystal-based DIPCS to become a reality, a methodology is needed that will enable large-area/wafer-scale fabrication, have the capability to multiplex different devices in a single process flow, require relatively simple process recipes, and have the ability to define both two- and three-dimensional structures.

Of these methods, summarized in Table 1.1, only MBIL is applicable to two- and three-dimensional photonic crystals, requires a relatively simple process recipe, and is wafer-scale compatible. A significant drawback of MBIL is its inability to produce integrated photonic circuits containing a multiplicity of photonic crystal devices. This is in part due to the limited research in the area of device fabrication based on MBIL. In fact, there is an incomplete fundamental understanding of MBIL itself. The methodology presented in this thesis directly addresses the incomplete understanding of MBIL and will introduce a

methodology which will enable MBIL to produce integrated devices based on a photo-mask concept.

1.1.4 Multi-Beam Interference

The fabrication of two-dimensional photonic crystal structures by MBIL was demonstrated in 1997 by Berger [63, 64] and three-dimensional photonic crystal structures were demonstrated in 2000 by Campbell [65]. These resulting structures are illustrated in Fig. 1.5. The three-dimensional interference patterns used to define these structures have been modeled as plane wave interference [69–72]. While the form of the model differs in the literature, the resulting intensity distribution of N interfering plane waves can be given in the most general of terms as

$$I_T(\mathbf{r}) = \sum_{i=1}^{N} \left(\frac{1}{2} E_i^2 + \sum_{j>i}^{N} E_i E_j e_{ij} \cos((\mathbf{k}_j - \mathbf{k}_i) \cdot \mathbf{r} + \phi_i - \phi_j) \right) \tag{1.7}$$

where a single plane wave is described as

$$\boldsymbol{\mathcal{E}}_i(\mathbf{r}, t) = E_i \cos(\omega t - \mathbf{k}_i \cdot \mathbf{r} + \phi_i) \hat{\mathbf{e}}_i \, . \tag{1.8}$$

Specific configurations of wavevectors have been presented that will produce all 14 three-dimensional Bravais lattices through the interference of four noncoplanar beams [70, 71]. These are given by defining the basis vectors, given in Fig. 1.6, of these lattices by

$$\mathbf{a} = a \cdot (1, 0, 0) \tag{1.9}$$

$$\mathbf{b} = b \cdot (\cos\gamma, \sin\gamma, 0) \tag{1.10}$$

$$\mathbf{c} = c \cdot (\cos\beta, (\cos\alpha - \cos\beta\cos\gamma)/\sin\gamma, \delta) \tag{1.11}$$

where

$$\delta = [\sin^2\beta - (\cos\alpha - \cos\beta\cos\gamma)^2/\sin^2\gamma]^{1/2} \, . \tag{1.12}$$

The solutions for the four recording wavevectors and the recording wavelength are given

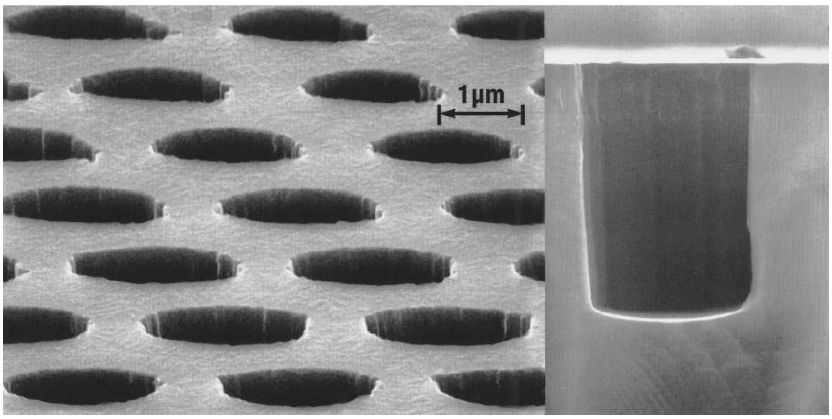

(a)

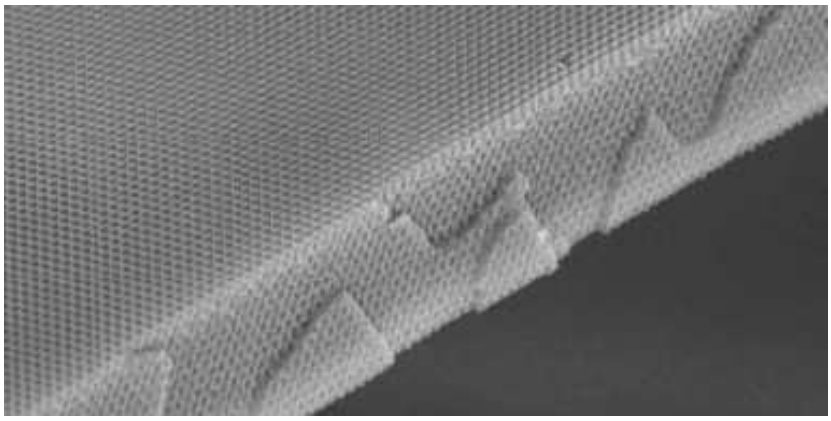

(b)

Figure 1.5: (a) Gallium arsenide sample etched by reactive ion etching through a photoresist which was exposed to the irradiance pattern of Fig. 2 in [63]. The good verticality of the etching process shows that deeper holes can easily be realized. (b) Polymeric photonic crystal generated by exposure of a 10-μm film of photoresist to the interference pattern. The top surface is a (111) plane; the film has been fractured along the $(11\bar{1})$ cleavage planes [65].

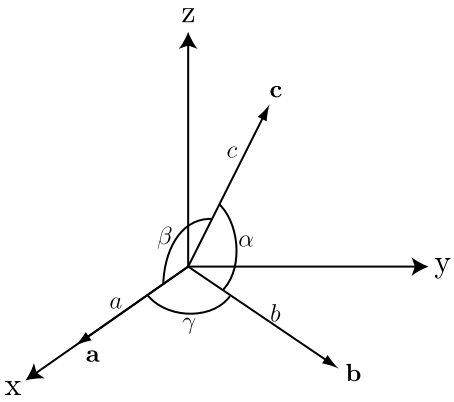

Figure 1.6: Orientation of basis vectors used to define translation symmetry of a lattice.

by

$$\mathbf{k}_1 = k_o(l, m, n) \tag{1.13}$$

$$\mathbf{k}_2 = k_o\left(l - \frac{\lambda}{a}, m + \frac{\lambda\cos\gamma}{a\sin\gamma}, n + \frac{\lambda(\cos\beta - \cos\alpha\cos\gamma)}{a\delta\sin^2\gamma}\right) \tag{1.14}$$

$$\mathbf{k}_3 = k_o\left(l, m - \frac{\lambda}{b\sin\gamma}, n - \frac{\lambda(\cos\beta\cos\gamma - \cos\alpha)}{b\delta\sin^2\gamma}\right) \tag{1.15}$$

$$\mathbf{k}_4 = k_o\left(l, m, n - \frac{\lambda}{c\delta}\right) \tag{1.16}$$

where

$$l = \frac{\lambda(bc\sin^2\alpha + ac\cos\gamma\sin^2\beta + ab\cos\beta\sin^2\gamma}{2abc\delta^2\sin^2\gamma} \tag{1.17}$$

$$m = \frac{\lambda[-b(\cos\beta\cos\gamma - \cos\alpha) + c\sin^2\beta]}{2bc\delta^2\sin\gamma} \tag{1.18}$$

$$n = \frac{\lambda}{2c\delta} \tag{1.19}$$

$$\begin{aligned}\lambda = 2abc\delta^2[a^2b^2 + b^2c^2\sin^4\alpha\csc^4\gamma + a^2c^2\sin^4\beta\csc^4\gamma + 2abc\csc^2\gamma \\ \times(a\cos\alpha\sin^2\beta + b\cos\beta\sin^2\alpha + c\cos\gamma\sin^2\alpha\sin^2\beta\csc^2\gamma)]^{-\frac{1}{2}}\ .\end{aligned} \tag{1.20}$$

From these equations, specific configurations of recording wavevectors for all 5 two-dimensional and 14 three-dimensional Bravais lattices can be calculated.

This procedure guarantees the translational symmetry of the interference pattern but fails to consider the infinite number of sets of basis vectors and the impact on the contrast and crystallography of the interference pattern. The absolute contrast and quality of the

periodic motifs that make up the interference pattern are highly dependent on the polarizations and intensities of the individual beams. To ensure that the resultant pattern as a whole is a "good" quality interference pattern, Cai [69,71] introduced a concept of *uniform contrast* defined by two simple ideas: (1) the contrast of the interference terms should be as nearly uniform as possible and (2) the contrast of the whole should be as great as possible. For both three- and four-beam interference, constraints on the intensities and polarizations of the individual beams are given to satisfy this concept of uniform contrast. However, there is an incomplete understanding of the concept of uniform contrast. A basic and incorrect assumption has been made about the form of Eq. 1.7 in terms of the coefficients of the resulting spatial cosines. In the literature, these are most often assumed to be equal and positive. If this assumption is not taken, a more thorough and complete understanding of multi-beam interference is possible.

1.1.5 Multi-Beam-Interference Lithography

A number of different photonic crystal structures have been fabricated through multi-beam interference. The first method (and currently the most common) used to perform MBIL involves splitting a single laser beam into multiple beams using beamsplitters [63–67,73,74]. The resulting beams are directed onto a sample plane at appropriate incident angles. The previous method assumes a single exposure. This results in one-dimensional interference patterns requiring at least two beams, two-dimensional interference patterns requiring at least three beams, and three-dimensional interference patterns requiring at least four beams. Less complex experimental configurations are required if multiple exposures are utilized [75,76]. Table-top beam splitting can be completely eliminated by using specially designed prisms [77], multiple diffractive elements [78], or phase-masks [79–83].

1.2 Research Objectives

Given the previous research conducted in the areas of photonic crystal technology and multi-beam-interference lithography, MBIL is a promising methodology to enable the fabrication and integration of a multiplicity of photonic crystal structures and devices, in parallel, across an entire wafer. However, for this methodology to be successful, multi-beam interference must be understood completely. Previous research has not yet uncovered the richness of its capabilities. The main objective of this research is to examine both three- and four-beam interference and its applicability to fabricating two- and three-dimensional photonic crystal structures.

The main contributions of this research are given below.

1. A general expression for the multi-beam interference of N monochromatic plane waves is derived and given. This is provided as a foundation for subsequent analysis and aims to address inconsistencies in the literature.

2. The concept of a *condition for primitive-lattice-vector-direction equal contrasts* is introduced and the appropriate nomenclature given. This condition provides a non-linear constraint for maximizing absolute contrast which results in a lithographically useful interference pattern.

3. A detailed analysis of three-beam interference is presented.

4. All *conditions for primitive-lattice-vector-direction equal contrasts* in three-beam interference are given and described. Additionally, for each condition, the subordinate condition for unity absolute contrast is given.

5. The extent of the types of crystallographic space groups that can be generated with three-beam interference is completely described.

6. A detailed analysis of four-beam interference is also presented.

7. All *conditions for primitive-lattice-vector-direction equal contrasts* in four-beam interference are given and described. Additionally, for each condition, the subordinate condition for unity absolute contrast is given.

8. Band gap maps are calculated for square and hexagonal lattices of circular holes/rods.

9. Band structures are calculated for square and hexagonal lattices of circular holes/rods that exhibit the largest band gaps.

10. Band gap maps are calculated for square and hexagonal lattices defined by three-beam interference. These are compared and contrasted to the circular cases.

11. Band structures are calculated for square and hexagonal lattices defined by three-beam interference that exhibit the largest band gaps. These are compared and contrasted to the circular cases.

12. Band gap maps are calculated for simple cubic, face-centered cubic, and body-centered cubic lattices of spherical masses/vacancies.

13. Band structures are calculated for simple cubic, face-centered cubic, and body-centered cubic lattices of spherical masses/vacancies that exhibit the largest band gaps.

14. Band gap maps are calculated for simple cubic, face-centered cubic, and body-centered cubic lattices defined by four-beam interference. These are compared and contrasted to the spherical cases.

15. Band structures are calculated for simple cubic, face-centered cubic, and body-centered cubic lattices defined by four-beam interference that exhibit the largest band gaps. These are compared and contrasted to the spherical cases.

16. A fabrication configuration for multi-beam interference is designed and constructed. This design includes a real-time monitoring capability to allow for stability analysis

and a straightforward verification of theoretical concepts without the need for processing samples.

17. The fabrication configuration is used to fabricate a number of hexagonal photonic crystals. This fabrication includes processing for both positive and negative resists. The resulting SEMs are presented.

1.3 Thesis Overview

The research objectives discussed in the previous section are rigorously examined in subsequent chapters.

Chapter 2 provides a solid and complete foundation for describing the interference of any number of monochromatic plane waves. The resulting expression is used as a basis for the analysis of both three- and four-beam interference within this thesis. Chapter 2 also provides an in depth description of three-beam interference in terms of contrast and crystallography. The concept and nomenclature for *conditions for primitive-lattice-vector-direction equal contrasts* are introduced as a more correct and complete description for nonlinear conditions that can be satisfied to produce lithographically useful interference patterns. Subordinate conditions for unity absolute contrast are also described in detail.

Chapter 3 provides an in depth description of four-beam interference. This treatment follows similarly to that in Chapter 2. This chapter describes four-beam interference in terms of contrast and the appropriate *conditions for primitive-lattice-vector-direction equal contrasts* are introduced. Similarly, subordinate conditions for unity absolute contrast are also described in detail. Three different lattices are used as examples. They are the simple cubic, the face-centered cubic, and the body-centered cubic lattices. Specific examples for each lattice are described for each *condition for primitive-lattice-vector-direction equal contrasts*.

Chapter 4 introduces modeling techniques for photonic crystals. Some conventions are described to minimize confusion within this thesis and the literature and the techniques

used to calculate the band structures in this thesis are described. This chapter focuses on comparing the band structures and resulting maximum band gaps of two-dimensional lattices of circular rods or holes to those lattice defined by three-beam interference. Both hexagonal and square lattices are examined. Band gap maps are calculated for both square and hexagonal lattices. Lattices of interest (those producing maximum band gaps) are discussed more thoroughly.

Chapter 5 focuses on comparing the band structures and resulting maximum band gaps of three-dimensional lattices of spherical masses or vacancies to those lattices defined by four-beam interference. This treatment follows similarly of that in Chapter 4. Three lattices are examined for each *condition for primitive-lattice-vector-direction equal contrasts*. They are the simple cubic, the face-centered cubic, and the body-centered cubic lattices. Unlike the two-dimensional cases presented in Chapter 4, there does not exist many structures that exhibit complete band gaps. Those that are found, though, are described in detail.

Chapter 6 describes the fabrication procedures used in this thesis to define two-dimensional photonic crystals through multi-beam interference. The design and construction of a three-beam interference configuration is described. A real-time monitoring capability is included and described for stability analysis and provides a straightforward method for verifying theoretical concepts without fabrication. This chapter also provides extensive alignment procedures and design plots for the hexagonal and square lattices. A number of hexagonal lattices are fabricated by defining both negative and positive resist. The fabrication procedures and recipes used are described.

Chapter 7 summarizes the research presented in this thesis. Potential areas of continued research are discussed.

Included within this thesis are four appendices. Appendix A provides the methods used to solve for the optimized plane wave parameters given each *condition for primitive-lattice-vector-direction equal contrasts* in both three- and four-beam interference. Using the method of Lagrangian multipliers, two formulations of the Lagrangian functions for

each condition are discussed and given. The appendix aims to provide a foundation for the method used to optimize contrast and an explanation for utilizing an enhanced formulation which resulted in more efficient calculations.

Appendix B provides program listings that can be used to replicate the band structure calculations in this thesis. These are provided as a tool for understanding the methods used to model these structures using the MIT Photonic Bands software.

Appendix C provides the complete set of band gap maps for the three-dimensional structures discussed in this thesis. While the main focus is on those structures that exhibit complete band gaps, these calculations are critical to understanding the behavior of the simple cubic, the face-centered cubic, and the body-centered cubic lattices under the different *conditions for primitive-lattice-vector-direction equal contrasts*.

Appendix D illustrates the first irreducible Brillouin zones for the lattices of interest in this thesis.

CHAPTER 2

MODELING THREE-BEAM INTERFERENCE

The analysis and modeling of multi-beam interference presented in this thesis is based upon plane wave interference. In this chapter, a systematic approach to modeling three-beam interference is presented. First, an accurate and extensive description of general multi-beam interference is given. This is done to address discrepancies in the literature and to provide a unified solid foundation for the subsequent analysis. In terms of three-beam interference, the analysis will be focused on linearly polarized light. A complete description of three-beam interference will be given in terms of contrast, absolute contrast, and crystallography. Specific solutions are given for a number of cases by presenting the optimized plane wave wave parameters and illustrations of the resulting interference patterns.

2.1 Multi-Beam Interference

To understand how parameters such as polarization and electric field amplitude affect the resulting interference patterns, an expression for the intensity distribution is needed. First, an expression for the interference of N linearly polarized, monochromatic plane waves is developed. The real electric field, $\boldsymbol{\mathcal{E}}_i$, of the ith plane wave is represented in terms of its complex vector phasor, $\mathbf{E}_i$, angular frequency, ω, initial phase, ϕ_i, and polarization vector, $\hat{\mathbf{e}}_i$, as

$$\boldsymbol{\mathcal{E}}_i(\mathbf{r}, t) = \mathbf{Re}\left[\mathbf{E}_i(\mathbf{r}) \exp(j\omega t)\right] \tag{2.1}$$

where its complex vector phasor is

$$\mathbf{E}_i(\mathbf{r}) = E_i \exp\left[-j(\mathbf{k}_i \cdot \mathbf{r} - \phi_i)\right] \hat{\mathbf{e}}_i \tag{2.2}$$

such that the resulting real field is expressed as

$$\boldsymbol{\mathcal{E}}_i(\mathbf{r}, t) = E_i \cos\left(\omega t - \mathbf{k}_i \cdot \mathbf{r} + \phi_i\right) \hat{\mathbf{e}}_i \ . \tag{2.3}$$

The time average intensity distribution for a single monochromatic plane wave, I_i, is related to the square of the electric field. This intensity is expressed as

$$\begin{aligned} I_i(\mathbf{r}) &= \langle \boldsymbol{\mathcal{E}}_i(\mathbf{r},t) \cdot \boldsymbol{\mathcal{E}}_i(\mathbf{r},t) \rangle \\ &= \frac{1}{2}\mathbf{Re}[\mathbf{E}_i(\mathbf{r}) \cdot \mathbf{E}_i^*(\mathbf{r})] \\ &= \frac{1}{2}E_i^2 \, . \end{aligned} \tag{2.4}$$

For the interference of two linearly polarized, monochromatic plane waves, the total complex electric field phasor is

$$\mathbf{E}_T(\mathbf{r}) = \mathbf{E}_1(\mathbf{r}) + \mathbf{E}_2(\mathbf{r}) \tag{2.5}$$

such that the total real field is

$$\begin{aligned} \boldsymbol{\mathcal{E}}_T(\mathbf{r},t) &= \boldsymbol{\mathcal{E}}_1(\mathbf{r},t) + \boldsymbol{\mathcal{E}}_2(\mathbf{r},t) \\ &= E_1 \cos\left(\omega t - \mathbf{k}_1 \cdot \mathbf{r} + \phi_1\right) \hat{\mathbf{e}}_1 + E_2 \cos\left(\omega t - \mathbf{k}_2 \cdot \mathbf{r} + \phi_2\right) \hat{\mathbf{e}}_2 \, . \end{aligned} \tag{2.6}$$

The time average intensity distribution for the interference pattern, I_T, is related to the square of the total electric field as

$$\begin{aligned} I_T(\mathbf{r}) &= \langle \boldsymbol{\mathcal{E}}_T(\mathbf{r},t) \cdot \boldsymbol{\mathcal{E}}_T(\mathbf{r},t) \rangle \\ &= \langle \boldsymbol{\mathcal{E}}_1(\mathbf{r},t) \cdot \boldsymbol{\mathcal{E}}_1(\mathbf{r},t) + \boldsymbol{\mathcal{E}}_2(\mathbf{r},t) \cdot \boldsymbol{\mathcal{E}}_2(\mathbf{r},t) + 2\boldsymbol{\mathcal{E}}_1(\mathbf{r},t) \cdot \boldsymbol{\mathcal{E}}_2(\mathbf{r},t) \rangle \\ &= I_1(\mathbf{r}) + I_2(\mathbf{r}) + 2J_{12}(\mathbf{r}) \end{aligned} \tag{2.7}$$

where the interference term, J_{12}, is defined as

$$\begin{aligned} J_{12}(\mathbf{r}) &= \langle \boldsymbol{\mathcal{E}}_1(\mathbf{r},t) \cdot \boldsymbol{\mathcal{E}}_2(\mathbf{r},t) \rangle \\ &= \frac{1}{2}\mathbf{Re}[\mathbf{E}_1(\mathbf{r}) \cdot \mathbf{E}_2^*(\mathbf{r})] \\ &= \frac{1}{2}E_1 E_2 e_{12} \cos((\mathbf{k}_2 - \mathbf{k}_1) \cdot \mathbf{r} + \phi_1 - \phi_2) \end{aligned} \tag{2.8}$$

and the polarization efficiency factor, e_{12}, is defined as

$$e_{12} = \hat{\mathbf{e}}_1 \cdot \hat{\mathbf{e}}_2. \tag{2.9}$$

For the interference of N linearly polarized, monochromatic plane waves, the time average intensity distribution is expressed as [84, 85]

$$\begin{aligned} I_T(\mathbf{r}) &= \langle \boldsymbol{\mathcal{E}}_T(\mathbf{r},t) \cdot \boldsymbol{\mathcal{E}}_T(\mathbf{r},t) \rangle \\ &= \left\langle \sum_{i=1}^{N} \left(\boldsymbol{\mathcal{E}}_i(\mathbf{r},t) \cdot \boldsymbol{\mathcal{E}}_i(\mathbf{r},t) + \sum_{j>i}^{N} 2\, \boldsymbol{\mathcal{E}}_i(\mathbf{r},t) \cdot \boldsymbol{\mathcal{E}}_j(\mathbf{r},t) \right) \right\rangle \\ &= \sum_{i=1}^{N} \left(I_i(\mathbf{r}) + \sum_{j>i}^{N} 2J_{ij}(\mathbf{r}) \right) \\ &= \sum_{i=1}^{N} \left(\frac{1}{2}E_i^2 + \sum_{j>i}^{N} E_i E_j e_{ij} \cos((\mathbf{k}_j - \mathbf{k}_i) \cdot \mathbf{r} + \phi_i - \phi_j) \right) . \end{aligned} \tag{2.10}$$

Equation (2.10) represents the three-dimensional interference pattern of N linearly polarized, monochromatic plane waves. Proper selection of wavevectors ($\mathbf{k}_i$), polarization vectors ($\hat{\mathbf{e}}_i$), and electric field amplitudes (E_i) can produce interference patterns with a wide range of contrast and group symmetries. Generally, these should be chosen such that the configuration produces a high-quality interference pattern.

2.2 Three-Beam Interference

In general, the interference of three linearly polarized plane waves will produce an interference pattern invariant in the z direction when the periodicity exists in the xy plane. Primitive basis vectors ($\mathbf{a}$ and $\mathbf{b}$) in the xy plane define the translational symmetry of the interference pattern. The reciprocal lattice vectors ($\mathbf{A}$ and $\mathbf{B}$) are expressed as

$$\begin{aligned} \mathbf{A} &= 2\pi \frac{\mathbf{b} \times \hat{\mathbf{z}}}{\mathbf{a} \cdot \mathbf{b} \times \hat{\mathbf{z}}} \\ \mathbf{B} &= 2\pi \frac{\hat{\mathbf{z}} \times \mathbf{a}}{\mathbf{a} \cdot \mathbf{b} \times \hat{\mathbf{z}}} . \end{aligned} \tag{2.11}$$

For three-beam interference, the three recording wavevectors are found by finding the circumcenter vector ($\mathbf{P}$) of a triangle defined by the two reciprocal lattice vectors $\mathbf{A}$ and $\mathbf{B}$ by

$$\mathbf{P} = \frac{1}{2} \frac{|\mathbf{A}|^2 (\mathbf{B} \times \hat{\mathbf{z}}) + |\mathbf{B}|^2 (\hat{\mathbf{z}} \times \mathbf{A})}{\mathbf{A} \cdot \mathbf{B} \times \hat{\mathbf{z}}} . \tag{2.12}$$

The projections of the recording wavevectors on the xy plane are then defined as vectors from the circumcenter to each vertex such that

$$\mathbf{k}_{1,xy} = -\mathbf{P} \tag{2.13}$$

$$\mathbf{k}_{2,xy} = \mathbf{A} - \mathbf{P} \tag{2.14}$$

$$\mathbf{k}_{3,xy} = \mathbf{B} - \mathbf{P}\,. \tag{2.15}$$

The z component of the individual wavevectors is adjusted accordingly such that

$$|\mathbf{k}_i| = nk_o \tag{2.16}$$

where $k_o = 2\pi/\lambda$ and n is the index of refraction of the recording medium. In general, the relationship between the set of basis vectors and the recording wavelength is

$$\frac{\lambda}{n} \leq \frac{2\sin^2\gamma}{(\frac{1}{|\mathbf{a}|^2} + \frac{1}{|\mathbf{b}|^2} + \frac{2\cos\gamma}{|\mathbf{a}||\mathbf{b}|})^{\frac{1}{2}}} \tag{2.17}$$

where γ is the angle between $\mathbf{a}$ and $\mathbf{b}$. The significance of Eq. (2.17) must be fully understood. A given two-dimensional lattice has an infinite number of sets of primitive basis vectors that can define the translation symmetry of the lattice. Given the methodology above, two different sets of primitive basis vectors that define the same translational symmetry will not provide an identical set of recording wavevectors. While the translational symmetry of the interference patterns will be identical, the locations of other symmetry elements will differ. Thus, given the methodology above, the choice of $\mathbf{a}$ and $\mathbf{b}$ corresponds not only to a particular translational symmetry of the final interference pattern, but also to other symmetry elements and their locations within a primitive unit cell.

Equation (2.10) is rewritten for the three-beam case. Without losing a general sense of the intensity contours of the interference pattern, the initial phases of the interfering beams are set to zero ($\phi_i = 0$) if no two interfering wavevectors are equal. With this assumption, Eq. (2.10) reduces to

$$I_T = I_0\Big[1 + V_{12}\cos(\mathbf{G}_{21}\cdot\mathbf{r}) + V_{13}\cos(\mathbf{G}_{31}\cdot\mathbf{r}) + V_{23}\cos(\mathbf{G}_{32}\cdot\mathbf{r})\Big] \tag{2.18}$$

where the DC intensity term is

$$I_0 = \frac{1}{2}\sum_{k=1}^{3} E_k^2, \tag{2.19}$$

the interference coefficient is

$$V_{ij} = \frac{E_i E_j e_{ij}}{I_0}, \tag{2.20}$$

and the spatial wavevector is

$$\mathbf{G}_{ij} = \mathbf{k}_i - \mathbf{k}_j \, . \tag{2.21}$$

It should be noted that there is a fundamental relationship between the desired reciprocal lattice vectors and the spatial wavevectors $\mathbf{G}_{ij}$'s. $\mathbf{A}$ and $\mathbf{B}$ correspond to $\mathbf{G}_{21}$ and $\mathbf{G}_{31}$, respectively, while $\mathbf{G}_{32}$ is a dependent reciprocal lattice vector, defined as $(\mathbf{G}_{31} - \mathbf{G}_{21})$ or $(\mathbf{B} - \mathbf{A})$.

If $\phi_i = 0$, the lattice points are defined at the origin ($\mathbf{r} = 0$) and all equivalent points in the two-dimensional periodic interference pattern. In general, the lattice points are defined at

$$\mathbf{p} = -\frac{g_{12}(\mathbf{G}_{31} \times \hat{\mathbf{z}}) + g_{13}(\hat{\mathbf{z}} \times \mathbf{G}_{21})}{\mathbf{G}_{21} \cdot (\mathbf{G}_{31} \times \hat{\mathbf{z}})} \, , \tag{2.22}$$

where

$$g_{ij} = \phi_i - \phi_j \, , \tag{2.23}$$

and all equivalent points in the three-dimensional periodic interference pattern.

2.3 Contrast

Of the seventeen plane symmetry groups, five of these can be realized through the interference of three linearly polarized plane waves [72]. These are the *p2*, *pmm*, *cmm*, *p4m*, and *p6m* plane symmetry groups. Here we analyze each of the five plane symmetry groups and discuss how contrast affects the overall quality of the interference pattern produced.

Absolute contrast (V_{abs}) is a function of the intensity extrema in an intensity distribution and is defined as

$$V_{abs} = \frac{I_{max} - I_{min}}{I_{max} + I_{min}} \tag{2.24}$$

where I_{max} and I_{min} are the maximum and minimum intensities, respectively. Two equivalent primitive unit cell representations are used in this section: 1) the conventional primitive unit cell defined by **a** and **b** and 2) the Wigner-Seitz proximity primitive unit cell whose sides are perpendicular bisectors of the shortest lattice vectors. The boundaries of the conventional unit cell and the Wigner-Seitz proximity unit cell will be shown in the subsequent figures as dashed and dotted lines, respectively. The latter are centered at $\mathbf{r} = 0$. All of the *xy* plane can be filled by either unit cell with translations by integer combinations of the primitive basis vectors. Each primitive unit cell contains all of the information about the interference pattern. Consistent with the previous assumption that $\phi_i = 0$, an intensity maximum or minimum occurs at the $\mathbf{r} = 0$ lattice point (and consequently at all lattice points throughout the interference pattern).

The quality of the interference pattern can be improved by applying and optimizing one of two *conditions for primitive-lattice-vector-direction equal contrasts* [84, 85]. High-quality patterns will have high absolute contrast and exhibit equal contrasts in multiple lattice-vector directions. This results in localized areas of intensity extrema at the lattice points. This is important for two reasons: 1) in lithography, photoresist more readily delineates patterns in response to high-contrast intensity distributions and 2) the resulting intensity distribution will have equal modulation of intensity in multiple basis vector directions through each lattice point. In a fabricated structure defined by three-beam interference, this produces isolated, oval rods (or cavities) at lattice points instead of a continuous structure (or continuous void) between lattice points.

The nonlinear constraints applied during the optimization determine the locations of symmetry elements within the unit cell of the periodic interference pattern. Lithographically speaking, these determine the shape of the intensity contours that will define the final structures. Within three-beam interference, there is one set of nonlinear constraints that has been applied during the optimization process and is referred to in the literature as the *uniform contrast condition* [69, 84]. These lithographically useful interference patterns

are produced by choosing the plane wave parameters such that all three interference coefficients V_{ij} are equal. Mathematically, the resulting interference patterns have equal contrasts in the two primitive lattice vector directions (**a**, **b**) from each lattice point. If the assumption about including all three interference coefficients is relaxed, a more fundamental and complete understanding of multi-beam interference is possible, while still achieving equal contrasts in more than one primitive lattice vector direction. That is, all three interference coefficients do not have to be equal and positive. Avoiding the previously ambiguous terminology of *uniform contrast* [69, 71, 84], a more descriptive nomenclature is introduced here: namely, *condition for primitive-lattice-vector-direction equal contrasts*.

In actuality, multiple *conditions for primitive-lattice-vector-direction equal contrasts* for multi-beam-interference lithography exist including the three-beam interference case treated in this section. For two-dimensionally periodic interference patterns produced through three-beam interference, there are three spatial cosines as described by Eq. (2.18). However, only two are required to produce two-dimensional periodicity. Consequently, two *conditions for primitive-lattice-vector-direction equal contrasts* exist. Based on the present research, a symbolic designation $C_n^{(m)}$ is introduced to differentiate between the various *conditions for primitive-lattice-vector-direction equal contrasts*. The quantity n is the total number of interfering beams and m the number of nonzero interference coefficients (number of interfering-beam pairs). Consequently, the resulting non-zero interference coefficients V_{ij} of Eq. (2.18) are denoted by $V_n^{(m)}$ similarly. In our previously published work for three-beam interference [84], a second *uniform contrast condition* was introduced along with the original *uniform contrast condition*. However, given the new nomenclature and symbolic designation introduced in this work, a more complete description is denoted by $C_3^{(3)}$ and $C_3^{(2)}$ for the first and second *uniform contrast conditions*, respectively, for three-beam interference [84].

Considering our previous work [84] and work that is presented here, it is important to note the relationships between the interference coefficient $V_n^{(m)}$ and the absolute contrast

V_{abs}. This indicates that configurations of wavevectors and polarizations can result in interference coefficients that are positive *or* negative. The physical meaning of this statement is as follows: if a configuration satisfies a *condition for primitive-lattice-vector-direction equal contrasts* and results in a *positive* interference coefficient, $V_n^{(m)} > 0$, volumes of *high electric field intensity* surround the lattice points. Similarly, if a configuration satisfies a *condition for primitive-lattice-vector-direction equal contrasts* and results in a *negative* interference coefficient, $V_n^{(m)} < 0$, volumes of *low electric field intensity* surround the lattice points. However, regardless of the sign or magnitude of the interference coefficient, $V_n^{(m)}$, determined by the polarization states and amplitudes of the recording beams, the intensity contours will be identical (but differing in intensity value) provided the recording wavevectors remain unchanged. Consequently, another superscript can be added to the given symbolic designation to describe more accurately the interference pattern resulting in ${}^{\pm}C_n^{(m)}$ where ± denotes either a *positive* or *negative* interference coefficient. This concept of positive and negative interference coefficients enables the pairing of the interference pattern with positive and negative photoresists in a manner analogous to pairing positive and negative photoresist with light- and dark-field masks in conventional lithography. Given a particular lithographic process chemistry, a designer has the ability to choose between these "light-field" and "dark-field" interference patterns.

2.3.1 Condition for primitive-lattice-vector-direction equal contrasts $C_3^{(3)}$

The first *condition for primitive-lattice-vector-direction equal contrasts* ($C_3^{(3)}$) is satisfied by choosing the plane wave properties such that the three interference coefficients (V_{ij}) in Eq. (2.18) are equal [71]. The interference coefficient ($V_3^{(3)}$) is defined as

$$V_3^{(3)} = V_{12} = V_{13} = V_{23} \ \ [\text{Condition } C_3^{(3)}] \ . \tag{2.25}$$

This condition of equal contrasts guarantees that at each lattice point, an equal modulation of intensity occurs in three lattice directions (**a**, **b**, and **a** + **b**). It also dictates that the other, opposite intensity extrema will lie at $2\mathbf{a}/3 + \mathbf{b}/3$ and $\mathbf{a}/3 + 2\mathbf{b}/3$ from each lattice point.

This corresponds to the centroids of three lattice points defined by two sets of vectors: the first being **a** and **a** + **b** and the second being **b** and **a** + **b**. For three-beam-interference, constraints on the electric field amplitudes, E_i, as a function of the polarization states, $\hat{\mathbf{e}}_i$, exist for $C_3^{(3)}$ to be satisfied. The constraints are [69]

$$E_2 = \frac{e_{13}}{e_{23}} E_1 \tag{2.26}$$

$$E_3 = \frac{e_{12}}{e_{23}} E_1 \ . \tag{2.27}$$

When the constraints in Eqs. (2.26) and (2.27) are satisfied, Eq. (2.20) is simplified to

$$V_3^{(3)} = \frac{2e_{12}e_{13}e_{23}}{e_{12}^2 + e_{13}^2 + e_{23}^2} \ . \tag{2.28}$$

A relationship between the interference coefficient ($V_3^{(3)}$) and the absolute contrast (V_{abs}) exist. For three-beam interference, the relationship is

$$V_{abs} = \left| \frac{9}{4/V_3^{(3)} + 3} \right| \ . \tag{2.29}$$

In summary, $C_3^{(3)}$ is defined as follows [84, 85]:

> The first *condition for primitive-lattice-vector-direction equal contrasts* is satisfied when the parameters of the three recording beams are chosen such that all three interference coefficients (V_{ij}) are equal. This results in an interference pattern in which 1) from each lattice point, there is equal modulation of intensity in the **a**, **b**, and **a** + **b** directions, and 2) in each primitive unit cell there is one intensity maxima (minima) located at the lattice point and two equivalent intensity minima (maxima) at $2\mathbf{a}/3 + \mathbf{b}/3$ and $\mathbf{a}/3 + 2\mathbf{b}/3$ from the lattice point.

2.3.1.1 Subordinate condition for unity absolute contrast for $^{+}C_3^{(3)}$

While this equal contrasts condition guarantees equal modulation of intensity in specific lattice directions, maximization of the absolute contrast in Eq. (2.29) is a separate operation. This corresponds to either the maximization or minimization of the interference coefficient

($V_3^{(3)}$). From Eq. (2.29), solutions with values of $V_3^{(3)} = 2/3$ or $-1/3$ for $C_3^{(3)}$ result in unity absolute contrast ($V_{abs} = 1$, $I_{min} = 0$); however this may not always be achievable given an arbitrary arrangement of wavevectors. An optimal solution is one that maximizes absolute contrast, while satisfying one of the two *conditions for primitive-lattice-vector-direction equal contrasts*. This ensures that the interference pattern produced can easily be imaged in a photosensitive material. In general, this process of maximizing the contrast can be performed through constrained nonlinear optimization. As derived above, absolute contrast (V_{abs}) is related to the interference coefficient $V_3^{(3)}$ when the $C_3^{(3)}$ *condition for primitive-lattice-vector-direction equal contrasts* is satisfied. Maximization or minimization of the interference coefficient will in turn maximize absolute contrast. Modern personal computers are able to perform this optimization in a few seconds. Detailed information regarding the approach used to determine these optimized parameters is described in Appendix A.

Finding an optimal solution that satisfies $C_3^{(3)}$ is more involved than for $C_3^{(2)}$, because two fundamentally different types of interference patterns exist that result from satisfying $C_3^{(3)}$. These two cases can be identified by the sign of the interference coefficient ($V_3^{(3)}$) from Eq. (2.28). If a solution is found such that the sign of $V_3^{(3)}$ is positive, maximum intensity extrema will be located at the lattice points. Conversely, if a solution is found such that the sign of $V_3^{(3)}$ is negative, minimum intensity extrema will be located at the lattice points. Considering all possible solutions to Eq. (2.28) for optimal values of the interference coefficient ($V_3^{(3)} = 2/3$ or $-1/3$) subject to the allowed values of the efficiency terms (e_{ij}), given by the inequalities

$$|e_{13} + e_{23}| \leq 2\cos\left(\frac{\cos^{-1}(e_{12})}{2}\right) \tag{2.30}$$

$$|e_{12} + e_{23}| \leq 2\cos\left(\frac{\cos^{-1}(e_{13})}{2}\right) \tag{2.31}$$

$$|e_{12} + e_{13}| \leq 2\cos\left(\frac{\cos^{-1}(e_{23})}{2}\right), \tag{2.32}$$

only two sets of solutions to obtain unity absolute contrast exist. For $V_3^{(3)} = 2/3$, unity absolute contrast occurs when the solution satisfies the following (corresponding to 4 solutions:

all signs are positive or two signs are negative):

$$e_{12} = \pm 1 \tag{2.33}$$

$$e_{13} = \pm 1 \tag{2.34}$$

$$e_{23} = \pm 1 \ . \tag{2.35}$$

This results in electric field amplitudes of

$$E_2 = \pm E_1 \tag{2.36}$$

$$E_3 = \pm E_1 \ . \tag{2.37}$$

This solution describes an impractical configuration for three-beam interference in which all recording wavevectors are coplanar and is not necessarily experimentally achievable. Thus, in general, an optimization must be performed to solve for a solution that maximizes absolute contrast for $V_3^{(3)} > 0$.

2.3.1.2 Subordinate condition for unity absolute contrast for ${}^{-}C_3^{(3)}$

For $V_3^{(3)} = -1/3$, unity absolute contrast occurs when the solution satisfies the following (corresponding to 4 solutions: all signs are negative or two signs are positive):

$$e_{12} = \pm \frac{1}{2} \tag{2.38}$$

$$e_{13} = \pm \frac{1}{2} \tag{2.39}$$

$$e_{23} = \pm \frac{1}{2} \ . \tag{2.40}$$

This results in electric field amplitudes of

$$E_2 = \pm E_1 \tag{2.41}$$

$$E_3 = \pm E_1 \ . \tag{2.42}$$

The physical representation of Eqs. (2.38)-(2.40) implies that all three of the polarization vectors are coplanar and make equal angles (120°) with each other [or any combination of

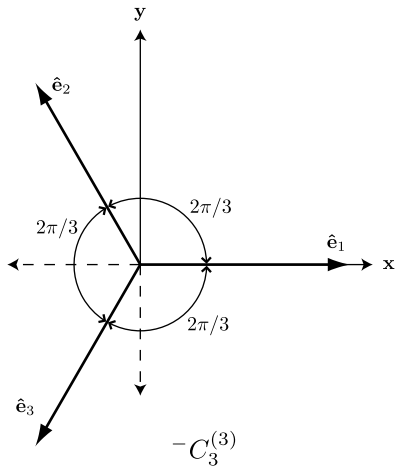

Figure 2.1: Orientation of polarizations for the subordinate condition for unity absolute contrast [or any combination of the polarization vectors ($\hat{\mathbf{e}}_i$) where one, multiple, or all are inverted ($-\hat{\mathbf{e}}_i$)] for $^{-}C_3^{(3)}$ where $V_3^{(3)} = -1/3$.

the polarization vectors ($\hat{\mathbf{e}}_i$) where one, multiple, or all are inverted ($-\hat{\mathbf{e}}_i$)]. The orientation of the resulting polarization vectors described in Eqs. (2.38)-(2.40) is illustrated in Fig. 2.1. In general, solutions of this form in which unity absolute contrast is achieved ($V_{abs} = 1$), while satisfying $C_3^{(3)}$ for $V_3^{(3)} = -1/3$ *always* exist. This can be proven using the following approach. In an arbitrary case, $\mathbf{k}_1$ and $\mathbf{k}_2$ represent two of the three recording wavevectors. All combinations of polarizations, $\hat{\mathbf{e}}_1$ and $\hat{\mathbf{e}}_2$, such that $e_{12} = 1/2$ can be found. For each combination, a third polarization vector, $\hat{\mathbf{e}}_3$, can be calculated such that $e_{13} = e_{23} = 1/2$. These calculated polarization vectors, for $\hat{\mathbf{e}}_3$, will trace out a line in three-dimensional space such that the polarization space of any third recording wavevector will include at least two points on this line, each corresponding to a solution that satisfies $C_3^{(3)}$ and unity absolute contrast is achieved.

2.3.2 Condition for primitive-lattice-vector-direction equal contrasts $C_3^{(2)}$

The second *condition for primitive-lattice-vector-direction equal contrasts* ($C_3^{(2)}$) is satisfied by choosing the plane wave properties such that two of the interference coefficients in Eq. (2.18) are equal and the third is zero. For example,

$$V_3^{(2)} = V_{12} = V_{13},\ V_{23} = 0\ \ [\text{Condition } C_3^{(2)}]\ . \tag{2.43}$$

This condition of equal contrasts guarantees that at each lattice point, an equal modulation of intensity occurs in two primitive lattice directions (**a** and **b**). It also dictates that the other, opposite intensity extrema will lie at $\mathbf{a}/2 + \mathbf{b}/2$ from each lattice point. This corresponds to the centroid of a parallelogram defined by the set of vectors **a** and **b**. For three-beam-interference, constraints on the polarization states, $\hat{\mathbf{e}}_i$, and electric field amplitudes, E_i, for this *condition for primitive-lattice-vector-direction equal contrasts* to be satisfied exist. The constraints are

$$e_{23} = 0 \tag{2.44}$$

$$E_3 = \frac{e_{12}}{e_{13}} E_2 \ . \tag{2.45}$$

When the constraints in Eqs. (2.44) and (2.45) are satisfied, Eq. (2.20) simplifies to

$$V_3^{(2)} = \frac{2E_1E_2e_{12}e_{13}^2}{E_1^2e_{13}^2 + E_2^2e_{13}^2 + E_2^2e_{12}^2} \ . \tag{2.46}$$

A relationship between the interference coefficient ($V_3^{(2)}$) and the absolute contrast (V_{abs}) exist. For three-beam-interference, the relationship is

$$V_{abs} = \left|2V_3^{(2)}\right| \ . \tag{2.47}$$

Given a configuration of polarizations that satisfy Eqs. (2.44) and (2.45), the absolute contrast [or interference coefficient in Eq. (2.46)] is maximized by setting the electric field ratio E_2/E_1 equal to

$$\frac{E_2}{E_1} = \frac{e_{13}}{\sqrt{e_{12}^2 + e_{13}^2}} \ . \tag{2.48}$$

The interference coefficient can then be rewritten solely in terms of polarization as

$$V_3^{(2)} = \frac{2e_{12}e_{13}}{\sqrt{e_{12}^2 + e_{13}^2}} \ . \tag{2.49}$$

In summary, $C_3^{(2)}$ is defined as follows [84, 85]:

> The second *condition for primitive-lattice-vector-direction equal contrasts* is satisfied when the parameters of the three recording beams are chosen such

that two interference coefficients (V_{ij}) are equal and the third is zero. With $V_{23} = 0$, this results in an interference pattern in which 1) from each lattice point, there is equal modulation of intensity in the **a** and **b** directions, and 2) in each primitive unit cell there is one intensity maxima (minima) located at the lattice point and one intensity minima (maxima) at $\mathbf{a}/2 + \mathbf{b}/2$ from the lattice point.

It should be noted that $C_3^{(2)}$ can be applied with two other sets of constraints. While it was arbitrarily chosen to set $V_{23} = 0$, either of the other two interference coefficients can be set to zero. However, the description for the locations of the other intensity extrema and directions of equal modulation of intensity will differ. In the discussions following, references to $C_3^{(2)}$ will assume the derivation above.

2.3.2.1 Subordinate condition for unity absolute contrast for $C_3^{(2)}$

Finding an optimal solution that satisfies $C_3^{(2)}$ is performed similarly. Considering all possible solutions to Eq. (2.49) for optimal values of the interference coefficient ($V_3^{(2)} = \pm 1/2$) subject to the allowed values of the efficiency terms (e_{ij}), given by the inequality

$$|e_{12} + e_{13}| \leq \frac{\sqrt{2}}{2}, \tag{2.50}$$

only one set of solutions to obtain unity absolute contrast exists. This occurs when the solution satisfies the following (corresponding to 4 solutions):

$$e_{12} = \pm\frac{\sqrt{2}}{2} \tag{2.51}$$

$$e_{13} = \pm\frac{\sqrt{2}}{2} \tag{2.52}$$

$$e_{23} = 0\ . \tag{2.53}$$

This results in electric field amplitudes of

$$E_2 = \pm\frac{\sqrt{2}}{2}E_1 \tag{2.54}$$

$$E_3 = \pm\frac{\sqrt{2}}{2}E_1\ . \tag{2.55}$$

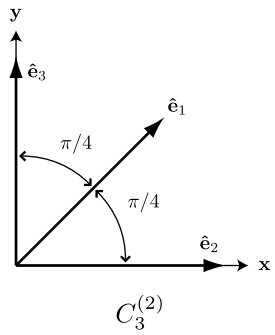

Figure 2.2: Orientation of polarizations for the subordinate condition for unity absolute contrast [or any combination of the polarization vectors ($\hat{\mathbf{e}}_i$) where one, multiple, or all are inverted ($-\hat{\mathbf{e}}_i$)] for $C_3^{(2)}$ where $V_3^{(2)} = 1/2$.

The physical representation of Eq. (2.51) implies that all three of the polarization vectors are coplanar, such that $\hat{\mathbf{e}}_2$ and $\hat{\mathbf{e}}_3$ are orthogonal and $\hat{\mathbf{e}}_1$ bisects the other two [or any combination of the polarization vectors ($\hat{\mathbf{e}}_i$) where one, multiple, or all are inverted ($-\hat{\mathbf{e}}_i$)]. The orientation of the resulting polarization vectors described in Eq. (2.51) is illustrated in Fig. 2.2. In general, solutions of this form in which unity absolute contrast is achieved ($V_{abs} = 1$), while satisfying $C_3^{(2)}$ for $V_3^{(2)} = \pm 1/2$ *always* exist. This can be proven using a similar methodology to that above.

Finding solutions that exhibit unity absolute contrast ($V_{abs} = 1, I_{min} = 0$) that satisfy $C_3^{(3)}$ (with $V_3^{(3)} < 0$) or $C_3^{(2)}$ rely on total destructive interference. This ensures that at some points in space, $I_T = 0$. However, this occurs for only one of two fundamentally different interference patterns when maximizing absolute contrast, while satisfying $C_3^{(3)}$. The sign of $V_3^{(2)}$ does not distinguish between different types of interference patterns for $C_3^{(2)}$ because the contours of the motifs around intensity maxima and minima are identical for $V_3^{(2)}$ interference patterns. Given a bias intensity value of I_b (where $I_{min} \leq I_b \leq I_{max}$), these two identical surfaces are described as

$$\begin{aligned} I_{max} - I_b &= I(\mathbf{r}) \\ I_{min} + I_b &= I(\mathbf{r} + \mathbf{a}/2 + \mathbf{b}/2) \end{aligned} \tag{2.56}$$

Two interference patterns with coefficients of $V_3^{(2)}$ and $-V_3^{(2)}$ are identical when either is translated by $\mathbf{a}/2 + \mathbf{b}/2$. The sign of $V_3^{(2)}$ does, however, determine whether an intensity

maxima ($V_3^{(2)} > 0$) or minima ($V_3^{(2)} < 0$) is located at a lattice point ($\mathbf{r} = 0$). This distinction based upon the sign of the interference coefficient is similar to the use of dark and light field masks in conventional lithography. The choice of one type of interference pattern over another (or the use of dark or light field masks) will depend upon process parameters. However, maximizing absolute contrast for $C_3^{(3)}$ with $V_3^{(3)} > 0$ is more complicated and explicit solutions can only be expressed in a few situations of higher-order symmetry.

2.4 Crystallography in Three-Beam Interference

2.4.1 Plane Symmetry Group *p2*

The *p2* plane symmetry group is obtained from general three-beam-interference. This plane group is characterized as having four unique points of 2-fold symmetry, as shown in Fig. 2.3. This figure also illustrates the symmetry elements and their general locations for each of the seventeen plane groups [71]. Of these, the interference patterns of three linearly polarized plane waves can exhibit the symmetry in five of these plane groups, while an additional four are possible if elliptical polarization is utilized [72]. Figure 2.3 can be used to identify the symmetry elements present in any two-dimensional interference pattern.

Higher-order symmetry groups will emerge as relationships between primitive basis vectors and interference coefficients vary. The values of contrast for interference patterns with this symmetry range from 0 to 1, depending on the constraints applied. However, both *conditions for primitive-lattice-vector-direction equal contrasts* can be applied and absolute contrast maximized to obtain unity absolute contrast ($V_{abs} = 1$), provided sets of constraints are not satisfied for higher-order plane groups. Contrast for interference patterns with higher-order symmetries will be discussed in more detail later.

2.4.2 Plane Symmetry Group *pmm*

The *pmm* symmetry group is the next higher symmetry plane group obtainable with three-beam interference. This plane group is characterized as having four unique reflection axes and four unique points of 2-fold symmetry, as shown in Fig. 2.3. This plane symmetry

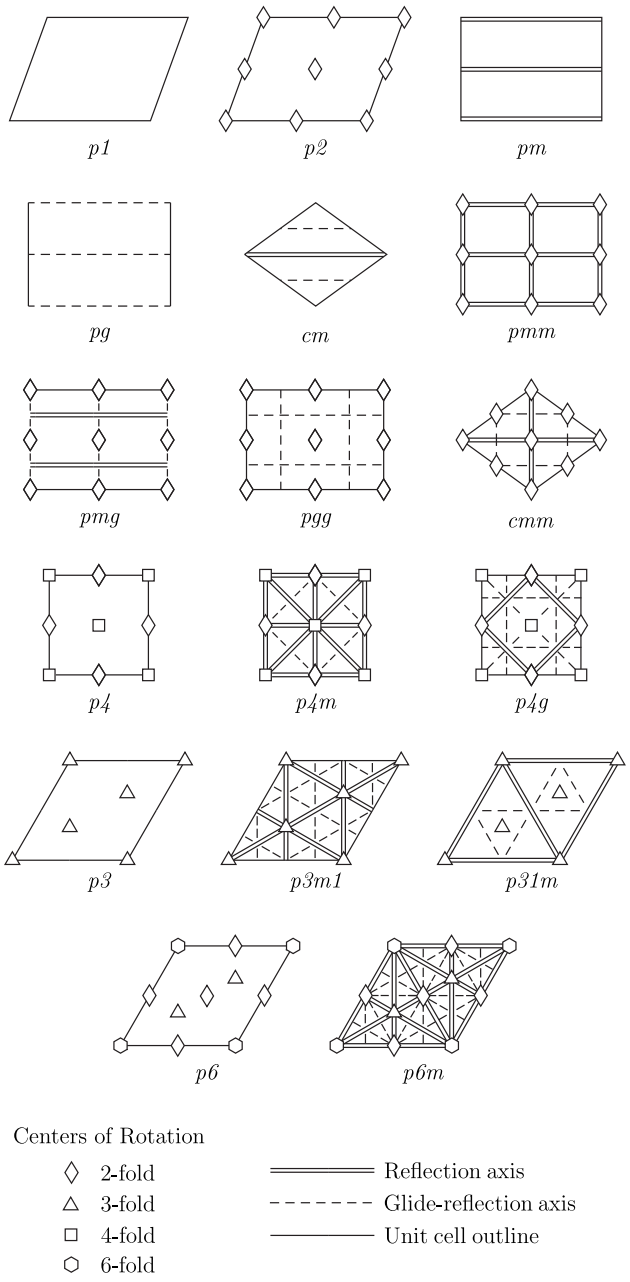

Figure 2.3: Seventeen plane groups. Illustration shows locations of symmetry elements for each plane group [86]. Unit cell outlines correspond to conventional primitive unit cells illustrated in subsequent figures as dashed lines.

group is realized when plane wave parameters are chosen such that they satisfy one of three sets of constraints:

1. $V_{23} = 0$ ($e_{23} = 0$) and $\mathbf{a} \cdot \mathbf{b} = 0$

2. $V_{12} = 0$ ($e_{12} = 0$) and $\mathbf{a} \cdot (\mathbf{a} + \mathbf{b}) = 0$

3. $V_{13} = 0$ ($e_{13} = 0$) and $\mathbf{b} \cdot (\mathbf{a} + \mathbf{b}) = 0$.

When one of these sets of constraints is satisfied, only two of the three interference terms are present in Eq. (2.18) and the corresponding spatial wavevectors ($\mathbf{G}_{ij}$) are orthogonal. Ensuring that $V_{ij} = 0$ is not the only constraint for $C_3^{(2)}$. However, this symmetry can still exist when $C_3^{(2)}$ is satisfied until parameters satisfy constraints for the *p4m* plane symmetry group, which arises when $C_3^{(2)}$ is satisfied and a set of primitive basis vectors ($\mathbf{a}$ and $\mathbf{b}$, $\mathbf{a}$ and $\mathbf{a} + \mathbf{b}$, or $\mathbf{a} + \mathbf{b}$ and $\mathbf{b}$) are equal in magnitude. Typical interference patterns exhibiting *pmm* plane group symmetry can be seen in Fig. 2.4 and Fig. 2.5 along with the corresponding design parameters.

The interference patterns illustrated in this section are constructed such that a full range of intensity contours can be observed. Overlayed on these contour plots are normalized, semi-transparent gray-scale images of the interference patterns. These images, however, are to illustrate locations of intensity extrema and not an indication of actual absolute contrast.

The situations in both figures begin with an identical set of basis vectors and identical polarization unit vectors. Figure 2.4 satisfies $C_3^{(2)}$, while Fig. 2.5 does not satisfy any *condition for primitive-lattice-vector-direction equal contrasts*. Since $C_3^{(2)}$ is satisfied and absolute contrast is maximized in Fig. 2.4, it exhibits unity absolute contrast ($V_{abs} = 1$) with an interference coefficient $V_3^{(2)} = 1/2$. Figure 2.5 does not satisfy a *condition for primitive-lattice-vector-direction equal contrasts* and has an absolute contrast of $V_{abs} = 0.585$. For the *pmm* plane group, absolute contrast can vary from 0 to 1, depending upon the chosen plane wave parameters. However, when $C_3^{(2)}$ can be applied and absolute contrast is

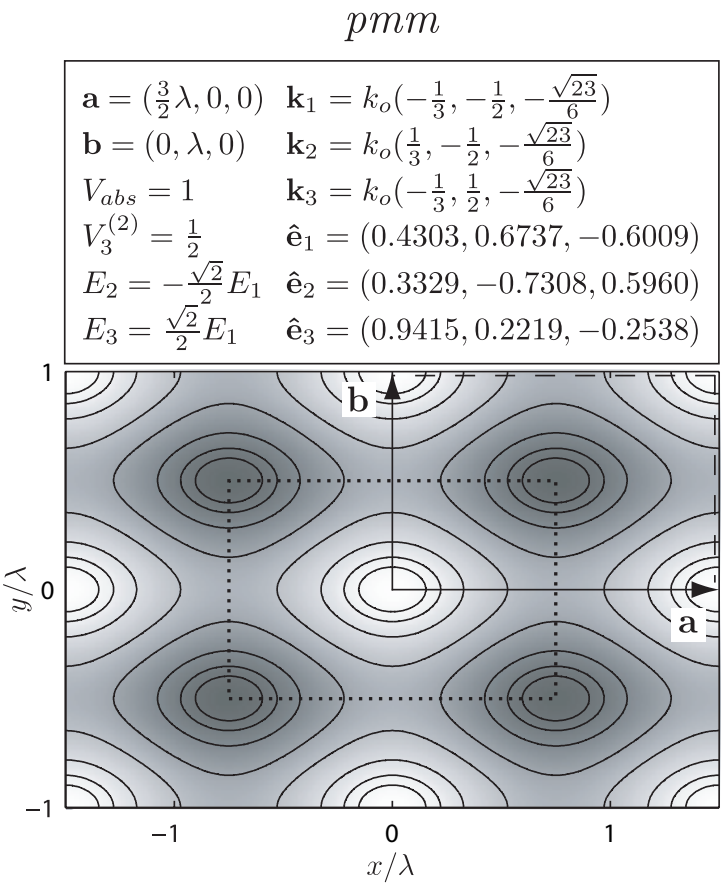

Figure 2.4: Design parameters and associated interference pattern exhibiting *pmm* plane group symmetry. $C_3^{(2)}$ has been applied and absolute contrast maximized resulting in unity absolute contrast (V_{abs} = 1), with zero intensity at intensity nulls. The conventional primitive unit cell (dashed line) and the Wigner-Seitz proximity unit cell (dotted line) are shown.

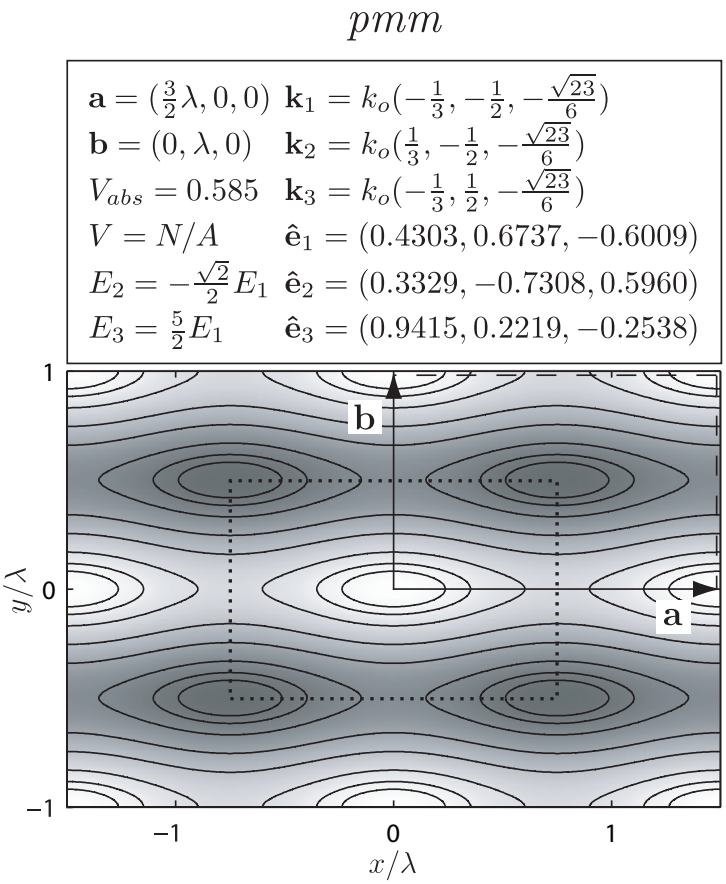

Figure 2.5: Design parameters and associated interference pattern exhibiting *pmm* plane group symmetry. No *condition for primitive-lattice-vector-direction equal contrasts* has been applied. The conventional primitive unit cell (dashed line) and the Wigner-Seitz proximity unit cell (dotted line) are shown.

maximized, unity absolute contrast ($V_{abs} = 1$) can always be achieved.

2.4.3 Plane Symmetry Group *cmm*

The *cmm* symmetry group (along with the *pmm* plane symmetry group) is the next higher symmetry group after *p2*. This plane group is characterized as having two unique reflection axes, two unique glide reflection axes, and four unique points of 2-fold symmetry, as shown in Fig. 2.3. This plane symmetry group is realized when plane wave parameters are chosen such that they satisfy one of three sets of constraints:

1. $V_{12} = V_{13}$ and $|\mathbf{a}| = |\mathbf{b}|$
2. $V_{13} = V_{23}$ and $|\mathbf{a}| = |\mathbf{a} + \mathbf{b}|$
3. $V_{12} = V_{23}$ and $|\mathbf{b}| = |\mathbf{a} + \mathbf{b}|$.

When one of these sets of constraints is satisfied, all three interference terms may be present. Two of the three corresponding spatial wavevectors ($\mathbf{G}_{ij}$) will be equal in magnitude, while the third (if present) will be an exterior bisector of the previous two. This symmetry will still exist when both *conditions for primitive-lattice-vector-direction equal contrasts* are applied until parameters satisfy constraints for either the *p4m* or *p6m* plane symmetry groups. The *p6m* plane group will emerge when $C_3^{(3)}$ is satisfied and a set of primitive basis vectors ($\mathbf{a}$ and $\mathbf{b}$) make an angle of 120° with each other. The *p4m* plane group will emerge when $C_3^{(2)}$ is satisfied and a set of primitive basis vectors ($\mathbf{a}$ and $\mathbf{b}$, $\mathbf{a}$ and $\mathbf{a} + \mathbf{b}$, or $\mathbf{a} + \mathbf{b}$ and $\mathbf{b}$) make an angle of 90° with each other. Typical interference patterns with *cmm* plane group symmetry are illustrated in Figs. 2.6 and 2.7 along with the corresponding design parameters.

The design in Fig. 2.6 satisfies $C_3^{(3)}$, while Fig. 2.7 satisfies $C_3^{(2)}$. Figure 2.6 illustrates one of the two fundamentally different interference patterns possible with the application of $C_3^{(3)}$, exhibiting peaks of intensity at lattice points. It has an absolute contrast (V_{abs}) of 0.8946 and an interference coefficient $V_3^{(3)} = 0.5666$. This design is optimized for this type

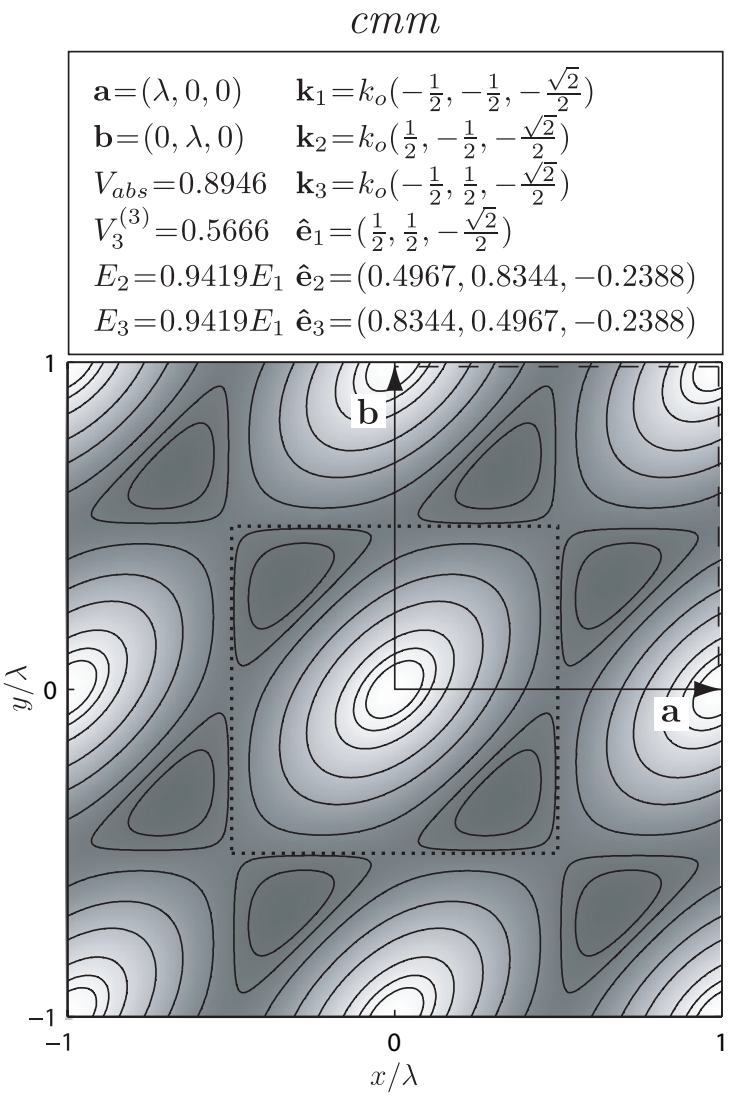

Figure 2.6: Design parameters and associated interference pattern exhibiting *cmm* plane group symmetry. This design results in one of two fundamentally different interference patterns when $C_3^{(3)}$ is satisfied, possessing intensity peaks at lattice points. The conventional primitive unit cell (dashed line) and the Wigner-Seitz proximity unit cell (dotted line) are shown.

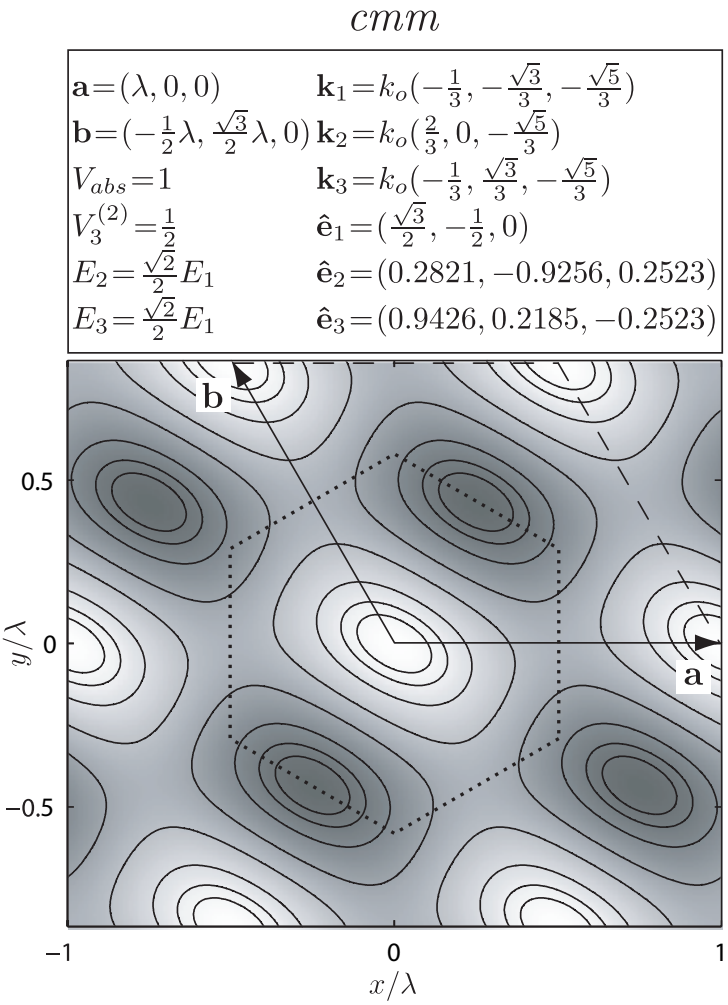

Figure 2.7: Design parameters and associated interference pattern exhibiting *cmm* plane group symmetry. $C_3^{(2)}$ has been applied and absolute contrast maximized resulting in unity absolute contrast (V_{abs} = 1), with zero intensity at intensity nulls. The conventional primitive unit cell (dashed line) and the Wigner-Seitz proximity unit cell (dotted line) are shown.

of interference pattern, for $V_3^{(3)} > 0$. However, if we allow $V_3^{(3)} < 0$, a solution such that unity absolute contrast ($V_{abs} = 1$) is achieved exists. Figure 2.7 illustrates a design with unity absolute contrast ($V_{abs} = 1$) and an interference coefficient $V_3^{(2)} = 1/2$. Like the *pmm* plane group, absolute contrast can vary from 0 to 1, depending upon the chosen plane wave parameters. However, when $C_3^{(3)}$ (for $V_3^{(3)} < 0$) and $C_3^{(2)}$ can be applied, unity absolute contrast ($V_{abs} = 1$) can always be achieved.

2.4.4 Plane Symmetry Group *p4m*

The *p4m* plane symmetry group is the next higher symmetry group after *cmm* and *pmm*. This plane group is characterized as having six unique reflection axes, two unique glide reflection axes, two 4-fold symmetry points, and two 2-fold symmetry points, as shown in Fig. 2.3. This plane symmetry group is realized when plane wave parameters are chosen such that they satisfy one of three sets of constraints:

1. $V_{12} = V_{13}$, $V_{23} = 0$, $|\mathbf{a}| = |\mathbf{b}|$, and $\mathbf{a} \cdot \mathbf{b} = 0$

2. $V_{13} = V_{23}$, $V_{12} = 0$, $|\mathbf{a}| = |\mathbf{a} + \mathbf{b}|$, and $\mathbf{a} \cdot (\mathbf{a} + \mathbf{b}) = 0$

3. $V_{12} = V_{23}$, $V_{13} = 0$, $|\mathbf{a} + \mathbf{b}| = |\mathbf{b}|$, and $(\mathbf{a} + \mathbf{b}) \cdot \mathbf{b} = 0$.

When one of these sets of constraints is satisfied, only two of the three interference terms are present in Eq. (2.18) and the corresponding spatial wavevectors ($\mathbf{G}_{ij}$) are orthogonal and equal in magnitude. This plane group can emerge only if $C_3^{(2)}$ has been applied. Therefore, designs that satisfy the conditions above can always be optimized and exhibit unity absolute contrast ($V_{abs} = 1$). A typical interference pattern with *p4m* plane group symmetry is illustrated in Fig. 2.8 along with the corresponding design parameters. Figure 2.8 illustrates a design that results in unity absolute contrast ($V_{abs} = 1$) and an interference coefficient $V_3^{(2)} = 1/2$.

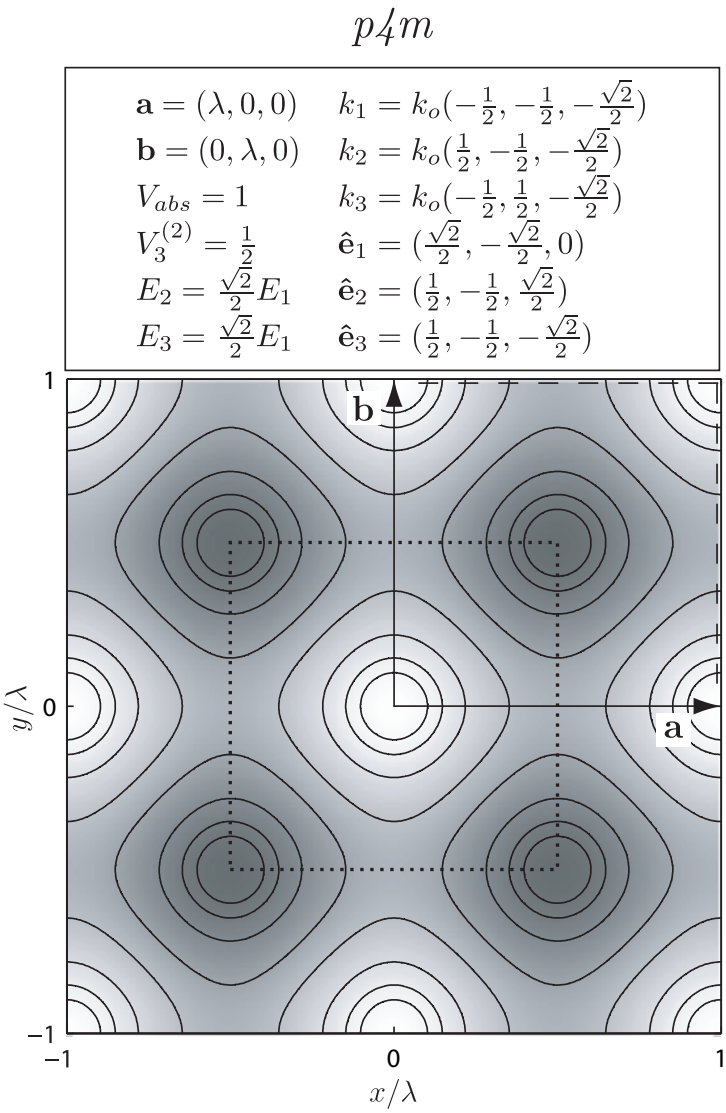

Figure 2.8: Design parameters and associated interference pattern exhibiting *p4m* plane group symmetry. $C_3^{(2)}$ has been applied and absolute contrast maximized resulting in unity absolute contrast (V_{abs} = 1), with zero-intensity at intensity nulls. The conventional primitive unit cell (dashed line) and the Wigner-Seitz proximity unit cell (dotted line) are shown.

2.4.5 Plane Symmetry Group *p6m*

The *p6m* plane symmetry group is the highest symmetry group possible with three-beam-interference lithography. This plane group is characterized as having six unique reflection axes, three 2-fold symmetry points, three 3-fold symmetry points, and one 6-fold symmetry point, as shown in Fig. 2.3. This plane symmetry group can only be realized when plane wave parameters are chosen such that they satisfy the following set of constraints:

- $V_{12} = V_{13} = V_{23}$, $|\mathbf{a}| = |\mathbf{b}|$, and $\mathbf{a} \cdot \mathbf{b} = -0.5$.

When this set of constraints is satisfied, all three interference terms are present in Eq. (2.18) and the corresponding spatial wavevectors ($\mathbf{G}_{ij}$) are equal in magnitude. One will bisect the other two, which make an angle of 120° with each other. This plane group can emerge only if $C_3^{(3)}$ has been applied. Therefore, designs that satisfy the conditions above can always be optimized and exhibit unity absolute contrast ($V_{abs} = 1$). A typical interference pattern with *p6m* plane group symmetry is illustrated in Fig. 2.9 along with the corresponding design parameters. Figure 2.9 illustrates a design that results in unity absolute contrast ($V_{abs} = 1$) and an interference coefficient $V_3^{(3)} = -1/3$.

The design in Fig. 2.9 illustrates one of the two fundamentally different interference patterns possible when $C_3^{(3)}$ is satisfied. In this particular case, intensity minima are located at the lattice points. Again, another design such that intensity maxima are located at the lattice points exists. Particularly for this hexagonal lattice design, it is important to have a full understanding of the range of contrast possible. As discussed before, if we allow $V_3^{(3)} < 0$, unity absolute contrast is possible ($V_{abs} = 1$, $V_3^{(3)} = -1/3$), resulting in intensity minima at lattice points. However, it may be desirable for intensity maxima to be located at these points. Figure 2.10 illustrates the maximum contrast for the *p6m* plane group, for $V_3^{(3)} > 0$, as a function of the zenith angle of the recording wavevectors ($\mathbf{k}_i$). Figure 2.10 indicates that the lowest optimized absolute contrast available to designers is 0.6, for $V_3^{(3)} > 0$, when $C_3^{(3)}$ is satisfied. This occurs when all three recording wavevectors are orthogonal,

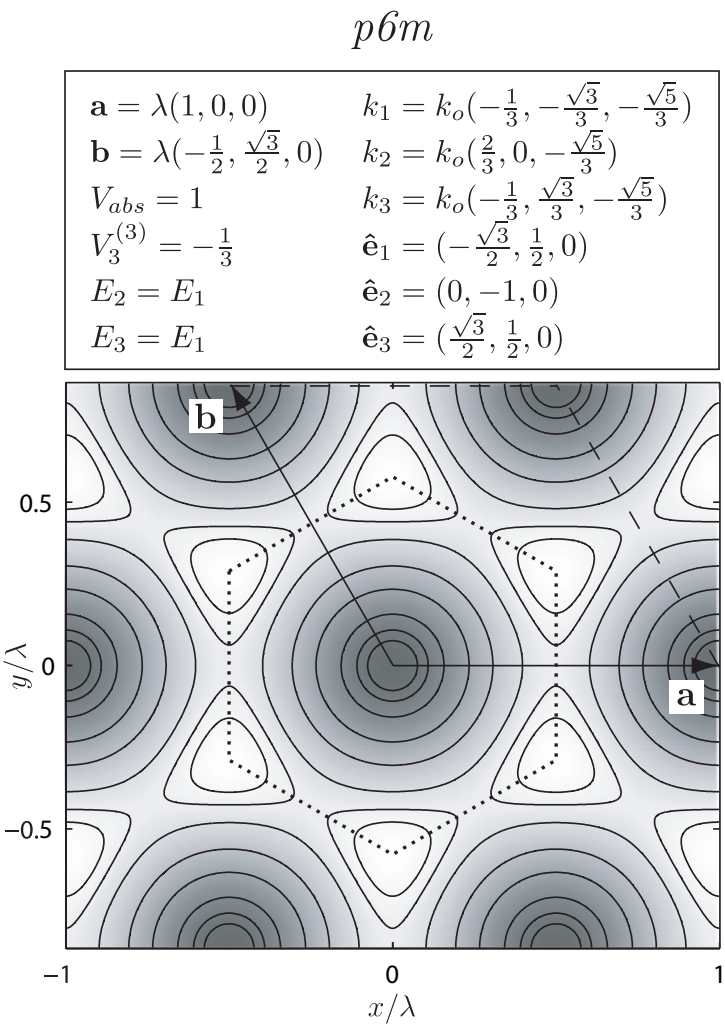

Figure 2.9: Design parameters and associated interference pattern exhibiting *p6m* plane group symmetry. This design results in one of two fundamentally different interference patterns when $C_3^{(3)}$ is satisfied, possessing intensity nulls at lattice points. Polarization unit vectors are coplanar (*xy* plane) and 120° apart from each other. The conventional primitive unit cell (dashed line) and the Wigner-Seitz proximity unit cell (dotted line) are shown.

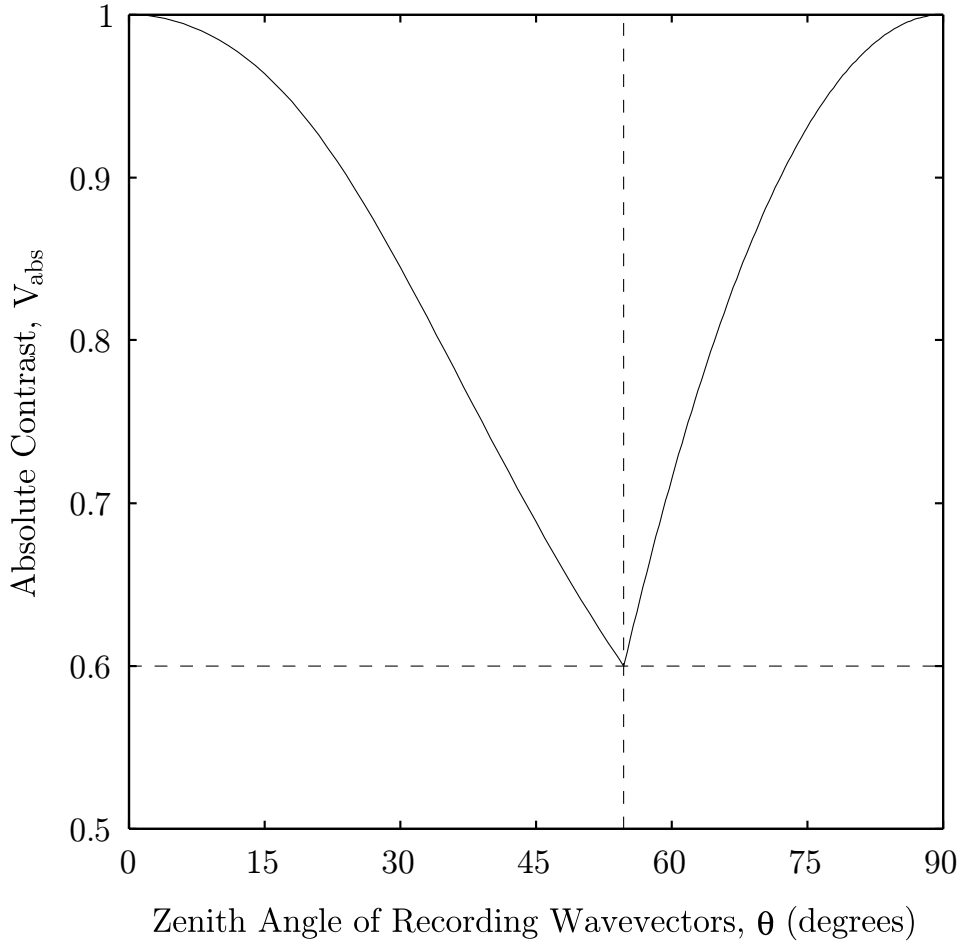

Figure 2.10: Plot of maximum contrast obtainable for an interference pattern exhibiting *p6m* plane group symmetry as a function of wavevector zenith angle when the ${}^{+}C_3^{(3)}$ *condition for primitive-lattice-vector-direction equal contrasts* is satisfied and optimized. The minimum occurs for $V_{abs} = 0.6$ at $\theta = \tan^{-1}\sqrt{2} \approx 54.7°$ or when all three recording wavevectors are orthogonal. The minimum shown, in actuality, is the global minimum for all configurations of three wavevectors. Configuration of wavevectors is illustrated in Fig. 2.11.

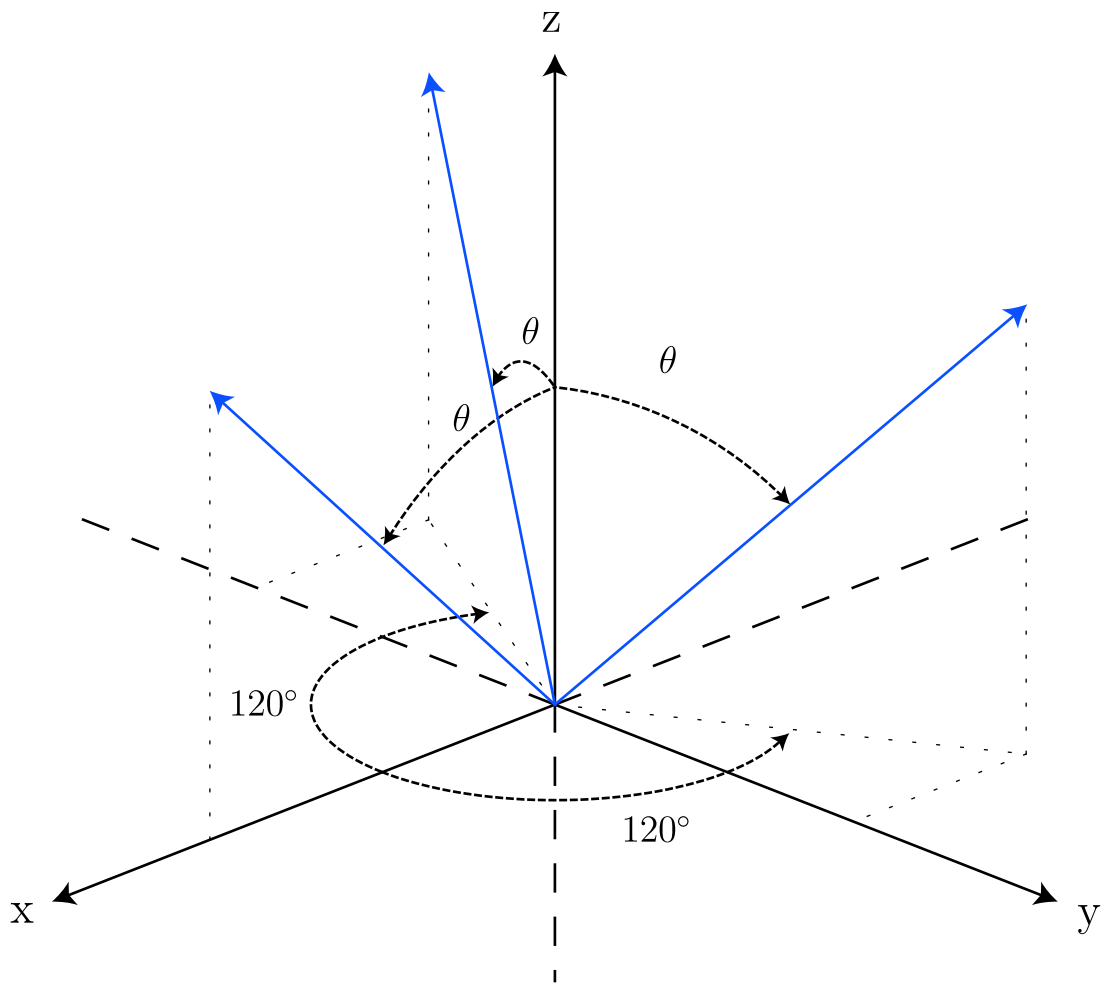

Figure 2.11: Wavevector configuration required for hexagonal lattice interference pattern with *p6m* plane group symmetry. $C_3^{(3)}$ must be satisfied.

possessing a zenith angle $\theta = \tan^{-1}\sqrt{2} \approx 54.7°$. In fact, this is the lowest optimized absolute contrast for all configurations of recording wavevectors when $C_3^{(3)}$ is satisfied and absolute contrast is maximized for $V_3^{(3)} > 0$. This can be demonstrated through a nonlinear minimization algorithm to search for the configuration of recording wavevectors resulting in the lowest maximum absolute contrast.

2.5 Summary

The relationships between the sets of constraints that result in the various plane groups discussed above can be determined when these constraints are viewed together. Figure 2.12 illustrates these relationships. As more restrictions are placed upon the primitive basis vectors (**a** and **b**) and interference coefficients (V_{ij}), higher plane group symmetries emerge. In general, the interference of three arbitrary linear polarized plane waves will produce *p2* symmetry. Figure 2.12 summarizes all the sets of constraints required to produce the other four plane symmetry groups and the relationships between them. This present methodology results in, at most, three sets of constraints (in terms of **a**, **b**, and V_{ij}) for each plane group. While single sets of constraints would result if the constraints were in terms of the spatial lattice vectors ($\mathbf{G}_{ij}$) and interference coefficients (V_{ij}), an intuitive understanding about the basis vectors (**a** and **b**) and recording vectors ($\mathbf{k}_i$) would be more difficult to grasp. Moreover, the present methodology clearly demonstrates the opportunity for interference patterns with equivalent translational symmetries to exhibit different plane group symmetries.

Applying one of the two *conditions for primitive-lattice-vector-direction equal contrasts* and maximizing absolute contrast is a procedure to ensure that the designed interference pattern most accurately represents the translational symmetry of the desired lattice and results in a high-quality, lithographically useful interference pattern. A second *condition for primitive-lattice-vector-direction equal contrasts* was introduced and a complete description of equal contrasts was given. It is shown that unity absolute contrast ($V_{abs} = 1$) can

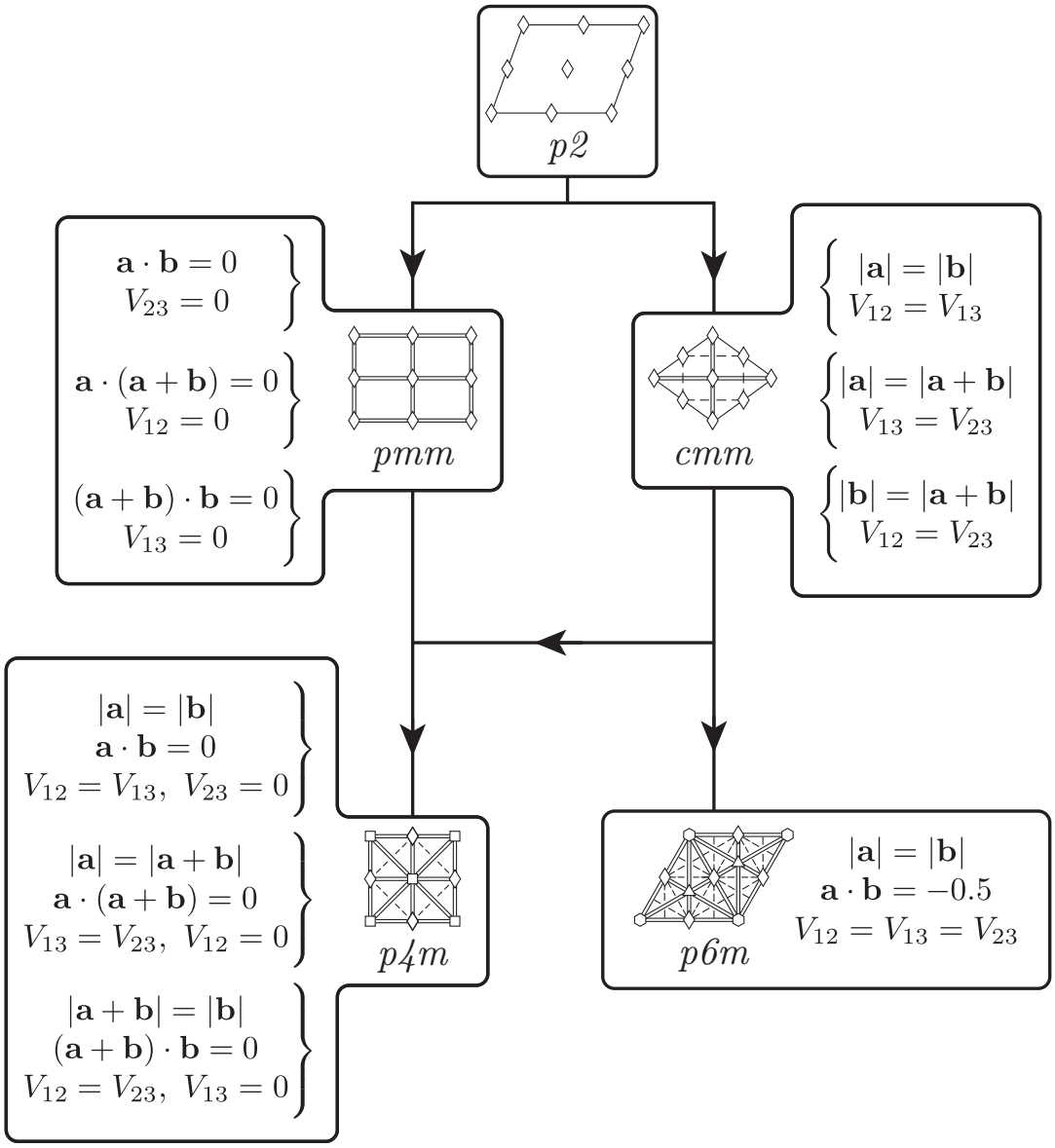

Figure 2.12: Flow chart illustrating relationships between conditions required for each of the five plane symmetry groups to exist in three-beam interference. In general, *p2* plane group symmetry occurs for general three-beam interference. As more restrictions are placed upon the primitive basis vectors (**a** and **b**) and interference coefficients (V_{ij}), higher plane group symmetries emerge.

always be achieved when either of the two *conditions for primitive-lattice-vector-direction equal contrasts* are applied and absolute contrast is maximized. This is very important to the success of holographic or lithographic processes. However, this can only be achieved for $C_3^{(3)}$ for $V_3^{(3)} < 0$, when intensity minima are located at lattice points. Finally, the lowest contrast available to designers when $C_3^{(3)}$ is satisfied and absolute contrast is maximized for $V_3^{(3)} > 0$ is $V_{abs} = 0.6$. This occurs when all three recording wavevectors are orthogonal to each other.

Adjustment of beam intensities and polarizations have a significant impact on the contrast and plane symmetry of three-beam-interference patterns. However, proper tuning of such can result in high-quality, symmetric motifs about lattice points for any configuration of three wavevectors.

CHAPTER 3

MODELING FOUR-BEAM INTERFERENCE

The analysis and modeling of multi-beam interference presented in this thesis is based upon plane wave interference. In this chapter, a systematic approach to modeling four-beam interference is presented. In terms of four-beam interference, the analysis will be focused on linearly polarized light. A complete description of four-beam interference will be given in terms of contrast and absolute contrast. Specific solutions are given for three cases by presenting the optimized plane wave parameters and illustrations of the resulting interference patterns. These include the simple cubic, face-centered cubic, and body-centered cubic lattices.

3.1 Four-Beam Interference

In general, the interference of four linearly polarized, monochromatic planes waves will produce a three-dimensional, periodic interference pattern. The primitive basis vectors **a**, **b**, and **c** are used to define the translational symmetry of the desired interference pattern. The corresponding reciprocal lattice vectors **A**, **B**, and **C** are expressed as

$$\begin{aligned} \mathbf{A} &= 2\pi \frac{\mathbf{b} \times \mathbf{c}}{\mathbf{a} \cdot \mathbf{b} \times \mathbf{c}} \\ \mathbf{B} &= 2\pi \frac{\mathbf{c} \times \mathbf{a}}{\mathbf{a} \cdot \mathbf{b} \times \mathbf{c}} \\ \mathbf{C} &= 2\pi \frac{\mathbf{a} \times \mathbf{b}}{\mathbf{a} \cdot \mathbf{b} \times \mathbf{c}} \, . \end{aligned} \tag{3.1}$$

A set of four wavevectors that will produce an interference pattern with the translational symmetry given by **a**, **b**, and **c** is found by locating the circumcenter (**P**) of a pyramid (tetrahedron) defined in terms of the three reciprocal lattices vectors **A**, **B**, and **C** as

$$\mathbf{P} = \frac{1}{2} \frac{|\mathbf{A}|^2(\mathbf{B} \times \mathbf{C}) + |\mathbf{B}|^2(\mathbf{C} \times \mathbf{A}) + |\mathbf{C}|^2(\mathbf{A} \times \mathbf{B})}{\mathbf{A} \cdot \mathbf{B} \times \mathbf{C}} \, . \tag{3.2}$$

The four recording wavevectors are then given by

$$\mathbf{k}_1 = -\mathbf{P} \tag{3.3}$$

$$\mathbf{k}_2 = \mathbf{A} - \mathbf{P} \tag{3.4}$$

$$\mathbf{k}_3 = \mathbf{B} - \mathbf{P} \tag{3.5}$$

$$\mathbf{k}_4 = \mathbf{C} - \mathbf{P}\,. \tag{3.6}$$

Unlike the three-beam case [84], the choice of the primitive basis vectors determines the wavelength required to produce the desired interference pattern. The recording wavelength needed has a magnitude of $\lambda = 2\pi/|\mathbf{P}|$. Given this methodology, it is clear that different sets of primitive basis vectors that define the same translational symmetry will produce different sets of recording wavevectors. While the translation symmetry of each will be identical, the locations of symmetry elements and stationary points within the interference pattern will differ.

Equation (2.10) is rewritten in the case of four-beam interference as

$$\begin{aligned} I_T = I_0\Big[1 &+ V_{12}\cos(\mathbf{G}_{21}\cdot\mathbf{r}) + V_{13}\cos(\mathbf{G}_{31}\cdot\mathbf{r}) \\ &+ V_{14}\cos(\mathbf{G}_{41}\cdot\mathbf{r}) + V_{23}\cos(\mathbf{G}_{32}\cdot\mathbf{r}) \\ &+ V_{24}\cos(\mathbf{G}_{42}\cdot\mathbf{r}) + V_{34}\cos(\mathbf{G}_{43}\cdot\mathbf{r})\Big]\,. \end{aligned} \tag{3.7}$$

where the DC intensity term is

$$I_0 = \frac{1}{2}\sum_{k=1}^{4} E_k^2, \tag{3.8}$$

the interference coefficient is

$$V_{ij} = \frac{E_i E_j e_{ij}}{I_0}, \tag{3.9}$$

and $\mathbf{G}_{ij} = \mathbf{k}_i - \mathbf{k}_j$. The expression results in a DC intensity term and six spatial cosines corresponding to the six interfering-beam pairs. It should be noted that there is a fundamental relationship between the desired reciprocal lattice vectors and the spatial cosine wavevectors. $\mathbf{G}_{21}$, $\mathbf{G}_{31}$, and $\mathbf{G}_{41}$ are equal to $\mathbf{A}$, $\mathbf{B}$, and $\mathbf{C}$ respectively while $\mathbf{G}_{32}$, $\mathbf{G}_{42}$, and $\mathbf{G}_{43}$ are equal to $(\mathbf{B}-\mathbf{A})$, $(\mathbf{C}-\mathbf{A})$, and $(\mathbf{C}-\mathbf{B})$ respectively.

If $\phi_i = 0$, lattice points are defined at the origin ($\mathbf{r} = 0$) and all equivalent points in the three-dimensional periodic interference pattern. In general, the lattice points are defined at

$$\mathbf{p} = -\frac{g_{12}(\mathbf{G}_{31} \times \mathbf{G}_{41}) + g_{13}(\mathbf{G}_{41} \times \mathbf{G}_{21}) + g_{14}(\mathbf{G}_{21} \times \mathbf{G}_{31})}{\mathbf{G}_{21} \cdot (\mathbf{G}_{31} \times \mathbf{G}_{41})} , \tag{3.10}$$

where

$$g_{ij} = \phi_i - \phi_j , \tag{3.11}$$

and all equivalent points in the three dimensional periodic interference pattern.

In the present work, three lattices are treated; simple cubic, face-centered cubic, and body-centered cubic. Using the above methodology, the required recording wavevectors are calculated for the desired translational symmetry given by its primitive lattice vectors. Table 3.1 summarizes the primitive lattice vectors and the calculated wavevectors. The recording wavevector term k_o is defined as $k_o = 2\pi/\lambda = |\mathbf{P}|$.

3.2 Contrast

Proper selection of the recording wavevectors, $\mathbf{k}_i$, has been shown to produce interference patterns with the translational symmetry of all fourteen Bravais lattices [70]. The usefulness of an interference pattern for lithography can be improved by systematically selecting the plane wave parameters of the recording beams. This is done most often through nonlinear optimization by maximizing the absolute contrast of the interference pattern where the absolute contrast is defined as

$$V_{abs} = \frac{I_{max} - I_{min}}{I_{max} + I_{min}} . \tag{3.12}$$

The nonlinear constraints applied during the optimization determine the locations of symmetry elements, intensity extrema, and saddle points within the unit cell of the periodic interference pattern. Lithographically speaking, these determine the shape of the intensity contours that will define the final structures. Within four-beam interference, as in three-beam interference, there is one set of nonlinear constraints that has been applied during

Table 3.1: Primitive Basis Vectors and the Corresponding Recording Wavevectors.

	Primitive Lattice Vectors			Wavevectors			
	a	**b**	**c**	$\mathbf{k}_1$	$\mathbf{k}_2$	$\mathbf{k}_3$	$\mathbf{k}_4$
Cubic	$\frac{\sqrt{3}}{2}\lambda[1\ 0\ 0]$	$\frac{\sqrt{3}}{2}\lambda[0\ 1\ 0]$	$\frac{\sqrt{3}}{2}\lambda[0\ 0\ 1]$	$k_o\frac{1}{\sqrt{3}}[-1\ -1\ -1]$	$k_o\frac{1}{\sqrt{3}}[1\ -1\ -1]$	$k_o\frac{1}{\sqrt{3}}[-1\ 1\ -1]$	$k_o\frac{1}{\sqrt{3}}[-1\ -1\ 1]$
FCC	$\frac{3\sqrt{3}}{4}\lambda[1\ 1\ 0]$	$\frac{3\sqrt{3}}{4}\lambda[0\ 1\ 1]$	$\frac{3\sqrt{3}}{4}\lambda[1\ 0\ 1]$	$k_o\frac{1}{3\sqrt{3}}[-3\ -3\ -3]$	$k_o\frac{1}{3\sqrt{3}}[-1\ -1\ -5]$	$k_o\frac{1}{3\sqrt{3}}[-5\ -1\ -1]$	$k_o\frac{1}{3\sqrt{3}}[-1\ -5\ -1]$
BCC	$\frac{\sqrt{3}}{4}\lambda[-1\ 1\ 1]$	$\frac{\sqrt{3}}{4}\lambda[1\ -1\ 1]$	$\frac{\sqrt{3}}{4}\lambda[1\ 1\ -1]$	$k_o\frac{1}{\sqrt{3}}[-1\ -1\ -1]$	$k_o\frac{1}{\sqrt{3}}[-1\ 1\ 1]$	$k_o\frac{1}{\sqrt{3}}[1\ -1\ 1]$	$k_o\frac{1}{\sqrt{3}}[1\ 1\ -1]$

the optimization process and is referred to in the literature as the *uniform contrast condition* [71, 87]. These lithographically useful interference patterns are produced by choosing the plane wave parameters such that all six interference coefficients V_{ij} are equal. Mathematically, the resulting interference patterns have equal contrasts in the three primitive lattice vector directions (**a**, **b**, **c**) from each lattice point. If the assumption about including all six interference coefficients is relaxed, a more fundamental and complete understanding of multi-beam interference is possible while still achieving equal contrasts in more than one primitive lattice vector direction. That is, all six interference coefficients do not have to be equal and positive. Avoiding the previously ambiguous terminology of *uniform contrast* [69, 71, 84], a more descriptive nomenclature is also used here: namely, *condition for primitive-lattice-vector-direction equal contrasts*.

In actuality, there exist multiple *conditions for primitive-lattice-vector-direction equal contrasts* for multi-beam-interference lithography including the four-beam interference case treated in this section [87, 88]. For three-dimensionally periodic interference patterns produced through four-beam interference, there are six spatial cosines as described by Eq. (3.7). However, only three are required to produce three-dimensional periodicity. Consequently, there exists four *conditions for primitive-lattice-vector-direction equal contrasts*. Based on the present research, a symbolic designation $C_n^{(m)}$ is introduced to differentiate between the various *conditions for primitive-lattice-vector-direction equal contrasts*. The quantity n is the total number of interfering beams and m the number of nonzero interference coefficients (number of interfering-beam-pairs).

Considering our previous work [84] and work that is presented here, it is important to note the relationships between the interference coefficient $V_n^{(m)}$ and the absolute contrast V_{abs}. This suggests that configurations of wavevectors and polarizations can result in interference coefficients that are positive *or* negative. The physical meaning of this statement is as follows: If a configuration satisfies a *condition for primitive-lattice-vector-direction equal contrasts* and results in a *positive* interference coefficient, $V_n^{(m)} > 0$, volumes of *high*

electric field intensity surround the lattice points. Similarly, if a configuration satisfies a *condition for primitive-lattice-vector-direction equal contrasts* and results in a *negative* interference coefficient, $V_n^{(m)} < 0$, volumes of *low electric field intensity* surround the lattice points. However, regardless of the sign or magnitude of the interference coefficient, $V_n^{(m)}$, determined by the polarization states and amplitudes of the recording beams, the intensity contours will be identical (but differing in intensity value) provided the recording wavevectors remain unchanged. Consequently, another superscript can be added to the given symbolic designation to describe more accurately the interference pattern resulting in ${}^{\pm}C_n^{(m)}$ where ± denotes either a *positive* or *negative* interference coefficient. This concept of positive and negative interference coefficients enables the pairing of the interference pattern with positive and negative photoresists in a manner analogous to pairing positive and negative photoresist with light- and dark-field masks in conventional lithography. Given a particular lithographic process chemistry, a designer has the ability to choose between these "light-field" and "dark-field" interference patterns.

For each lattice, a nonlinear optimization for maximizing absolute contrast is used here to determine the plane wave parameters while satisfying the nonlinear constraints given by each *condition for primitive-lattice-vector-direction equal contrasts*. While subordinate conditions for unity absolute contrast ($V_{abs} = 1$ with $I_{min} = 0$) are discussed, these subordinate conditions cannot always be satisfied. However, the nonlinear optimization nevertheless produces solutions that maximize the absolute contrast given a particular configuration of recording wavevectors. Detailed information regarding the approach used to determine these optimized parameters is described in Appendix A.

3.2.1 Condition for primitive-lattice-vector-direction equal contrasts $C_4^{(6)}$

The previously discussed *uniform contrast condition* within four-beam interference [71,87] corresponds to a symbolic designation of $C_4^{(6)}$. Each of the six interference coefficients (corresponding to an interfering-beam-pair) contributes to the modulation of intensity within

the interference pattern as

$$V_4^{(6)} = V_{12} = V_{13} = V_{14} = V_{23} = V_{24} = V_{34} \ \ [\text{Condition } C_4^{(6)}] \ . \tag{3.13}$$

Applying this condition leads to the following set of constraints on the polarizations and amplitudes of the recording beams [71]:

$$e_{12}e_{34} = e_{13}e_{24} = e_{14}e_{23} \ , \tag{3.14}$$

$$\frac{E_2}{E_1} = \frac{e_{13}}{e_{23}} \ , \tag{3.15}$$

$$\frac{E_3}{E_1} = \frac{e_{12}}{e_{23}} \ , \tag{3.16}$$

$$\frac{E_4}{E_1} = \frac{e_{12}}{e_{24}} \ . \tag{3.17}$$

Once these constraints are satisfied, the interference coefficient is written in terms of the polarization efficiency factors as [71]

$$V_4^{(6)} = \frac{2e_{12}e_{13}e_{23}}{e_{12}^2 + e_{13}^2 + e_{23}^2 + e_{13}^2e_{23}^2/e_{34}^2} \ . \tag{3.18}$$

When $C_4^{(6)}$ is satisfied, one set of global intensity extrema (maxima or minima) are located at the lattice points (vertices of the primitive unit cell with the origin at $\mathbf{r} = 0$) and the other set of global intensity extrema (minima or maxima) are located at the face centers of the primitive unit cell ($\mathbf{r} = \mathbf{a}/2 + \mathbf{b}/2$, $\mathbf{r} = \mathbf{a}/2 + \mathbf{c}/2$, $\mathbf{r} = \mathbf{b}/2 + \mathbf{c}/2$). Additional stationary points (saddle points) occur at the body center ($\mathbf{r} = \mathbf{a}/2 + \mathbf{b}/2 + \mathbf{c}/2$) and edge centers ($\mathbf{r} = \mathbf{a}/2$, $\mathbf{r} = \mathbf{b}/2$, $\mathbf{r} = \mathbf{c}/2$) of the primitive unit cell. Given the locations of the intensity extrema, the absolute contrast is written in terms of the interference coefficient as

$$V_{abs} = \left| \frac{4}{1/V_4^{(6)} + 2} \right| \ . \tag{3.19}$$

3.2.1.1 Subordinate condition for unity absolute contrast for ${}^{-}C_4^{(6)}$

There also exist two subordinate conditions for unity absolute contrast ($V_{abs} = 1$ with $I_{min} = 0$) for $C_4^{(6)}$. Considering Eq. (3.19), unity absolute contrast occurs when the interference

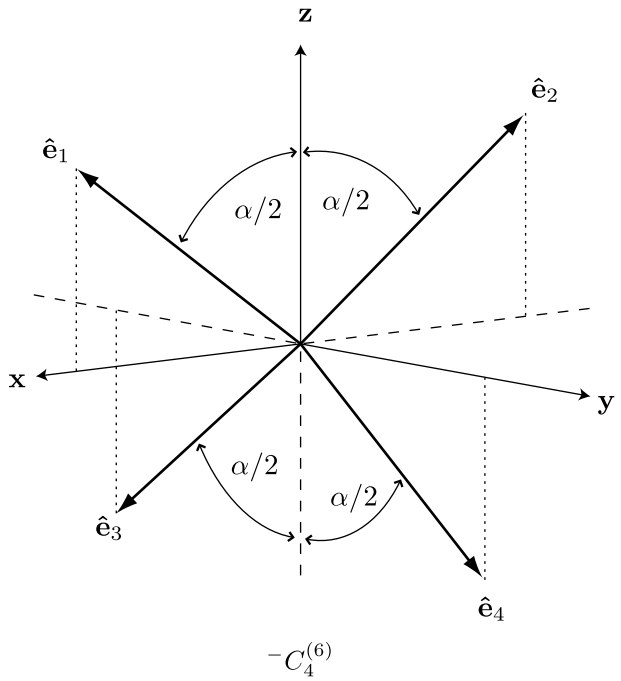

Figure 3.1: Orientation of polarizations for the subordinate condition for unity absolute contrast [or any combination of the polarization vectors ($\hat{\mathbf{e}}_i$) where one, multiple, or all are inverted ($-\hat{\mathbf{e}}_i$)] for $^{-}C_4^{(6)}$ where $V_4^{(6)} = -1/3$. $\alpha = \cos^{-1}(-1/3) \approx 109.47^\circ$

coefficient $V_4^{(6)}$ equals $-1/6$ or $1/2$. In order for $V_4^{(6)} = -1/6$, an example of $^{-}C_4^{(6)}$, the additional constraints on the polarizations are

$$e_{ij} = e_{12} = e_{13} = e_{14} = e_{23} = e_{24} = e_{34} = -1/3 \tag{3.20}$$

($\sim 109.47^\circ$ between polarization vectors) or one of an additional 15 orientations of the polarization vectors which are obtained by inverting ($-\hat{\mathbf{e}}_i$) any single, any pair, any triplet, or all of the polarization vectors. The orientation of the resulting polarization vectors described in Eq. (3.20) (which define the vertices of a regular tetrahedron) is illustrated in Fig. 3.1. For Fig. 3.1 and subsequent illustrations of the subordinate conditions for unity absolute contrast, the orientations of the polarizations are fixed relative to each other. However, the set of polarization vectors, as a whole, may have any arbitrary rotational orientation relative to the origin. In these illustrations, the specific orientation of the set of polarizations are chosen symmetrically with respect to the Cartesian axes for ease of visualization.

3.2.1.2 *Subordinate condition for unity absolute contrast for* ${}^{+}C_4^{(6)}$

In order for $V_4^{(6)} = 1/2$, an example of ${}^{+}C_4^{(6)}$, the additional constraints on the polarizations are

$$e_{ij} = e_{12} = e_{13} = e_{14} = e_{23} = e_{24} = e_{34} = 1 \tag{3.21}$$

(parallel polarization vectors) or one of an additional 15 orientations of the polarization vectors which are obtained by inverting ($-\hat{\mathbf{e}}_i$) any single, any pair, any triplet, or all of the polarization vectors. This constraint indicates that the recording wavevectors are coplanar and polarizations are collinear. In this case, the resulting interference pattern will be invariant in at least one direction, i.e. exhibit only two-dimensional periodicity. Thus, optimizing the orientations of polarizations for wavevectors that exhibit three-dimensional periodicity will result in an absolute contrast $V_{abs} < 1$ while satisfying ${}^{+}C_4^{(6)}$.

A nonlinear optimization to maximize absolute contrast is used to determine the plane wave parameters. Solutions for both ${}^{-}C_4^{(6)}$ and ${}^{+}C_4^{(6)}$ are summarized in Tables 3.2 and 3.3 respectively. Intensity contours for each of these solutions are also illustrated in Fig. 3.2 with volumes of higher intensity being enclosed.

3.2.2 Condition for primitive-lattice-vector-direction equal contrasts $C_4^{(5)}$

A second *condition for primitive-lattice-vector-direction equal contrasts* ($C_4^{(5)}$) occurs when five of the six interference coefficients (corresponding to interfering-beam-pairs) contribute to the modulation of intensity within the interference pattern as

$$V_4^{(5)} = V_{12} = V_{13} = V_{14} = V_{23} = V_{24},\ V_{34} = 0\ \ [\text{Condition } C_4^{(5)}]\ . \tag{3.22}$$

Applying this condition leads to the following set of constraints on the polarizations and amplitudes of the recording beams:

$$e_{13}e_{24} = e_{14}e_{23} \tag{3.23}$$

$$e_{34} = 0 \tag{3.24}$$

Table 3.2: Optimized Plane Wave Parameters[a] for Lattices Maximizing Absolute Contrast for ${}^{-}C_4^{(6)}$.

Lattice	E_2/E_1	E_3/E_1	E_4/E_1	$\hat{\mathbf{e}}_1$	$\hat{\mathbf{e}}_2$	$\hat{\mathbf{e}}_3$	$\hat{\mathbf{e}}_4$	$V_4^{(6)}$	V_{abs}
Cubic	1	−1	−1	$\begin{pmatrix}-0.7887\\0.5774\\0.2113\end{pmatrix}$	$\begin{pmatrix}0.2113\\-0.5774\\0.7887\end{pmatrix}$	$\begin{pmatrix}-0.7887\\-0.5774\\0.2113\end{pmatrix}$	$\begin{pmatrix}0.2113\\0.5774\\0.7887\end{pmatrix}$	−1/6	1.0
FCC	−4.4930	4.4930	−1.6271	$\begin{pmatrix}0.4083\\-0.8165\\0.4083\end{pmatrix}$	$\begin{pmatrix}-0.7607\\-0.5902\\0.2702\end{pmatrix}$	$\begin{pmatrix}-0.2702\\0.5902\\0.7607\end{pmatrix}$	$\begin{pmatrix}0.6804\\-0.2722\\0.6804\end{pmatrix}$	−0.0575	0.2599
BCC	1	−1	−1	$\begin{pmatrix}-0.7887\\0.5774\\0.2113\end{pmatrix}$	$\begin{pmatrix}0.2113\\-0.5774\\0.7887\end{pmatrix}$	$\begin{pmatrix}-0.7887\\-0.5774\\0.2113\end{pmatrix}$	$\begin{pmatrix}0.2113\\0.5774\\0.7887\end{pmatrix}$	−1/6	1.0

[a]Electric field amplitude ratios and polarization vectors with resulting interference coefficient and absolute contrast.

Table 3.3: Optimized Plane Wave Parameters[a] for Lattices Maximizing Absolute Contrast for ${}^{+}C_4^{(6)}$.

Lattice	E_2/E_1	E_3/E_1	E_4/E_1	$\hat{\mathbf{e}}_1$	$\hat{\mathbf{e}}_2$	$\hat{\mathbf{e}}_3$	$\hat{\mathbf{e}}_4$	$V_4^{(6)}$	V_{abs}
Cubic	0.4472	1	0.4472	$\begin{pmatrix} -0.1310 \\ -0.6325 \\ 0.7634 \end{pmatrix}$	$\begin{pmatrix} 0.7071 \\ 0 \\ 0.7071 \end{pmatrix}$	$\begin{pmatrix} -0.1310 \\ 0.6325 \\ 0.7634 \end{pmatrix}$	$\begin{pmatrix} 0.7071 \\ 0 \\ 0.7071 \end{pmatrix}$	1/6	1/2
FCC	1.2186	1.2186	1.4556	$\begin{pmatrix} 0.4083 \\ -0.8165 \\ 0.4083 \end{pmatrix}$	$\begin{pmatrix} 0.5455 \\ -0.8361 \\ 0.0581 \end{pmatrix}$	$\begin{pmatrix} 0.0581 \\ -0.8361 \\ 0.5455 \end{pmatrix}$	$\begin{pmatrix} 0.6804 \\ -0.2722 \\ 0.6804 \end{pmatrix}$	0.3719	0.8531
BCC	−0.4472	−0.4472	−1	$\begin{pmatrix} 0.1310 \\ -0.7634 \\ 0.6325 \end{pmatrix}$	$\begin{pmatrix} 0.7071 \\ 0.7071 \\ 0 \end{pmatrix}$	$\begin{pmatrix} 0.7071 \\ 0.7071 \\ 0 \end{pmatrix}$	$\begin{pmatrix} -0.1310 \\ 0.7634 \\ 0.6325 \end{pmatrix}$	1/6	1/2

[a]Electric field amplitude ratios and polarization vectors with resulting interference coefficient and absolute contrast.

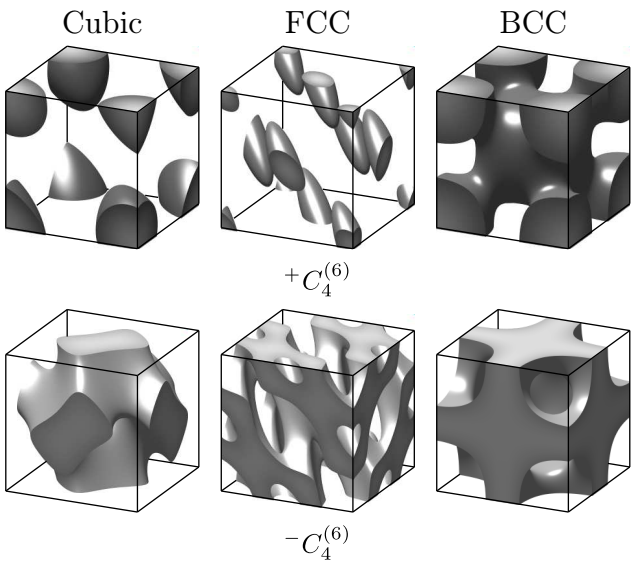

Figure 3.2: Intensity contours for interference patterns with body-centered cubic, face-centered cubic, and simple cubic periodicity that satisfy the $^{+}C_4^{(6)}$ (upper) and $^{-}C_4^{(6)}$ (lower) *conditions for primitive-lattice-vector-direction equal contrasts*.

(polarization vector $\hat{\mathbf{e}}_3$ orthogonal to $\hat{\mathbf{e}}_4$),

$$\frac{E_2}{E_1} = \frac{e_{13}}{e_{23}} \tag{3.25}$$

$$\frac{E_3}{E_1} = \frac{e_{12}}{e_{23}} \tag{3.26}$$

$$\frac{E_4}{E_1} = \frac{e_{12}}{e_{24}} \, . \tag{3.27}$$

Once these constraints are satisfied, the interference coefficient is written in terms of the polarization efficiency factors as

$$V_4^{(5)} = \frac{2e_{12}e_{13}e_{23}}{e_{12}^2 + e_{13}^2 + e_{23}^2 + e_{12}^2 e_{23}^2/e_{24}^2} \, . \tag{3.28}$$

When $C_4^{(5)}$ is satisfied, one set of global intensity extrema (maxima or minima) are located at the lattice points (vertices of the primitive unit cell with the origin at $\mathbf{r} = 0$) and the other set of global intensity extrema (minima or maxima) are located at a face center of the primitive unit cell ($\mathbf{r} = \mathbf{b}/2 + \mathbf{c}/2$). Additional stationary points (saddle points) occur at $\mathbf{r} = \mathbf{a}/2 + \mathbf{b}/4 + 3\mathbf{c}/4$, $\mathbf{r} = \mathbf{a}/2 + 3\mathbf{b}/4 + \mathbf{c}/4$, the edge centers ($\mathbf{r} = \mathbf{a}/2$, $\mathbf{r} = \mathbf{b}/2$, $\mathbf{r} = \mathbf{c}/2$), the body center ($\mathbf{r} = \mathbf{a}/2 + \mathbf{b}/2 + \mathbf{c}/2$) and the rest of the face centers ($\mathbf{r} = \mathbf{a}/2 + \mathbf{b}/2$,

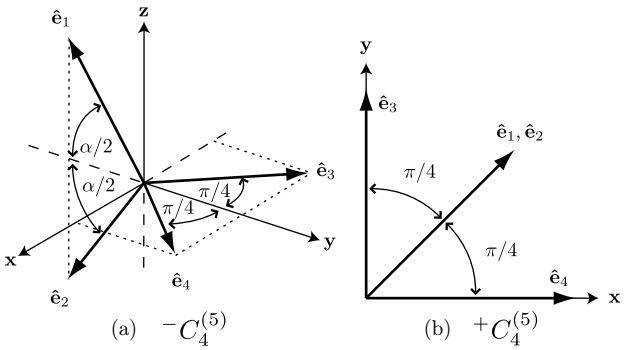

Figure 3.3: Orientation of polarizations for the subordinate conditions for unity absolute contrast [or any combination of the polarization vectors ($\hat{\mathbf{e}}_i$) where one, multiple, or all are inverted ($-\hat{\mathbf{e}}_i$)] for (a) ${}^{+}C_4^{(5)}$ where $V_4^{(5)} = 1/3$ and (b) ${}^{-}C_4^{(5)}$ where $V_4^{(5)} = -1/3$ and $\alpha = \cos^{-1}(-1/3) \approx 109.47°$.

$\mathbf{r} = \mathbf{a}/2 + \mathbf{c}/2$) of the primitive unit cell. Given the locations of the intensity extrema, the absolute contrast is written in terms of the interference coefficient as

$$V_{abs} = \left| \frac{4}{1/V_4^{(5)} + 1} \right| . \tag{3.29}$$

3.2.2.1 Subordinate condition for unity absolute contrast for ${}^{-}C_4^{(5)}$

There also exist two subordinate conditions for unity absolute contrast ($V_{abs} = 1$ with $I_{min} = 0$) for $C_4^{(5)}$. Considering Eq. (3.29), unity absolute contrast occurs when the interference coefficient $V_4^{(5)}$ equals $-1/6$ or $1/3$. In order for $V_4^{(5)} = -1/6$, an example of ${}^{-}C_4^{(5)}$, the additional constraints on the polarizations are

$$e_{12} = -1/3 \tag{3.30}$$

$$e_{13} = e_{14} = e_{23} = e_{24} = -1/\sqrt{6} \tag{3.31}$$

(109.47° or 114.09° between polarization vectors) or one of an additional 15 orientations of the polarization vectors which are obtained by inverting ($-\hat{\mathbf{e}}_i$) any single, any pair, any triplet, or all of the polarization vectors. The orientation of the resulting polarization vectors described in Eqs. (3.30) and (3.31) is illustrated in Fig. 3.3(a).

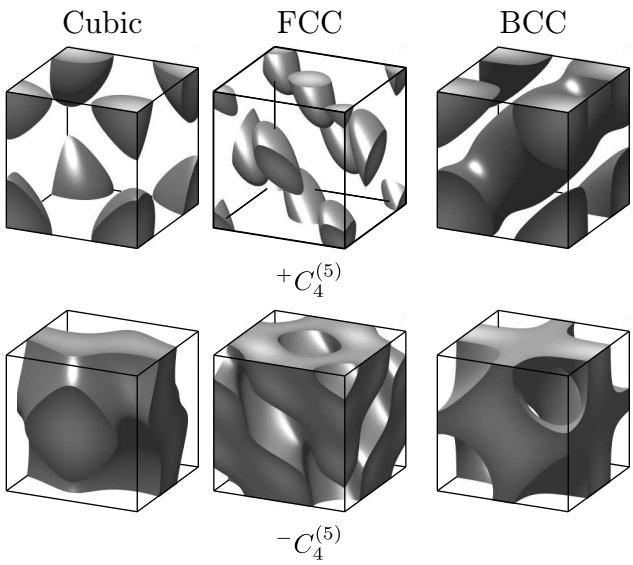

Figure 3.4: Intensity contours for interference patterns with body-centered cubic, face-centered cubic, and simple cubic periodicity that satisfy the $^{+}C_4^{(5)}$ (upper) and $^{-}C_4^{(5)}$ (lower) *conditions for primitive-lattice-vector-direction equal contrasts*.

3.2.2.2 Subordinate condition for unity absolute contrast for $^{+}C_4^{(5)}$

In order for $V_4^{(5)} = 1/3$, an example of $^{+}C_4^{(5)}$, the additional constraints on the polarizations are

$$e_{12} = 1 \tag{3.32}$$

$$e_{13} = e_{14} = e_{23} = e_{24} = 1/\sqrt{2} \tag{3.33}$$

(0° or 45° between polarization vectors) or one of an additional 15 orientations of the polarization vectors which are obtained by inverting ($-\hat{\mathbf{e}}_i$) any single, any pair, any triplet, or all of the polarization vectors. This constraint indicates that all six polarizations are coplanar with $\hat{\mathbf{e}}_3$ and $\hat{\mathbf{e}}_4$ orthogonal and $\hat{\mathbf{e}}_1$ and $\hat{\mathbf{e}}_2$ collinear, bisecting $\hat{\mathbf{e}}_3$ and $\hat{\mathbf{e}}_4$. The orientation of the resulting polarization vectors described in Eqs. (3.32) and (3.33) is illustrated in Fig. 3.3(b).

A nonlinear optimization to maximize absolute contrast is used to determine the plane wave parameters. Solutions for both $^{-}C_4^{(5)}$ and $^{+}C_4^{(5)}$ are summarized in Tables 3.4 and 3.5 respectively. Intensity contours for each of these solutions are also illustrated in Fig. 3.4 with volumes of higher intensity being enclosed.

Table 3.4: Optimized Plane Wave Parameters[a] for Lattices Maximizing Absolute Contrast for ${}^{-}C_4^{(5)}$.

Lattice	E_2/E_1	E_3/E_1	E_4/E_1	$\hat{\mathbf{e}}_1$	$\hat{\mathbf{e}}_2$	$\hat{\mathbf{e}}_3$	$\hat{\mathbf{e}}_4$	$V_4^{(5)}$	V_{abs}
Cubic	−0.7538	−0.7036	0.9213	$\begin{pmatrix} 0.2208 \\ -0.7912 \\ 0.5704 \end{pmatrix}$	$\begin{pmatrix} 0.7830 \\ 0.1911 \\ 0.5919 \end{pmatrix}$	$\begin{pmatrix} -0.8148 \\ -0.4532 \\ 0.3616 \end{pmatrix}$	$\begin{pmatrix} -0.1561 \\ 0.7721 \\ 0.6160 \end{pmatrix}$	-0.1860	0.9140
FCC	−1.8251	−0.53804	1.4018	$\begin{pmatrix} -0.7873 \\ 0.2063 \\ 0.5810 \end{pmatrix}$	$\begin{pmatrix} -0.3307 \\ -0.9105 \\ 0.2482 \end{pmatrix}$	$\begin{pmatrix} -0.2718 \\ 0.7163 \\ 0.6427 \end{pmatrix}$	$\begin{pmatrix} 0.7405 \\ -0.2711 \\ 0.6150 \end{pmatrix}$	-0.1201	.5461
BCC	1.3265	−0.9333	−1.2221	$\begin{pmatrix} -0.7830 \\ 0.5919 \\ 0.1911 \end{pmatrix}$	$\begin{pmatrix} 0.2208 \\ -0.5704 \\ 0.7912 \end{pmatrix}$	$\begin{pmatrix} -0.8148 \\ -0.3616 \\ 0.4532 \end{pmatrix}$	$\begin{pmatrix} 0.1561 \\ 0.6160 \\ 0.7721 \end{pmatrix}$	-0.1860	0.9140

[a]Electric field amplitude ratios and polarization vectors with resulting interference coefficient and absolute contrast.

Table 3.5: Optimized Plane Wave Parameters[a] for Lattices Maximizing Absolute Contrast for ${}^{+}C_4^{(5)}$.

Lattice	E_2/E_1	E_3/E_1	E_4/E_1	$\hat{\mathbf{e}}_1$	$\hat{\mathbf{e}}_2$	$\hat{\mathbf{e}}_3$	$\hat{\mathbf{e}}_4$	$V_4^{(5)}$	V_{abs}
Cubic	1	2	2	$\begin{pmatrix} 0.0 \\ -0.7071 \\ 0.7071 \end{pmatrix}$	$\begin{pmatrix} 0.0 \\ -0.7071 \\ 0.7071 \end{pmatrix}$	$\begin{pmatrix} -0.7071 \\ 0.0 \\ 0.7071 \end{pmatrix}$	$\begin{pmatrix} 0.7071 \\ 0.0 \\ 0.7071 \end{pmatrix}$	1/5	2/3
FCC	1	$\sqrt{2}$	$-\sqrt{2}$	$\begin{pmatrix} 0.7071 \\ -0.7071 \\ 0.0 \end{pmatrix}$	$\begin{pmatrix} 0.7071 \\ -0.7071 \\ 0.0 \end{pmatrix}$	$\begin{pmatrix} 0.0969 \\ -0.9031 \\ 0.4184 \end{pmatrix}$	$\begin{pmatrix} -0.9031 \\ 0.0969 \\ 0.4184 \end{pmatrix}$	1/3	1.0
BCC	1	2	-2	$\begin{pmatrix} 0.0 \\ -0.7071 \\ 0.7071 \end{pmatrix}$	$\begin{pmatrix} 0.0 \\ -0.7071 \\ 0.7071 \end{pmatrix}$	$\begin{pmatrix} -0.7071 \\ -0.7071 \\ 0.0 \end{pmatrix}$	$\begin{pmatrix} -0.7071 \\ 0.7071 \\ 0.0 \end{pmatrix}$	1/5	2/3

[a]Electric field amplitude ratios and polarization vectors with resulting interference coefficient and absolute contrast.

3.2.3 Condition for primitive-lattice-vector-direction equal contrasts $C_4^{(4)}$

A third *condition for primitive-lattice-vector-direction equal contrasts* ($C_4^{(4)}$) occurs when four of the six interference coefficients (corresponding to interfering-beam-pairs) contribute to the modulation of intensity within the interference pattern as

$$V_4^{(4)} = V_{12} = V_{13} = V_{14} = V_{23},\ V_{24} = V_{34} = 0\ \text{ [Condition } C_4^{(4)}\text{]}\,. \tag{3.34}$$

Applying this condition leads to the following set of constraints on the polarizations and amplitudes of the recording beams:

$$e_{24} = e_{34} = 0 \tag{3.35}$$

(polarization vectors are orthogonal),

$$\frac{E_2}{E_1} = \frac{e_{13}}{e_{23}} \tag{3.36}$$

$$\frac{E_3}{E_1} = \frac{e_{12}}{e_{23}} \tag{3.37}$$

$$\frac{E_4}{E_1} = \frac{e_{12}e_{13}}{e_{14}e_{23}}\,. \tag{3.38}$$

Once these constraints are satisfied, the interference coefficient is written in terms of the polarization efficiency factors as

$$V_4^{(4)} = \frac{2e_{12}e_{13}e_{23}}{e_{12}^2 + e_{13}^2 + e_{23}^2 + e_{12}^2e_{13}^2/e_{14}^2}\,. \tag{3.39}$$

When $C_4^{(4)}$ is satisfied, one set of global intensity extrema (maxima or minima) are located at the lattice points (vertices of the primitive unit cell with the origin at $\mathbf{r} = 0$) and the other set of global intensity extrema (minima or maxima) are located at $\mathbf{r} = \mathbf{a}/3 + 2\mathbf{b}/3 + \mathbf{c}/2$ and $\mathbf{r} = 2\mathbf{a}/3 + \mathbf{b}/3 + \mathbf{c}/2$. Additional stationary points (saddle points) occur at the edge centers ($\mathbf{r} = \mathbf{a}/2$, $\mathbf{r} = \mathbf{b}/2$, $\mathbf{r} = \mathbf{c}/2$), body center ($\mathbf{r} = \mathbf{a}/2 + \mathbf{b}/2 + \mathbf{c}/2$) and face centers ($\mathbf{r} = \mathbf{a}/2 + \mathbf{b}/2$, $\mathbf{r} = \mathbf{a}/2 + \mathbf{c}/2$, $\mathbf{r} = \mathbf{b}/2 + \mathbf{c}/2$) of the primitive unit cell, and also at $\mathbf{r} = \mathbf{a}/3 + 2\mathbf{b}/3$ and $\mathbf{r} = 2\mathbf{a}/3 + \mathbf{b}/3$. Given the locations of the intensity extrema, the absolute contrast is written in terms of the interference coefficient as

$$V_{abs} = \left|\frac{13}{4/V_4^{(4)} + 3}\right|\,. \tag{3.40}$$

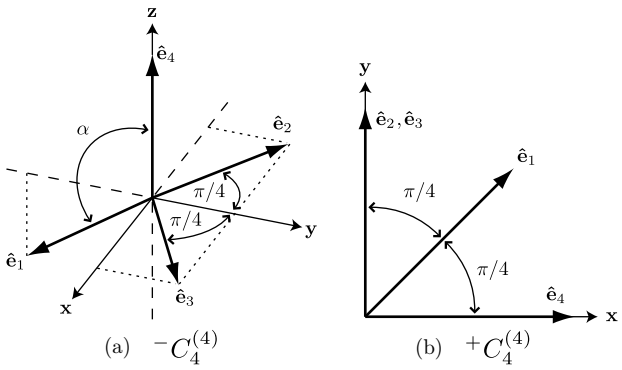

Figure 3.5: Orientation of polarizations for the subordinate conditions for unity absolute contrast [or any combination of the polarization vectors ($\hat{\mathbf{e}}_i$) where one, multiple, or all are inverted ($-\hat{\mathbf{e}}_i$)] for (a) ${}^{+}C_4^{(4)}$ where $V_4^{(4)} = 2/5$ (b) ${}^{-}C_4^{(4)}$ where $V_4^{(4)} = -1/4$ and $\alpha = \cos^{-1}(1/\sqrt{3}) \approx 125.26°$.

3.2.3.1 Subordinate condition for unity absolute contrast for ${}^{-}C_4^{(4)}$

There also exist two subordinate conditions for unity absolute contrast ($V_{abs} = 1$ with $I_{min} = 0$) for $C_4^{(4)}$. Considering Eq. (3.40), unity absolute contrast occurs when the interference coefficient $V_4^{(4)}$ equals $-1/4$ or $2/5$. In order for $V_4^{(4)} = -1/4$, an example of ${}^{-}C_4^{(4)}$, the additional constraints on the polarizations are

$$e_{12} = e_{13} = -1/\sqrt{6} \tag{3.41}$$

$$e_{14} = -1/\sqrt{3} \tag{3.42}$$

$$e_{23} = -1/2 \tag{3.43}$$

(114.09°, 125.26°, or 120° between polarization vectors) or one of an additional 15 orientations of the polarization vectors which are obtained by inverting ($-\hat{\mathbf{e}}_i$) any single, any pair, any triplet, or all of the polarization vectors. The orientation of the resulting polarization vectors described in Eqs. (3.41)-(3.43) is illustrated in Fig. 3.5(a).

3.2.3.2 *Subordinate condition for unity absolute contrast for* ${}^{+}C_4^{(4)}$

In order for $V_4^{(4)} = 2/5$, an example of ${}^{+}C_4^{(4)}$, the additional constraints on the polarizations are

$$e_{12} = e_{13} = e_{14} = 1/\sqrt{2} \tag{3.44}$$

$$e_{23} = 1 \tag{3.45}$$

(45° or 0° between polarization vectors) or one of an additional 15 orientations of the polarization vectors which are obtained by inverting ($-\hat{\mathbf{e}}_i$) any single, any pair, any triplet, or all of the polarization vectors. This constraint indicates that all six polarizations are coplanar with $\hat{\mathbf{e}}_4$ orthogonal to $\hat{\mathbf{e}}_2$ and $\hat{\mathbf{e}}_3$ (which are collinear) and $\hat{\mathbf{e}}_1$ bisecting $\hat{\mathbf{e}}_2$ and $\hat{\mathbf{e}}_4$. The orientation of the resulting polarization vectors described in Eqs. (3.44) and (3.45) is illustrated in Fig. 3.5(b).

A nonlinear optimization to maximize absolute contrast is used to determine the plane wave parameters. Solutions for both ${}^{-}C_4^{(4)}$ and ${}^{+}C_4^{(4)}$ are summarized in Tables 3.6 and Table 3.7 respectively. Intensity contours for each of these solutions are also illustrated in Fig. 3.6 with volumes of higher intensity being enclosed.

3.2.4 Condition for primitive-lattice-vector-direction equal contrasts $C_4^{(3)}$

The fourth, and final, *condition for primitive-lattice-vector-direction equal contrasts* ($C_4^{(3)}$) occurs when three of the six interference coefficients (corresponding to interfering-beam-pairs) contribute to the modulation of intensity within the interference pattern as

$$V_4^{(3)} = V_{12} = V_{13} = V_{14},\ V_{23} = V_{24} = V_{34} = 0\ \ [\text{Condition } C_4^{(3)}]\ . \tag{3.46}$$

Applying this condition leads to the following set of constraints on the polarizations and amplitudes of the recording beams:

$$e_{23} = e_{24} = e_{34} = 0 \tag{3.47}$$

Table 3.6: Optimized Plane Wave Parameters[a] for Lattices Maximizing Absolute Contrast for ${}^{-}C_4^{(4)}$.

Lattice	E_2/E_1	E_3/E_1	E_4/E_1	$\hat{\mathbf{e}}_1$	$\hat{\mathbf{e}}_2$	$\hat{\mathbf{e}}_3$	$\hat{\mathbf{e}}_4$	$V_4^{(4)}$	V_{abs}
Cubic	−0.78901	0.7769	−0.5049	$\begin{pmatrix} 0.6395 \\ -0.7594 \\ 0.1199 \end{pmatrix}$	$\begin{pmatrix} -0.4298 \\ -0.8161 \\ 0.3863 \end{pmatrix}$	$\begin{pmatrix} -0.6613 \\ 0.0841 \\ 0.7454 \end{pmatrix}$	$\begin{pmatrix} 0.7417 \\ -0.0752 \\ 0.6665 \end{pmatrix}$	-0.2488	0.9942
FCC	−0.8742	0.8915	−0.3104	$\begin{pmatrix} -0.1980 \\ -0.5870 \\ 0.7850 \end{pmatrix}$	$\begin{pmatrix} -0.9810 \\ 0.0610 \\ 0.1840 \end{pmatrix}$	$\begin{pmatrix} -0.2392 \\ 0.9353 \\ 0.2608 \end{pmatrix}$	$\begin{pmatrix} 0.1661 \\ -0.2252 \\ 0.9601 \end{pmatrix}$	-0.1994	0.7620
BCC	0.7769	−0.78901	−0.5049	$\begin{pmatrix} -0.7594 \\ 0.6395 \\ 0.1199 \end{pmatrix}$	$\begin{pmatrix} 0.0841 \\ -0.6613 \\ 0.7454 \end{pmatrix}$	$\begin{pmatrix} -0.8161 \\ -0.4298 \\ 0.3863 \end{pmatrix}$	$\begin{pmatrix} -0.0752 \\ 0.7417 \\ 0.6665 \end{pmatrix}$	-0.2488	0.9942

[a]Electric field amplitude ratios and polarization vectors with resulting interference coefficient and absolute contrast.

Table 3.7: Optimized Plane Wave Parameters[a] for Lattices Maximizing Absolute Contrast for ${}^{+}C_4^{(4)}$.

Lattice	E_2/E_1	E_3/E_1	E_4/E_1	$\hat{\mathbf{e}}_1$	$\hat{\mathbf{e}}_2$	$\hat{\mathbf{e}}_3$	$\hat{\mathbf{e}}_4$	$V_4^{(4)}$	V_{abs}
Cubic	−0.5956	0.4575	0.4782	$\begin{pmatrix} -0.7193 \\ 0.0251 \\ 0.6942 \end{pmatrix}$	$\begin{pmatrix} 0.7588 \\ 0.6405 \\ 0.1183 \end{pmatrix}$	$\begin{pmatrix} -0.7473 \\ -0.6585 \\ 0.0888 \end{pmatrix}$	$\begin{pmatrix} -0.6509 \\ 0.7524 \\ 0.1015 \end{pmatrix}$	0.2974	0.7903
FCC	−0.7226	−0.6966	0.6943	$\begin{pmatrix} -0.7201 \\ 0.6934 \\ 0.0268 \end{pmatrix}$	$\begin{pmatrix} 0.0071 \\ -0.9808 \\ 0.1947 \end{pmatrix}$	$\begin{pmatrix} 0.1083 \\ -0.9195 \\ 0.3779 \end{pmatrix}$	$\begin{pmatrix} -0.8840 \\ 0.0849 \\ 0.4598 \end{pmatrix}$	0.3948	0.9899
BCC	0.4575	−0.5956	0.4782	$\begin{pmatrix} 0.0251 \\ -0.7193 \\ 0.6942 \end{pmatrix}$	$\begin{pmatrix} -0.6585 \\ -0.7473 \\ 0.0888 \end{pmatrix}$	$\begin{pmatrix} 0.6405 \\ 0.7588 \\ 0.1183 \end{pmatrix}$	$\begin{pmatrix} 0.7524 \\ -0.6509 \\ 0.1015 \end{pmatrix}$	0.2974	0.7903

[a]Electric field amplitude ratios and polarization vectors with resulting interference coefficient and absolute contrast.

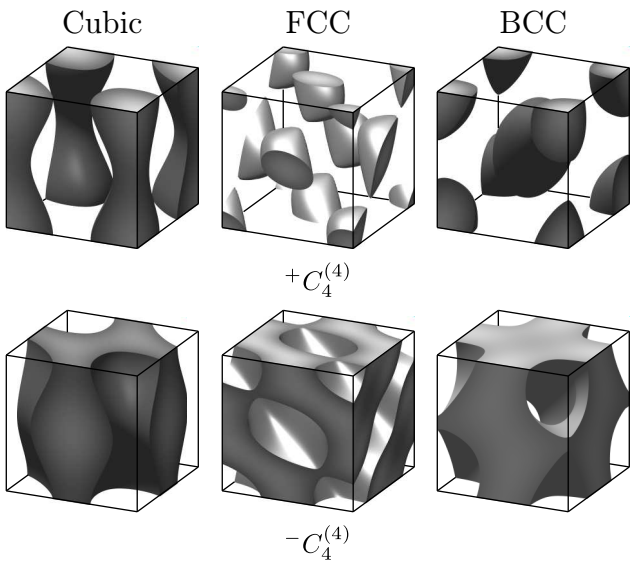

Figure 3.6: Intensity contours for interference patterns with body-centered cubic, face-centered cubic, and simple cubic periodicity that satisfy the ${}^{+}C_4^{(4)}$ (upper) and ${}^{-}C_4^{(4)}$ (lower) *conditions for primitive-lattice-vector-direction equal contrasts*.

(polarization vectors are orthogonal),

$$\frac{E_3}{E_2} = \frac{e_{12}}{e_{13}} \tag{3.48}$$

$$\frac{E_4}{E_2} = \frac{e_{12}}{e_{14}} \tag{3.49}$$

Once these constraints are satisfied, the interference coefficient is written in terms of the polarization efficiency factors and the electric field amplitudes as

$$V_4^{(3)} = \frac{2E_1E_2e_{12}}{E_1^2 + E_2^2(1 + e_{12}^2/e_{13}^2 + e_{12}^2/e_{14}^2)} \,. \tag{3.50}$$

When $C_4^{(3)}$ is satisfied, one set of global intensity extrema (maxima or minima) are located at the lattice points (vertices of the primitive unit cell with the origin at $\mathbf{r} = 0$) and the other set of global intensity extrema (minima or maxima) are located at the body center of the primitive unit cell ($\mathbf{r} = \mathbf{a}/2 + \mathbf{b}/2 + \mathbf{c}/2$). Additional stationary points (saddle points) occur at the edge centers ($\mathbf{r} = \mathbf{a}/2$, $\mathbf{r} = \mathbf{b}/2$, $\mathbf{r} = \mathbf{c}/2$) and the face centers ($\mathbf{r} = \mathbf{a}/2 + \mathbf{b}/2$, $\mathbf{r} = \mathbf{a}/2 + \mathbf{c}/2$, $\mathbf{r} = \mathbf{b}/2 + \mathbf{c}/2$) of the primitive unit cell. Given the locations of the intensity extrema, the absolute contrast is written in terms of the interference coefficient as

$$V_{abs} = \left|3V_4^{(3)}\right| \,. \tag{3.51}$$

Given a configuration of polarizations that satisfy Eqs. (3.47)-(3.49), the absolute contrast [or interference coefficient in Eq. (3.50)] is maximized by setting the electric field ratio E_2/E_1 equal to

$$\frac{E_2}{E_1} = \frac{1}{\sqrt{1 + e_{12}^2/e_{13}^2 + e_{12}^2/e_{14}^2}} . \tag{3.52}$$

The interference coefficient can then be rewritten solely in terms of polarization as

$$V_4^{(3)} = \frac{e_{12}e_{13}e_{14}}{\sqrt{e_{13}^2e_{14}^2 + e_{12}^2e_{14}^2 + e_{12}^2e_{13}^2}} . \tag{3.53}$$

Generally speaking, there is no difference in interference patterns satisfying ${}^{-}C_4^{(3)}$ and ${}^{+}C_4^{(3)}$ in that the contours around intensity maxima and minima are identical (differing only in intensity value). This particular *condition for primitive-lattice-vector-direction equal contrasts* in three dimensions is very similar to the *condition for primitive-lattice-vector-direction equal contrasts* in two dimensions designated as $C_3^{(2)}$ (previously called the *second uniform contrast condition* in two dimensions) in this regard [84]. Given a bias intensity value of I_b (where $I_{min} \leq I_b \leq I_{max}$), these two identical surfaces are described as

$$\begin{aligned} I_{max} - I_b &= I(\mathbf{r}) \\ I_{min} + I_b &= I(\mathbf{r} + \mathbf{a}/2 + \mathbf{b}/2 + \mathbf{c}/2) \end{aligned} \tag{3.54}$$

While the interference coefficient $V_4^{(3)}$ of a specific solution that satisfies $C_4^{(3)}$ will be positive or negative, this metric simply describes whether interference maxima or minima are located at lattice points ($\mathbf{r} = 0$ and all equivalent points in the periodic interference pattern). Two interference patterns with coefficients of $V_4^{(3)}$ and $-V_4^{(3)}$ are identical when either is translated by $\mathbf{a}/2 + \mathbf{b}/2 + \mathbf{c}/2$.

3.2.4.1 Subordinate condition for unity absolute contrast for $C_4^{(3)}$

There exists one subordinate condition for unity absolute contrast ($V_{abs} = 1$ with $I_{min} = 0$) for $C_4^{(3)}$. Considering Eq. (3.51), unity absolute contrast occurs when the interference coefficient $V_4^{(3)}$ equals $-1/3$ or $1/3$. The additional constraints on the polarizations are

$$e_{ij} = e_{12} = e_{13} = e_{14} = 1/\sqrt{3} \tag{3.55}$$

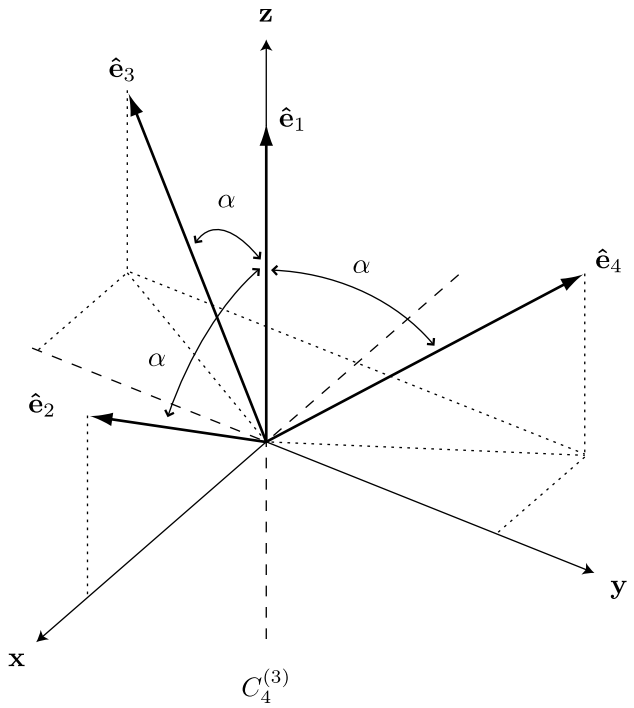

Figure 3.7: Orientation of polarizations for the subordinate conditions for unity absolute contrast [or any combination of the polarization vectors ($\hat{\mathbf{e}}_i$) where one, multiple, or all are inverted ($-\hat{\mathbf{e}}_i$)] for $C_4^{(3)}$ where $V_4^{(3)} = \pm 1/3$ and $\alpha = \cos^{-1}(\sqrt{3}/3) \approx 54.74°$.

(54.74° between polarization vectors) or one of an additional 15 orientations of the polarization vectors which are obtained by inverting ($-\hat{\mathbf{e}}_i$) any single, any pair, any triplet, or all of the polarization vectors. The orientation of the resulting polarization vectors described in Eq. (3.55) is illustrated in Fig. 3.7.

A nonlinear optimization to maximize absolute contrast is used to determine the plane wave parameters. Solutions for $C_4^{(3)}$ are summarized in Table 3.8. Intensity contours for each of these solutions are also illustrated in Fig. 3.8 with volumes of higher intensity being enclosed.

3.3 Summary

Optimized solutions for three different lattices with all four different *conditions for primitive-lattice-vector-direction equal contrasts* in three dimensions exhibiting the maximum possible absolute contrast have been given in Tables 3.3 through 3.8. These tables provide

Table 3.8: Optimized Plane Wave Parameters[a] for Lattices Maximizing Absolute Contrast for ${}^{+}C_4^{(3)}$.

Lattice	E_2/E_1	E_3/E_1	E_4/E_1	$\hat{\mathbf{e}}_1$	$\hat{\mathbf{e}}_2$	$\hat{\mathbf{e}}_3$	$\hat{\mathbf{e}}_4$	$V_4^{(3)}$	V_{abs}
Cubic	$2/3$	$-2/3$	$1/3$	$\begin{pmatrix} 0.5826 \\ -0.7867 \\ 0.2041 \end{pmatrix}$	$\begin{pmatrix} -0.5000 \\ -0.8090 \\ 0.3090 \end{pmatrix}$	$\begin{pmatrix} -0.3090 \\ 0.5000 \\ 0.8090 \end{pmatrix}$	$\begin{pmatrix} 0.8090 \\ -0.3090 \\ 0.5000 \end{pmatrix}$	$\sqrt{6}/9$	$\sqrt{6}/3$
FCC	$2/3$	$1/3$	$-2/3$	$\begin{pmatrix} -0.7144 \\ 0.6995 \\ 0.0149 \end{pmatrix}$	$\begin{pmatrix} -0.9045 \\ -0.3455 \\ 0.2500 \end{pmatrix}$	$\begin{pmatrix} -0.2500 \\ 0.9045 \\ 0.3455 \end{pmatrix}$	$\begin{pmatrix} 0.3455 \\ -0.2500 \\ 0.9045 \end{pmatrix}$	$\sqrt{6}/9$	$\sqrt{6}/3$
BCC	$1/3$	$2/3$	$2/3$	$\begin{pmatrix} -0.2041 \\ -0.5826 \\ 0.7867 \end{pmatrix}$	$\begin{pmatrix} -0.5000 \\ -0.8090 \\ 0.3090 \end{pmatrix}$	$\begin{pmatrix} -0.3090 \\ 0.5000 \\ 0.8090 \end{pmatrix}$	$\begin{pmatrix} 0.8090 \\ -0.3090 \\ 0.5000 \end{pmatrix}$	$\sqrt{6}/9$	$\sqrt{6}/3$

[a]Electric field amplitude ratios and polarization vectors with resulting interference coefficient and absolute contrast.

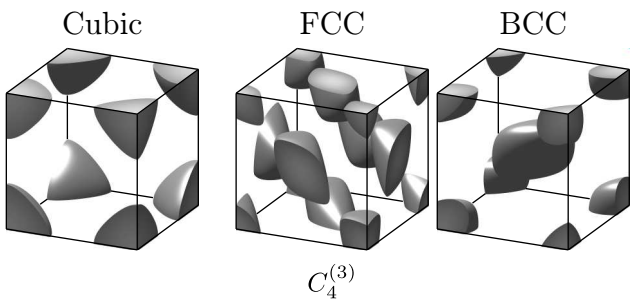

Figure 3.8: Intensity contours for interference patterns with body-centered cubic, face-centered cubic, and simple cubic periodicity that satisfy the $C_4^{(3)}$ *condition for primitive-lattice-vector-direction equal contrasts*.

guidelines for determining lithographic process parameters, and enable choosing between processes based on positive-tone or negative-tone photoresists. The lithographic process will be easier to implement and will provide greater processing latitude when an interference pattern with the largest absolute contrast is used.

From the quantitative descriptions of the *conditions for primitive-lattice-vector-direction equal contrasts* and the illustrations of the intensity contours for the three lattices, a more qualitative description of the resultant interference patterns can be given. For the $C_4^{(6)}$ and $C_4^{(3)}$, there is equal contrast in each of the primitive lattice directions (**a**, **b**, and **c**) from each lattice point. For $C_4^{(5)}$, there is equal contrast in two of the primitive lattice directions (**a** and **c**) from each lattice point. For $C_4^{(4)}$, there is equal contrast in two of the primitive lattice directions (**a** and **b**) from each lattice point. For the three lattices treated, there are significant differences in the absolute contrast of the optimized solutions between each *condition for primitive-lattice-vector-direction equal contrasts* and between the distinct ${}^{+}C_n^{(m)}$ and ${}^{-}C_n^{(m)}$ solutions. For the simple cubic lattice, the optimized absolute contrast ranges from 0.5 when satisfying ${}^{+}C_4^{(6)}$ to unity absolute contrast when satisfying ${}^{-}C_4^{(6)}$. For the face-centered cubic lattice, the optimized absolute contrast ranges from 0.2599 when satisfying ${}^{-}C_4^{(6)}$ to unity absolute contrast when satisfying ${}^{+}C_4^{(5)}$. For the body-centered cubic lattice, the optimized absolute contrast ranges from 0.5 when satisfying ${}^{+}C_4^{(6)}$ to unity absolute contrast when satisfying ${}^{-}C_4^{(6)}$. This paper has presented four different conditions

in the case of four-beam interference that will result in lithographically useful interference patterns suitable for lithographic processing. It also serves as a basis for determining and describing these interference patterns in terms of the crystallographic space groups which determine the symmetry of the patterns.

CHAPTER 4

THEORETICAL PERFORMANCE OF TWO-DIMENSIONAL PHOTONIC CRYSTAL STRUCTURES

4.1 Structure Modeling and Simulation

To analyze and design photonic crystal structures, it is often necessary to calculate a structure's supported electromagnetic modes. This allows for the calculation of metrics such as photonic band gap and other dispersion relationships. This is usually accomplished by solving the vector equation derived from Maxwell's equations given by [1]

$$\nabla \times \left(\frac{1}{\epsilon_r(\mathbf{r})} \nabla \times \mathbf{H}(\mathbf{r}) \right) = \left(\frac{\omega}{c} \right)^2 \mathbf{H}(\mathbf{r}) \, . \tag{4.1}$$

The problem reduces to an eigenvalue problem, resulting in the allowable electromagnetic modes of the structure. There exists both commercial and open-source software available for computational photonics. A free software package has been developed and maintained by Steven G. Johnson at the Massachusetts Institute of Technology along with the Joannopoulos Ab Initio Physics group. This software is called MIT Photonic-Bands. It computes fully-vectorial eigenmodes of Maxwell's equations with periodic boundary conditions by preconditioned conjugate-gradient minimization of the block Rayleigh quotient in a plane wave basis [89]. Included in the software package are utilities for extracting band structures and mode fields including a Scheme-based scriptable interface (Guile). All of the band structures and band structure related calculations in this thesis were performed using this software package. More information on the algorithms used to calculate the eigenmodes of periodic structures is available in the literature and will not be a focus in this thesis. However, proper attention must be paid to how these problems are configured within the software. Included in Appendix B are the Guile scripts that were used with the MIT Photonic-Bands software to calculate the band structures of all the structures in this

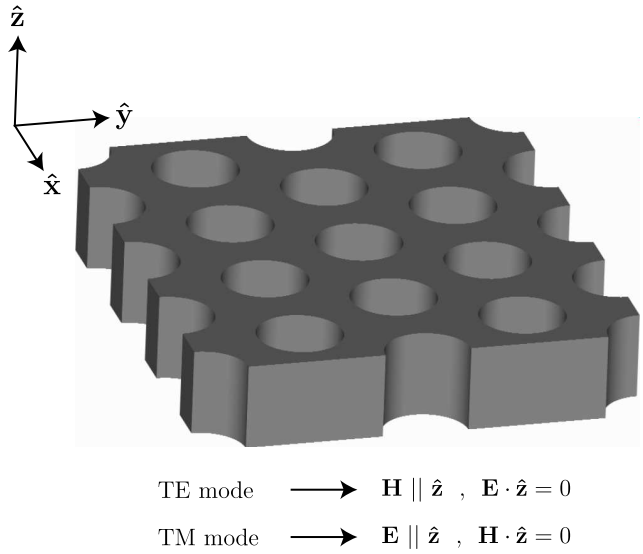

Figure 4.1: In two-dimensional photonic crystal structures invariant in the *z* direction, the TE mode is defined when the electric field is confined in the *xy* plane (the magnetic field is *z* direction). The TM mode is defined when the magnetic field is confined in the *xy* plane (the electric field is *z* direction).

thesis. The included scripts are given as a guide to correctly set up the software and not intended to recreate all of the illustrations within this thesis. Some of the plots here are the culmination of modeling hundreds of different structures, while the included scripts are intended to model just a single structure. Appropriately written Bash scripts are used to loop through variables of interest and parse the resulting output files to produce the illustrations presented here.

4.2 Conventions

It is appropriate to discuss some important conventions and definitions that will be used in this research. In dealing with two-dimensional photonic crystals invariant in the *z* direction, it is convenient to consider two distinct polarizations: TE and TM. In this research, the TE polarization is defined when the electric field is confined in the *xy* plane (the magnetic field is in the *z* direction). TM polarization is defined when the magnetic field is confined in the *xy* plane (the electric field is in the *z* direction). This convention is illustrated in Fig. 4.1. While this is the most common convention used in the literature, others exist. For

instance, in the commercially available software package BandSOLVE [90], the definition is reversed.

A commonly used metric to measure the size of a photonic band gap is the *gap-midgap ratio*, commonly referred to as the *band gap* (as a percentage). This is defined as

$$\text{bandgap size (\%)} = \textit{gap-midgap ratio} = \frac{\Delta\omega}{\omega_{mid}}\ (\%) \tag{4.2}$$

where

$$\Delta\omega = Min[\omega_{i+1}(k)] - Max[\omega_i(k)] \tag{4.3}$$

and

$$\omega_{mid} = (Min[\omega_{i+1}(k)] + Max[\omega_i(k)])/2 \tag{4.4}$$

and ω_{mid} is the mid-gap frequency for a band gap between the i and $i+1$ bands. This normalized and dimensionless metric is a more useful comparison between different structures due to the scalability of Maxwell's equations.

4.3 Modeling Two-Dimensional Lattices of Circular Rods/Holes

It is essential to understand how the performance of photonic crystal structures fabricated through multi-beam-interference lithography compares to other similar structures that are conventionally fabricated [85, 91]. Often times, square or hexagonal lattices of circular holes or rods are fabricated in silicon substrates. By solving for the allowable electromagnetic modes in these structures, band gap maps can be created to gain insight on the performance of these structures. Figure 4.2 illustrates a band gap map for a square lattice of circular silicon rods in air. A band gap map highlights areas of normalized frequency where a band gap arises as a function of some design parameter. In this case, an obvious choice is the normalized radius of the circular silicon rods. Similarly, a band gap map can be calculated for a square lattice of air holes in silicon. This is illustrated in Fig. 4.3. Both band gap maps show large areas of TM band gap, however only the square lattice of circular holes shows a significant TE band gap. Within these band gap maps are particular structures of interest, more specifically those that exhibit the largest TE, TM and complete band

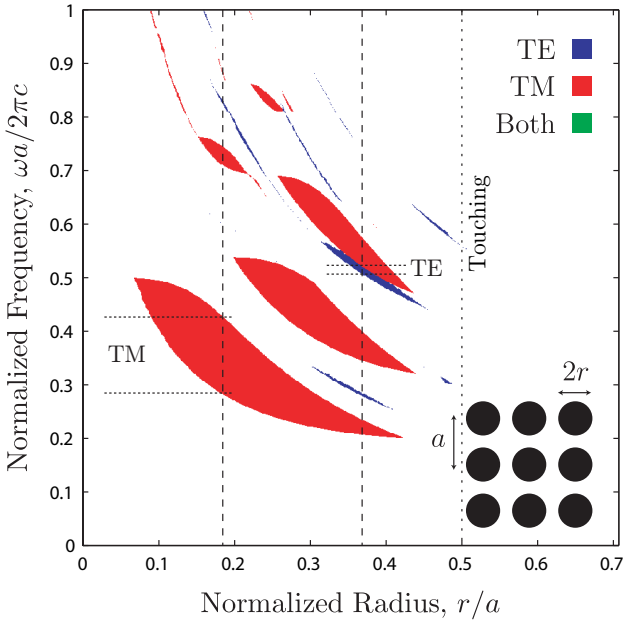

Figure 4.2: Band gap map for a square lattice of circular silicon ($\epsilon_r = 13$) rods in air ($\epsilon_r = 1$). Band gaps exist for TE (3.86%, $r/a = 0.37$) and TM (41.08%, $r/a = 0.18$) where vertical dashed lines indicate the corresponding normalized radii. Horizontal lines indicate the extent of the maximum band gap. Note that a complete band gap does not exist. The vertical dotted line indicates the normalized radius for the touching case.

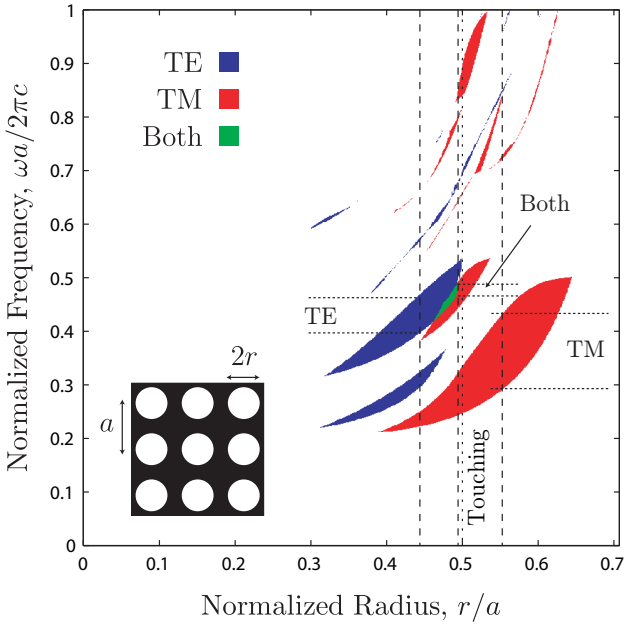

Figure 4.3: Band gap map for a square lattice of circular air ($\epsilon_r = 1$) holes in silicon ($\epsilon_r = 13$). Band gaps exist for TE (17.08%, $r/a = 0.44$), TM (39.61%, $r/a = 0.55$) and complete (4.80%, $r/a = 0.49$) where vertical dashed lines indicate the corresponding normalized radii. Horizontal lines indicate the extent of the maximum band gap. The vertical dotted line indicates the normalized radius for the touching case.

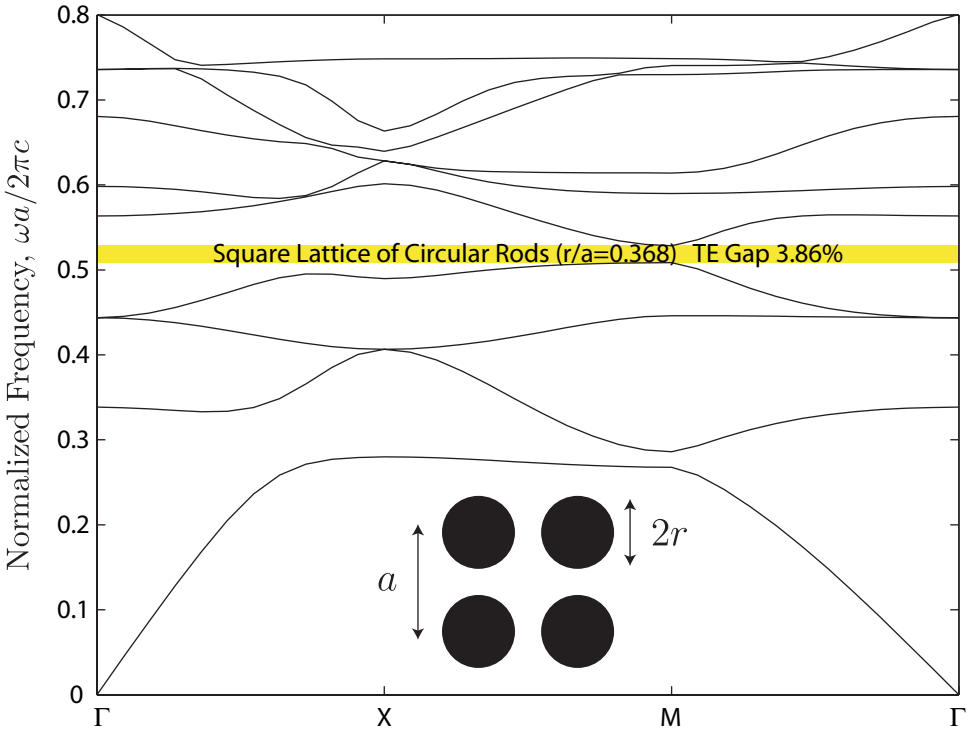

Figure 4.4: Band structure of a square lattice of circular rods corresponding to the largest TE band gap in Fig. 4.2.

gaps. The normalized radii at which these occur are indicated by dashed lines. Another radius of interest is the touching case, indicated by a dotted line. It is at this point where the circular holes or rods begin to overlap. The resulting structures and band structures for these lattices of interest are illustrated in Figs. 4.4 to 4.8.

The following lists the maximum band gap sizes, the corresponding normalized radii, r/a, and area fill factors, F, (percentage of silicon per unit cell) for the specific structures of interest. From the previously mentioned band gap maps, a square lattice of circular rods and holes has a maximum TE band gap size of 3.86% (r/a = 0.368, F = 42.6%) and 17.08% (r/a = 0.444, F = 38.1%) respectively. A square lattice of circular rods and holes has a maximum TM band gap size of 41.08% (r/a = 0.184, F = 10.7%) and 39.61% (r/a = 0.553, F = 10.7%) respectively. A square lattice of circular holes can exhibit a complete band gap with a maximum of 4.80% (r/a = 0.494, F = 23.2%).

Note the resulting structures and band diagrams for the cases that exhibit the maximum

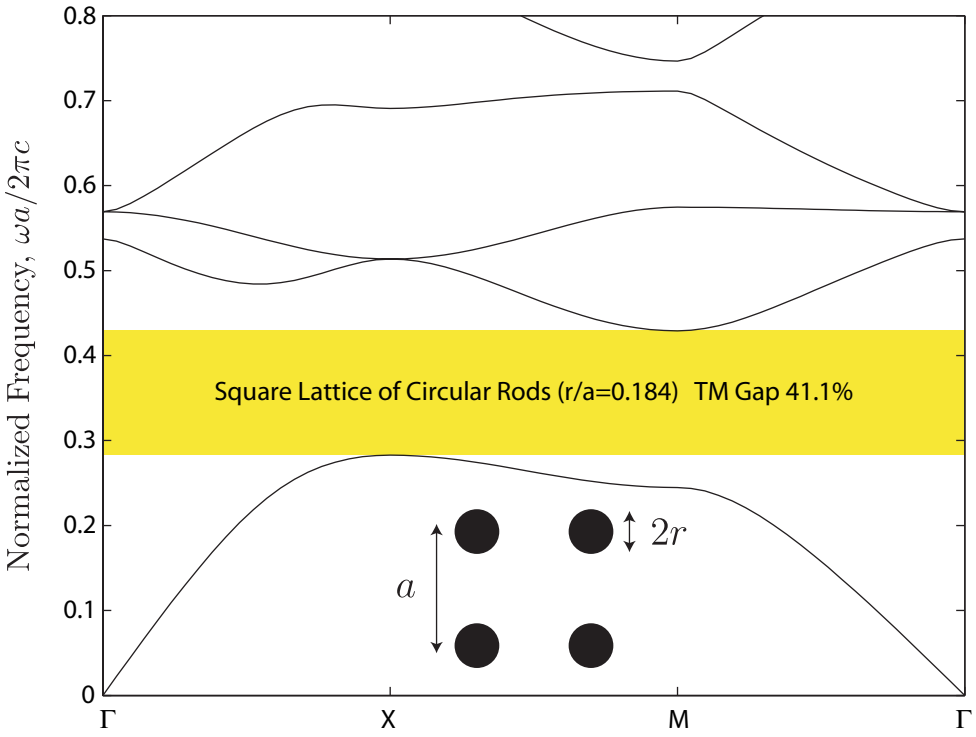

Figure 4.5: Band structure of a square lattice of circular rods corresponding to the largest TM band gap in Fig. 4.2.

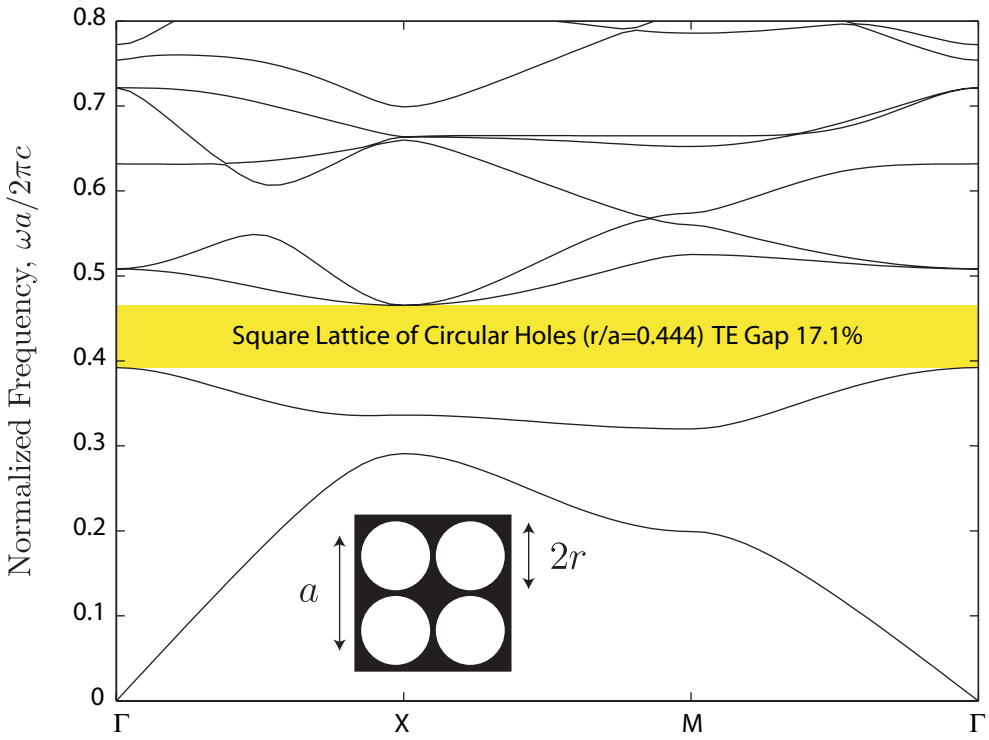

Figure 4.6: Band structure of a square lattice of circular holes corresponding to the largest TE band gap in Fig. 4.3.

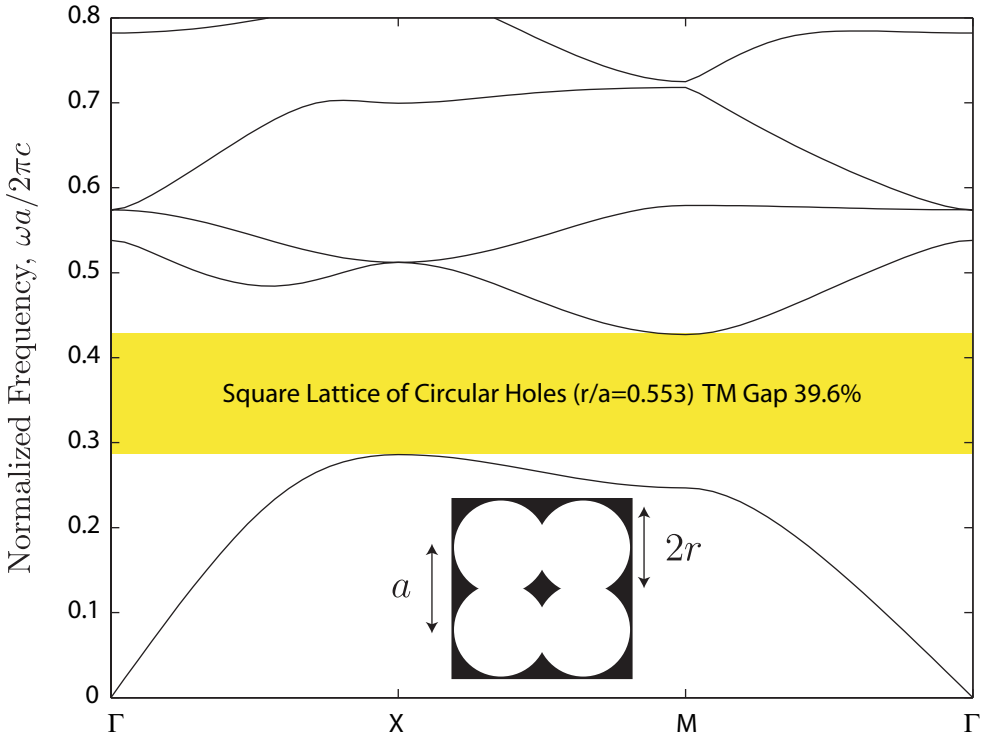

Figure 4.7: Band structure of a square lattice of circular holes corresponding to the largest TM band gap in Fig. 4.3.

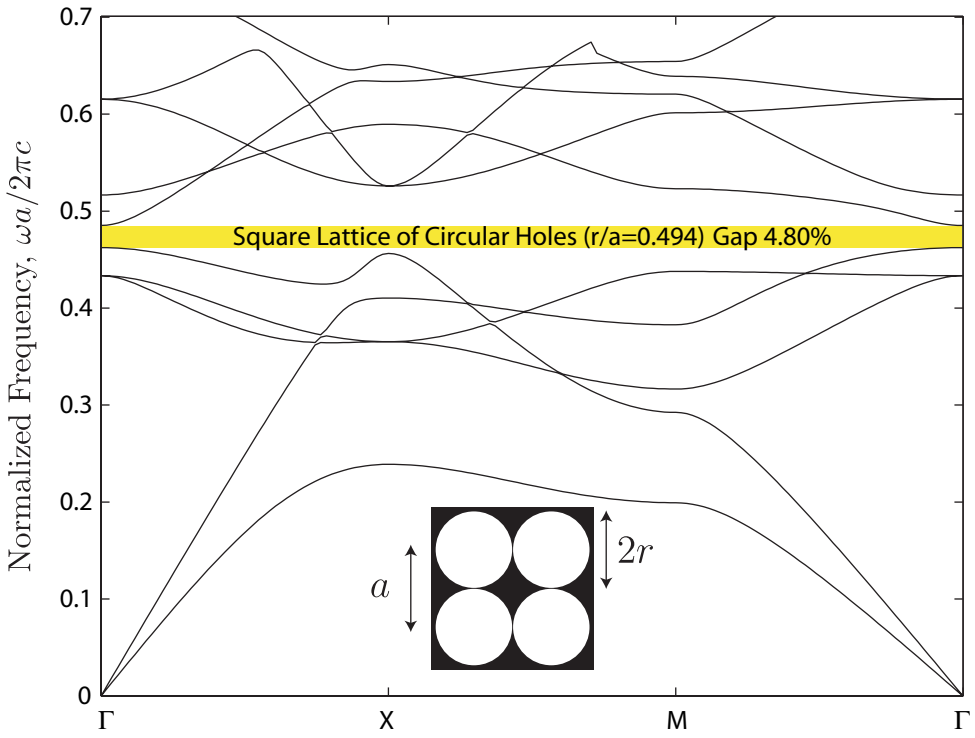

Figure 4.8: Band structure of a square lattice of circular holes corresponding to the largest complete band gap in Fig. 4.3.

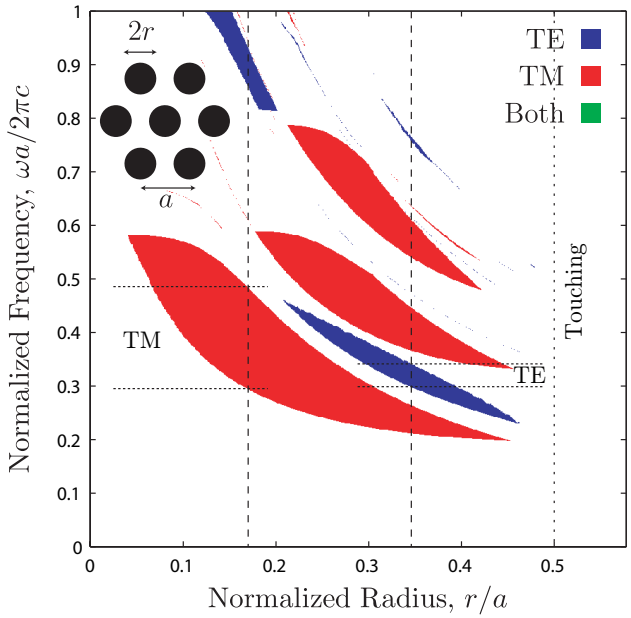

Figure 4.9: Band gap map for a hexagonal lattice of circular silicon ($\epsilon_r = 13$) rods in air ($\epsilon_r = 1$). Band gaps exist for TE (14.39%, $r/a = 0.35$) and TM (50.38%, $r/a = 0.17$) where vertical dashed lines indicate the corresponding normalized radii. Horizontal lines indicate the extent of the maximum band gap. Note that there is no complete band gap. The vertical dotted line indicates the normalized radius for the touching case.

TM band gap for the square lattices of circular rods and holes in Figs. 4.5 and 4.7 respectively. Not only are the area fill factors relatively small and nearly identical, but the band gap sizes differ by less than 1.5%. In fact, both of the resulting structures are comprised of little high dielectric material and could be described as being comprised of a lattice of rods (circular in Fig. 4.5 and rhombic-like in Fig. 4.7). What results are two very similar band diagrams, even though one is described as being a square lattice of circular rods and the other a square lattice of circular (yet overlapping) holes.

Similar calculations are performed for hexagonal lattices of circular rods or holes. These are shown in Figs. 4.9 and 4.10 respectively. In these cases, a hexagonal lattice of silicon rods in air possesses larger areas of TM band gap than TE. However, the hexagonal lattice of air holes in silicon is just the opposite and has the only significant complete band gap within the lattices of circular holes or rods. As in the square lattice case, these band gap maps contain particular structures of interest, more specifically those that exhibit

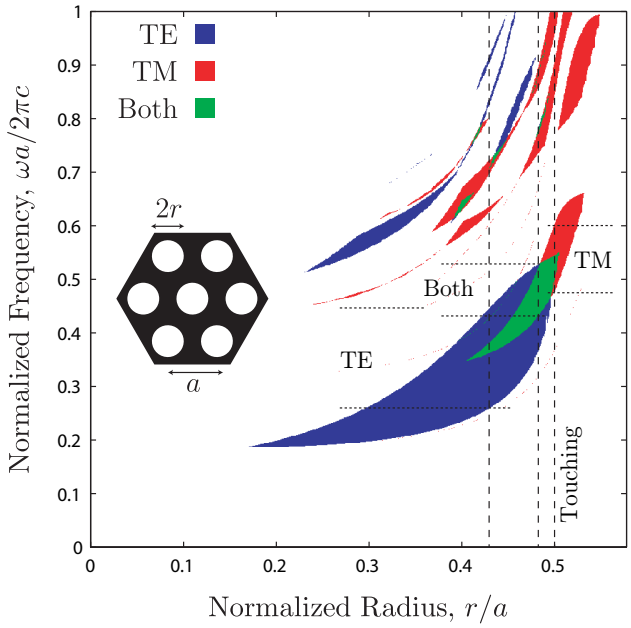

Figure 4.10: Band gap map for a hexagonal lattice of circular air ($\epsilon_r = 1$) holes in silicon ($\epsilon_r = 13$). Band gaps exist for TE (52.93%, $r/a = 0.43$), TM (23.37%, $r/a = 0.5$) and complete (19.55%, $r/a = 0.48$) where vertical dashed lines indicate the corresponding normalized radii. Horizontal lines indicate the extent of the maximum band gap. Note that the touching case occurs at the same radius as the case for the maximum TM band gap at $r/a = 0.5$.

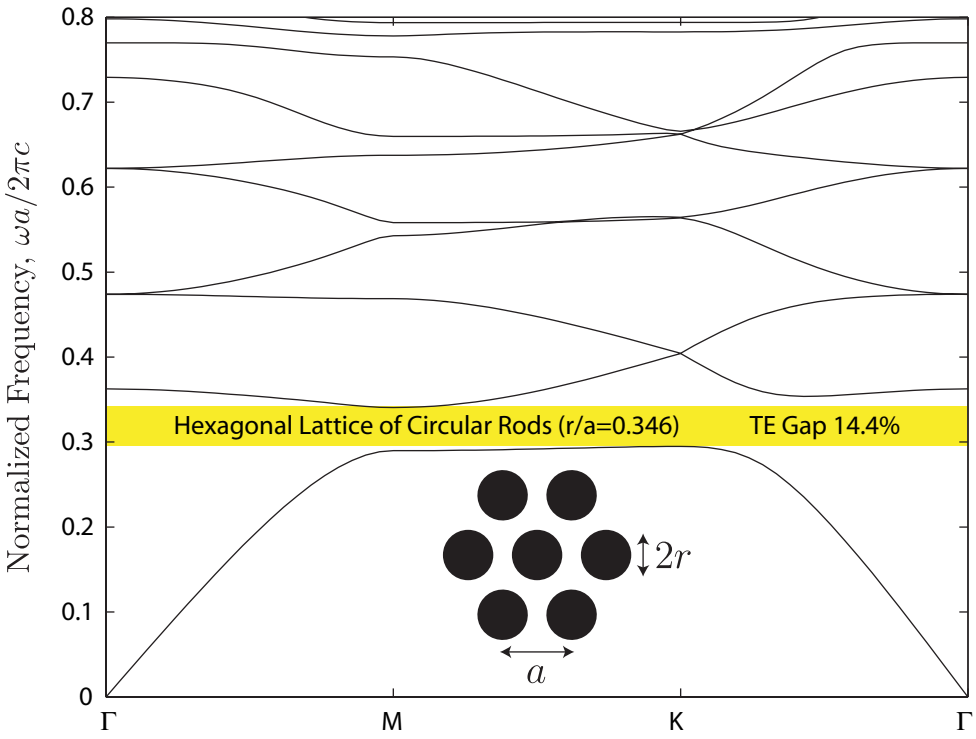

Figure 4.11: Band structure of a hexagonal lattice of circular rods corresponding to the largest TE band gap in Fig. 4.9.

the largest TE, TM and complete band gaps. The resulting structures and band structures for these lattices of interest are illustrated in Figs. 4.11 to 4.15.

The following lists the maximum band gap sizes, the corresponding normalized radii, r/a, and area fill factors, F, (percentage of silicon per unit cell) for the specific structures of interest. From the previously mentioned band gap maps, a hexagonal lattice of circular rods and holes has a maximum TE band gap size of 14.39% (r/a = 0.346, F = 43.4%) and 52.93% (r/a = 0.429, F = 33.1%) respectively. A hexagonal lattice of circular rods and holes has a maximum TM band gap size of 50.38% (r/a = 0.170, F = 10.5%) and 23.37% (r/a = 0.500, F = 9.1%) respectively. A hexagonal lattice of circular holes can exhibit a complete band gap with a maximum of 19.55% (r/a = 0.482, F = 15.6%).

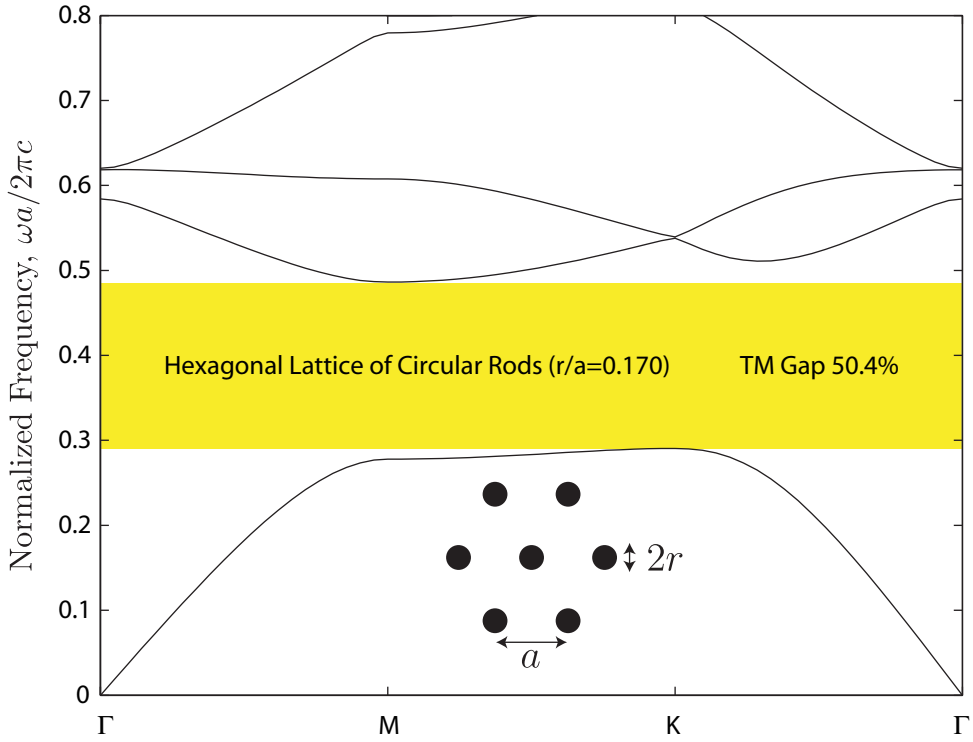

Figure 4.12: Band structure of a hexagonal lattice of circular rods corresponding to the largest TM band gap in Fig. 4.9.

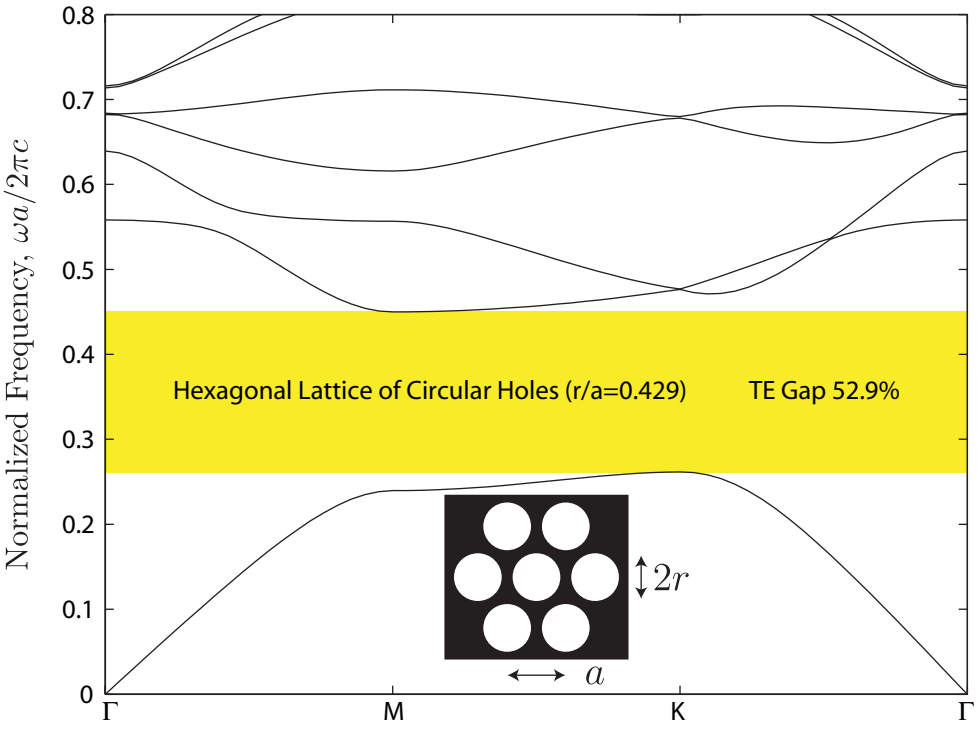

Figure 4.13: Band structure of a hexagonal lattice of circular holes corresponding to the largest TE band gap in Fig. 4.10.

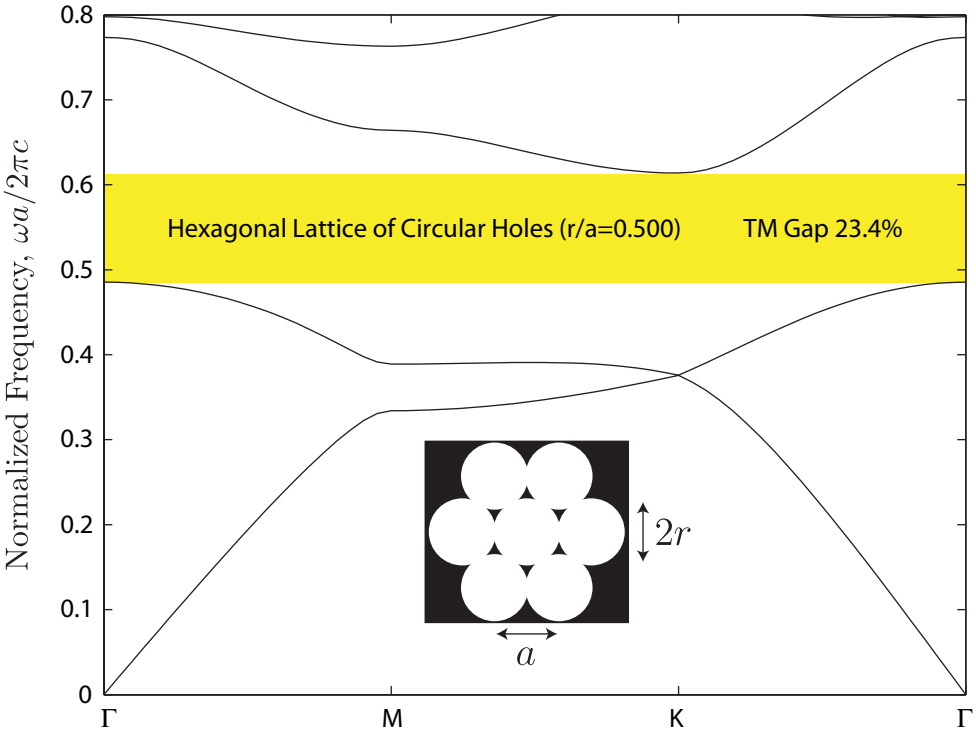

Figure 4.14: Band structure of a hexagonal lattice of circular holes corresponding to the largest TM band gap in Fig. 4.10.

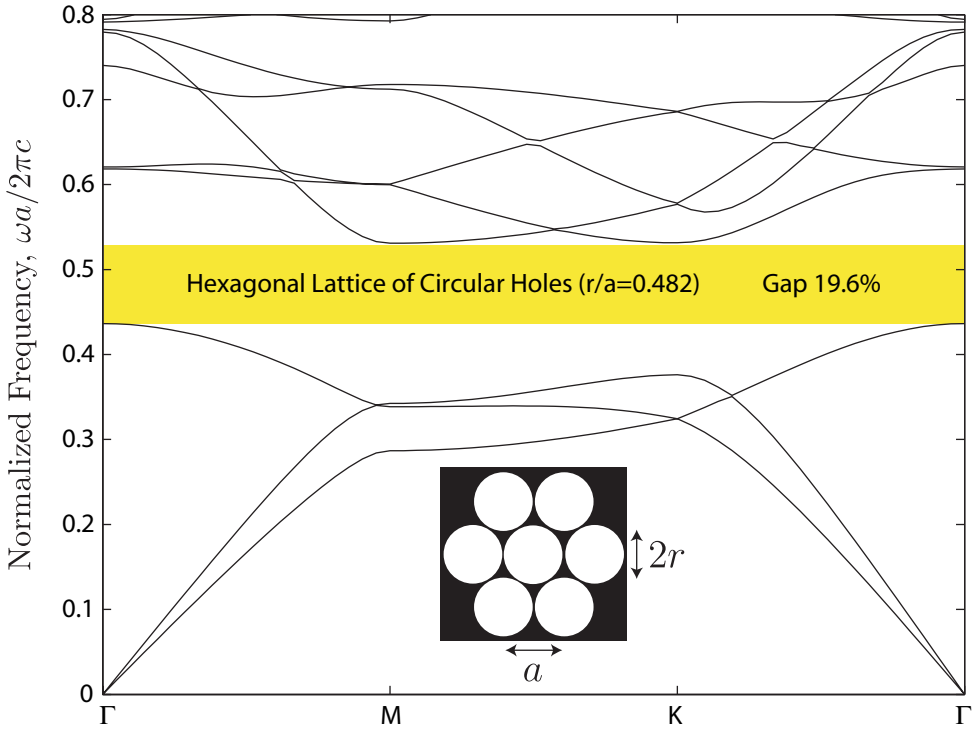

Figure 4.15: Band structure of a hexagonal lattice of circular holes corresponding to the largest complete band gap in Fig. 4.10.

4.4 Modeling Two-Dimensional Lattices Defined by Three-Beam-Interference Lithography

Given the performance of the lattices of circular rods or holes, it is necessary to compare and contrast the performance of similar structures defined by MBIL. To fabricate structures similar to a square lattice of circular rods or holes, a three-beam interference pattern defining a square lattice with *p4m* plane group symmetry is required (described in Chapter 2). The resulting structure will possess the same symmetry as the square lattice of circular rods or holes. Additionally, given the intensity contours of this type of interference pattern, both circular rod- and hole-type structures can be fabricated using the same interference pattern by adjusting the exposure dosage in the lithographic recipe. This is possible since the intensity contours around the peaks and nulls within the intensity distribution of this type of interference pattern ($C_3^{(2)}$) are identical (as described in Section 2.3.2.1).

Band gap maps, similar to those presented in the previous section, are calculated for lattices defined by MBIL as well. However, the design parameter for these structures is the normalized intensity value (I_{nrm}) of the interference pattern. Given a multi-beam-interference intensity distribution $I_T(\mathbf{r})$ from Eq. 2.10, I_{nrm} is related to an intensity value I by

$$I_{nrm} = \frac{I - Min[I_T(\mathbf{r})]}{Max[I_T(\mathbf{r})] - Min[I_T(\mathbf{r})]} \,. \tag{4.5}$$

I_{nrm}, ranging from 0 to 1, specifies an intensity contour that is identical given a specific type of interference pattern ($^{\pm}C_n^{(m)}$) regardless of the how the interference pattern was produced. The modeling of band structures of MBIL-defined photonic crystal structures are performed in terms of this normalized intensity value. In reality, the resulting structures depend upon the particular type of resist used and the method for transferring the photoresist mask into the substrate. However, for generality in subsequent plots, the normalized intensity value corresponds to a normalized intensity contour. The structure is defined as being bound by this contour encompassing larger normalized intensity values. For example, a

structure defined as being a rod, the contour encompassing larger normalized intensity values will define the high index dielectric while the smaller normalized intensity values will define the low index dielectric. For a structure defined as being a hole, the contour encompassing larger normalized intensity values will define the low index dielectric while the smaller normalized intensity values will define the high index dielectric. Figure 4.16(a) illustrates the band gap map for an MBIL-defined square lattice structure where the design parameter is the normalized intensity value. Values of normalized intensity greater than 0.5 most closely resemble circular rods while those less than 0.5 most closely resemble circular holes.

The portion of the band gap map for values of normalized intensity greater than 0.5 (left side of plot), behave similarly to that of Fig. 4.2 for a square lattice of circular rods. There are three large areas of TM band gap and no TE band gap. This result indicates that MBIL introduces little, if any, negative effects on the performance of a square lattice of rods. However, hole fabrication through MBIL is not promising even though the smaller area of TE band gap is present. In fact Fig. 4.2, the band gap map for a square lattice of circular rods, indicates that relatively small rod diameters ($r/a \approx 0.2$) are needed to maximize band gap size. Interference patterns exhibiting *p4m* plane group symmetry as seen in Fig. 4.16(b) contain contours that remain close to circular at these normalized radii. However, Fig. 4.3, the band gap map for a square lattice of circular holes, indicates that much larger radius holes ($r/a > 0.5$) are required to maximize bandgap. This is physically impossible given the contours of an interference pattern with *p4m* symmetry illustrated in Fig. 4.16(b).

These band gap maps contain particular structures of interest, more specifically those that exhibit the largest TE, TM and complete band gaps. The resulting structures and band structures for these lattices of interest are illustrated in Figs. 4.17 to 4.21.

The following lists the maximum band gap sizes, the corresponding normalized intensity values and area fill factors (percentage of silicon per unit cell) for the specific structures

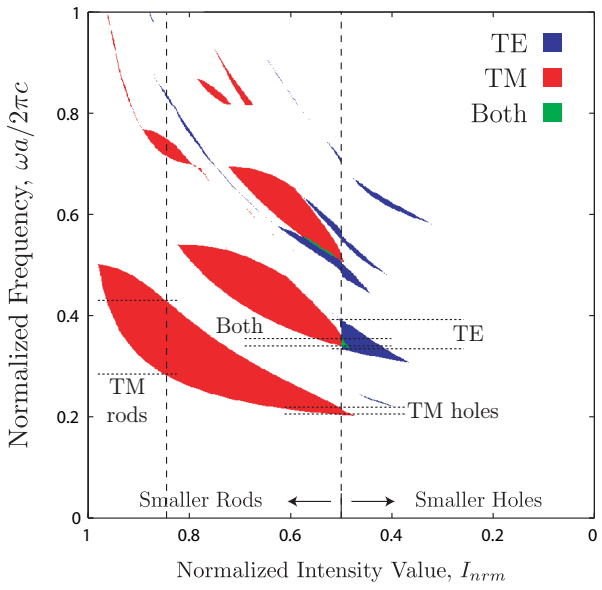

(a)

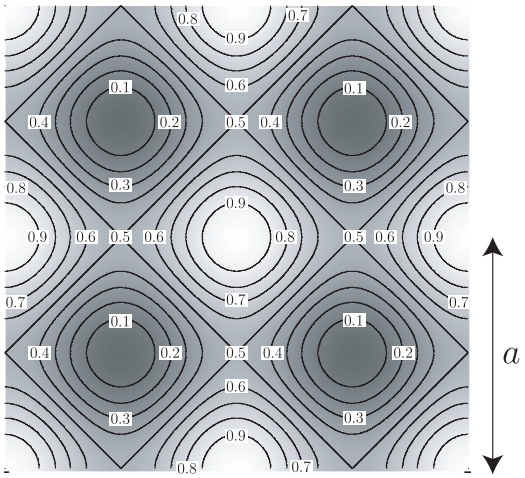

(b)

Figure 4.16: (a) Band gap map for MBIL-defined square lattice of rods where silicon ($\epsilon_r = 13$) structures defined by intensity contours of interference pattern in air ($\epsilon_r = 1$). For $I_{nrm} > 0.5$, a square lattice of rods exists and $I_{nrm} < 0.5$, a square lattice of holes exists. Band gaps exist for a square lattice of rods for TE (16.22%, $I_{nrm} = 0.5$), TM (41.06%, $I_{nrm} = 0.84$), and complete (5.66%, $I_{nrm} = 0.5$) and for a square lattice of holes for TE (16.22%, $I_{nrm} = 0.5$), TM (5.77%, $I_{nrm} = 0.5$), and complete (5.66%, $I_{nrm} = 0.5$) where vertical dashed lines indicate the corresponding normalized radii. Horizontal lines indicate the extent of the maximum band gap. Note that some of the radii for the maximum band gaps are identical. (b) Normalized intensity contour for an interference pattern for square lattice with $C_3^{(2)}$ satisfied and *p4m* plane group symmetry. Note that contours for normalized intensity values of I_{nrm} and $1 - I_{nrm}$ are identical.

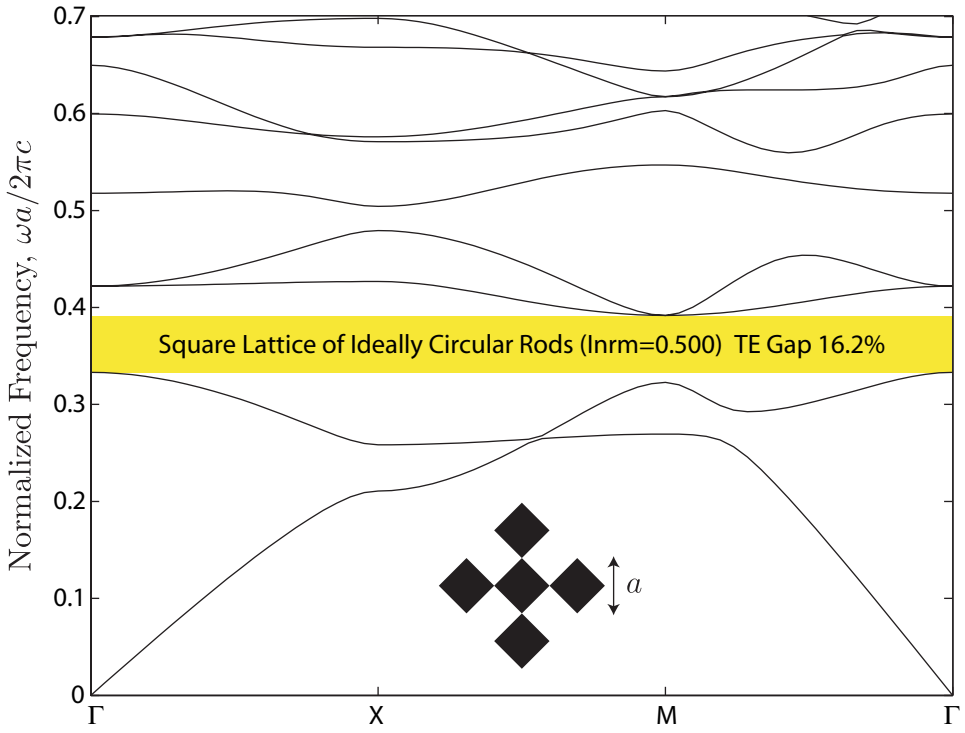

Figure 4.17: Band structure of a square lattice of MBIL-defined rods corresponding to the largest TE band gap in Fig. 4.16.

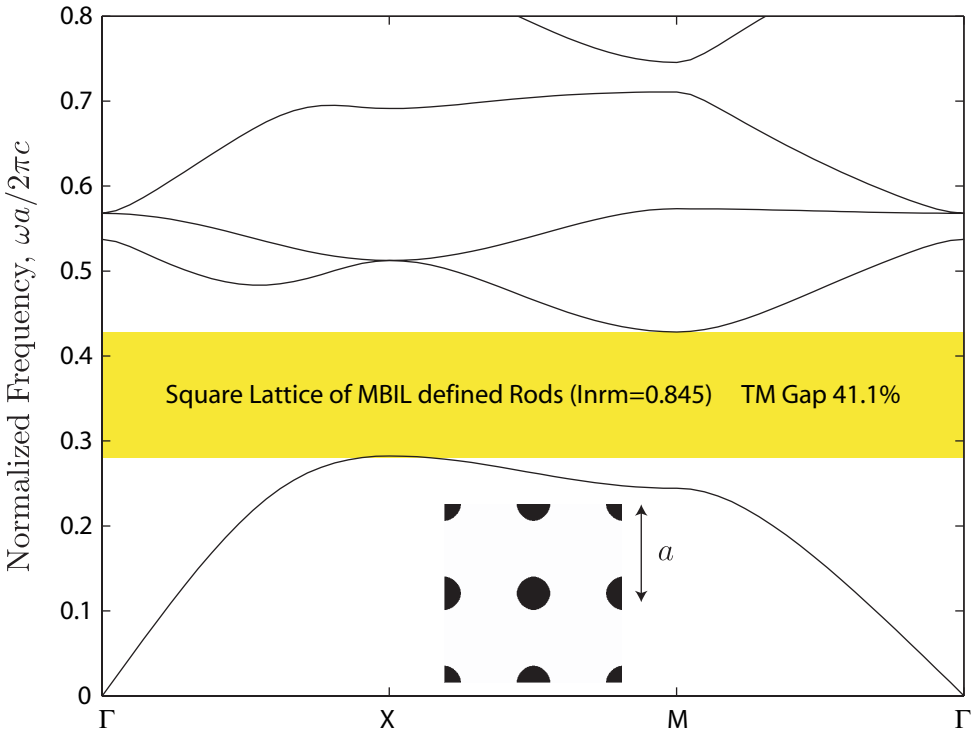

Figure 4.18: Band structure of a square lattice of MBIL-defined rods corresponding to the largest TM band gap in Fig. 4.16.

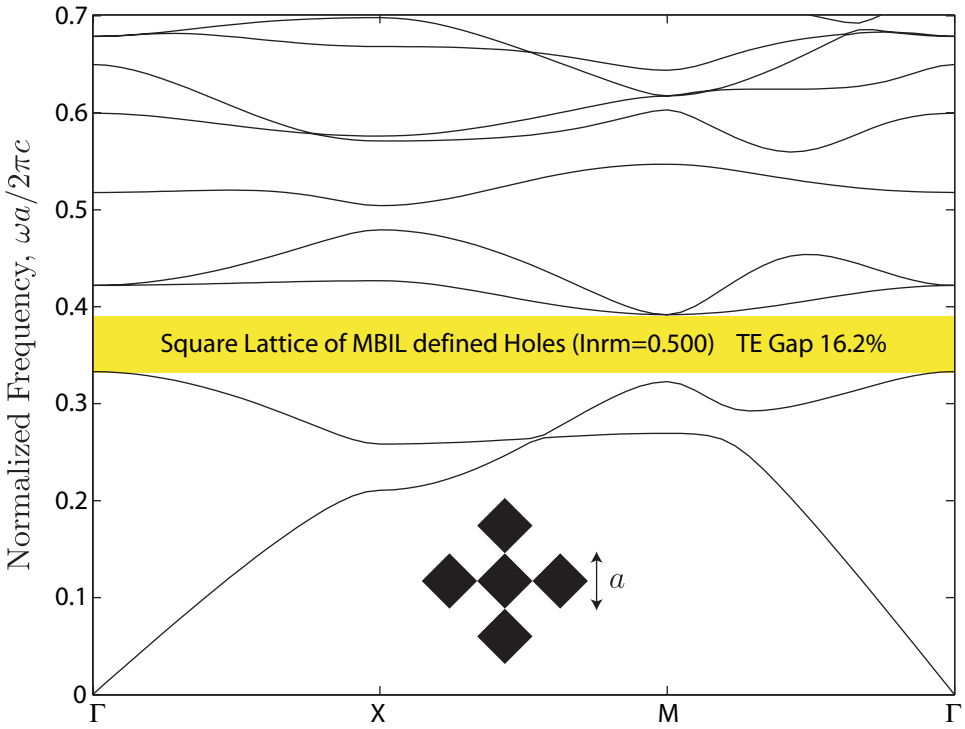

Figure 4.19: Band structure of a square lattice of MBIL-defined holes corresponding to the largest TE band gap in Fig. 4.16.

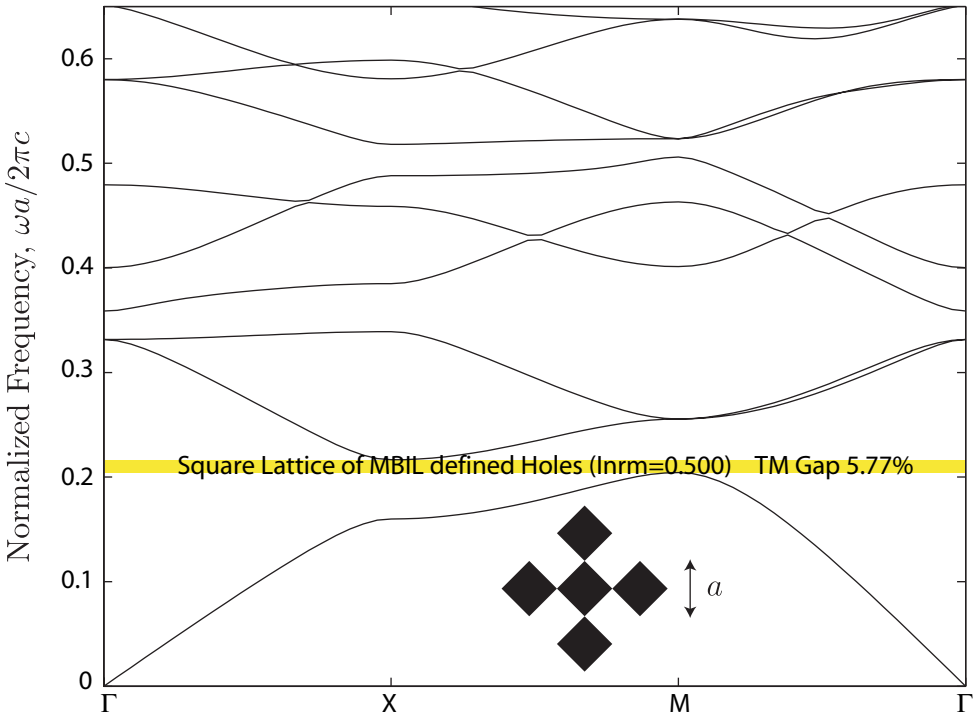

Figure 4.20: Band structure of a square lattice of MBIL-defined holes corresponding to the largest TM band gap in Fig. 4.16.

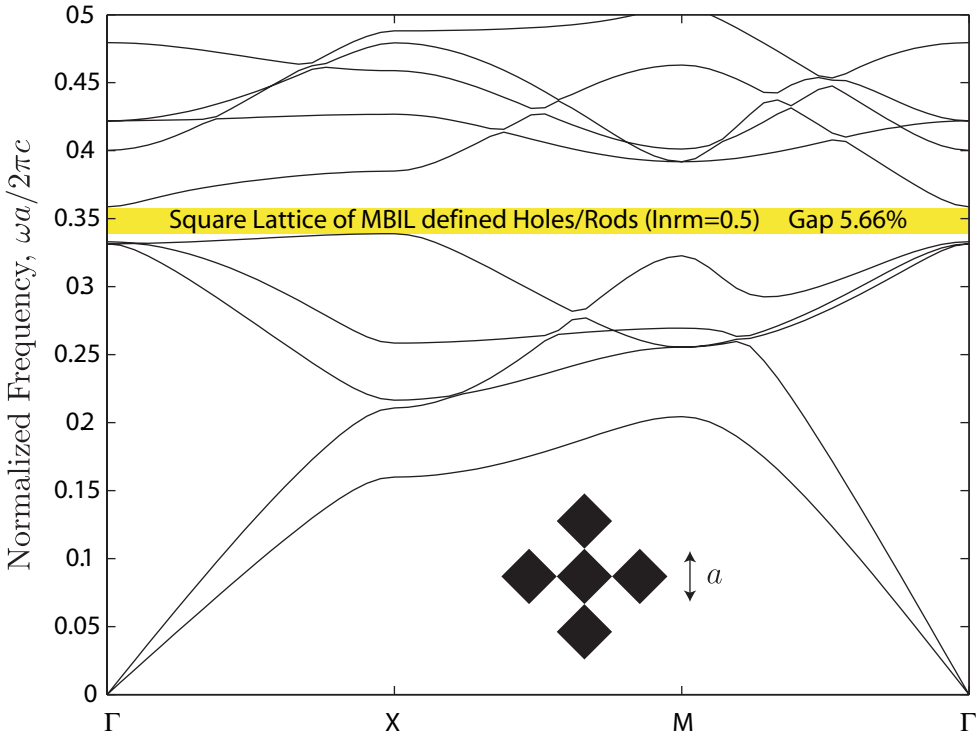

Figure 4.21: Band structure of a square lattice of MBIL-defined rods/holes corresponding to the largest complete band gap in Fig. 4.16.

of interest. From the previously mentioned band gap maps, a square lattice of rods and holes defined by multi-beam-interference lithography has a maximum TE band gap size of 16.22% (I_{nrm} = 0.500, F = 50.0%) and 16.22% (I_{nrm} = 0.500, F = 50.0%) respectively. A square lattice of rods and holes defined by multi-beam-interference lithography has a maximum TM band gap size of 41.06% (I_{nrm} = 0.845, F = 10.8%) and 5.77% (I_{nrm} = 0.500, F = 50.0%) respectively. A square lattice of circular holes or rods can exhibit a complete band gap with a maximum of 5.66% (I_{nrm} = 0.494, F = 50.0%).

To fabricate structures similar to a hexagonal lattice of circular rods or holes, a three-beam interference pattern possessing *p6m* plane group symmetry will be required. Unlike the interference patterns exhibiting *p4m* plane group symmetry, a single interference pattern cannot be used to fabricate both types of structures. Again, the design parameter when using MBIL to fabricate these structures is the normalized intensity value of the interference pattern. In reality, the resulting structures depend upon the particular type of resist

used and the method for transferring the photoresist mask into the substrate. In Fig. 4.22, the normalized intensity value corresponds to the intensity contours that bound higher normalized intensity values that will define the structure to be fabricated.

Figures 4.22(a) and 4.23(a) illustrate the band gap maps for the MBIL-defined hexagonal lattices of rods and holes respectively where the design parameter is the normalized intensity value. The band gap maps for MBIL-defined hexagonal lattices in Figs. 4.22 and 4.23 exhibit similar band gap maps when compared to the hexagonal lattices of circular rods and holes in Figs. 4.9 and 4.10. Figure 4.22 closely resembles Fig. 4.9 with three large areas of TM band gap and two smaller ares of TE band gap. This is not a surprise given that Fig. 4.9 indicates that optimized areas of band gap require relatively small normalized radii. Similarly, Fig. 4.23 closely resembles Fig. 4.10 with a large area of TM band gap, a smaller area of TE band gap, and an area of complete band gap.

These band gap maps contain particular structures of interest, more specifically those that exhibit the largest TE, TM and complete band gaps. The resulting structures and band structures for these lattices of interest are illustrated in Figs. 4.24 to 4.28.

The following lists the maximum band gap sizes, the corresponding normalized intensity values and area fill factors (percentage of silicon per unit cell) for the specific structures of interest. From the previously mentioned band gap maps, a hexagonal lattice of rods and holes defined by multi-beam-interference lithography has a maximum TE band gap size of 14.37% (I_{nrm} = 0.282, F = 45.2%) and 50.60% (I_{nrm} = 0.156, F = 36.8%) respectively. A hexagonal lattice of rods and holes defined by multi-beam-interference lithography has a maximum TM band gap size of 50.38% (I_{nrm} = 0.768, F = 12.7%) and 30.62% (I_{nrm} = 0.067, F = 12.7%) respectively. A hexagonal lattice of circular holes can exhibit a complete band gap with a maximum of 19.31% (I_{nrm} = 0.111, F = 24.3%).

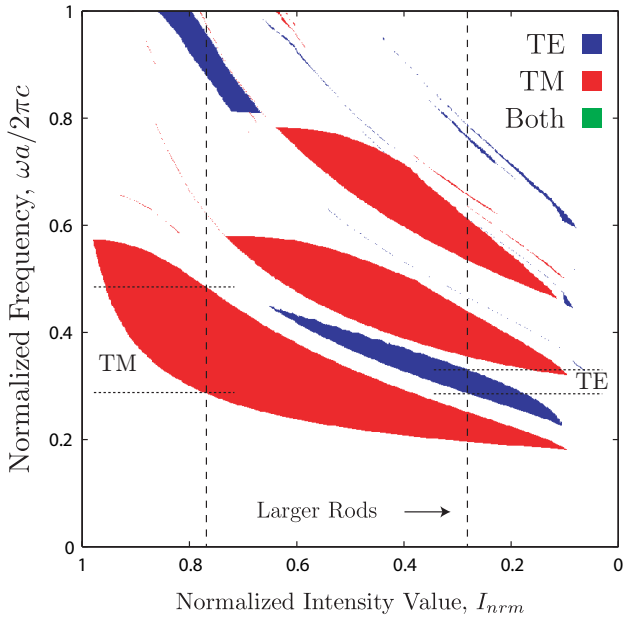

(a)

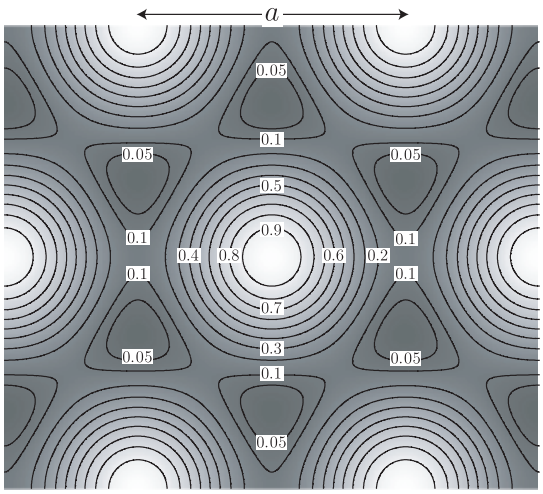

(b)

Figure 4.22: (a) Band gap map for MBIL-defined hexagonal lattice of rods where silicon ($\epsilon_r = 13$) structures defined by intensity contours of interference pattern in air ($\epsilon_r = 1$). Band gaps exist for TE (14.37%, $I_{nrm} = 0.28$) and TM (50.38%, $I_{nrm} = 0.77$) where vertical dashed lines indicate the corresponding normalized radii. Horizontal lines indicate the extent of the maximum band gap. Note that a complete band gap does not exist. (b) Normalized intensity contour for interference pattern for hexagonal lattice with ${}^{+}C_3^{(3)}$ satisfied and *p6m* plane group symmetry.

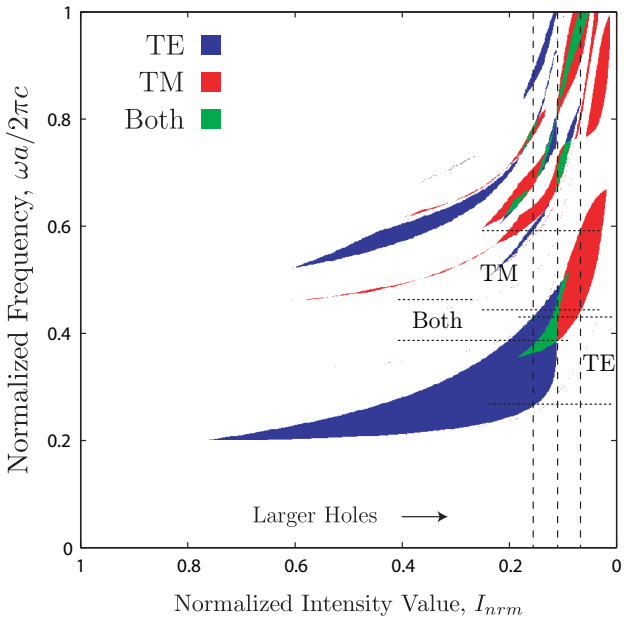

(a)

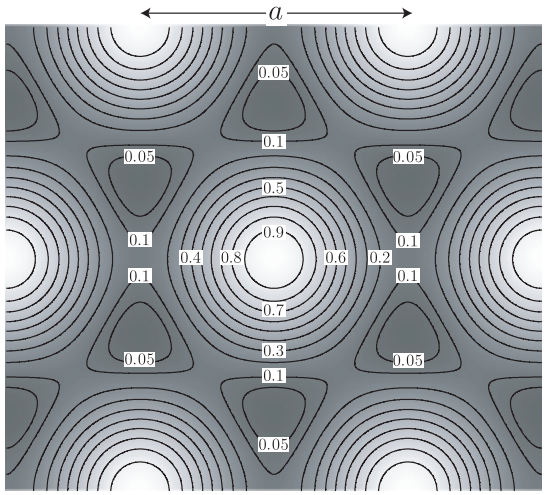

(b)

Figure 4.23: (a) Band gap map for MBIL-defined hexagonal lattice of holes where air ($\epsilon_r = 1$) structures defined by intensity contours of interference pattern in silicon ($\epsilon_r = 13$). Band gaps exist for TE (50.60%, $I_{nrm} = 0.16$), TM (30.62%, $I_{nrm} = 0.07$), and complete (19.31%, $I_{nrm} = 0.11$) where vertical dashed lines indicate the corresponding normalized radii. Horizontal lines indicate the extent of the maximum band gap. (b) Normalized intensity contour for interference pattern for hexagonal lattice with ${}^{+}C_3^{(3)}$ satisfied and *p6m* plane group symmetry.

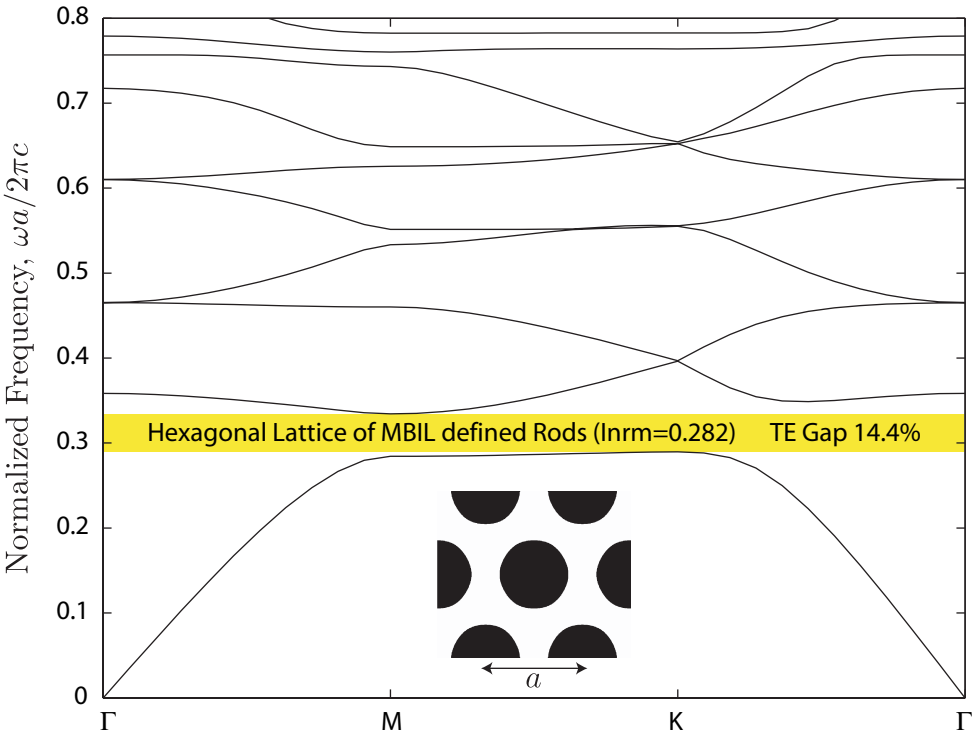

Figure 4.24: Band structure of a hexagonal lattice of MBIL-defined rods corresponding to the largest TE band gap in Fig. 4.22.

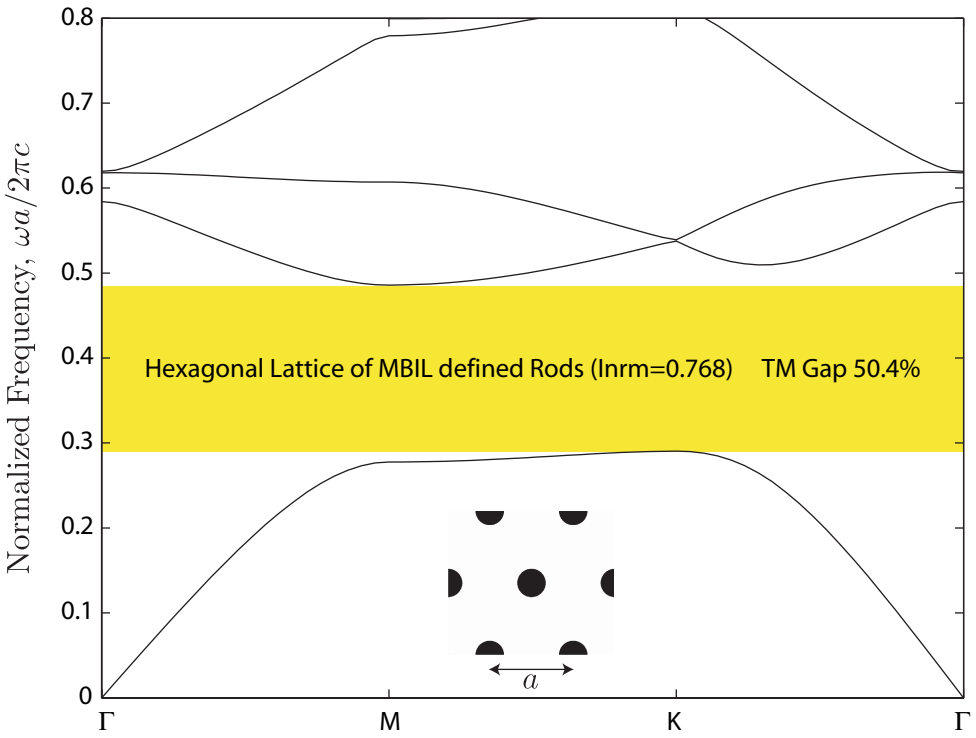

Figure 4.25: Band structure of a hexagonal lattice of MBIL-defined rods corresponding to the largest TM band gap in Fig. 4.22.

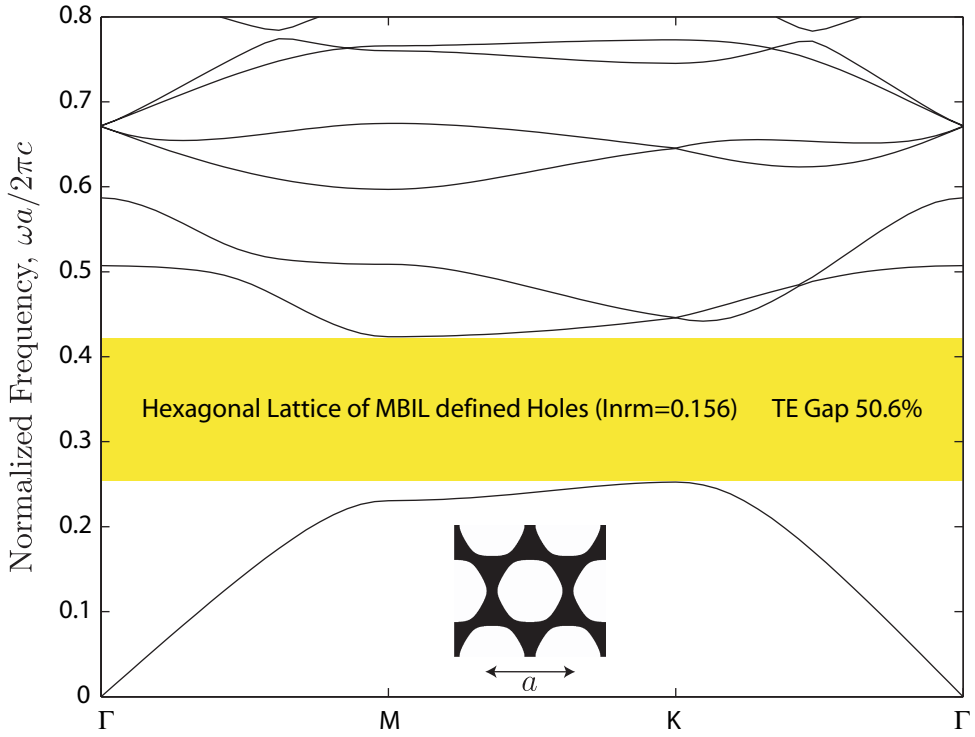

Figure 4.26: Band structure of a hexagonal lattice of MBIL-defined holes corresponding to the largest TE band gap in Fig. 4.23.

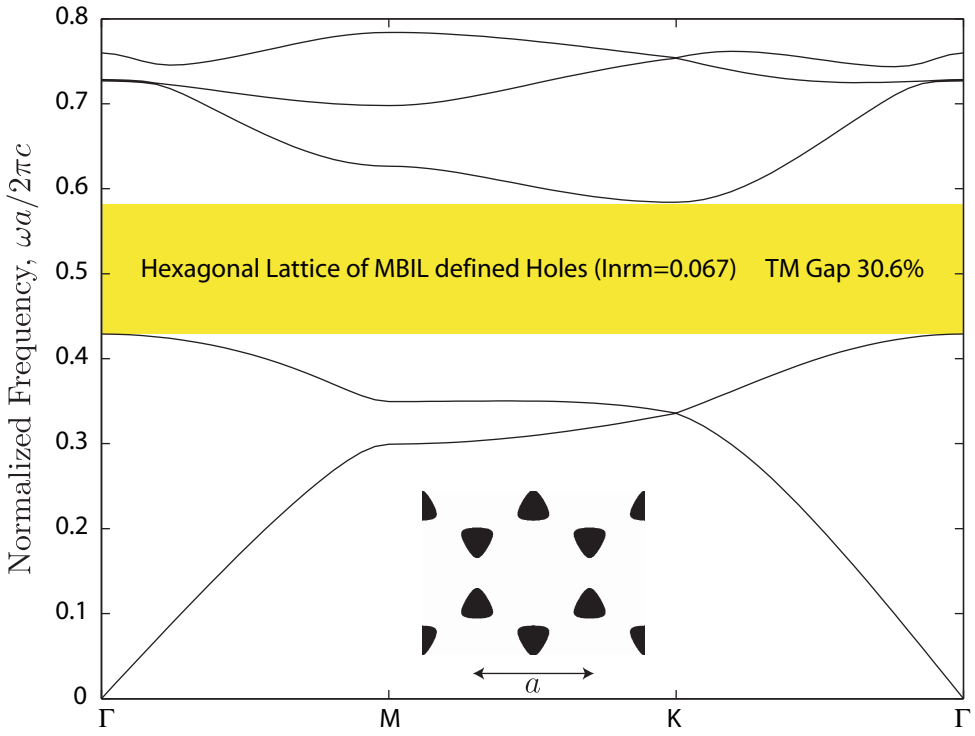

Figure 4.27: Band structure of a hexagonal lattice of MBIL-defined holes corresponding to the largest TM band gap in Fig. 4.23.

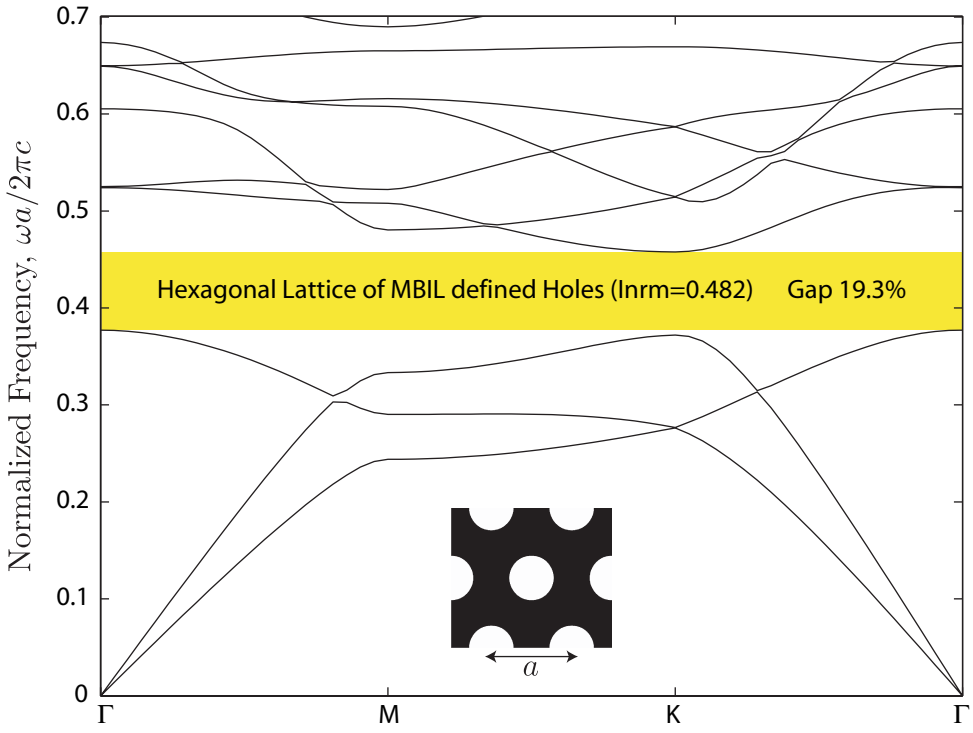

Figure 4.28: Band structure of a hexagonal lattice of MBIL-defined holes corresponding to the largest complete band gap in Fig. 4.23.

4.5 Summary

The maximum possible TE, TM and complete band gaps of the structures analyzed in this chapter are summarized in Tables 4.1 and 4.2. Additionally the corresponding area fill factors, normalized radii or normalized intensity value, and mid-gap frequency are given in Tables 4.3-4.8.

There is no significant reduction in the size of the TE band gaps of lattices of circular holes or rods when compared to similar structures fabricated via multi-beam-interference

Table 4.1: Maximum Band Gap Sizes for the Square Lattice Photonic Crystal

	Maximum Band Gap Size			
	Circular Holes	Circular Rods	MBIL Holes	MBIL Rods
TE	17.08%	3.86%	16.22%	16.22%
TM	39.61%	41.08%	5.77%	41.06%
Complete	4.80%	-	5.66%	5.66%

Table 4.2: Maximum Band Gap Sizes for the Hexagonal Lattice Photonic Crystal

	Maximum Band Gap Size			
	Circular Holes	Circular Rods	MBIL Holes	MBIL Rods
TE	52.93%	14.39%	50.60%	14.37%
TM	23.37%	50.38%	30.62%	50.38%
Complete	19.55%	-	19.31%	-

Table 4.3: Corresponding Fill Factors for the Square Lattice Photonic Crystal Structures with the Largest Band Gaps

	Area Fill Factors			
	Circular Holes	Circular Rods	MBIL Holes	MBIL Rods
TE	38.1%	42.6%	50%	50%
TM	10.7%	10.7%	50%	10.8%
Complete	23.2%	-	50%	50%

Table 4.4: Corresponding Fill Factors for the Hexagonal Lattice Photonic Crystal Structures with the Largest Band Gaps

	Area Fill Factors			
	Circular Holes	Circular Rods	MBIL Holes	MBIL Rods
TE	33.1%	43.4%	36.8%	45.2%
TM	9.1%	10.5%	12.7%	12.7%
Complete	15.6%	-	24.3%	-

Table 4.5: Corresponding Normalized Radii/Intensity Values for the Square Lattice Photonic Crystal Structures with the Largest Band Gaps

	Normalized Radius		Normalized Intensity Value	
	Circular Holes	Circular Rods	MBIL Holes	MBIL Rods
TE	0.444	0.368	0.5	0.5
TM	0.553	0.184	0.5	0.845
Complete	0.494	-	0.5	0.5

Table 4.6: Corresponding Normalized Radii/Intensity Values for the Hexagonal Lattice Photonic Crystal Structures with the Largest Band Gaps

	Normalized Radius		Normalized Intensity Value	
	Circular Holes	Circular Rods	MBIL Holes	MBIL Rods
TE	0.429	0.346	0.156	0.282
TM	0.500	0.170	0.067	0.768
Complete	0.482	-	0.111	-

Table 4.7: Corresponding Normalized Mid Gap Frequencies for the Square Lattice Photonic Crystal Structures with the Largest Band Gaps

	Normalized Mid Gap Frequency			
	Circular Holes	Circular Rods	MBIL Holes	MBIL Rods
TE	0.429	0.519	0.362	0.362
TM	0.357	0.356	0.210	0.355
Complete	0.474	-	0.349	0.349

Table 4.8: Corresponding Normalized Mid Gap Frequencies for the Hexagonal Lattice Photonic Crystal Structures with the Largest Band Gaps

	Normalized Mid Gap Frequency			
	Circular Holes	Circular Rods	MBIL Holes	MBIL Rods
TE	0.356	0.318	0.338	0.312
TM	0.550	0.388	0.506	0.388
Complete	0.484	-	0.417	-

lithography. Overall, this is no more than a 5% reduction in band gap size. In fact, the band gap of a square lattice of rods defined via multi-beam interference is 320% larger (from 3.86% to 16.22%) compared to the band gap of the square lattice of circular rods. There is, however, a significant reduction in the size of the TM band gap of a MBIL-defined square lattice of holes compared to the square lattice circular holes, 39.61% and 5.77% respectively. A square lattice interference pattern with *p4m* symmetry cannot replicate the larger radii that is required for the large band gaps. There is a significant improvement with an MBIL-defined hexagonal lattice of holes compared to the hexagonal lattice of circular holes, 30.62% to 23.37% respectively.

It has been noted that the MBIL-defined structures more closely resemble the circular structures when a relatively small normalized intensity value is used. This is because at these values, the intensity contours approach the circular case. There are four specific cases when the structures with the maximum band gap for the lattices with circular holes or rods have relatively small normalized radii. The corresponding MBIL-defined lattices exhibit nearly identical band gap sizes, area fill factors, and normalized mid gap frequencies. This occurs for the square lattice of rods (TM), hexagonal lattice of rods (TE and TM), and the hexagonal lattice of holes (TE).

CHAPTER 5

THEORETICAL PERFORMANCE OF THREE-DIMENSIONAL PHOTONIC CRYSTAL STRUCTURES

5.1 Structure Modeling and Simulation

The calculation of band structures of three-dimensional photonic crystals is performed similarly to those in two-dimensions. This is again accomplished by solving the vector equation derived from Maxwell's equations given by [1]

$$\nabla \times \left(\frac{1}{\epsilon_r(\mathbf{r})} \nabla \times \mathbf{H}(\mathbf{r}) \right) = \left(\frac{\omega}{c} \right)^2 \mathbf{H}(\mathbf{r}) \, . \tag{5.1}$$

There exists both commercial and open-source software available for computational photonics. A free software package has been developed and maintained by Steven G. Johnson at the Massachusetts Institute of Technology along with the Joannopoulos Ab Initio Physics group. This software is called MIT Photonic-Bands. It computes fully-vectorial eigenmodes of Maxwell's equations with periodic boundary conditions by preconditioned conjugate-gradient minimization of the block Rayleigh quotient in a plane wave basis [89]. Included in the software package are utilities for extracting band structures and mode fields including a Scheme-based scriptable interface (Guile). All of the band structures and band structure related calculations in this thesis were performed using this software package. More information on the algorithms used to calculate the eigenmodes of periodic structures is available in the literature and will not be a focus in this thesis. However, proper attention must be paid to how these problems are configured within the software. Included in Appendix B are the Guile scripts that were used with the MIT Photonic-Bands software to calculate the band structures of all the structures in this thesis. The included scripts are given as a guide to set up correctly the software and not intended to recreate all of the

illustrations within this thesis. Some of the plots here are the culmination of modeling hundreds of different structures, while the included scripts are intended to model just a single structure. Appropriately written Bash scripts are used to loop through variables of interest and parse the resulting output files to produce the illustrations presented here.

5.2 Conventions

Band gap maps, similar to those presented in Chapter 4, are presented for three-dimensional structures here. However, due to the limited number of structures that exhibit a complete gap, the band gap maps presented in this chapter are constructed differently. The band difference ratio, Ω_i for the *i*th band is plotted against the independent variable (normalized radius or normalized intensity value). The band difference ratio is defined as

$$\Omega_i = \frac{Min[\omega_{i+1}(k)] - Max[\omega_i(k)]}{(Min[\omega_{i+1}(k)] + Max[\omega_i(k)])/2} \ (\%) \ . \tag{5.2}$$

Thus, a band gap map is composed of a maximum of $N-1$ plots where N is the maximum number of bands calculated for each k-point. The band difference ratio equals the band gap size when $\Omega_i > 0$. Thus, given a band gap map for these three-dimensional structures, particular cases of interest are those that exhibit $\Omega_i > 0$.

Band gap maps for the face-centered cubic, body-centered cubic, and simple cubic lattices of spherical masses or vacancies are presented here. For these cases, the design parameter is the normalized radius (r/a) where a is the length of the cubic supercell edge and not the primitive unit cell. If a is the length of the cubic supercell edge and a_p is the length of the conventional primitive unit cell edge, then the ratio between the two for the three lattices are as follows:

$$\frac{a_p}{a} = 1 \qquad \text{Cubic} \tag{5.3}$$

$$\frac{a_p}{a} = \frac{\sqrt{2}}{2} \qquad \text{FCC} \tag{5.4}$$

$$\frac{a_p}{a} = \frac{\sqrt{3}}{2} \qquad \text{BCC} \ . \tag{5.5}$$

All normalized values used in the configuration files and the resulting calculations are written in terms of the cubic supercell edge length a. This means that the basis vectors that describe the translation symmetry of the lattices are in terms of a (not unity) and all k-points for which modes are calculated are in terms of $2\pi/a$. The configuration files included in Appendix B follow this convention.

5.3 Complete Band Gaps in Three Dimensions

In one- and two-dimensions, it is straightforward to design and fabricate structures with complete one- and two-dimensional photonic band gaps in the visible and infrared regimes. In one-dimension, semi-infinite multilayer films or Bragg mirrors are fabricated and commonly used in a number of devices. One of the most common structures that utilize Bragg mirrors is the VCSEL (vertical-cavity surface-emitting laser). In a VCSEL, a quantum well (or quantum wells) is grown between two parallel Bragg mirrors. The Bragg mirrors provide the feedback mechanism for the lasing action. VCSEL's, and subsequently the one-dimensional photonic crystal structure, can be fabricated for wavelengths in both the visible and infrared regimes depending on the composition of the active region and the structure of the Bragg mirrors.

As shown in Chapter 4, both square and hexagonal lattices of circular holes and rods can exhibit relatively large band gaps in silicon. These types of two-dimensional lattices can be fabricated using a number of commonly used techniques (see Chapter 1). However in three-dimensions, there are relatively few known structures that exhibit a complete bandgap and fewer that have been realized experimentally in the visible and/or infrared regimes. The first structure found to have a complete photonic band gap is the face-centered cubic (FCC) lattice of vacancies or masses [92]. Band gap maps for these two structures with a dielectric constants of $\epsilon_r = 13$ and $\epsilon_r = 1$ are illustrated in Figs. 5.1 and 5.2. The FCC lattice of dielectric masses in air exhibits a maximum band gap size of 13.9% while the FCC lattice of vacancies in a dielectric exhibits a maximum band gap size of 28.3%. Both

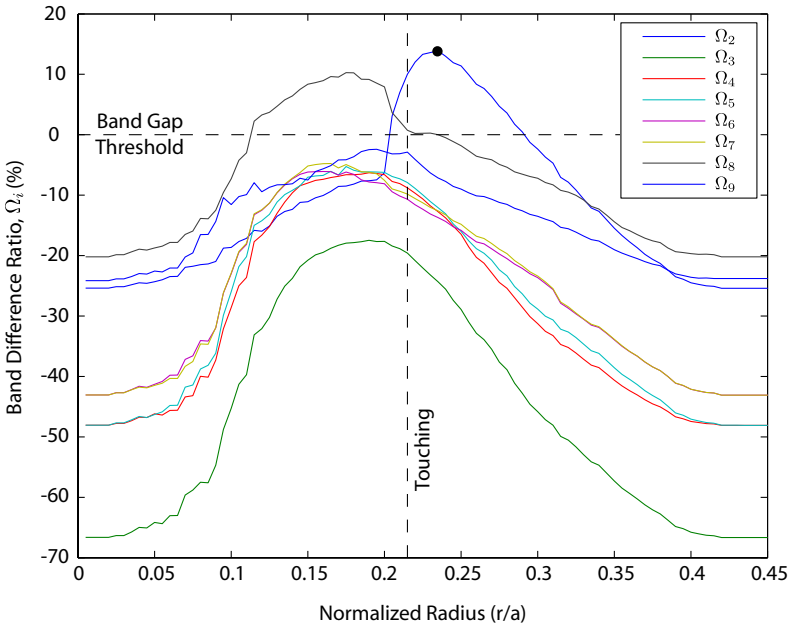

Figure 5.1: Band gap map for diamond cubic lattice of spherical masses. Indicated on the plot is the case with the maximum band gap (r/a = 0.235, Ω_2 = 13.9%). The horizontal dashed line indicates the band gap threshold where values of the band difference ratio above this line equate to the band gap size. The vertical dashed line indicates the close touching case.

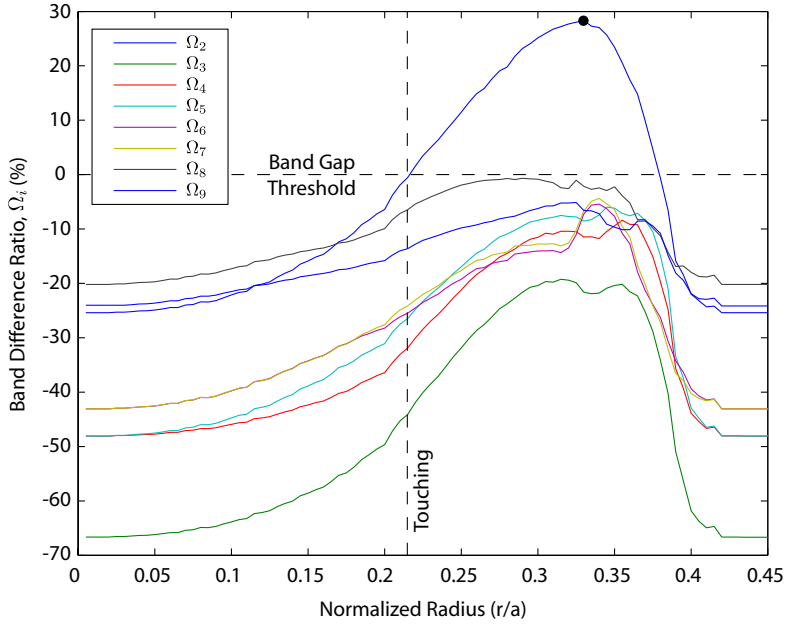

Figure 5.2: Band gap map for diamond cubic lattice of spherical vacancies. Indicated on the plot is the case with the maximum band gap (r/a = 0.330, Ω_2 = 28.3%). The horizontal dashed line indicates the band gap threshold where values of the band difference ratio above this line equate to the band gap size. The vertical dashed line indicates the close touching case.

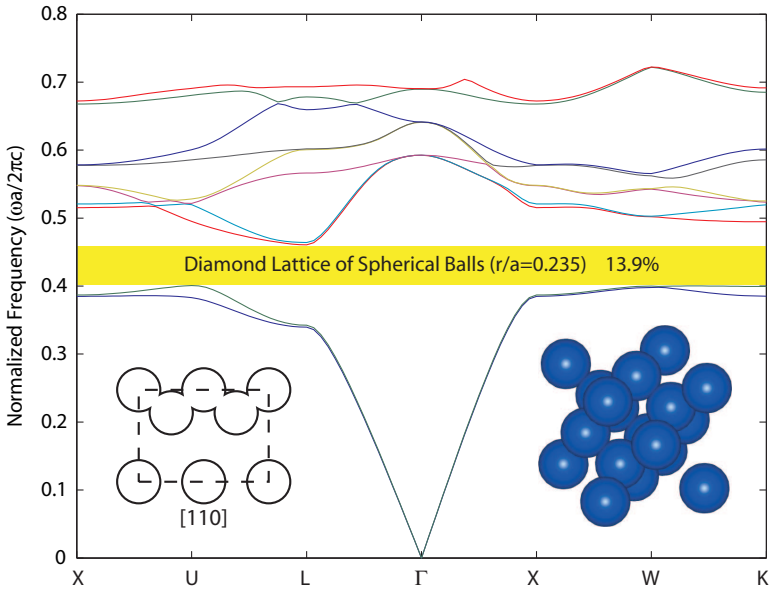

Figure 5.3: Band structure of a diamond cubic lattice of spherical masses corresponding to the largest band gap in Fig. 5.1 ($\Omega_2 = 13.9\%$, $r/a = 0.235$, $F = 42.3\%$). Included are a cubic supercell and a slice through the diagonal of the cubic supercell on a [110] plane. The irreducible Brillouin zone is illustrated in Appendix D.

of these cases occur for radii greater than the close-touching case, i.e. the spherical masses or vacancies overlap as seen in the slices through the cubic supercell within the figures. The band structures for these cases are illustrated in Figs. 5.3 and 5.4. Subset within each of these figures is a cubic supercell and a slice through the supercell on a [110] plane. These are included to aid in visualizing the modeled structure and emphasize the overlapping spherical masses and vacancies.

The first experimentally realized three-dimensional photonic crystal with a complete band gap was the Yablonovite structure [93] illustrated in Fig. 5.5(a). However, this structure was first fabricated on the centimeter scale before the micron scale required for operation in the infrared regime. The first photonic crystal to be fabricated on the micron scale was the woodpile structure proposed in 1994 [94, 95] and first fabricated in 1998 [96]. The structure, illustrated in Fig. 5.5(b), possesses a stop band between 10-14.5 μm of $\sim$ 12dB per unit cell. Although there exists a number of structures that both theoretically and experimentally exhibit complete band gaps, the challenge lies in fabricating these

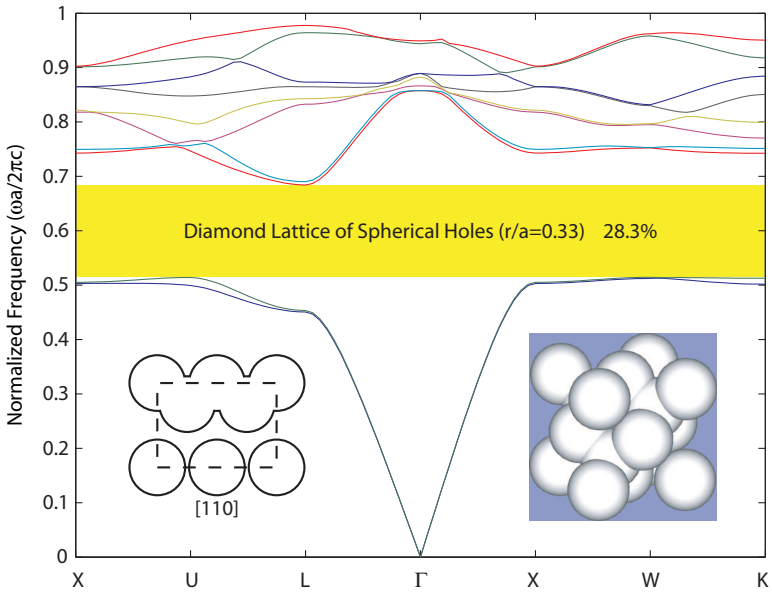

Figure 5.4: Band structure of a diamond cubic lattice of spherical vacancies corresponding to the largest band gap in Fig. 5.2 ($\Omega_2 = 28.3\%$, $r/a = 0.330$, $F = 17.2\%$). Included are a cubic supercell and a slice through the diagonal of the cubic supercell on a [110] plane. The irreducible Brillouin zone is illustrated in Appendix D.

structures in a straightforward manner. The following sections investigate two types of three-dimensional lattices: lattices of spherical masses and vacancies and lattices of MBIL-defined symmetrically-deformed spheroidal mass and vacancies. The face-centered cubic, body-centered cubic, and simple cubic lattices are analyzed and structures that exhibit complete band gaps are investigated.

5.4 Modeling Three-Dimensional Lattices of Spherical Masses/Vacancies

The face-centered cubic, body-centered cubic, and simple cubic lattices of spherical masses or vacancies are modeled in this section. While not all of the structures discussed here are experimentally straightforward, these and the band gap maps for the diamond cubic lattice presented in the previous section will provide a point of comparison for the MBIL-defined structures [91]. Table 5.1 lists the six types of lattices that have been modeled and indicates if a complete band gap exists. Given the permittivity contrast with the high index dielectric

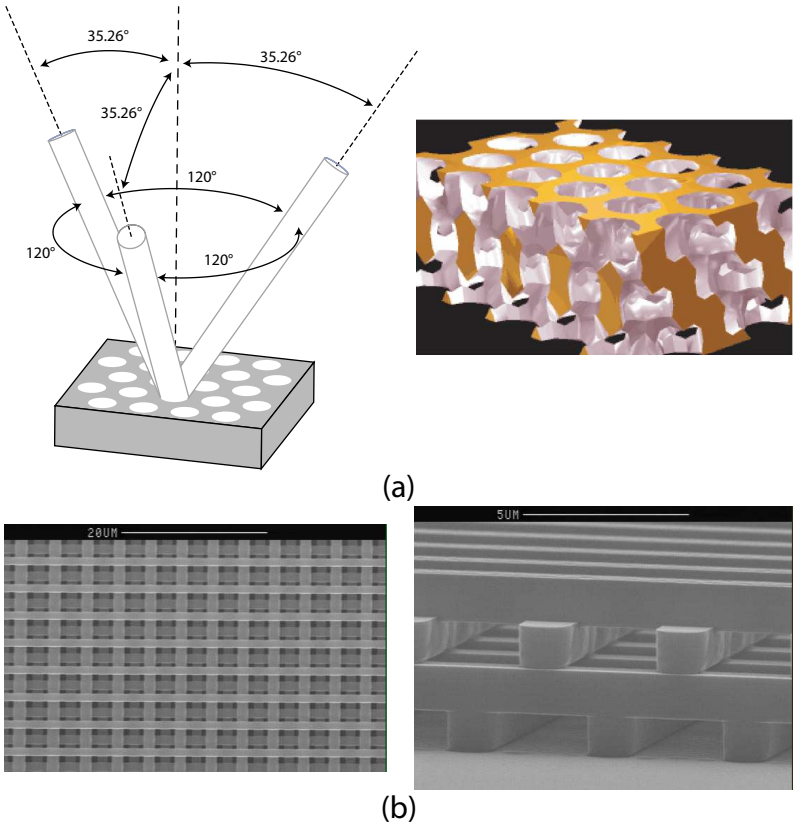

Figure 5.5: (a) The Yablonovite [93] (right) was the experimentally realized photonic crystal structure fabricated on the centimeter scale. (left) It is fabricated by systematically drilling three holes per lattice point in a hexagonal pattern and results in FCC periodicity. (b) The woodpile structure [94–96] was the first micron scale photonic crystal structure experimentally realized.

Table 5.1: Presence of a Complete Band Gap for FCC, BCC, and Cubic Lattices of Spherical Masses ($\epsilon_r = 13$) or Vacancies ($\epsilon_r = 1$)

	Spherical Masses	Spherical Vacancies
FCC	No	Yes
BCC	No	Yes
Simple Cubic	No	Yes

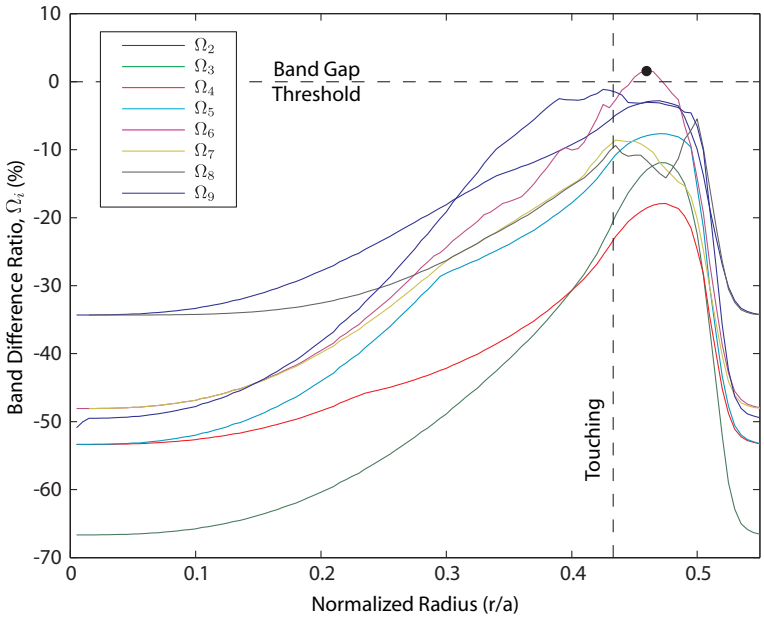

Figure 5.6: Band gap map for BCC lattice of spherical vacancies. Indicated on the plot is the case with the maximum band gap (r/a = 0.460, Ω_6 = 1.6%). The horizontal dashed line indicates the band gap threshold where values of the band difference ratio above this line equate to the band gap size. The vertical dashed line indicates the close touching case.

(ϵ_r = 13) and air (ϵ_r = 1), each exhibits a complete band gap with a lattice of spherical vacancies. The corresponding band gap maps for these lattices and the band structures for the cases with the maximum band gap size are illustrated in Figs. 5.6 to 5.11. The band gap maps for the remaining lattices of spherical masses still provide valuable information and are included in Appendix C.

The following lists the maximum band gap sizes and the corresponding normalized radii (r/a) and volume fill factors (F, percentage of silicon per unit cell) for the specific structures of interest. From the previously mentioned band gap maps, a body-centered cubic lattice of spherical vacancies has a complete band gap of 1.56% (r/a = 0.460, F = 20.1%), a face-centered cubic lattice of spherical vacancies has a complete band gap of 5.95% (r/a = 0.360, F = 22.2%), and a simple cubic lattice of spherical vacancies has a complete band gap of 7.29% (r/a = 0.605, F = 19.0%).

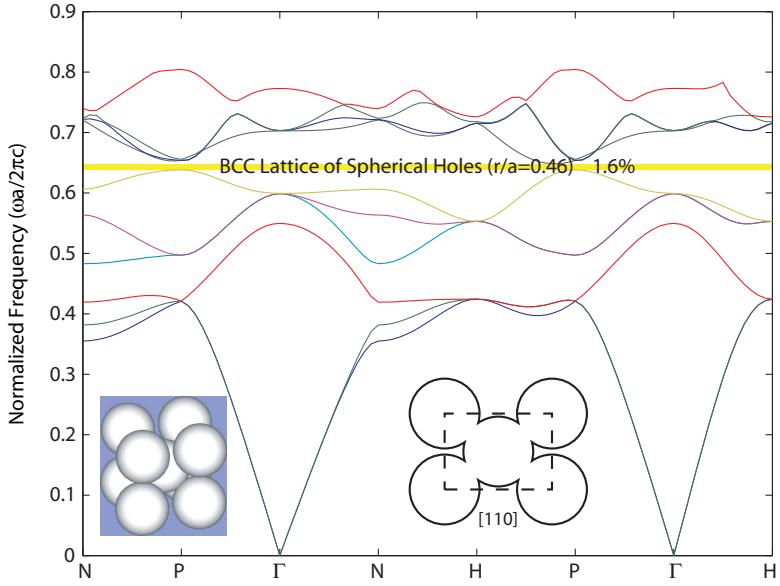

Figure 5.7: Band structure of a BCC lattice of spherical vacancies corresponding to the largest band gap in Fig. 5.6 ($\Omega_6 = 1.6\%$, $r/a = 0.460$, $F = 20.1\%$). Included are a cubic supercell and a slice through the diagonal of the cubic supercell on a [110] plane. The irreducible Brillouin zone is illustrated in Appendix D.

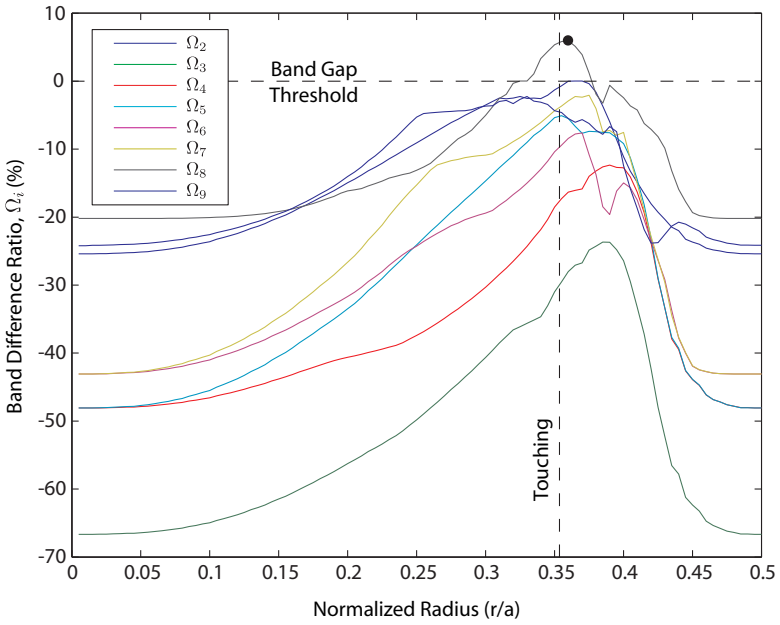

Figure 5.8: Band gap map for FCC lattice of spherical vacancies. Indicated on the plot is the case with the maximum band gap ($r/a = 0.360$, $\Omega_8 = 6.0\%$). The horizontal dashed line indicates the band gap threshold where values of the band difference ratio above this line equate to the band gap size. The vertical dashed line indicates the close touching case.

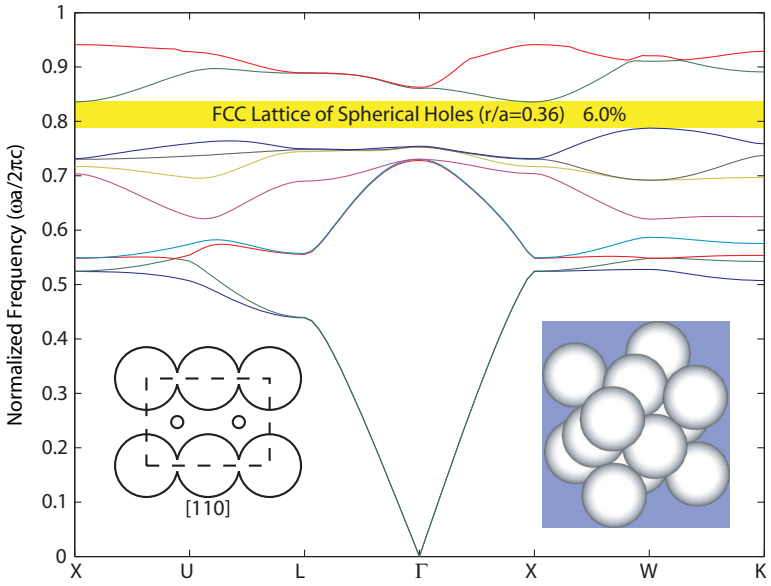

Figure 5.9: Band structure of a FCC lattice of spherical vacancies corresponding to the largest band gap in Fig. 5.8. ($\Omega_8 = 6.0\%$, $r/a = 0.360$, $F = 22.2\%$). Included are a cubic supercell and a slice through the diagonal of the cubic supercell on a [110] plane. The irreducible Brillouin zone is illustrated in Appendix D.

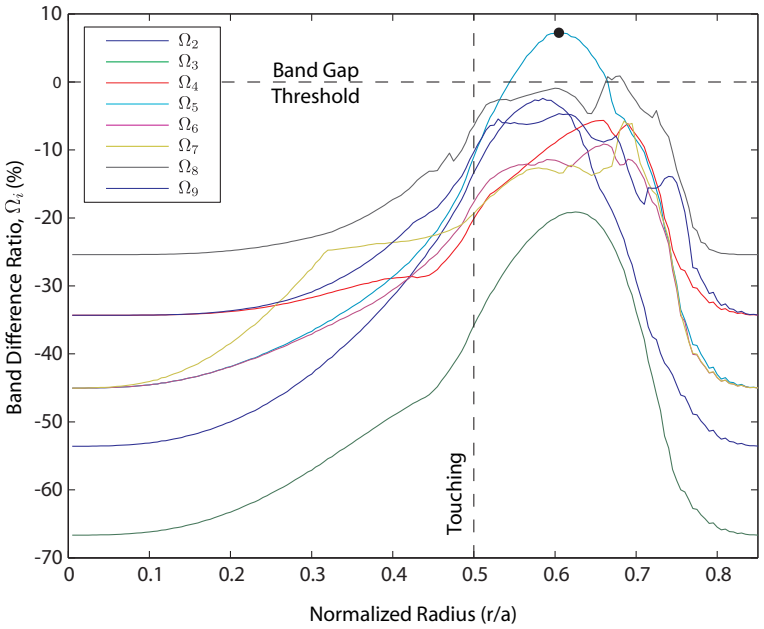

Figure 5.10: Band gap map for cubic lattice of spherical vacancies. Indicated on the plot is the case with the maximum band gap ($r/a = 0.605$, $\Omega_5 = 7.3\%$). The horizontal dashed line indicates the band gap threshold where values of the band difference ratio above this line equate to the band gap size. The vertical dashed line indicates the close touching case.

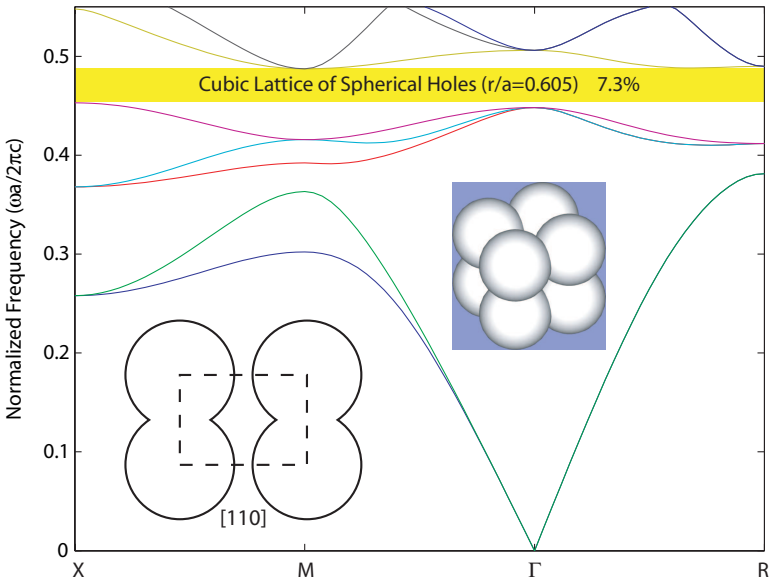

Figure 5.11: Band structure of a cubic lattice of spherical vacancies corresponding to the largest band gap in Fig. 5.10 ($\Omega_5 = 7.3\%$, $r/a = 0.605$, $F = 19.0\%$). Included are a cubic supercell and a slice through the diagonal of the cubic supercell on a [110] plane. The irreducible Brillouin zone is illustrated in Appendix D.

5.5 Modeling Three-Dimensional Lattices Defined by Four-Beam-Interference Lithography

In two dimensions, modeling was restricted to MBIL-defined structures that possessed the same plane group symmetry as the lattice of comparison. For instance, the hexagonal lattice of circular rods or holes has *p6m* plane group symmetry. A $C_3^{(3)}$ interference pattern with hexagonal translation symmetry has the same plane group symmetry, and thus was the best candidate for comparison. The square lattice of circular rods or holes had *p4m* plane group symmetry as does a $C_3^{(2)}$ interference pattern with square translation symmetry. Again, this was the best candidate for comparison. In three-dimensions, three lattices are analyzed. Of these, the MBIL-defined ($C_4^{(3)}$) simple cubic lattice has the same group symmetry as the simple cubic lattice of spherical masses or vacancies and the MBIL-defined ($C_4^{(6)}$) body-centered cubic lattice has the same group symmetry as the body-centered cubic lattice of spherical masses or vacancies. For this reason, each lattice (of masses or vacancies) is modeled with each type of *condition for primitive-lattice-vector-direction equal contrasts*

Table 5.2: Presence of a Complete Band Gap for MBIL-Defined Lattices of MBIL-Defined Symmetrically-Deformed Spheroidal Masses ($\epsilon_r = 13$) or Vacancies ($\epsilon_r = 1$)

		$C_4^{(6)}$	$C_4^{(5)}$	$C_4^{(4)}$	$C_4^{(3)}$
FCC	Masses	No	No	No	Yes
	Vacancies	No	No	No	
BCC	Masses	No	No	No	No
	Vacancies	No	No	No	
Simple Cubic	Masses	No	No	No	Yes
	Vacancies	No	No	No	

in order to develop a clear understanding of which MBIL-defined structures exhibit a complete band gap. These simulations result in 24 band gap maps. Each band gap map is plotted against the normalized intensity value for the given *condition for primitive-lattice-vector-direction equal contrasts*. For the band gap maps of both masses and vacancies, a ${}^{+}C_n^{(m)}$ interference pattern is used to defined the structures. A lattice of masses is defined such that the high index dielectric ($\epsilon_r = 13$) is encompassed by larger normalized intensity values with air ($\epsilon_r = 1$) everywhere else. A lattice of vacancies is defined such that air ($\epsilon_r = 1$) is encompassed by larger normalized intensity values with the high index dielectric ($\epsilon_r = 13$) everywhere else. Table 5.2 summarizes the presence of a complete band gap map for each case. Note that the column for the $C_4^{(3)}$ type interference patterns are not separated into masses and vacancies. From Chapter 3, it was shown that the contour lines for the normalized intensity values of I_{nrm} and $1 - I_{nrm}$ are identical. A single $C_4^{(3)}$ interference pattern can generate both spheroidal masses or vacancies depending on the process conditions. Thus band gap maps for both lattices of masses and vacancies based on $C_4^{(3)}$ interference patterns provide identical information (mirrored upon themselves).

Of the 24 cases, only two possess a complete band gap: the MBIL-defined simple cubic lattice of spheroidal masses defined by a $C_4^{(3)}$ interference pattern and the MBIL-defined face-centered cubic lattice of spheroidal masses defined by a $C_4^{(3)}$ interference pattern. Qualitatively, these structures are described as masses because the fill factors are

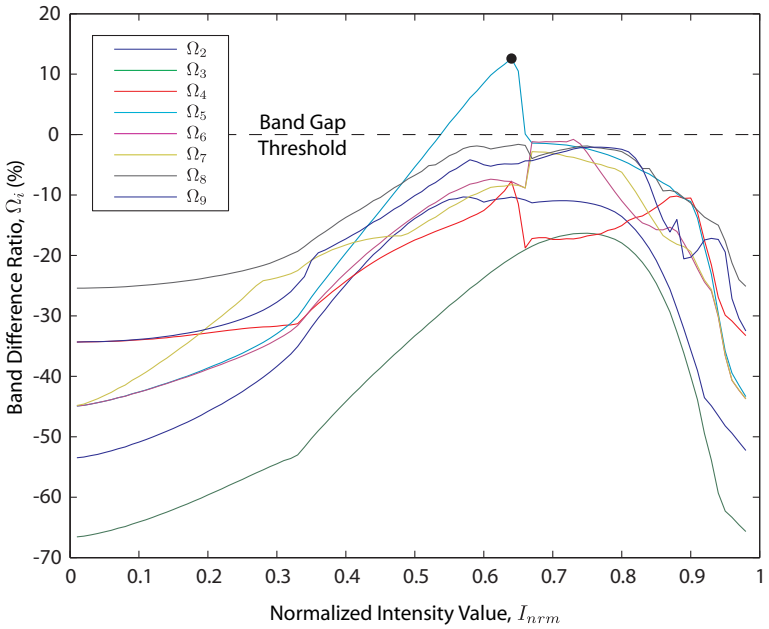

Figure 5.12: Band gap map for cubic lattice of masses defined via MBIL satisfying $C_4^{(3)}$ (I_{nrm} = 0.640, Ω_5 = 12.6%). The horizontal dashed line indicates the band gap threshold where values of the band difference ratio above this line equate to the band gap size.

less than 50%. The corresponding band gap maps and band diagrams are illustrated in Figs. 5.12 to 5.15.

Since a MBIL-defined FCC lattice does not have the same group symmetry as an FCC lattice of spherical masses or vacancies, special attention must be paid to the first irreducible Brillouin zone [97]. The first Brillouin zone must be reduced by the symmetries within the structure. Appendix D illustrates all of the Brillouin zones of the structures modeled in this thesis including the FCC lattice defined by a $C_4^{(3)}$ interference pattern.

5.6 Summary

The maximum possible complete band gaps of the structures analyzed in this chapter are summarized in Table 5.3. Additionally the corresponding fill factors, normalized radii or normalized intensity value, and mid-gap frequency are given in Tables 5.4-5.6.

Unlike the two-dimensional cases presented in this thesis, the MBIL-defined structures

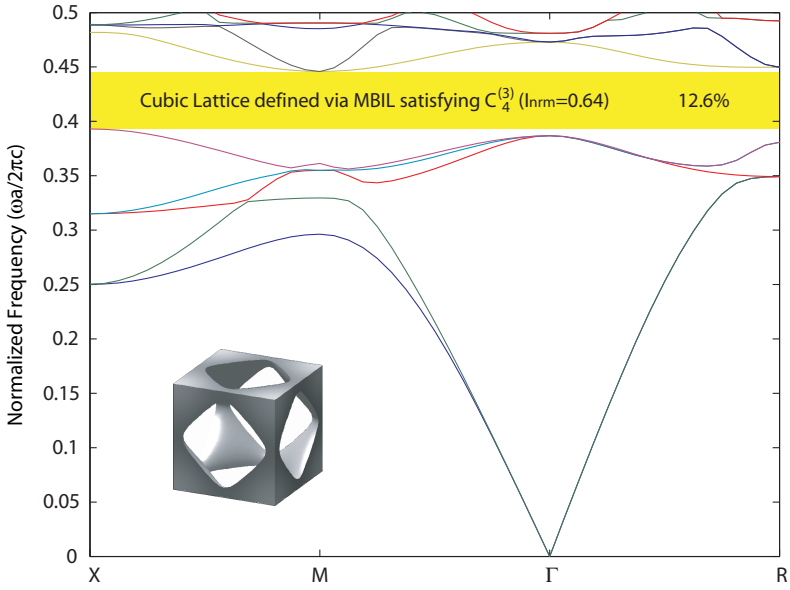

Figure 5.13: Band structure of a cubic lattice defined via MBIL satisfying $C_4^{(3)}$ corresponding to the largest band gap in Fig. 5.12 ($\Omega_5 = 12.6\%$, $I_{nrm} = 0.640$, $F = 25.9\%$). Included are a cubic supercell. The irreducible Brillouin zone is illustrated in Appendix D.

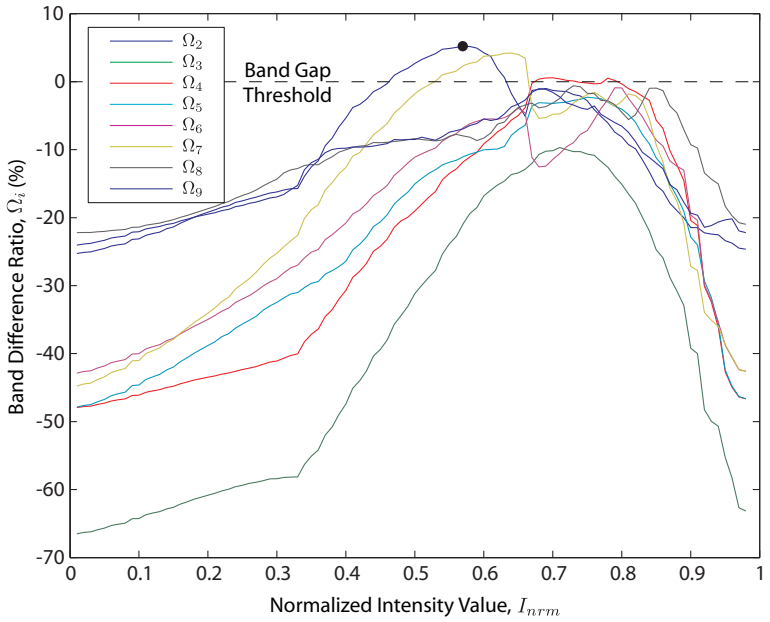

Figure 5.14: Band gap map for FCC lattice of masses defined via MBIL satisfying $C_4^{(3)}$ ($I_{nrm} = 0.570$, $\Omega_2 = 5.1\%$). The horizontal dashed line indicates the band gap threshold where values of the band difference ratio above this line equate to the band gap size.

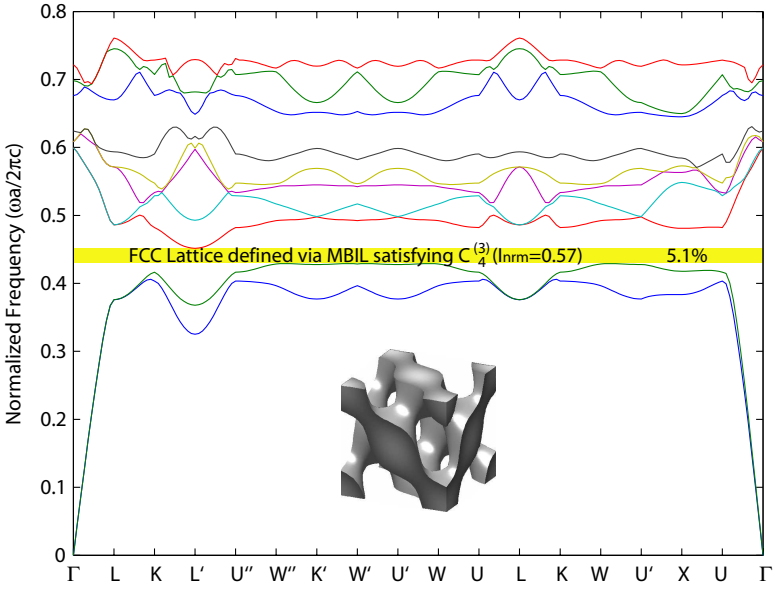

Figure 5.15: Band structure of a fcc lattice defined via MBIL satisfying $C_4^{(3)}$ corresponding to the largest band gap in Fig. 5.14 ($\Omega_2 = 5.1\%$, $I_{nrm} = 0.570$, $F = 37.8\%$). Included are a cubic supercell. The irreducible Brillouin zone is illustrated in Appendix D.

Table 5.3: Maximum Band Gap Sizes for Three-Dimensional Photonic Crystal Structures

	Maximum Band Gap Size			
	Spherical Masses	Spherical Vacancies	MBIL-Defined Masses	MBIL-Defined Vacancies
Face-centered cubic	-	5.95%	5.10%	-
Body-centered cubic	-	1.56%	-	-
Simple Cubic	-	7.29%	12.6%	-

Table 5.4: Corresponding Fill Factors for the Three-Dimensional Photonic Crystal Structures with the Largest Band Gaps

	Fill Factor			
	Spherical Masses	Spherical Vacancies	MBIL-Defined Masses	MBIL-Defined Vacancies
Face-centered cubic	-	22.2%	37.8%	-
Body-centered cubic	-	20.1%	-	-
Simple Cubic	-	19.0%	25.9%	-

Table 5.5: Corresponding Normalized Radii/Intensity Values for the Three-Dimensional Photonic Crystal Structures with the Largest Band Gaps

	Normalized Radii		Normalized Intensity Value	
	Spherical Masses	Spherical Vacancies	MBIL-Defined Masses	MBIL-Defined Vacancies
Face-centered cubic	-	0.360	0.570	-
Body-centered cubic	-	0.460	-	-
Simple Cubic	-	0.605	0.640	-

Table 5.6: Corresponding Normalized Mid Gap Frequencies for the Three-Dimensional Photonic Crystal Structures with the Largest Band Gaps

	Normalized Mid Gap Frequency			
	Spherical Masses	Spherical Vacancies	MBIL-Defined Masses	MBIL-Defined Vacancies
Face-centered cubic	-	0.773	0.440	-
Body-centered cubic	-	0.643	-	-
Simple Cubic	-	0.470	0.419	-

that exhibit the maximum band gap size do not resemble those lattices composed of spherical masses or vacancies that exhibit the maximum band gap size. While a body-centered cubic lattice of spherical vacancies can posses a band gap (albeit a small one of 1.56%), the corresponding MBIL-defined structures do not possess a band gap. The fact that the MBIL-defined cubic lattice defined by a $C_4^{(3)}$ interference pattern has the same group symmetry as the cubic lattice of spherical vacancies which possesses a band gap (7.29%), it is expected that the corresponding MBIL-defined structure will as well. Interestingly, an increase of $\sim 73\%$ in band gap size was found from 7.29% to 12.6%. Qualitatively, though, the MBIL-defined structure was composed of masses. However, the fill factors indicate that the structures are mostly air. This can be explained by the fact that the cubic lattice of spherical vacancies overlap, i.e. the normalized radius is greater than the close-touching radius. As mentioned before, structures defined by the $C_4^{(3)}$ interference patterns can be defined as being masses or vacancies depending upon the interference pattern being utilized.

CHAPTER 6

FABRICATION OF PHOTONIC CRYSTAL STRUCTURES VIA MULTI-BEAM-INTERFERENCE LITHOGRAPHY

The photonic crystal structures presented here were fabricated at the Georgia Institute of Technology using a combination of resources in the Optics Laboratory and the Microelectronic Research Center cleanroom. The following fabrication methodology results in a straightforward experimental configuration and fabrication procedures for fabricating these structures.

6.1 Ultraviolet-Based Lithography

From a chemistry standpoint, using an ultraviolet-based process source is advantageous due to the availability of UV-based lithographic materials. While some groups have fabricated photonic crystal structures using visible light laser sources [67, 77, 81], these processes require unconventional photoresist formulations to enhance absorption in the visible part of the spectrum. Even with this enhancement, relatively large exposure doses are still required. This approach was tested experimentally using a Spectra Physics BeamLok 2025 Argon Ion laser providing a 514.5 nm laser source and Microchem's SU-8 2005 photoresist modified with Spectra Group Limited's H-Nu 535 line of photoinitiators. It is concluded that the additional time required to prepare custom photoresists and the demanding stability requirements due to extended exposure times make the process impractical. Instead, in this research, a Spectra Physics BeamLok 2065-5S Argon Ion laser with etalon and etalon controller provides stable, single frequency operation at 363.8 nm with frequency jitter of < 10 MHz for < 1 sec and < 20 MHz for < 2 min for fabrication. Given a value of 20 MHz jitter in frequency and exposure times of well under 2 minutes, one can expect a change

in recording wavelength over the exposure time of no more than $\Delta\lambda = 4.41 \times 10^{-6}$ nm. For a hexagonal lattice with a lattice constant of 1.5 λ or 545.7 nm, the lattice constant of the interference pattern is expected to change by no more than 1.3×10^{-6} %. In order for one period of the interference pattern to be completely washed out during an exposure, the sample area would have to be over 40 meters in diameter. The wavelength instability in this configuration is clearly not a limiting factor.

Many photoresists designed for operation at 365 nm (mercury i-line) exist due to the microelectronics industry. Existing lithography recipes are easily adapted to this technique by replacing resist exposure via a mask aligner tool with resist exposure by the multi-beam-interference lithography configuration described in this thesis.

6.2 Three-Beam-Interference Configuration

Literature has focused little on the details of recording configurations for MBIL and more on the resulting structures. More complicated designs such as those using single refractive or diffractive elements [77, 83] are described but are limited to single specific structures. A facility to perform general multi-beam interference was designed, tested, and constructed in this research [85, 98]. Designs for two-, and three-beam interference are presented. Particular attention is focused on phase front quality, reduction of unwanted reflections, stability, and design versatility (in terms of wavevector configuration and individual beam intensity and polarization state). Appropriate optical substrates and coatings for use at the recording wavelength are required.

The optimized solutions of MBIL designs require a fabrication configuration which provides complete control over the intensity and polarization of each beam. This is accomplished with a variable-ratio beamsplitter with output linear polarization direction control for each recording beam. Each consists of three half-wave plates and a polarizing beamsplitter cube (each designed to operate at 363.8 nm). The non-birefringent beamsplitter

consists of two precision right-angle prisms cemented together. The four faces are antireflection coated with a multilayer dielectric coating to minimize reflections within the optical configuration. The hypotenuse of one of the prisms is coated with a multilayer dielectric polarizing beamsplitter coating. This coating reflects S-polarized light (vertical to table) while transmitting P-polarized light (horizontal to table). Ghost beams are eliminated by using a cube beamsplitter as opposed to a slab beamsplitter. The half-wave plates rotate the plane of polarization of the input beam eliminating the need to physically manipulate the laser. The plane of polarization is essentially reflected about the plane of the crystalline optic axis normal to the surface of the half-wave plate. Operation of these polarization optics are illustrated in Fig. 6.1(a) and 6.1(b) including the corresponding Jones matrices. Figure 6.2 illustrates the configuration of a single variable-ratio beamsplitter with output linear polarization direction control. Similarly, the Jones matrices for the input linear beam and both output beams are given for completeness.

Given a linearly polarized input beam, the intensities and polarizations of the two output beams are adjusted by placing a half-wave plate in the path of the input and the two output beams of the beamsplitter. The half-wave plate at the input rotates the linearly polarized light, thereby allowing control over the intensity of each output beam. An additional half-wave plate is placed in the path of each of the two linearly polarized output beams, thereby allowing control over the direction of the linear polarization of each beam. In a multi-beam-interference configuration, a half-wave plate in the path of an output beam of one variable-ratio beamsplitter with output linear polarization direction control is used as the half-wave plate in the path of an input beam in another variable-ratio beamsplitter with output linear polarization direction control. Additional mirrors are used to steer the beams in the appropriate directions. Figure 6.3 illustrates the configuration used in this research. The heights above the optical table of the optics that compose both variable-ratio beamsplitters with output linear polarization direction control and mirrors M1, M2 and M3 are set equal to that of the input laser beam. Mirrors M2 and M3 control the incident angle

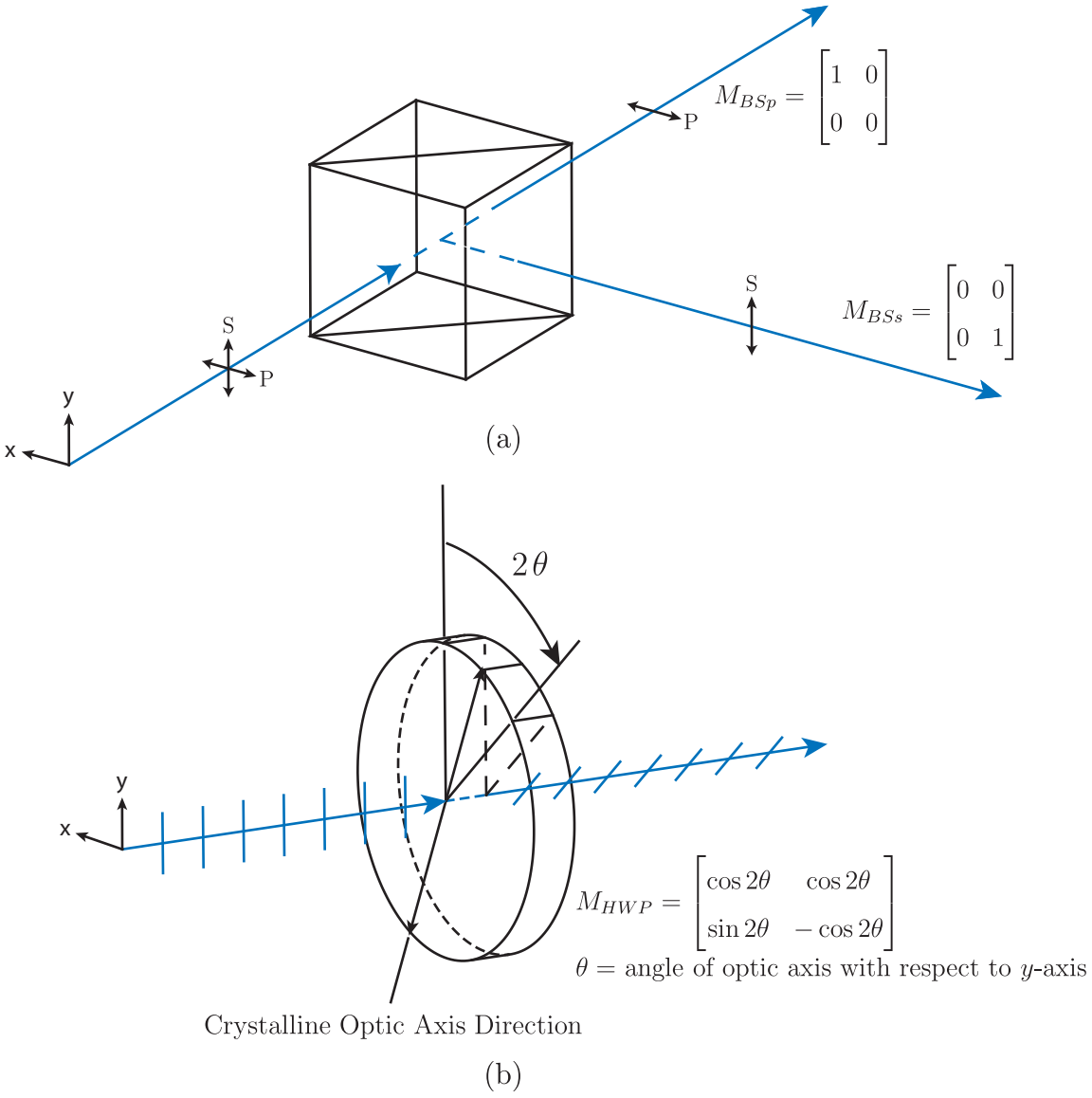

Figure 6.1: (a) Operation of a polarizing beamsplitter including Jones matrices for each output beam. P-polarized (horizontal to table) light passes through while S-polarized (vertical to table) is reflected at the interface. Extinction ratios can exceed 100:1. (b) Operation of half-wave plate including Jones matrix. Given linearly polarized input light, the plane of polarization is essentially reflected about the plane of the crystalline optic axis of the half-wave plate.

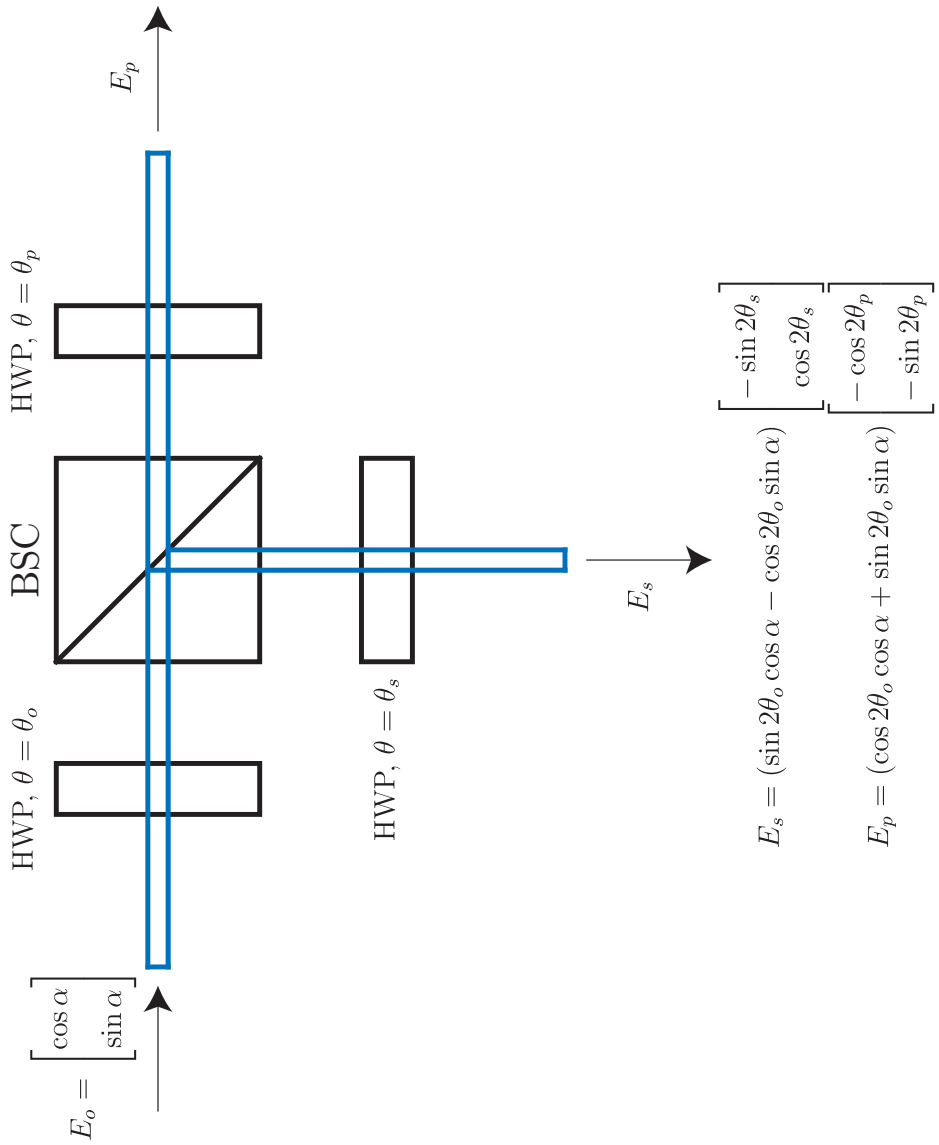

Figure 6.2: Illustration of a single variable-ratio beamsplitter with output linear polarization direction control using one polarizing beamsplitter and three half-wave plates. The Jones matrix for each output beam is given.

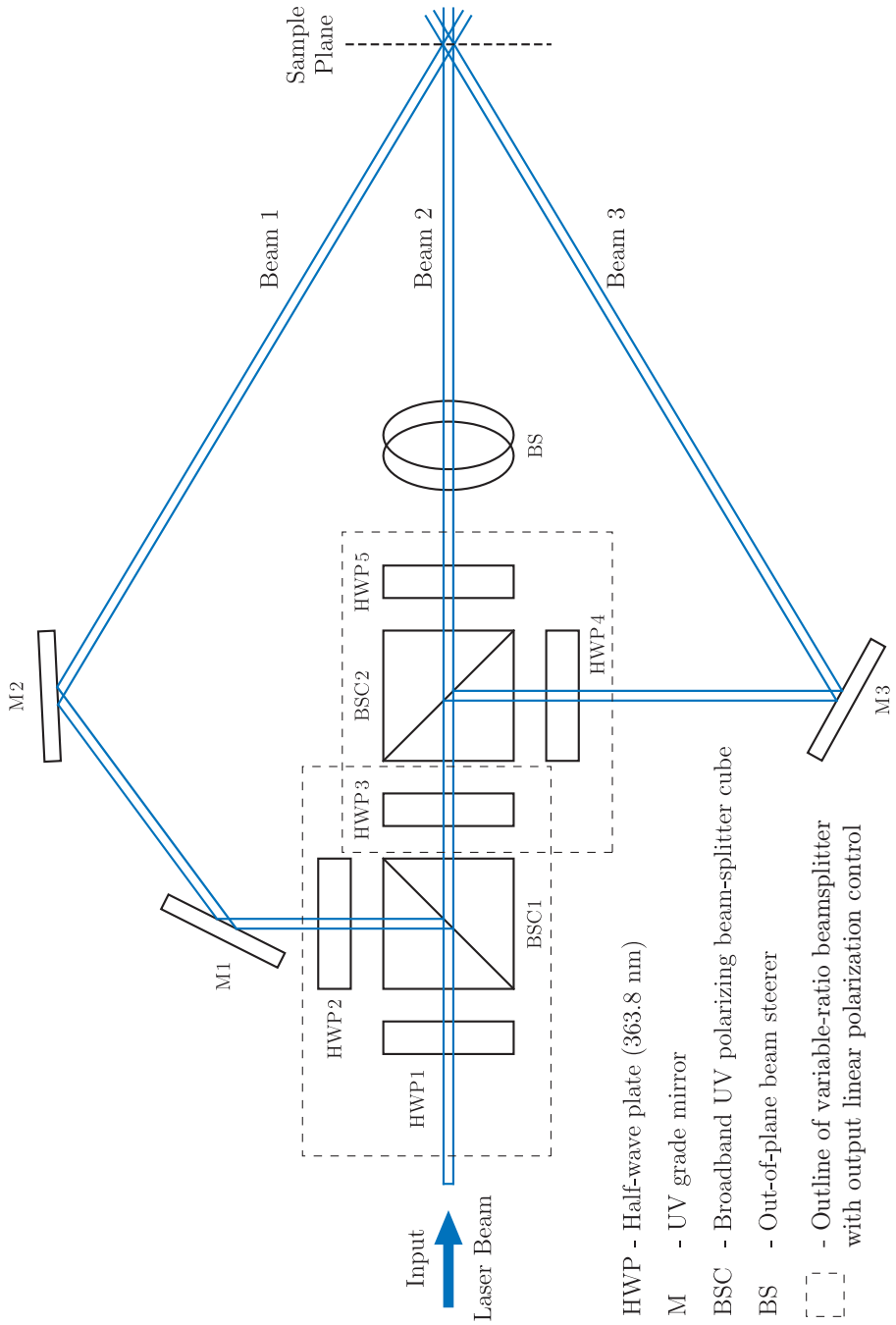

Figure 6.3: Three-beam-interference configuration. Each recording beam is controlled in direction and polarization.

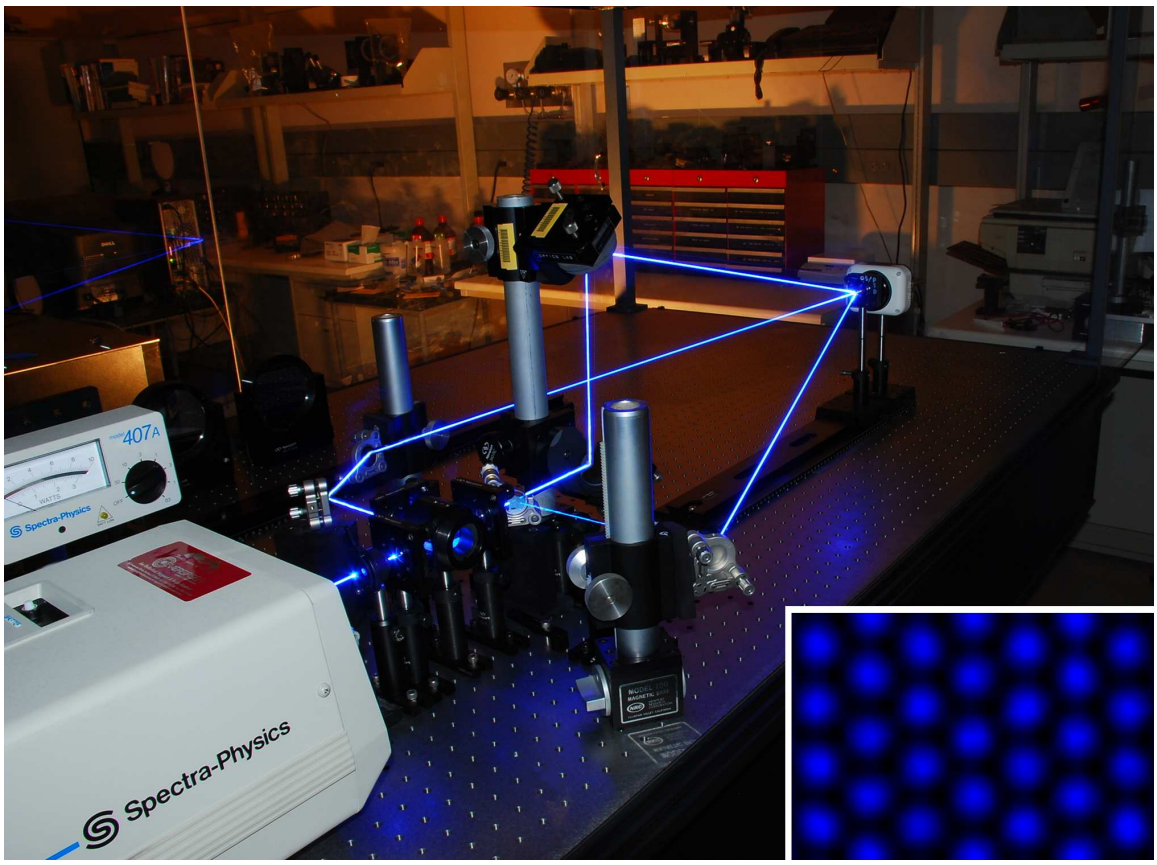

Figure 6.4: Photograph of operating three-beam interference configuration in room 260 in the Microelectronic Research Center. Three beam converge onto sample plane where an objective and CCD camera is present for real-time monitoring of the interference pattern. Inset is an image of the interference pattern captured using the real-time monitoring capability.

upon the sample plane of beams 1 and 3, respectively. The out-of-plane beam steerer BS in the path of beam 2 is composed of two mirrors. The first is set at the height of the previously mentioned optics and adjusted such that the beam is reflected perpendicularly to the optical table. The second is set at a variable height and oriented accordingly to control the incident angle of beam 2 upon the sample plane. A photograph is included in Fig. 6.4 illustrating the configuration of the optics and the paths of the three recording beams. The photograph shows the orientation of the optics to direct the beams toward the sample plane.

With this configuration, there are a number of exposure options available. They include the following:

1. Single exposure, two-beam interference (one-dimensional photonic crystals)

2. Single exposure, three-beam interference (one- and two-dimensional photonic crystals)

3. Multiple exposure, two-beam interference (two- and three-dimensional photonic crystals)

4. Multiple exposure, three-beam interference (two- and three-dimensional photonic crystals)

An additional dependent variable-ratio beamsplitter with output linear polarization direction control can be incorporated in the configuration in Fig. 6.3 to add a fourth interfering beam. This allows for single exposure, four-beam interference for three-dimensional photonic crystals.

6.3 Real-Time Monitoring of Interference Patterns

The facility also includes the ability to monitor the interference pattern in real-time. It has been reported that a microscope objective can be used to record the intensity pattern resulting from multi-beam interference by placing photosensitive film directly after the objective for pattern magnification [63]. With advances in digital image capture devices, real-time monitoring of the "magnified" pattern is possible. This real-time monitoring system is invaluable in terms of stability analysis, confirmation of translational symmetry, confirmation of group symmetry, and general concept verification.

The interference pattern within the sample plane is also monitored in real time. The interference pattern is magnified (using a microscope objective), and the image is captured using a cooled 3.2 Megapixel Olympus Q-Color3 Imaging System digital CCD camera. Both the microscope objective and CCD camera are present in Fig. 6.4. A Newport microscope objective lens with a 0.85 NA and 2.9-mm focal length (60x) provides sufficient

magnification and a large enough acceptance angle for the designs considered in this thesis. The objective is placed at the sample plane such that the interfering beams enter at the front lens assembly. The camera is placed after the mounting threads some distance away such that the CCD array is illuminated by all three recording beams. Using this method, designs are easily verified. Interference patterns are monitored in real-time, and the effects of changing the polarization of each individual beam are observed instantly without fabrication. This method is used to verify the theories and the designs before beginning the more time-consuming fabrication process. It should be noted and understood that the interference pattern imaged using the CCD camera is different than the interference pattern produced at the sample plane. The microscope objective changes the relative orientation of both the recording wavevectors and the polarizations that are used to create the interference pattern on the CCD array. However, for the designs considered in this thesis, the real-time monitoring still provides useful information. One, the type of lattice (one-dimensional grating, two-dimensional square lattice, or two-dimensional hexagonal lattice) does not change during imaging. Two, a correctly configured multi-beam-interference experiment will still result in an image with high contrast. Three, many of the configurations described in this thesis optimized for photoresist exposure are also optimized for real-time monitoring. This includes the one-dimensional grating design and the two-dimensional hexagonal lattice with *p6m* plane group symmetry defined using a ${}^{-}C_3^{(3)}$ interference pattern.

6.4 Alignment procedures

Given the general configuration for multi-beam interference illustrated in Figs. 6.3 and 6.4, it is worthwhile to construct design plots that illustrate the relationships between critical experimental configuration parameters and the lattice constant of the resulting photonic crystal. They show the extent of photonic crystals which can be fabricated given the current MBIL configuration and provide guidelines for an initial alignment of the configuration. Highlighted within each of these plots are areas of experimental feasibility. These

emphasize areas that are experimentally feasible given the physical constraints of the environment: size of opto-mechanics, size of optics table, etc. It has been determined that there are five critical experimental configuration parameters. These are the perpendicular distance from the optic axis (z axis) to mirrors M2 and M3 (y_M), the distance along the optic axis from mirror M2 and M3 to the sample plane (z_{sp}), the distance along the optic axis from mirror M2 and M3 to the beam-steerer pair BS (z_{BS}), the perpendicular distance above the plane containing the input laser beam and normal to the x axis to the top mirror of the beam-steerer pair BS (x_{BS}), and the perpendicular distance above the plane containing the input laser beam to sample plane spot (x_{sp}). These critical experimental configuration parameters are labeled in Fig. 6.5. An additional parameter of interest is the incident angle of the recording beams on the sample plane, θ_{air}. This parameter will be needed in order to calculate the optimized plane wave parameters to produce a lithographically useful interference pattern.

6.4.1 Alignment for One-Dimensional Grating

Three different photonic crystal structures are experimentally evaluated in this thesis: a one-dimensional grating, a two-dimensional square lattice, and a two-dimensional hexagonal lattice. Each photonic crystal structure has associated with it a number of design plots. For a one-dimensional grating, beam 2 is blocked and thus x_{BS} and z_{BS} are irrelevant. A restriction on x_{sp} of $x_{sp} = 0$ is made such that beam 1 and beam 3 are parallel to the optics table. For the one-dimensional grating case, only two critical experimental configuration parameters are of interest: y_M and z_{sp}. The relationship between these two parameters and the lattice constant a are

$$\tan\theta_{air} = \frac{y_M}{z_{sp}} \tag{6.1}$$

$$\frac{a}{\lambda} = \frac{1}{2\sin\theta_{air}} \tag{6.2}$$

and illustrated in Fig. 6.6. The configuration is aligned for a grating period of 1.18 a/λ or 430 nm with $y_M = 16.51$ cm and $z_{sp} = 35.36$ cm. The intensities of beams 1 and 3

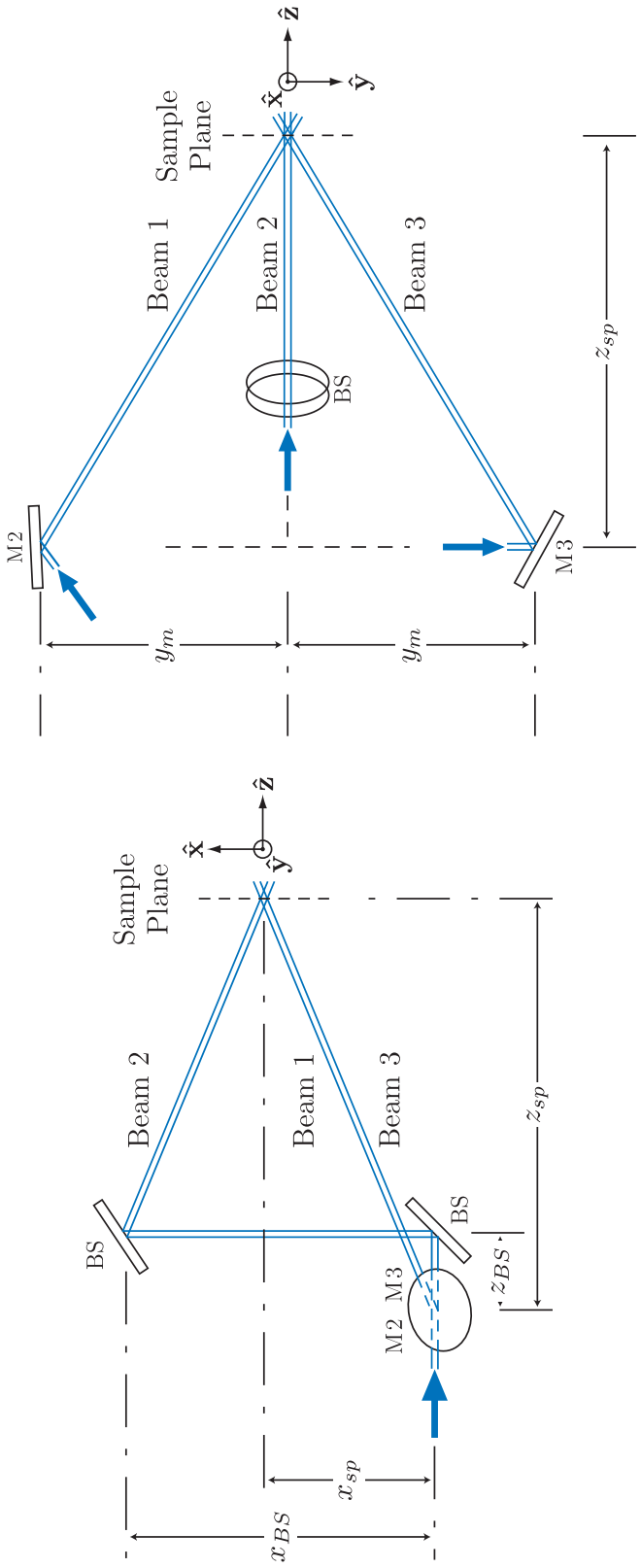

Figure 6.5: Three-beam-interference configuration. Critical experimental configuration parameters are illustrated.

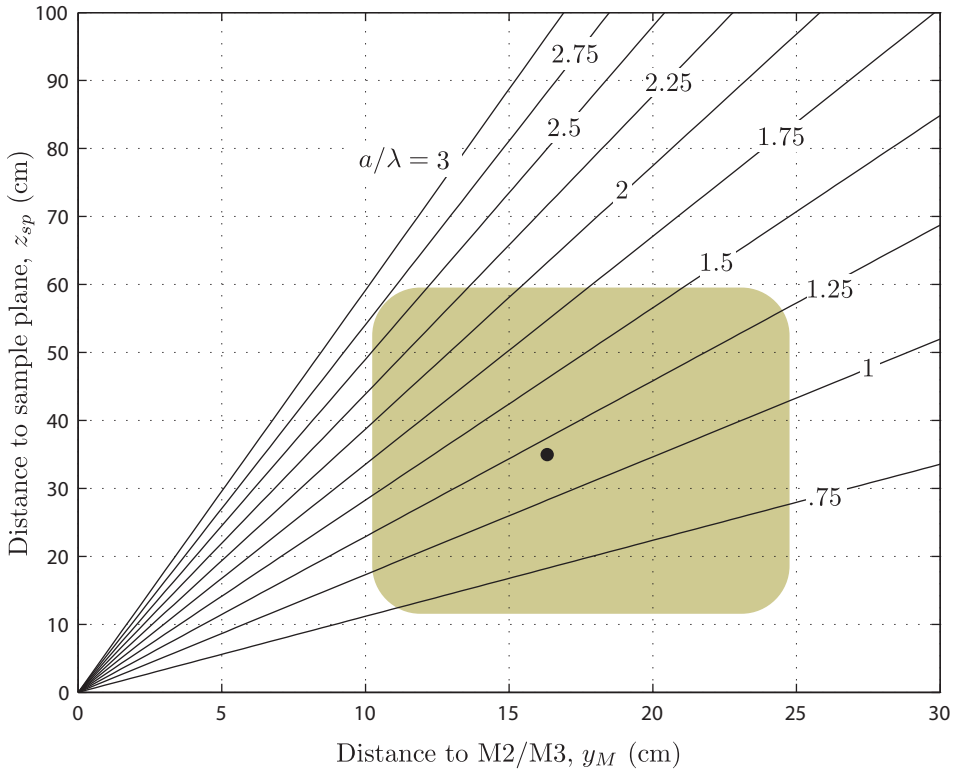

Figure 6.6: Design plot for aligning the recording beams needed to create a two-dimensional hexagonal interference pattern. The relationship between the critical experimental configuration parameters y_M, z_{sp} and a is illustrated. Highlighted is the area of experimental feasibility. The design used in this research is marked with a dot on the plot.

are adjusted to be equal by adjusting HWP1 and HWP3, and the polarizations are oriented vertically, in the x direction, (as described in Sec. 6.2) for maximum contrast by adjusting HWP2 and HWP4.

The alignment procedure and resulting interference pattern are verified using the real-time monitoring system. The microscope objective is placed at the sample plane and the CCD camera captures the magnified interference pattern illustrated in Fig. 6.7(a). The image captured is very high in contrast and extremely stable. This verifies that three-beam interference configuration functions properly for beams 1 and 3.

Figure 6.7(b) is a plot of a single row of pixel values for the magnified interference pattern in Fig. 6.7(a). Ideally, the intensity along the dotted line in Fig. 6.7(a) is a sinusoid of the form $a\cos(2\pi/Tx + \phi)$. However, due to imperfect states of polarization and the finite extent of the pixels on the CCD array, there is a DC component in the experimental data. The pixel values fit extremely well to a sinusoidal curve with a DC component.

6.4.2 Alignment for Two-Dimensional Hexagonal Lattice

For a two-dimensional hexagonal lattice, all five critical experimental configuration parameters are relevant. However, a restriction is placed upon z_{BS}. This is done because a is a function of y_M, x_{BS}, and z_{BS}. Since this four-dimensional relationship is difficult to visualize, the polarization optics and beam steerer are placed as close as possible and the resulting value of z_{BS} is used for the design plots included here. Given a value of $z_{BS} = 7.62$ cm, the relationships between the remaining four critical experimental configuration parameters are

$$\frac{a}{\lambda} = \frac{2}{3\sin\theta_{air}} \tag{6.3}$$

$$\tan\frac{\pi}{6} = \frac{x_{sp}}{y_M} \tag{6.4}$$

$$\tan\theta_{air} = \frac{y_M\tan\frac{\pi}{3} - x_{sp}}{z_{sp}} \tag{6.5}$$

$$\tan\theta_{air} = \frac{x_{BS} - x_{sp}}{z_{sp} - z_{BS}} \tag{6.6}$$

and illustrated in Figs. 6.8 - 6.10. Highlighted within each of these plots are areas of

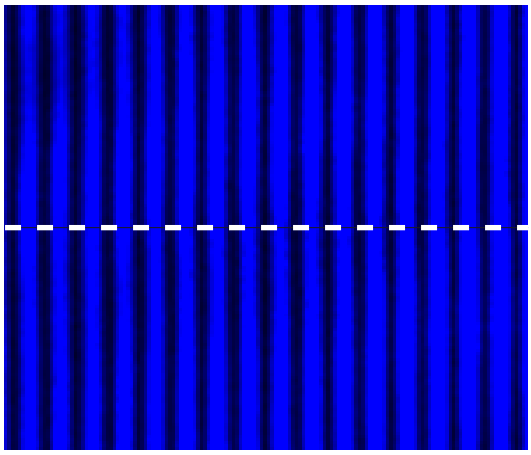

(a)

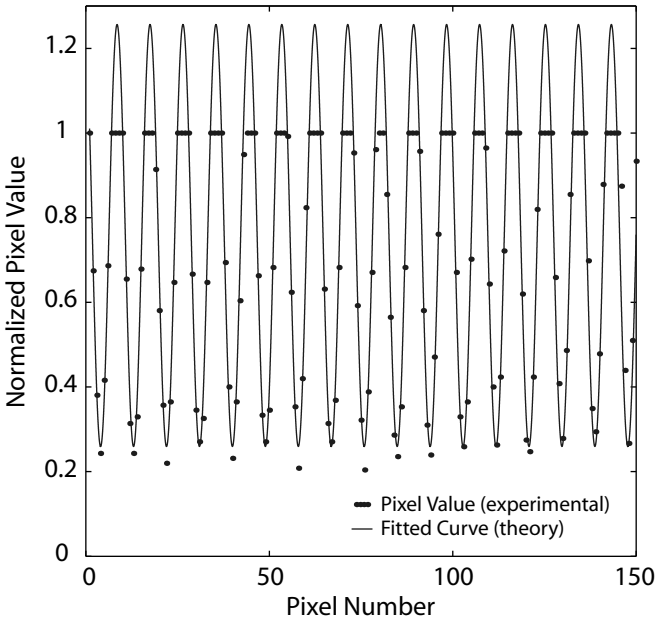

(b)

Figure 6.7: (a) Captured image of magnified one-dimensional interference pattern. (b) Plot of pixel values for approximately 17 periods (dashed line in part (a)) and fitted sinusoidal curve in the form $a\cos(2\pi x/T + \phi) + c$ where $a = 0.4986$, $T = 8.984$, $\phi = 0.34$, and $c = 0.7579$ with an R-square value of 0.93 and a RMSE of 6.092%. Note that saturated pixels in (a) are excluded in the curve fitting analysis in (b).

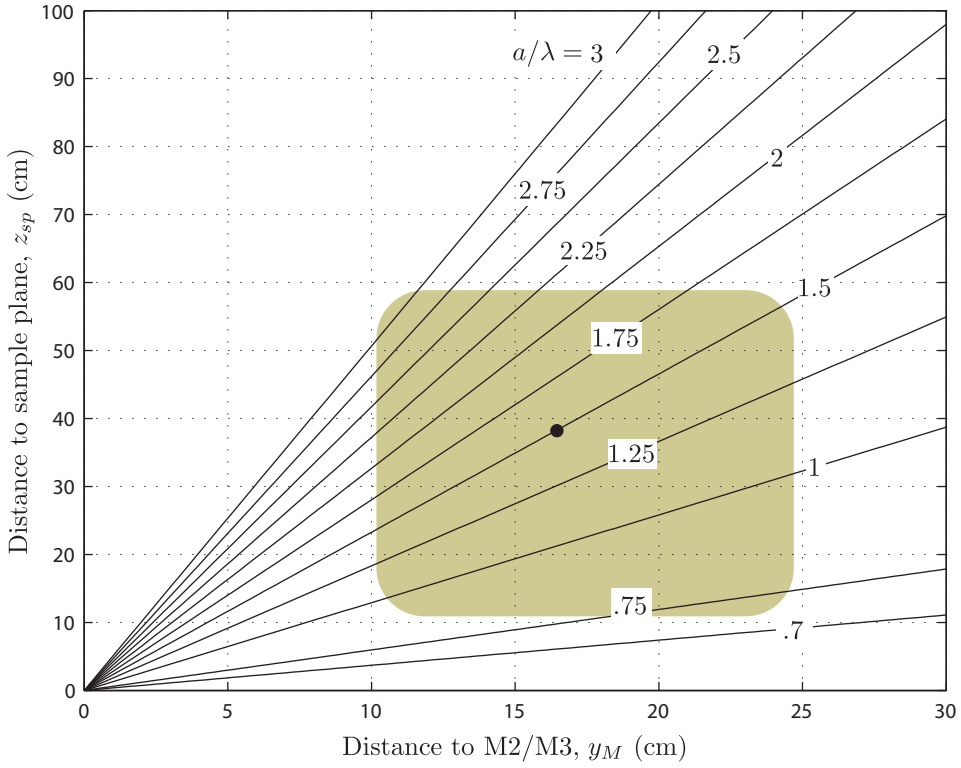

Figure 6.8: Design plot for aligning the recording beams needed to create a two-dimensional hexagonal interference pattern. The relationship between the critical experimental configuration parameters y_M, z_{sp}, and a is illustrated. Highlighted is the area of experimental feasibility. The design used in this research is marked with a dot on the plot.

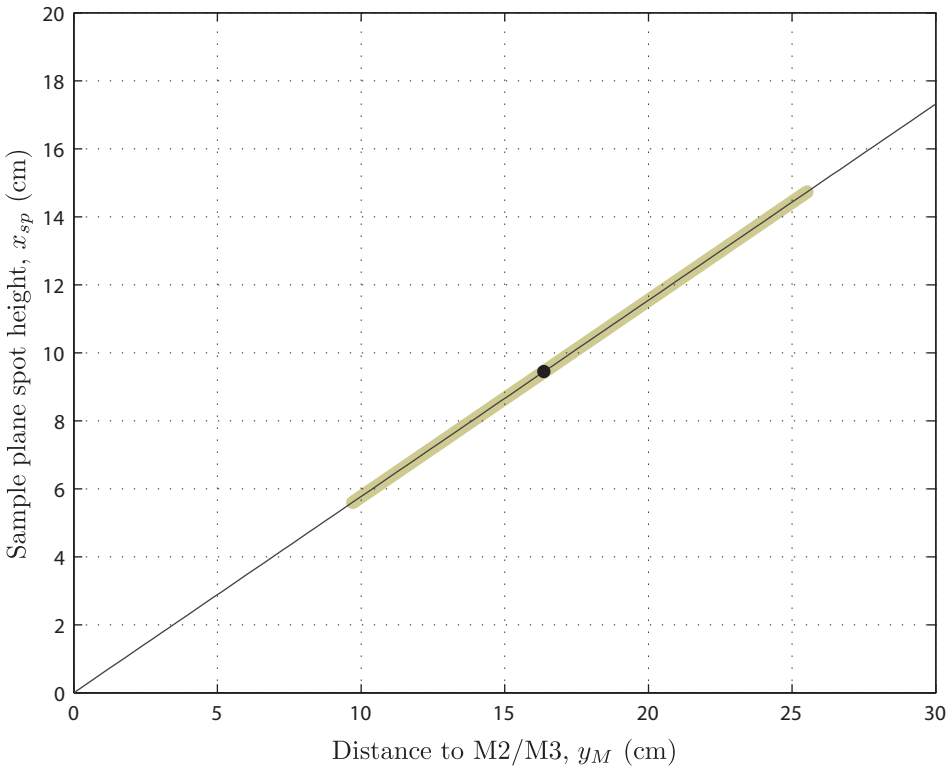

Figure 6.9: Design plot for aligning the recording beams needed to create a two-dimensional hexagonal interference pattern. The relationship between the critical experimental configuration parameters y_M and x_{sp} is illustrated. Highlighted is the area of experimental feasibility. The design used in this research is marked with a dot on the plot.

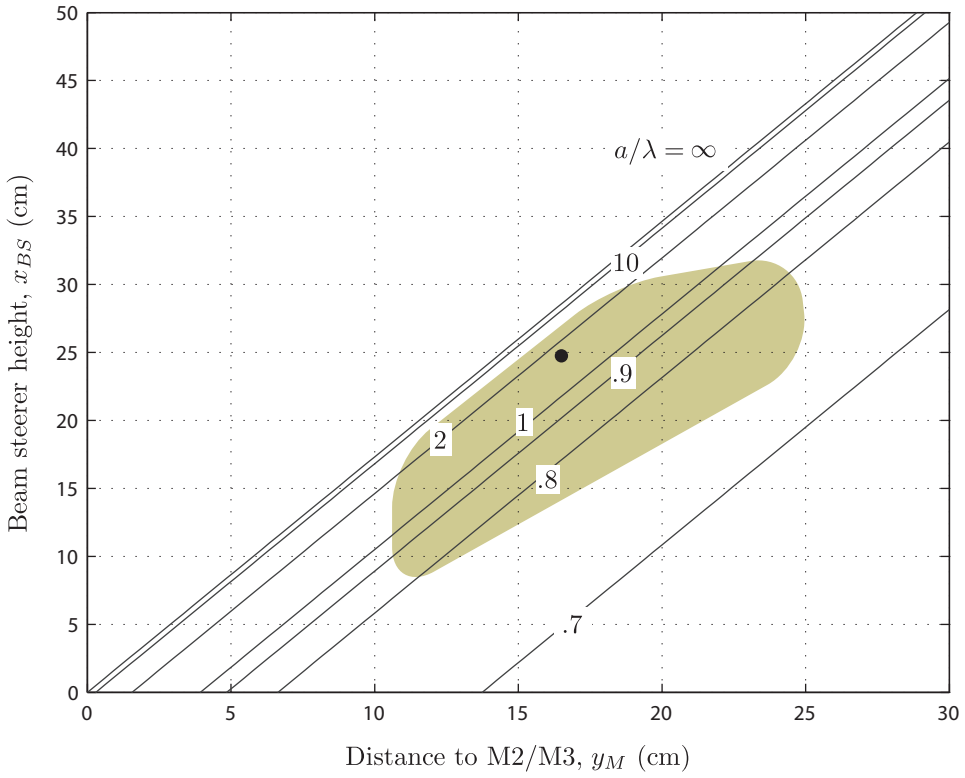

Figure 6.10: Design plot for aligning the recording beams needed to create a two-dimensional hexagonal interference pattern. The relationship between the critical experimental configuration parameters y_M, x_{BS}, and a is illustrated. Highlighted is the area of experimental feasibility. The design used in this research is marked with a dot on the plot.

experimental feasibility for the specific configuration used in this research. Given these design constraints, a lattice constant of 1.5 λ or 545.7 nm is chosen. The values of the resulting critical experimental configuration parameters are as follows: $a/\lambda = 1.5$, $y_M = 16.51$ cm, $z_{sp} = 38.43$ cm, $x_{sp} = 9.53$ cm, $x_{BS} = 24.82$ cm, and $z_{BS} = 7.62$ cm. The multi-beam-interference configuration is adjusted to reflect these parameters as an initial alignment.

The fine adjustment of the recording beams is facilitated by the use of an alignment card specifically designed and fabricated for the desired photonic crystal lattice. The alignment card required for a hexagonal lattice (illustrated in Fig. 6.11) includes six alternating holes (approximately the diameter of the laser beam) and alignment marks (cross) creating an equilateral regular hexagon. Given the diameter of the circumscribed circle of the hexagon, D, and the distance from the alignment card to the mirror (sample plane), z_{ac}, the lattice constant, a, of the interference pattern is calculated as

$$a = \frac{2\lambda}{3D}\sqrt{D^2 + 4z_{ac}^2}\,. \tag{6.7}$$

The fabrication and positioning of the alignment card is performed with the aid of Fig. 6.12. This plot illustrates the relationship between the distance separating the mirror (sample plane) and the alignment card (z_{ac}), the diameter of the circumcircle of the hexagon on the alignment card (D), and the lattice constant (a). In this research a diameter of the circumcircle of the hexagon on the alignment card of $D = 5.08$ cm was used resulting in a distance separating the mirror (sample plane) and the alignment card of $z_{ac} = 5.12$ cm. All relevant configuration and alignment parameters, including the angle of incidence on the sample plane θ_{air}, are summarized in Table 6.1. After an initial alignment is performed by positioning the optics and opto-mechanics using the values in Table 6.1, a fine adjustment is performed by using the alignment card. A mirror is placed in the sample plane at the sample plane spot height x_{sp}. The alignment card is positioned at a distance of z_{ac} from the mirror and mirrors M2, M3, and the beam steerer BS are adjusted such that each beam passes through the appropriate hole on the alignment card, reflects off the mirror in the

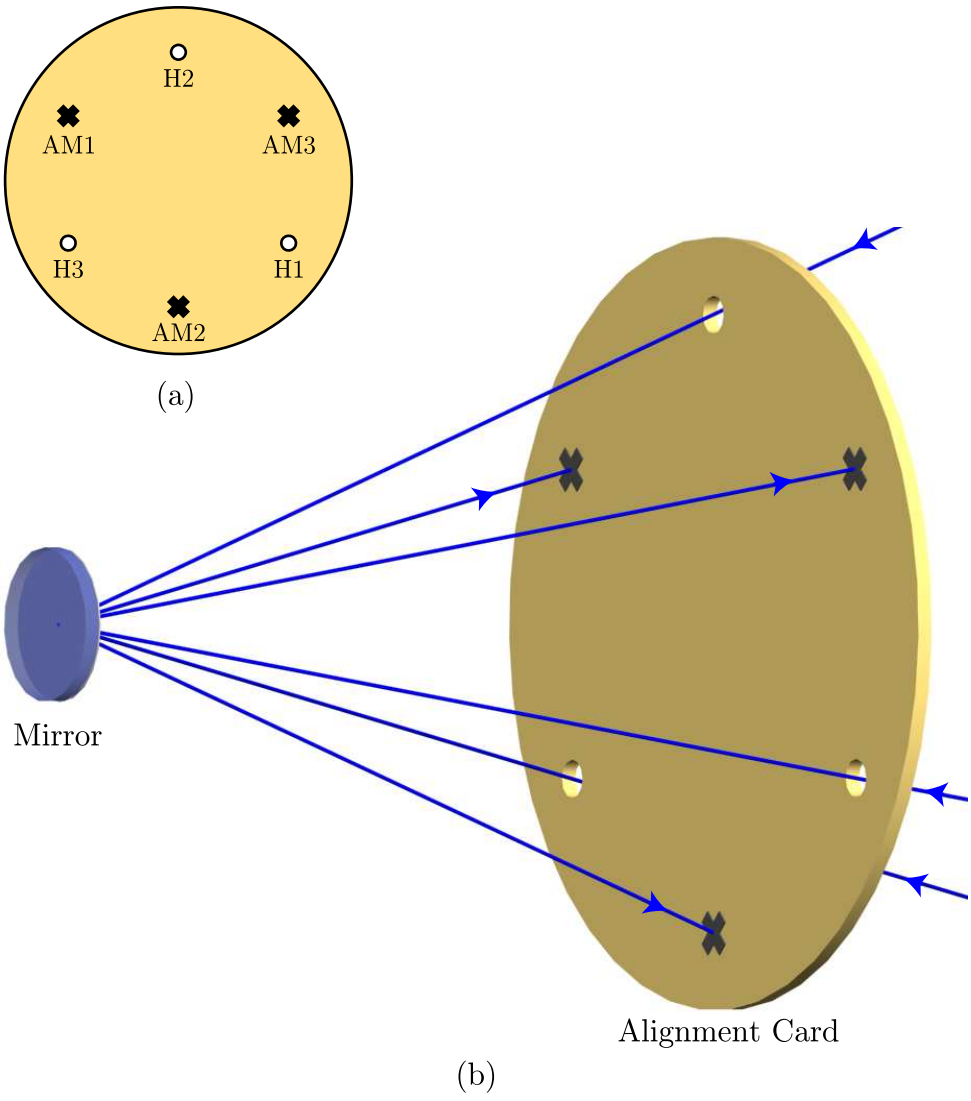

Figure 6.11: Alignment card used to facilitate fabrication of two-dimensional hexagonal lattice. The multi-beam-interference configuration is adjusted such that the three separate beams pass through holes H1, H2, and H3, reflect off the mirror and are projected onto alignment marks AM1, AM2, and AM3, respectively. This procedure aids in positioning the three beams to be rotationally symmetric about the normal of the mirror which lies in the sample plane.

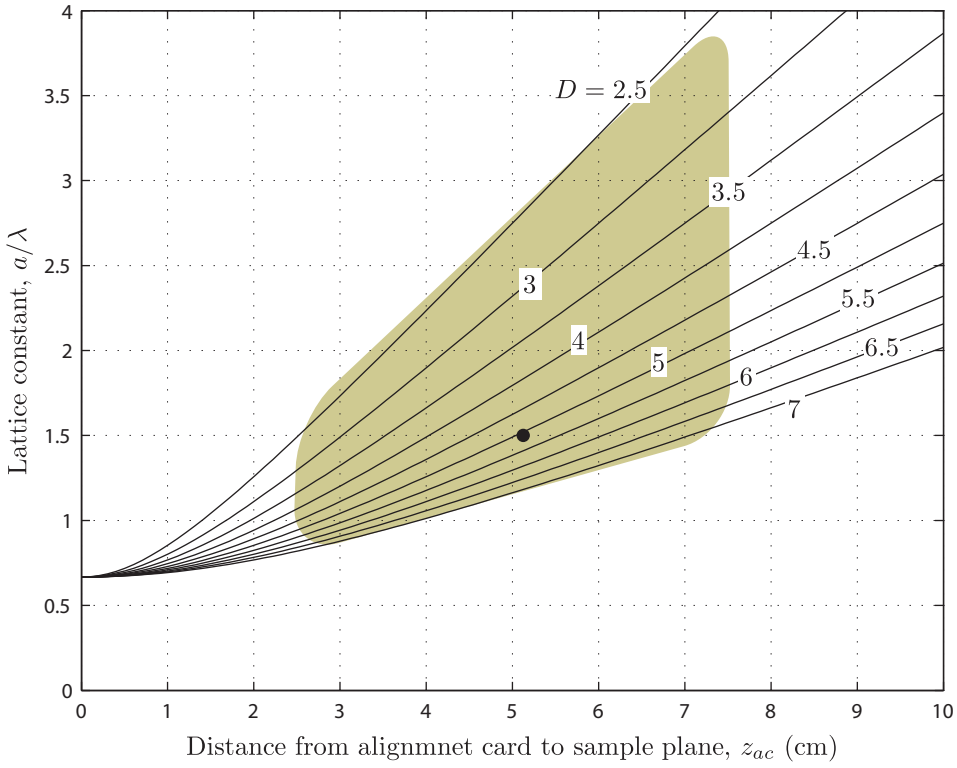

Figure 6.12: Design plot for aligning the recording beams needed to create a two-dimensional hexagonal interference pattern. The relationship between the critical experimental configuration parameters z_{ac}, D, and a is illustrated. Highlighted is the area of experimental feasibility. The design used in this research is marked with a dot on the plot.

Table 6.1: Critical Experimental Configuration and Alignment Parameters and Spherical Zenith Angle (θ_{air}) for a Hexagonal Lattice

Parameter	Value
a/λ	1.5
y_M	16.51 cm
z_{sp}	38.43 cm
x_{sp}	9.53 cm
x_{BS}	24.82 cm
D	5.08 cm
z_{ac}	5.12 cm
θ_{air}	26.39°

sample plane, and projects on an opposite alignment mark. This procedure guarantees three rotationally symmetric beams with respect to the optic axis needed to create a hexagonal lattice interference pattern.

In order to create an interference pattern with *p6m* plane group symmetry and high contrast, the polarizations and intensities of the recording beams are adjusted accordingly. Given the two fundamentally different types of interference patterns (${}^{+}C_3^{(3)}$ and ${}^{-}C_3^{(3)}$) and the different indices of refraction of the two recording media (1.736 for the Shipley 1813 positive resist and 1.58 for the Futurrex NR7-1500P negative resist), there are four different configurations of the polarizations and beam intensities. Though the angle of incidence on the sample plane θ_{air} of the interfering beams are equal for each case, the beams refract at different angles θ_{PR} depending on the index of refraction of the recording media n_{PR}. Using Snell's Law

$$n_{air}\sin(\theta_{air}) = n_{PR}\sin(\theta_{PR})\,, \tag{6.8}$$

the angles of the recording beams within the photoresist are calculated. The beam intensities and polarizations within the photoresist are calculated via the nonlinear optimization outlined in Appendix A. While the beam intensities calculated within the photoresist are used as the beam intensities in air, the calculated polarizations within the photoresist are not used directly as the polarization of the beams in air. The polarization direction of each recording beam must be adjusted correctly such that the resulting refracted beam within the photoresist has the correct polarization direction. An additional experimentally useful parameter, $\psi_{x,i}$, is extracted from this data to aid in correctly adjusting the polarization of the recording beams in air. The polarization rotation angle, $\psi_{z,i}$, (described in Appendix A) is first used to calculate the polarization needed in the recording beams propagating in air. Since $\psi_{z,i}$ is calculated with respect to $\hat{\mathbf{z}} \times \mathbf{k}_i$, the value of $\psi_{z,i}$ does not change through refraction at interfaces normal to $\hat{\mathbf{z}}$ (even though the Cartesian coordinates of the polarization vector of the incident and refracted beams are not equal). While this is not true in general due to different transmission coefficients for the TE and TM components, in the situations

considered in this thesis, the difference in the intensities of the TE and TM components is $< 5\%$ and is ignored. Next, a rotation angle $\psi_{x,i}$ is calculated with respect to $\hat{\mathbf{x}} \times \mathbf{k}_i$ in the exact same fashion as $\psi_{z,i}$ described in Appendix A. This is again a counter-clockwise angular rotation (when looking anti-parallel to the wavevector $\mathbf{k}_i$) where when $\psi_{x,i} = 0$, $\hat{\mathbf{e}}_{x,i} = \hat{\mathbf{x}} \times \mathbf{k}_i$. This parameter is useful since the polarization direction of $\psi_{x,i} = 0$ is parallel to the optics table, and thus straightforward to locate experimentally. Using this value, a Glan-Thompson polarizer is placed in the path of each recording beam and the axis of polarization is rotated to $\psi_{x,i} + \pi/2$. A power meter is used to monitor the beam after the polarizer and the appropriate half-wave plate (HWP2 for beam 1, HWP5 for beam 2, HWP4 for beam 3) is rotated until the beam intensity is minimized. The three input halfwave plates are adjusted as well to the correct intensities.

The four solutions are summarized in Table 6.2. After alignment, the mirror is removed, and the microscope objective is placed at the sample plane and adjusted to accept the three interfering beams. Finally, the CCD camera is placed behind the objective and illuminated by all three recording beams. As discussed in Chapter 2, two fundamentally different types of interference patterns exist for $C_3^{(3)}$. Figure 6.13(a) illustrates an interference pattern for the configuration summarized in Table 6.2 for ${}^{+}C_3^{(3)}$, Shipley 1813. Also included in Fig. 6.13(b) are the expected intensity contours of the given interference pattern. The interference pattern has peaks of intensity located at the lattice points and a very high absolute contrast apparent from the low intensity between lattice points. Figure 6.13(c) is a plot of a single row of pixel values for the magnified interference pattern in Fig. 6.13(a). Ideally, the intensity along the dotted line in Fig. 6.13(a) is a sinusoid of the form $a(\cos(2\pi/Tx + 2\phi) + \cos(\pi/Tx + \phi))$. However, due to imperfect states of polarization and the finite extent of the pixels on the CCD array, there is a DC component in the experimental data. The pixel values fit extremely well to this curve with a DC component.

The second type of interference pattern is also verified using this method. The halfwave plates in the variable-ratio beamsplitters with output linear polarization direction

Table 6.2: Summary of Parameters for Hexagonal Interference Patterns with *p6m* Plane Group Symmetry for use in Defining Photoresists

Parameter	${}^{+}C_3^{(3)}$, Shipley 1813	${}^{-}C_3^{(3)}$, Shipley 1813	${}^{+}C_3^{(3)}$, Futurrex NR7-1500P	${}^{-}C_3^{(3)}$, Futurrex NR7-1500P
θ_{PR}	14.83°	14.83°	16.34°	16.34°
$\mathbf{k_1}/(n_{PR}k_o)$	$\begin{bmatrix}0.13 & 0.22 & 0.97\end{bmatrix}$	$\begin{bmatrix}0.13 & 0.22 & 0.97\end{bmatrix}$	$\begin{bmatrix}0.14 & 0.24 & 0.96\end{bmatrix}$	$\begin{bmatrix}0.14 & 0.24 & 0.96\end{bmatrix}$
$\mathbf{k_2}/(n_{PR}k_o)$	$\begin{bmatrix}-0.26 & 0 & 0.97\end{bmatrix}$	$\begin{bmatrix}-0.26 & 0 & 0.97\end{bmatrix}$	$\begin{bmatrix}-0.28 & 0 & 0.96\end{bmatrix}$	$\begin{bmatrix}-0.28 & 0 & 0.96\end{bmatrix}$
$\mathbf{k_3}/(n_{PR}k_o)$	$\begin{bmatrix}0.13 & -0.22 & 0.97\end{bmatrix}$	$\begin{bmatrix}0.13 & -0.22 & 0.97\end{bmatrix}$	$\begin{bmatrix}0.14 & -0.24 & 0.96\end{bmatrix}$	$\begin{bmatrix}0.14 & -0.24 & 0.96\end{bmatrix}$
E_2/E_1	-1.08	1	-1.09	1
E_3/E_1	1	1	1	1
V_{abs}	0.96	1	0.96	1
$V_3^{(3)}$	0.63	$-1/3$	0.62	$-1/3$
$\hat{\mathbf{e}}_\mathbf{1}$	$\begin{bmatrix}-0.99 & 0.04 & 0.12\end{bmatrix}$	$\begin{bmatrix}-0.87 & 0.5 & 0\end{bmatrix}$	$\begin{bmatrix}-0.99 & 0.05 & 0.13\end{bmatrix}$	$\begin{bmatrix}-0.87 & 0.5 & 0\end{bmatrix}$
$\hat{\mathbf{e}}_\mathbf{2}$	$\begin{bmatrix}0.97 & 0 & 0.26\end{bmatrix}$	$\begin{bmatrix}0 & -1 & 0\end{bmatrix}$	$\begin{bmatrix}0.96 & 0 & 0.28\end{bmatrix}$	$\begin{bmatrix}0 & -1 & 0\end{bmatrix}$
$\hat{\mathbf{e}}_\mathbf{3}$	$\begin{bmatrix}-0.99 & -0.04 & 0.12\end{bmatrix}$	$\begin{bmatrix}0.87 & 0.5 & 0\end{bmatrix}$	$\begin{bmatrix}-0.99 & -0.05 & 0.13\end{bmatrix}$	$\begin{bmatrix}0.87 & 0.5 & 0\end{bmatrix}$
$\psi_{z,1}$	28.66°	0°	28.23°	0°
$\psi_{z,2}$	90°	0°	90°	0°
$\psi_{z,3}$	151.34°	0°	151.76°	0°
$\psi_{x,1}$	−88.68°	−117.35°	−89.11°	−117.35°
$\psi_{x,2}$	90°	0°	90°	0°
$\psi_{x,3}$	−91.32°	117.35°	−90.89°	117.35°

control are adjusted accordingly. Figure 6.14(a) illustrates an interference pattern for the configuration summarized in Table 6.2 for ${}^{-}C_3^{(3)}$, Shipley 1813. Also included in Fig. 6.14(b) are the expected intensity contours of the given interference pattern. The interference pattern has nulls of intensity located at the lattice points and a very high absolute contrast apparent from the high level of intensity between lattice points. Figure 6.14(c) is a plot of a single row of pixel values for the magnified interference pattern in Fig. 6.14(a). Ideally, the intensity along the dotted line in Fig. 6.14(a) is a sinusoid of the form $-a(\cos(2\pi/Tx + 2\phi) + \cos(\pi/Tx + \phi))$. However, due to imperfect states of polarization and the finite extent of the pixels on the CCD array, there is a DC component in the experimental data. The pixel values fit extremely well to this curve with a DC component.

6.4.3 Alignment for Two-Dimensional Square Lattice

For a two-dimensional square lattice, four critical experimental configuration parameters are relevant. Beams 1 and 3 are adjusted to be parallel to the optics table by setting $x_{sp} = 0$. Again, a restriction is placed upon z_{BS}. This is done because a is a function of y_M, x_{BS}, and z_{BS}. Since this four-dimensional relationship is difficult to visualize, the polarization optics and beam steerer are placed as close as possible and the resulting value of z_{BS} is used for the design plots included here. Given a value of $z_{BS} = 7.62$ cm, the relationships between the remaining three critical experimental configuration parameters are illustrated in Figs. 6.15 and 6.16. Highlighted within each of these plots are areas of experimental feasibility for the specific configuration used in this research. Given these design constraints, a lattice constant of 1.5 λ or 545.7 nm is chosen. The values of the resulting critical experimental configuration parameters are as follows: $a/\lambda = 1.5$, $y_M = 16.51$ cm, $z_{sp} = 30.89$ cm, $x_{sp} = 0$ cm, $x_{BS} = 12.44$ cm, and $z_{BS} = 7.62$ cm. The multi-beam-interference configuration is adjusted to reflect this parameters.

The fine adjustment of the recording beams is facilitated by the use of an alignment card specifically designed and fabricated for the desired photonic crystal lattice. The alignment

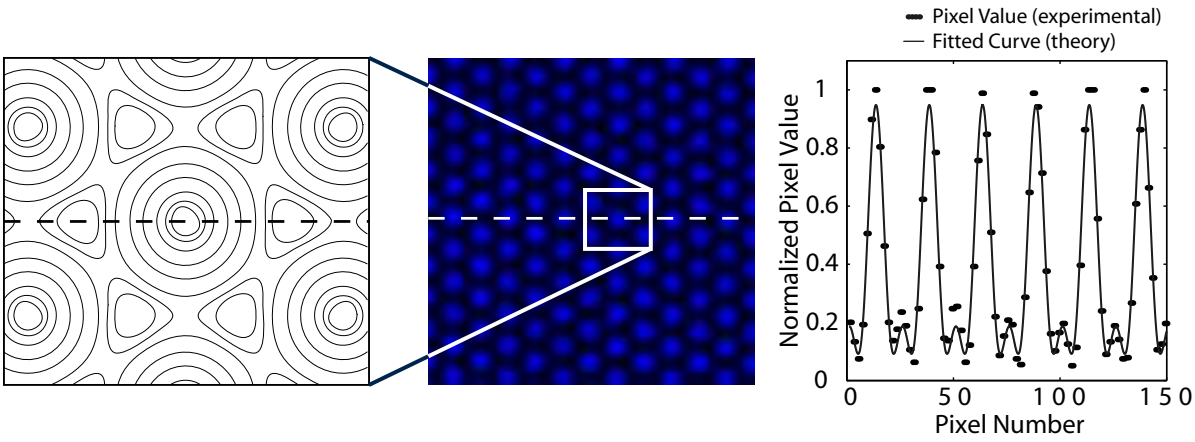

Figure 6.13: (a) Plot of calculated intensity contours. (b) Captured image of magnified hexagonal interference pattern ($C_3^{(3)}$, $V > 0$). (c) Plot of pixel values (dashed line) and fitted sinusoidal curve in the form $a(\cos(2\pi x/T + 2\phi) + \cos(\pi x/T + \phi)) + c$ where $a = 0.1904$, $T = 12.51$, $\phi = 2.855$, and $c = 0.377$ with an R-square value of 0.9433 and a RMSE of 6.65%. Note that saturated pixels in (b) are excluded in the curve fitting analysis in (c).

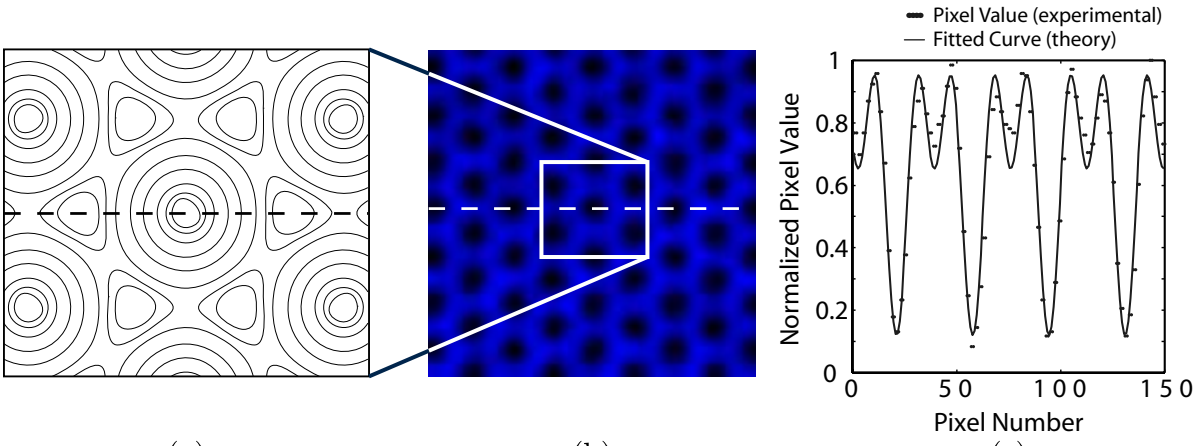

Figure 6.14: (a) Plot of calculated intensity contours. (b) Captured image of magnified hexagonal interference pattern ($C_3^{(3)}$, $V > 0$). (c) Plot of pixel values (dashed line) and fitted sinusoidal curve in the form $-a(\cos(2\pi x/T + 2\phi) + \cos(\pi x/T + \phi)) + c$ where $a = 0.2670$, $T = 18.33$, $\phi = 2.601$, and $c = 0.6534$ with an R-square value of 0.9418 and a RMSE of 6.651%. Note that saturated pixels in (b) are excluded in the curve fitting analysis in (c).

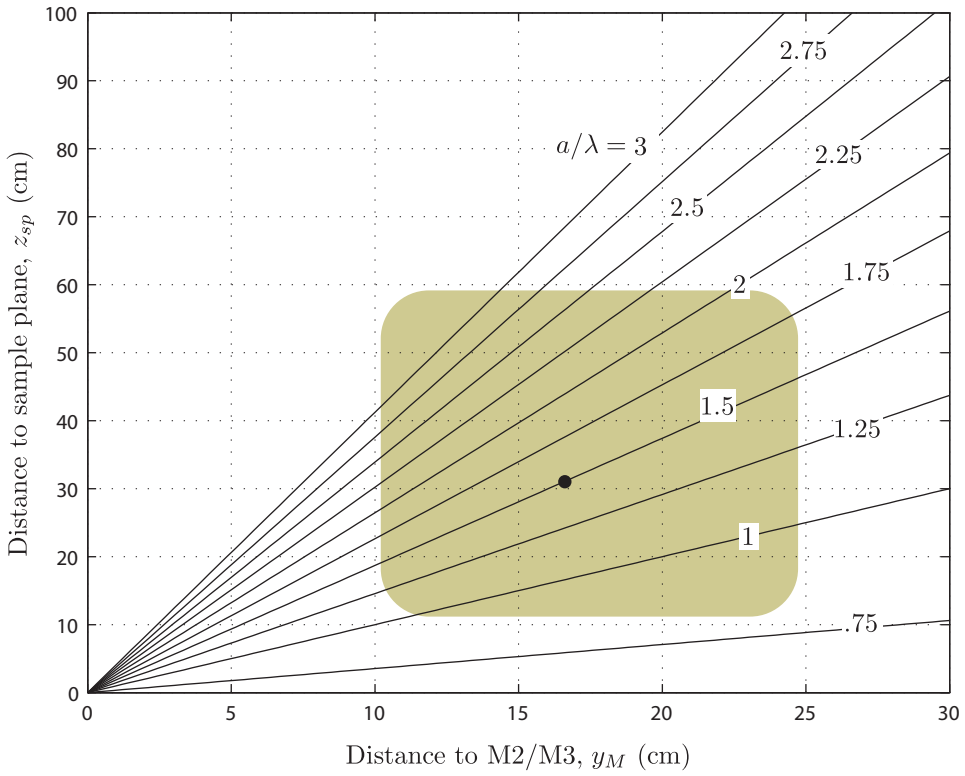

Figure 6.15: Design plot for aligning the recording beams needed to create a two-dimensional hexagonal interference pattern. The relationship between the critical experimental configuration parameters y_M, z_{sp}, and a is illustrated. Highlighted is the area of experimental feasibility. The design used in this research is marked with a dot on the plot.

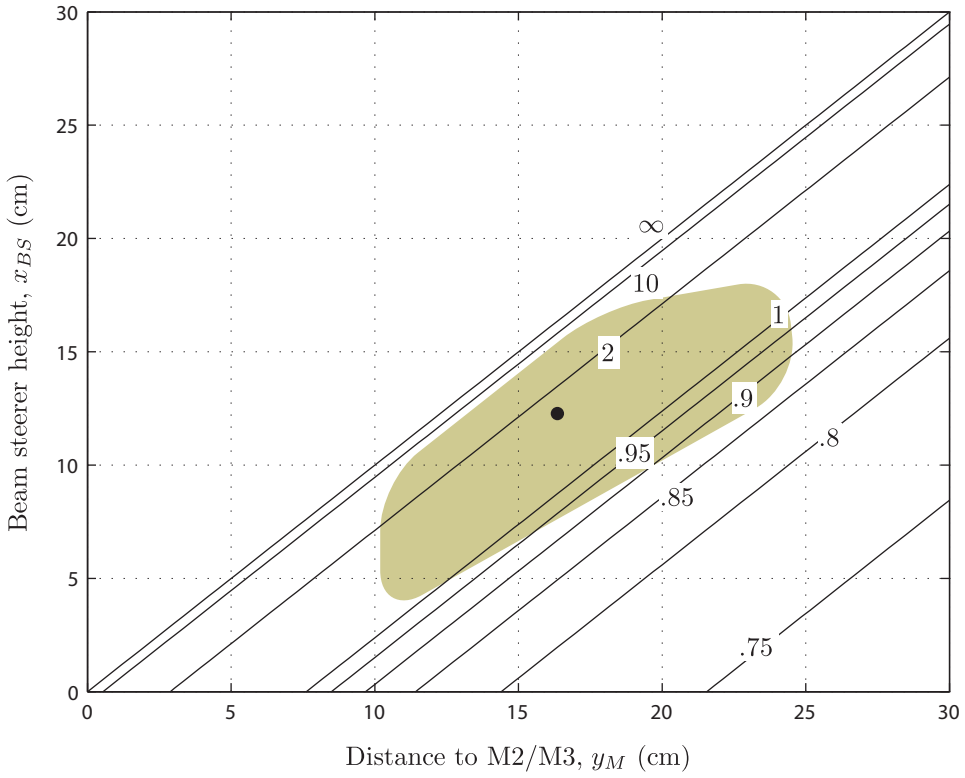

Figure 6.16: Design plot for aligning the recording beams needed to create a two-dimensional hexagonal interference pattern. The relationship between the critical experimental configuration parameters y_M, x_{BS}, and a is illustrated. Highlighted is the area of experimental feasibility. The design used in this research is marked with a dot on the plot.

Table 6.3: Critical Experimental Configuration and Alignment Parameters and Spherical Zenith Angle (θ_{air}) for Square Lattice

Parameter	Value
a/λ	1.5
y_M	16.51 cm
z_{sp}	30.89 cm
x_{sp}	0 cm
x_{BS}	12.44 cm
D	5.08 cm
z_{ac}	4.75 cm
θ_{air}	28.13°

card required for a square lattice (illustrated in Fig. 6.17) includes three holes (approximately the diameter of the laser beam) and an alignment mark (cross) creating a square. Given the diameter of the circumscribed circle of the square, D, and the distance from the alignment card and the mirror (sample plane), z_{ac}, the lattice constant, a, of the interference pattern is calculated as

$$a = \frac{\sqrt{2}\lambda}{2D}\sqrt{D^2 + 4z_{ac}^2}\,. \tag{6.9}$$

The fabrication and positioning of the alignment card is performed with the aid of Fig. 6.18. This plot illustrates the relationship between the distance separating the mirror (sample plane) and the alignment card (z_{ac}), the diameter of the circumcircle of the hexagon on the alignment card (D), and the lattice constant (a). In this research a diameter of the circumcircle of the hexagon on the alignment card of $D = 5.08$ cm was used resulting in a distance separating the mirror (sample plane) and the alignment card of $z_{ac} = 4.75$ cm. All configuration and alignment parameters are summarized in Table 6.3. After an initial alignment is performed by positioning the optics and opto-mechanics using the values in Table 6.1, a fine adjustment is performed by using the alignment card. A mirror is placed in the sample plane at the sample plane spot height x_{sp}. The alignment card is positioned at a distance of z_{ac} from the mirror and at the sample plane spot height x_{sp} and mirrors

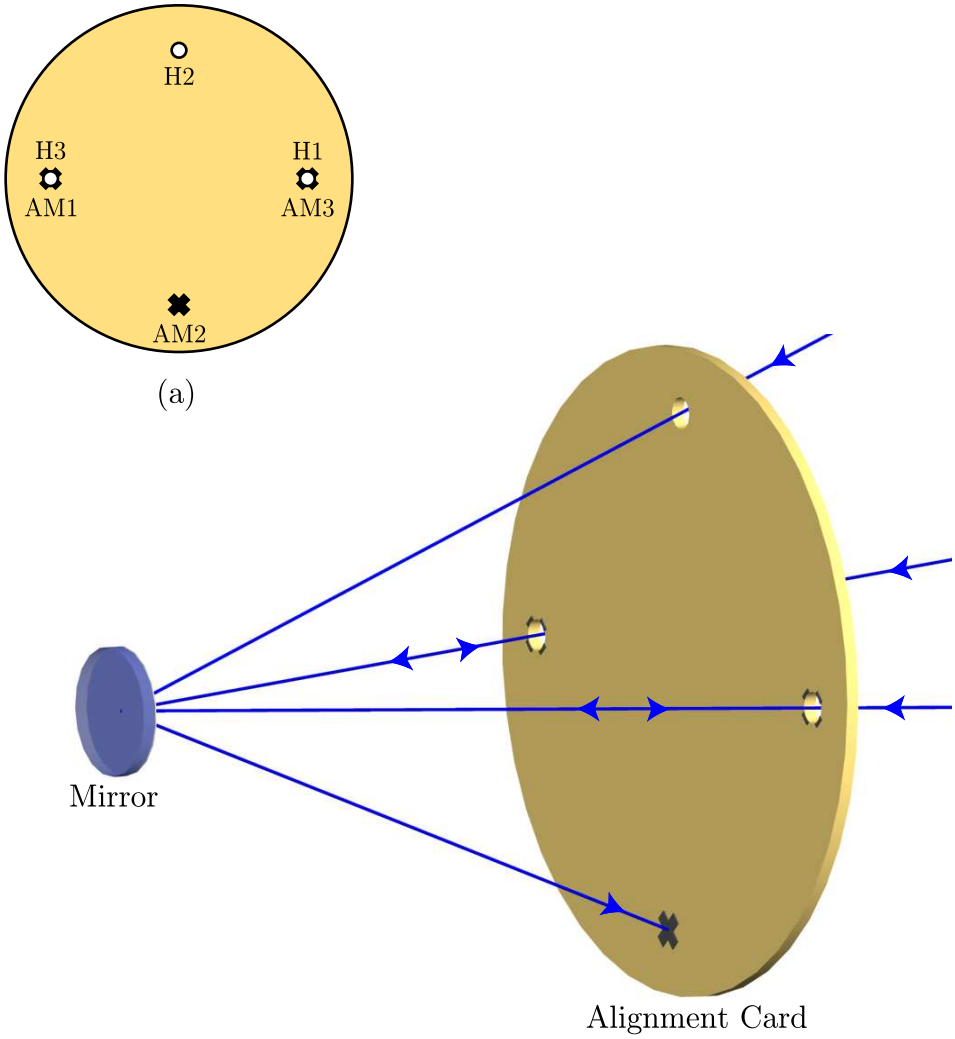

Figure 6.17: Alignment card used to facilitate fabrication of two-dimensional square lattice. The multi-beam-interference configuration is adjusted such that the three separate beams pass through holes H1, H2, and H3, reflect off the mirror and are projected onto alignment marks AM1, AM2, and AM3, respectively. This procedure aids in forming the three beams such that the projection of each recording wavevector on the sample plane is equal in magnitude and the projections of beams 1 and 3 are collinear of which the projection of beam 2 bisects the other two.

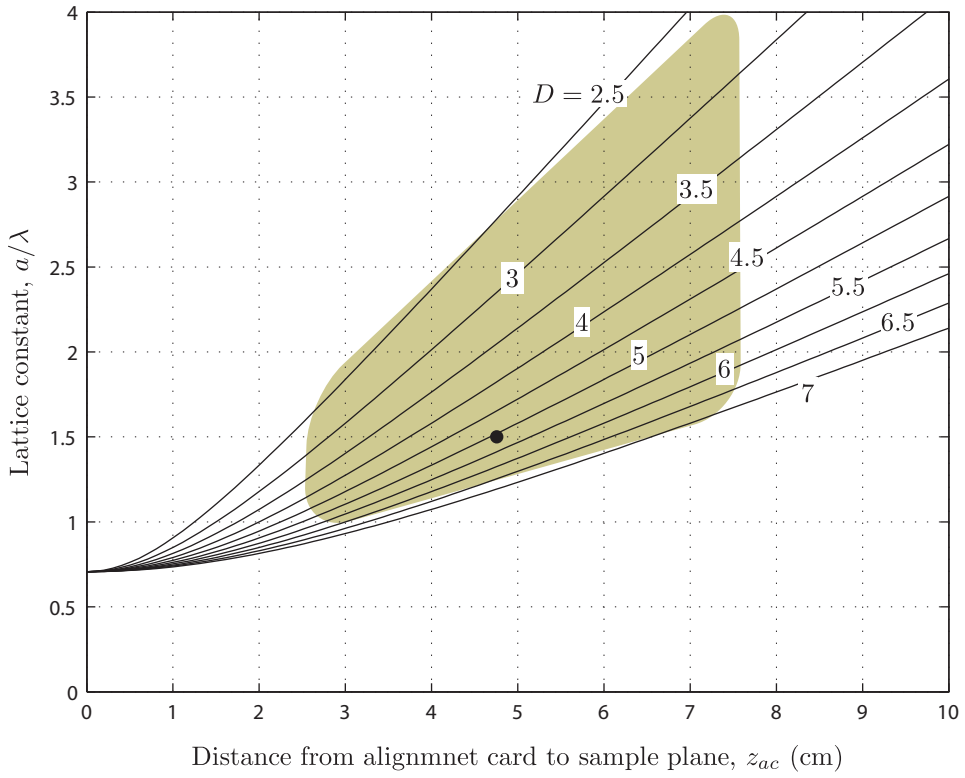

Figure 6.18: Design plot for aligning the recording beams needed to create a two-dimensional hexagonal interference pattern. The relationship between the critical experimental configuration parameters z_{ac}, D, and a is illustrated. Highlighted is the area of experimental feasibility. The design used in this research is marked with a dot on the plot.

M1, M3, and the beam steerer BS are adjusted such that each beam passes through the appropriate hole on the alignment card, reflects off the mirror in the sample plane, and projects on an opposite alignment mark or hole. This procedure guarantees two properties of the wavevectors needed to create a square lattice interference pattern with *p4m* plane group symmetry. First, the projection of each recording wavevector on the sample plane is equal in magnitude. Second, the projections of beams 1 and 3 are collinear of which the projection of beam 2 is orthogonal the other two.

In order to create an interference pattern with *p4m* plane group symmetry and high contrast, the polarizations and intensities of the recording beams are adjusted accordingly. Given the one type of interference pattern and the different indices of refraction of the two recording media (1.736 for the Shipley 1813 positive resist and 1.58 for Futurrex NR7-1500P negative resist), there are two different configurations of the polarizations and beam intensities. Similarly to the procedures discussed in Section 6.4.2, the two solutions are calculated and summarized in Table 6.4. After alignment, the mirror is removed and the microscope objective is placed at the sample plane and adjusted to accept the three interfering beams. Finally, the CCD camera is placed behind the objective and illuminated by all three recording beams. As discussed in Chapter 2, only one type of interference patterns exists for $C_3^{(2)}$. Figure 6.19(a) illustrates an interference pattern which satisfies $C_3^{(2)}$ and has been optimized. Also included in Fig. 6.19(b) are the expected intensity contours of the given interference pattern. Figure 6.19(c) is a plot of a single row of pixel values for the magnified interference pattern in Fig. 6.19(a). Ideally, the intensity along the dotted line in Fig. 6.19(a) is a sinusoid of the form $-a(\cos(2\pi/Tx + 2\phi) + \cos(\pi/Tx + \phi))$. However, due to imperfect states of polarization and the finite extent of the pixels on the CCD array, there is a DC component in the experimental data. The pixel values fit extremely well to this curve with a DC component.

Table 6.4: Summary of Parameters for Square Interference Patterns with *p4m* Plane Group Symmetry for Use in Defining Photoresists

Parameter	${}^{+}C_3^{(2)}$, Shipley 1813	${}^{+}C_3^{(2)}$, Futurrex NR7-1500P
θ_{PR}	15.75°	17.36°
$\mathbf{k_1}/(n_{PR}k_o)$	$\begin{bmatrix}0 & 0.27 & 0.96\end{bmatrix}$	$\begin{bmatrix}0 & 0.30 & 0.95\end{bmatrix}$
$\mathbf{k_2}/(n_{PR}k_o)$	$\begin{bmatrix}-0.27 & 0 & 0.96\end{bmatrix}$	$\begin{bmatrix}-0.30 & 0 & 0.95\end{bmatrix}$
$\mathbf{k_3}/(n_{PR}k_o)$	$\begin{bmatrix}0 & -0.27 & 0.96\end{bmatrix}$	$\begin{bmatrix}0 & -0.30 & 0.95\end{bmatrix}$
E_2/E_1	$\sqrt{2}$	$\sqrt{2}$
E_3/E_1	1	1
V_{abs}	1	1
$V_3^{(3)}$	0.5	0.5
$\hat{\mathbf{e}}_1$	$\begin{bmatrix}0.23 & -0.94 & 0.26\end{bmatrix}$	$\begin{bmatrix}0.96 & -0.26 & 0.08\end{bmatrix}$
$\hat{\mathbf{e}}_2$	$\begin{bmatrix}0.84 & -0.48 & 0.24\end{bmatrix}$	$\begin{bmatrix}0.84 & 0.48 & 0.26\end{bmatrix}$
$\hat{\mathbf{e}}_3$	$\begin{bmatrix}0.96 & 0.26 & 0.07\end{bmatrix}$	$\begin{bmatrix}0.22 & 0.93 & 0.29\end{bmatrix}$
$\psi_{z,1}$	103.27°	164.43°
$\psi_{z,2}$	61.25°	118.47°
$\psi_{z,3}$	15.46°	77.10°
$\psi_{x,1}$	13.27°	74.42°
$\psi_{x,2}$	61.25°	118.47°
$\psi_{x,3}$	105.46°	167.10°

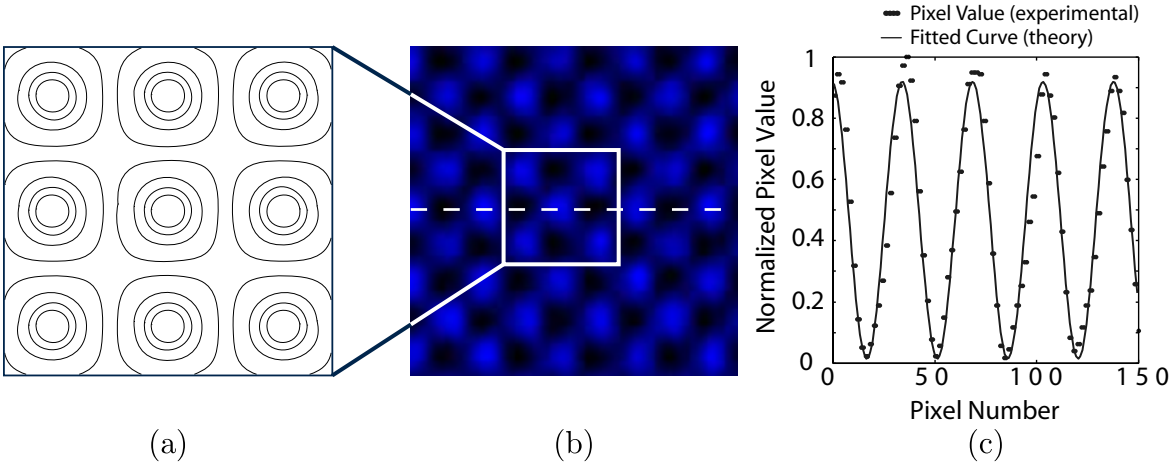

Figure 6.19: (a) Plot of calculated intensity contours. (b) Captured image of magnified square interference pattern (${}^{+}C_3^{(2)}$). (c) Plot of pixel values (dashed line) and fitted sinusoidal curve in the form $a\cos(2\pi x/T + \phi) + c$ where $a = 0.4532$, $T = 34.58$, $\phi = 0.00$, and $c = 0.4676$ with an R-square value of 0.9473 and a RMSE of 7.499%. Note that saturated pixels in (b) are excluded in the curve fitting analysis in (c).

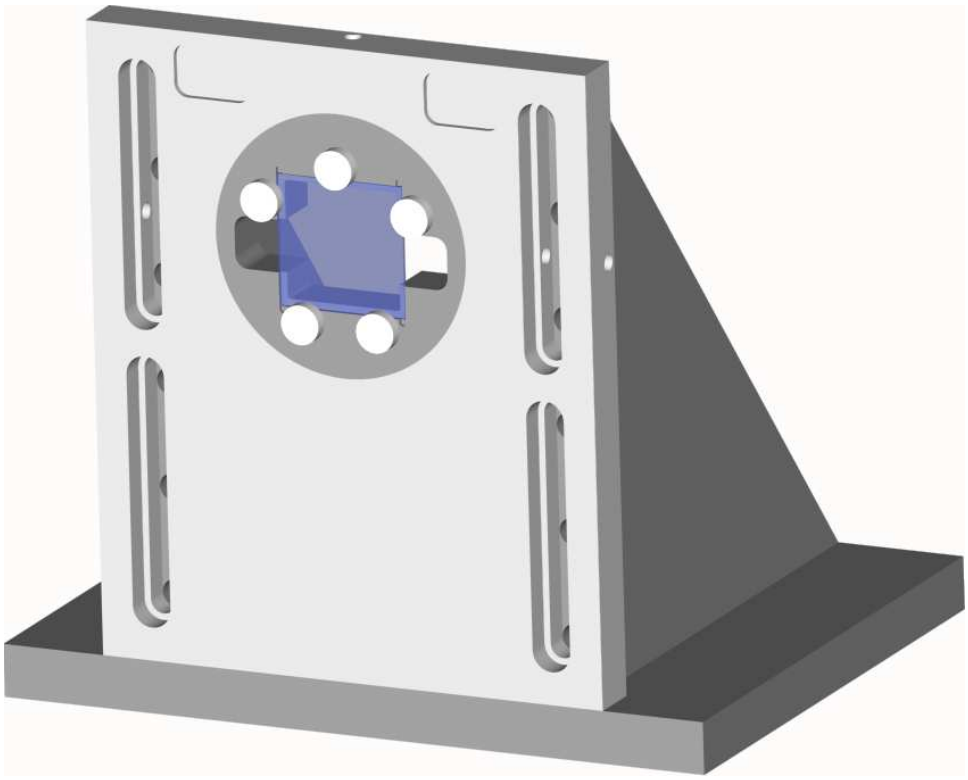

Figure 6.20: Custom sample mount used for alignment and exposure of multi-beam-interference experiments.

6.5 Fabrication

A custom sample mount (illustrated in Fig. 6.20) is constructed to aid in both alignment and fabrication. It includes height adjustment, substrate rotation and interchangeable sample chucks. These custom sample chucks for different substrate sizes are fabricated with assistance from the ECE machine shop. During alignment and fabrication, both the mirror and samples utilize the same type of substrate (3.175 cm $\times$ 3.175 cm $\times$ 1 mm, UV grade fused silica). Once the configuration is aligned properly using the procedures provided in the previous sections, the sample fixture and chuck are fixed in position. The mirror is then replaced by a sample substrate. This assures proper exposure conditions on the sample and minimizes repositioning of the optomechanics and the sample mount.

The sample is cleaned and prepared for exposure by

1. Ultrasonic Acetone bath for 1 min

2. Ultrasonic DI water bath for 1 min

3. DI rinse and N_2 blow dry

4. Dehydration bake in 110°C oven for 30 min

5. Spin on 1 μm of photoresist

   (a) Shipley 1813 - 500 rpm,100 rpm/s,5 sec; 5000 rpm,1000 rpm/s,45 sec

   (b) Futurrex NR7-1500p - 500 rpm,100 rpm/s,5 sec; 5000 rpm,1000 rpm/s,45 sec

6. Softbake

   (a) Shipley 1813 - 115°C hotplate for 4 min

   (b) Futurrex NR7-1500p - 150°C hotplate for 4 min

Steps 1-6 are performed in the cleanroom environment provided by the Microelectronic Research Center. Next, the sample is taken to room 260 in the MiRC where the multi-beam-interference configuration is located. Multiple exposures are performed on a single sample by adjusting the height of the sample mount between exposures. A range of exposure dosages are given. The sum of intensities of the three interfering beams is adjusted to 65 mW.

7. MBIL exposure is performed at exposure times of 0.02, 0.04, 0.06, 0.08, 0.1, 0.2, 0.5, 1, 2, and 4 sec on each sample

The sample is then taken back to the MiRC cleanroom for further processing.

8. Post-exposure bake

   (a) Shipley 1813 - none

   (b) Futurrex NR7-1500p - 100°C hotplate for 4 min

9. Development

(a) Shipley 1813 - Microposit 319 developer for 25 sec with agitation

(b) Futurrex NR7-1500p - RD6:water at 3:1 ratio for 90 sec with agitation

10. Descum in Vision RIE for 10 sec - 60mT, 400 W, O_2 at 50 sccm

11. Oxide etch in Vision RIE for 10 min @ 350 Å/min - 20 mT, 200 W, CHF_3 at 50 sccm, O_2 at 5 sccm

12. Sputter 150Å of Cu in Unifilm sputter

Following the development, etch and sputter steps, properly processed samples produce diffraction of ambient light from the surface visible to the naked eye. While this does not guarantee a successfully fabricated structure, it is a good indicator. To verify that the process results in the desired structures, the sample is coated in a thin layer of copper to facilitate imaging with the Zeiss SEM Ultra60.

The fabricated structures are verified at two stages of the fabrication process through Scanning Electron Microscopy (SEM): the defined photoresist following development and the completed structure following the etching process. Since the structures have nanoscale attributes (periods on the order of 100's of nm's, features on the order of 10's of nm's), a high resolution SEM is required. The Microelectronics Research Center cleanroom provides access to the Zeiss SEM Ultra60. The Zeiss SEM Ultra60 provides ultra high resolution imaging at low accelerating voltage, an extra large 6-axis motorized fully eucentric stage with fine stage control, and a high efficiency In-lens SE detector for high contrast surface imaging. The company specifies a resolution as low as 1 nm. This is more than adequate for this research.

This research also requires imaging of non-conductive structures. Better results are achieved when SEM's are used to image conductive samples such as silicon or metals. These conductive materials minimize charge buildup which negatively affects image quality. This is circumvented by coating non-conductive samples (such as structures made of

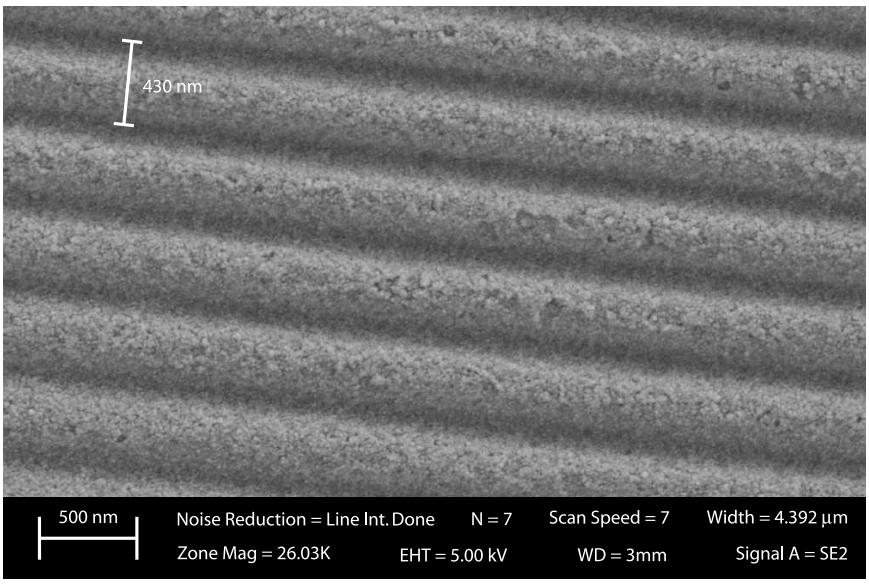

Figure 6.21: SEM image capture of a gold sputtered one-dimensional grating defined by two-beam-interference lithography. Grating is fabricated in Futurrex NR7-1500P photoresist on fused silica substrate.

photoresist or fused silica) in metal. This is performed by sputtering a thin layer of copper onto the sample.

A number of designs were fabricated using this procedure. First, a one-dimensional grating is fabricated using the Futurrex NR7-1500p negative resist. From Sec. 6.4.1, a high contrast interference pattern is produced using the multi-beam interference configuration, viewed using the real-time monitoring system, and the processing procedures were applied to the sample. In this case, an RIE etch is not performed (skipping steps 10 and 11) and only the defined photoresist is Cu sputtered. Strong diffraction of ambient light is observed with the naked eyed before and after the sample is coated with a 150 Å layer of copper. Figure 6.21 shows the resulting SEM image.

Next, multiple hexagonal lattices of rods with *p6m* plane group symmetry are fabricated with a lattice constant of 545.7 nm. From Sec. 6.4.2, a high contrast interference pattern is produced using the multi-beam interference configuration (using the parameters in Table 6.1 and Table 6.2 for ${}^{-}C_3^{(2)}$ Shipley 1813), and the processing procedures were applied to the sample. Strong diffraction of ambient light is observed with the naked eyed before and

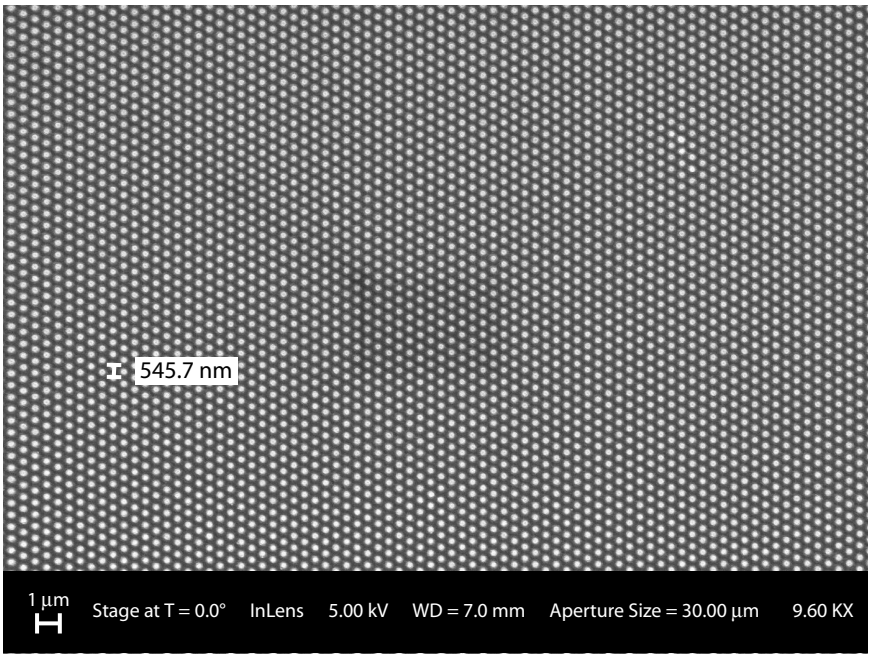

Figure 6.22: SEM of hexagonal photonic crystal of rods define by three-beam-interference lithography. Shipley 1813 positive photoresist is defined by a ${}^{-}C_3^{(3)}$ interference pattern, developed, and copper sputtered. a = 545.7 nm, $r \approx 0.25a \approx 136$ nm

after the sample is coated with a thin layer of copper. Figure 6.22 shows the SEM of a hexagonal photonic crystal of rods. Like the one-dimensional grating discussed previously, step 10 and 11 are skipped, and the developed photoresist is sputter with copper. Figure 6.23 shows the SEM of a identically fabricated sample at a different location. An important difference between Figs. 6.22 and 6.23 is the rod size within the lattice; $r \approx 0.25a \approx 136$ nm and $r \approx 0.115a \approx 63$ nm, respectively. This highlights not only the resolution capabilities of the resist but also the successful ability to fabricate identical lattices with different size rods (or holes) by adjusting the exposure dosage only. Figure 6.24 shows an SEM of a similarly fabricated sample, however, steps 10 and 11 are executed and the resulting fused silica structure is copper sputtered and imaged.

Next, multiple hexagonal lattices of holes with *p6m* plane group symmetry are fabricated with a lattice constant of 545.7 nm without changing the incidence of the recording beams on the sample plane. From Sec. 6.4.2, a high contrast interference pattern is produced using the multi-beam interference configuration (using the parameters in Table 6.1

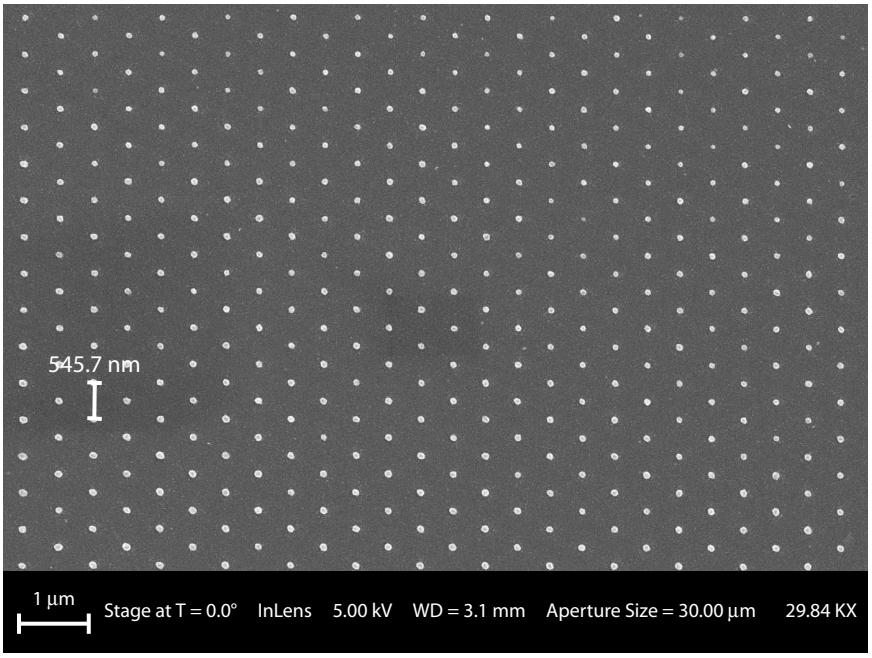

Figure 6.23: SEM of hexagonal photonic crystal of rods define by three-beam-interference lithography. Shipley 1813 positive photoresist is defined by a ${}^{-}C_3^{(3)}$ interference pattern, developed, and copper sputtered. a = 545.7 nm, $r \approx 0.115a \approx 63$ nm

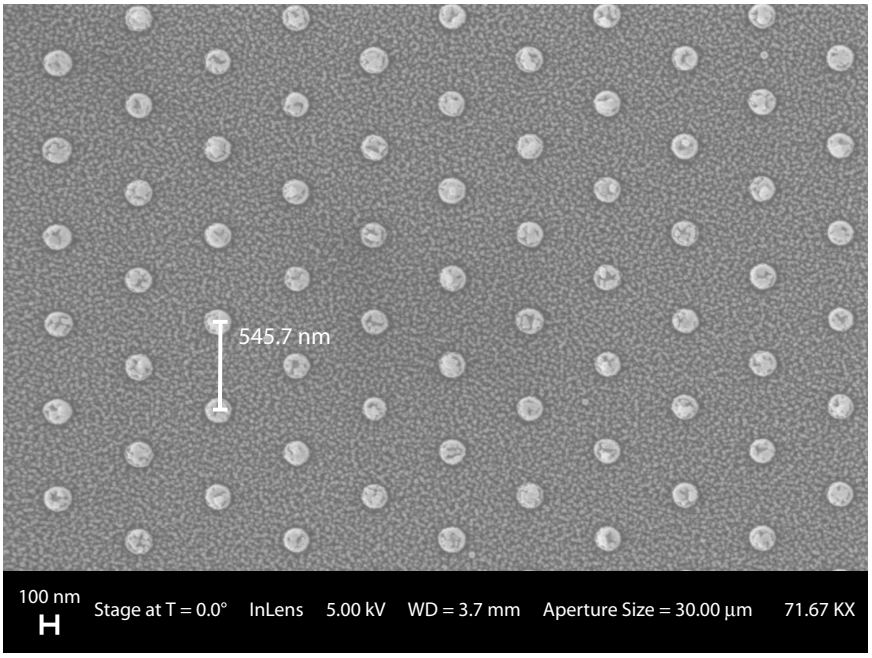

Figure 6.24: SEM of hexagonal photonic crystal of rods define by three-beam-interference lithography. Shipley 1813 positive photoresist is defined by a ${}^{-}C_3^{(3)}$ interference pattern, developed, substrate etched, resist removed and copper sputtered. a = 545.7 nm, $r \approx 0.16a \approx 87$ nm

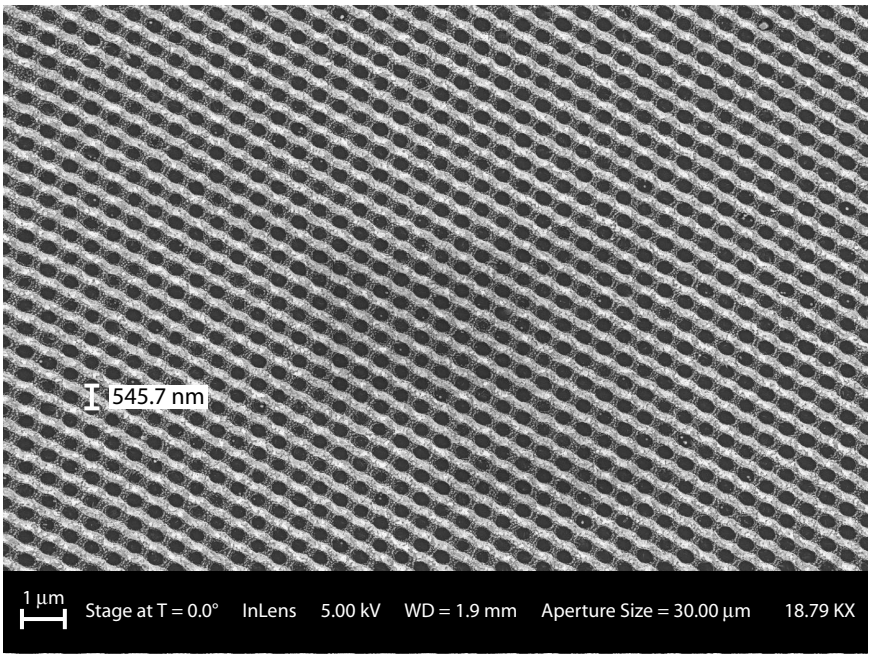

Figure 6.25: SEM of hexagonal photonic crystal of holes define by three-beam-interference lithography. Shipley 1813 positive photoresist is defined by a ${}^{+}C_3^{(3)}$ interference pattern, developed, and copper sputtered. a = 545.7 nm, $r \approx 0.30a \approx 166$ nm

and Table 6.2 for ${}^{+}C_3^{(3)}$ Shipley 1813), and the processing procedures were applied to the sample. Strong diffraction of ambient light is observed with the naked eyed before and after the sample is coated with a thin layer of copper. Figure 6.25 shows the SEM of a hexagonal photonic crystal of holes. Like the one-dimensional grating discussed previously, step 10 and 11 are skipped, and the developed photoresist is sputter with copper. Figure 6.26 shows an SEM of a similarly fabricated sample, however, steps 10 and 11 are executed and the resulting fused silica structure is copper sputtered and imaged.

Finally, a hexagonal lattice of rods with *p6m* plane group symmetry are fabricated with a lattice constant of 545.7 nm in a negative resist. From Sec. 6.4.2, a high contrast interference pattern is produced using the multi-beam interference configuration (using the parameters in Table 6.1 and Table 6.2 for ${}^{+}C_3^{(3)}$ Futurrex NR7-1500p), and the processing procedures were applied to the sample. Strong diffraction of ambient light is observed with the naked eyed before and after the sample is coated with a thin layer of copper. Figure 6.27 shows the SEM of a hexagonal photonic crystal of rods. Like the one-dimensional

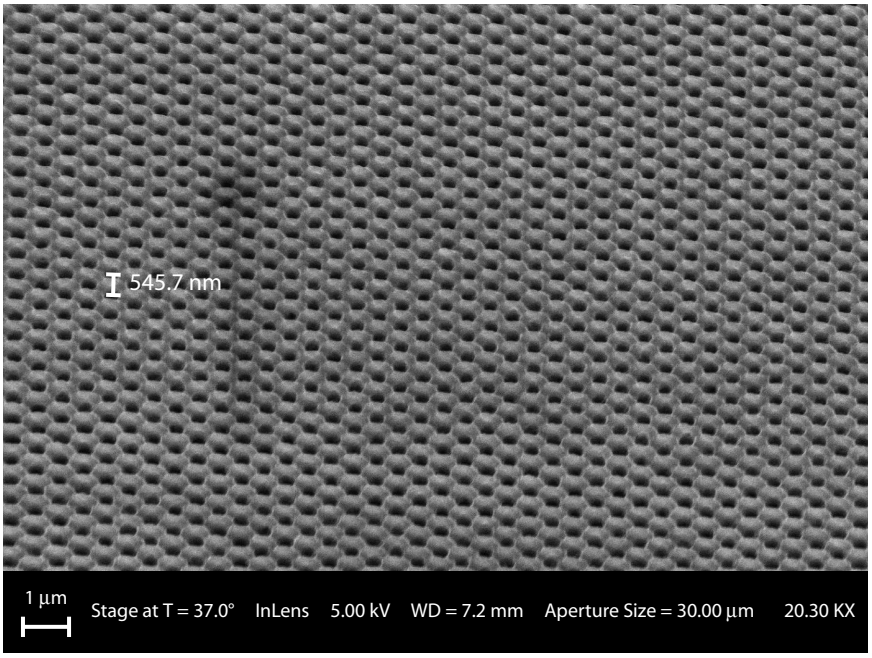

Figure 6.26: SEM of hexagonal photonic crystal of holes define by three-beam-interference lithography. Shipley 1813 positive photoresist is defined by a ${}^{+}C_3^{(3)}$ interference pattern, developed, substrate etched, resist removed and copper sputtered. a = 545.7 nm, $r \approx 0.31a \approx 171$ nm

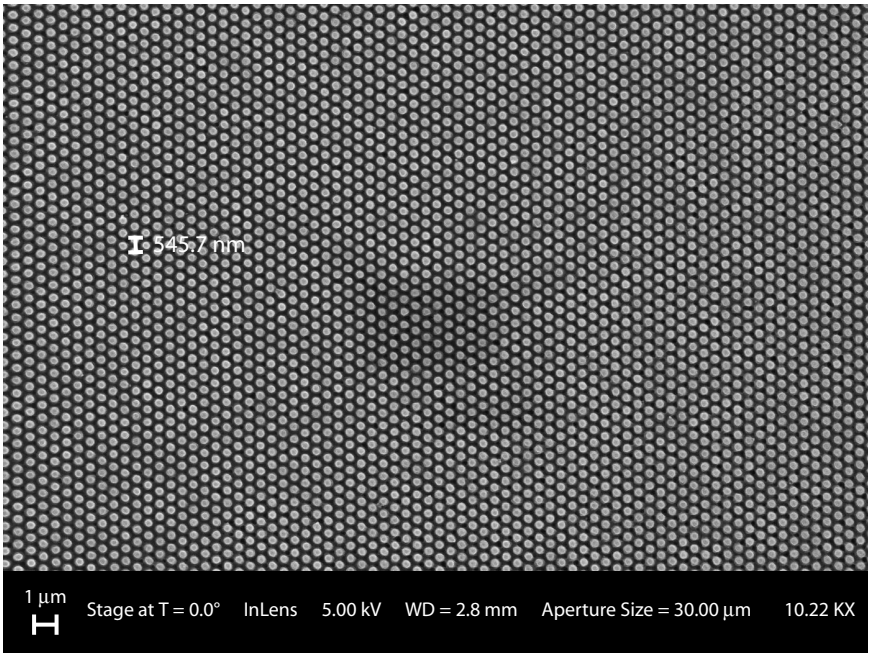

Figure 6.27: SEM of hexagonal photonic crystal of holes define by three-beam-interference lithography. Futurrex NR7-1500p negative photoresist is defined by a ${}^{+}C_3^{(3)}$ interference pattern, developed, and copper sputtered. a = 545.7 nm, $r \approx 0.34a \approx 188$ nm

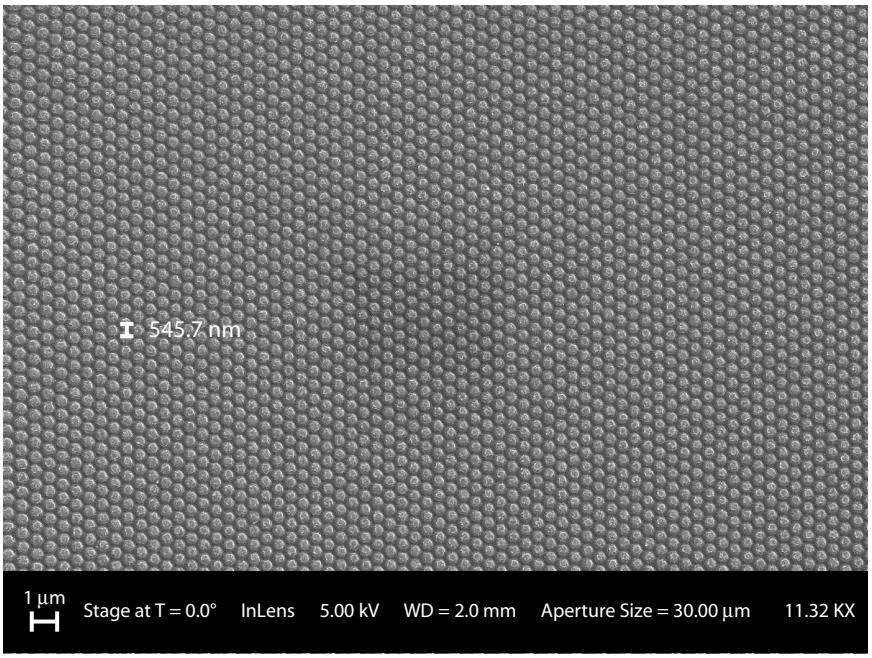

Figure 6.28: SEM of hexagonal photonic crystal of holes define by three-beam-interference lithography. Futurrex NR7-1500p negative photoresist is defined by a ${}^{+}C_3^{(3)}$ interference pattern, developed, and copper sputtered. a = 545.7 nm, $r \approx 0.40a \approx 219$ nm

grating discussed previously, step 10 and 11 are skipped, and the developed photoresist is sputtered with copper. Figure 6.28 shows an SEM of a similarly fabricated sample. In this case, a large area ($\approx$ 1 cm^2) photonic crystal is fabricated by expanding each of the recording beams. This is facilitated by positioning a diverging lens (fused silica, plano-concave lens with a -50 mm effective focal length) between mirror M2 and the sample for beam 1, beam steerer BS and the sample plane for beam 2, and mirror M3 and the sample plane for beam 3 such that each beam impinges a spot size with a diameter of $\approx$ 1.13 cm on the sample plane and adjusting the exposure time to 2 seconds. This results in a photonic crystal with approximately one billion rods.

6.6 Summary

In this chapter, a configuration for performing three-beam-interference lithography was described. Given the general configuration presented here, design plots illustrating the relationships between critical experimental configuration parameters were presented. Within

these plot, areas of experimental feasibility are highlighted to depict the extent of photonic crystals possible. A real-time monitoring system was also described. By incorporating a microscope objective and a CCD camera, interference patterns can be viewed in real time. This ability facilitates stability analysis and allows designers to verify theoretical concepts without having to perform a more time-consuming fabrication process. Multiple structures were fabricated and imaged using SEM. It is proven that MBIL can be successfully used in both positive and negative resists, both types of interference patterns can be used similarly to light- and dark-field masks, and large photonic crystals are possible. Also, the rod or hole diameter can be fine tuned by adjusted the exposure dosage. Finally, a brief description of silicon double inversion is presented as a starting point for the integration of three-dimensional structures defined by MBIL with silicon.

CHAPTER 7

CONCLUSIONS

The objective of this thesis has been to develop a multi-beam-interference-based methodology for the fabrication of photonic crystal structures. Using multi-beam-interference lithography (MBIL), photonic crystal structures are defined lithographically in photosensitive materials. The resulting structures are defined by the intensity contours of the interference patterns. This has been accomplished in the context of the interference of three and four monochromatic, linearly polarized plane waves including modeling of band structures and fabricating photonic crystal structures. In this chapter, the main accomplishments are summarized and potential areas of future research are discussed.

7.1 Summary of Results

7.1.1 Modeling Three-Beam Interference

An expression for the interference of N linearly polarized, monochromatic plane waves was developed as a basis for analysis of both three- and four-beam interference. This detailed derivation also clarified some discrepancies that have appeared in the literature. While the functional form of the expressions in the literature and those in this thesis are the same, the precise descriptions of the various terms has previously been ambiguous from source to source. The derivation in this thesis begins with a description of a single plane wave, and proceeds to two and multi-beam interference. In terms of three-beam interference, a procedure for calculating the necessary recording wavevectors to produce an interference pattern with a specified translational symmetry was given. This procedure clearly demonstrates that the choice in primitive basis vectors can have a profound effect on the resulting interference pattern. In fact, given a lattice periodicity, there exists an infinite set of recording

wavevectors that will produce an interference pattern with the given translational symmetry. A clarified, unified terminology for the description of conditions for lithographically useful interference patterns (high contrast and localized intensity extrema) as the *conditions for primitive-lattice-vector-direction equal contrasts* was introduced. Based on the present research, a symbolic designation $C_n^{(m)}$ is introduced to differentiate between the various *conditions for primitive-lattice-vector-direction equal contrasts*. The quantity n is the total number of interfering beams and m the number of nonzero interference coefficients (number of interfering-beam pairs). Consequently, the resulting non-zero interference coefficients V_{ij} are denoted by $V_n^{(m)}$ similarly. By satisfying one of these conditions during the optimization of absolute contrast, the plane wave parameters required to produce a lithographically useful interference pattern can be calculated. A detailed description of the optimization method used to maximize contrast (using the method of Lagrangian multipliers) is included in Appendix A. This Appendix describes two formulations of the Lagrangian functions used to perform the optimizations in this thesis. An enhanced formulation developed in this thesis was shown to improve significantly both processing time and numerical stability. Within the scope of three-beam interference, it was found that two *conditions for primitive-lattice-vector-direction equal contrasts* exist. Each results in interference patterns with different intensity extrema locations which, in turn, have a direct impact on the plane group symmetry of the interference pattern. Within the scope of the *conditions for primitive-lattice-vector-direction equal contrasts*, two fundamentally different interference patterns result. These types of interference patterns are determined by the sign of the interference coefficient, $V_n^{(m)}$. The sign determines whether an intensity maxima ($V_n^{(m)} > 0$) or minima ($V_n^{(m)} < 0$) is located at the $\mathbf{r} = 0$ lattice point. Additionally, the subordinate conditions for unity absolute contrast for each condition are specified. Within the subordinate conditions for unity absolute contrast, it was found that for ${}^{+}C_3^{(3)}$ interference patterns, this condition cannot always be satisfied. In fact, it can only be satisfied if

all three polarizations are collinear which equates to the three recording wavevectors being coplanar. Unfortunately, this arrangement is experimentally impractical in most cases. However, for the ${}^{-}C_3^{(3)}$ and $C_3^{(2)}$ interference patterns, the subordinate conditions for unity absolute contrast can always be satisfied given an arbitrary configuration of the recording wavevectors. The totality of constraints on the plane wave parameters to produce the five of seventeen plane groups possible with three-beam interference was also given.

7.1.2 Modeling Four-Beam Interference

As in the three-beam case, a procedure for calculating the necessary recording wavevectors to produce an interference pattern with a specified translational symmetry was given. Again, a clarified, unified terminology for the description of lithographically useful interference patterns as the *conditions for primitive-lattice-vector-direction equal contrasts* was introduced. By satisfying one of these conditions during the optimization of absolute contrast, the plane wave parameters required to produce a lithographically useful interference pattern can be calculated. Within the scope of four-beam interference, it was found that four *conditions for primitive-lattice-vector-direction equal contrasts* exist. Additionally, the subordinate conditions for unity absolute contrast for each condition are specified. Unlike the two-dimensional case, none of these subordinate conditions can always be satisfied; however, for the lattices treated here, a few are satisfied. Specifically, these are the cubic lattice defined by a ${}^{-}C_4^{(6)}$ interference pattern, the body-centered cubic lattice defined by a ${}^{-}C_4^{(6)}$ interference pattern, and a face-centered cubic defined by a ${}^{+}C_4^{(5)}$ interference pattern. For each condition, three different lattices are analyzed: the simple cubic, the face-centered cubic, and the body-centered cubic. For each lattice and each condition, an example is given, contrast is optimized, and the resulting plane wave parameters are calculated. For the simple cubic lattice, the optimized absolute contrast ranges from 0.5 when satisfying ${}^{+}C_4^{(6)}$ to unity absolute contrast when satisfying ${}^{-}C_4^{(6)}$. For the face-centered cubic lattice, the optimized absolute contrast ranges from 0.2599 when satisfying ${}^{-}C_4^{(6)}$ to unity absolute

contrast when satisfying ${}^{+}C_4^{(5)}$. For the body-centered cubic lattice, the optimized absolute contrast ranges from 0.5 when satisfying ${}^{+}C_4^{(6)}$ to unity absolute contrast when satisfying ${}^{-}C_4^{(6)}$.

7.1.3 Theoretical Performance of Two-Dimensional Photonic Crystal Structures

The method used to calculate the band structures within this thesis is introduced and explained. The modeling in this thesis utilized the MIT Photonic Bands software package to perform these calculations. The convention for TE and TM polarizations in two-dimensions is given in order to be consistent with the majority of literature and to clarify other polarization notations that appear in the literature. Two different two-dimensional lattices are analyzed: the square lattice and the hexagonal lattice. These lattices are modeled as circular holes/rods or are defined by the intensity contours of a three-beam-interference pattern. Using the design parameters of the normalized radius or the normalized intensity contour value, band gap maps are calculated and presented. These band gap maps are produced by calculating the band structures of lattices using a range of normalized radii or normalized intensity contours. Frequency ranges are highlighted within these ranges to illustrate when lattices exhibit TE, TM, or complete band gaps.

There is no significant reduction in the size of the TE band gaps of lattices of circular holes or rods when compared to similar structures fabricated via MBIL. Overall, there is no more than a 5% reduction in band gap size. In fact, the band gap of a square lattice of rods defined via multi-beam interference is 320% larger (from 3.86% to 16.22%) compared to the band gap of the square lattice of circular rods. There is, however, a significant reduction in the size of the TM band gap of a MBIL-defined square lattice of holes (39.61%) compared to the square lattice circular holes (5.77%). A square lattice interference pattern with *p4m* symmetry cannot replicate the larger radii that are required for the larger band gaps. There is a significant improvement (31% larger) with an MBIL-defined hexagonal lattice of holes (30.62%) compared to the hexagonal lattice of circular holes (23.37%).

Complete band gaps were also found for both lattices of circular holes and those defined by multi-beam interference for both the square and hexagonal lattices. The square lattice of holes defined by multi-beam interference was 18% larger (from 4.80% to 5.66%) while the hexagonal lattice of holes defined by multi-beam interference was 1% smaller (from 19.55% to 19.31%). Interestingly, while no complete band gap exists for a square lattice of circular rods, a band gap of 5.66% exists when this lattice is defined by multi-beam interference.

It has been noted that the MBIL-defined structures more closely resemble the circular structures at relatively small values of normalized intensity. This is because the intensity contours approach the circular case as I_{nrm} approaches 0. There are four specific cases when the lattices with the maximum band gap are made up of circular holes or rods with relatively small normalized radii. The corresponding MBIL-defined lattices exhibit nearly identical band gap sizes, area fill factors, and normalized mid gap frequencies. This occurs for the square lattice of rods (TM), hexagonal lattice of rods (TE and TM), and the hexagonal lattice of holes (TE).

7.1.4 Theoretical Performance of Three-Dimensional Photonic Crystal Structures

The band structures of three-dimensional photonic crystal structures were calculated in a similar manner as was used to calculate the band structures of the two-dimensional photonic crystal structures. Three different lattices were analyzed: the simple cubic, the face-centered cubic, and the body-centered cubic. Unlike the two-dimensional cases, there are relatively few structures that can produce a complete band gap and even fewer that are directly experimentally feasible. For this reason, band gap maps for each lattice are modeled as spherical masses/vacancies (6 band gap maps) and those defined by multi-beam interference satisfying each of the *conditions for primitive-lattice-vector-direction equal contrasts* (24 band gap maps). This amounts to the calculation of 30 band gaps maps, where the 24 band gap maps originate from the three lattices, the four different conditions ($C_n^{(m)}$), and

the two different types of interference patterns within each condition ($^{\pm}C_n^{(m)}$). Only five combinations produced a band gap: the simple cubic lattice of spherical vacancies, the simple cubic lattice of masses defined by a $C_4^{(3)}$ interference pattern, the face-centered cubic lattice of spherical vacancies, the face-centered cubic lattice of masses defined by a $C_4^{(3)}$ interference pattern, and the body-centered cubic lattice of spherical vacancies. Unlike the two-dimensional cases presented in this thesis, none of the MBIL-defined structures that exhibit the maximum band gap size resemble those lattices composed of spherical masses or vacancies that exhibit the maximum band gap size. While a body-centered cubic lattice of spherical vacancies can posses a band gap (albeit a small one of 1.56%), the corresponding MBIL-defined structures do not possess a band gap. The fact that the MBIL-defined cubic lattice defined by a $C_4^{(3)}$ interference pattern has the same group symmetry as the cubic lattice of spherical vacancies and the lattice of spherical vacancies possesses a band gap (7.29%), it is expected that the corresponding MBIL-defined structure will possess a band gap as well. Interestingly, an increase of $\sim 73\%$ in band gap size from 7.29% to 12.6% was found.

7.1.5 Fabrication of Photonic Crystals Defined by Multi-Beam-Interference Lithography

The fabrication apparatus and procedures used to fabricate two-dimensional photonic crystals via three-beam interference was presented. The three-beam-interference configuration was designed and constructed with a focus on phase front quality, reduction of unwanted reflections, stability, and design versatility. This was accomplished, in part, through a number of custom fabricated opto-mechanics, sample mount, and sample chucks. The operation of the polarization optics required for complete control of the polarization and intensity of each interfering beam is analyzed. By integrating the appropriate number of variable-ratio beamslitters with output linear polarization control, a single linearly polarized laser beam

can be split multiple times while maintaining individual control over the plane wave properties of each beam. A real-time monitoring capability was integrated within the multi-beam-interference configuration, which enabled stability analysis and verification of theoretical concepts without fabrication. This is accomplished by placing an objective at the sample plane such that the interfering beams enter at the front lens assembly. A digital CCD camera is placed after the mounting threads some distance away such that the CCD array is illuminated by all three recording beams. Specific alignment procedures for the one-dimensional grating, two-dimensional square lattice, and two-dimensional hexagonal lattice are presented. These procedures include design plots that illustrate the relationships between critical experimental configuration parameters to aid in the rough alignment of the optical components. Alignment cards, specific to the lattices, are then used for fine alignment of the recording beams. These are used in conjunction with a mirror placed in the sample plane at the sample spot. The correct alignment is verified when reflected beams are projected onto the corresponding alignment marks. After beam alignment, the intensities and polarizations of each beam are adjusted to correspond to the optimized plane wave parameters given by the contrast maximization condition. For the square and hexagonal lattices with lattice constants of $a = 1.5\lambda$, all experimental parameters are given for multiple process conditions. These process conditions include both positive (Shipley 1813) and negative (Futurrex NR-7 1500p) resists and, when applicable, both fundamental types of interference patterns ($V_n^{(m)} > 0$ and $V_n^{(m)} < 0$). A number of hexagonal lattices were fabricated. The required processing steps were presented for both negative and positive tone photoresists. Resulting structures included copper sputtered photoresist and copper sputtered RIE etched fused silica. Hexagonal lattices fabricated using a positive resist (Shipley 1813) have rods and holes ranging in radius from 63 nm to 171 nm. Additionally a large area photonic crystal was defined using a negative resist (Futurrex NR-7 1500p) with an estimated area of ≈ 1 cm^2 corresponding to 1×10^9 lattice points.

7.2 Future Research

In order to realize the potential of multi-beam-interference lithography as a method for fabricating photonic crystal structures, further research is required. Several potential avenues of research are highlighted in the following sections.

7.2.1 Photo Mask

Research to date has not focused on methodologies for the large-scale, cost-effective integration of the PC-based devices into manufacturable dense integrated photonic circuits and systems (DIPCS). Photonic crystal technology has the potential to provide smaller, faster, less expensive, and higher-reliability devices. Additionally the processing required to fabricate these devices will be more reproducible with single substrate, monolithic fabrication. While multi-beam-interference lithography (MBIL) represents a promising methodology for the fabrication of PC structures, it lacks in the ability to produce PC-based integrated photonic circuits. *The emphasis of future research should be to develop a methodology for the fabrication and integration of a multiplicity of photonic crystal devices and structures, in parallel, across an entire wafer based on a photo-mask implementation of multi-beam-interference lithography*. The present research targeted the needed description of MBIL as an enabling initial step. By utilizing diffractive elements, a photo-mask would be able to combine both MBIL and conventional lithography techniques into a single fabrication technology while taking advantage of the inherent positive attributes of both.

This new approach for fabricating photonic crystal structures and devices would be based on a unique interferometric photo-mask that produces customized beams at various locations across a wafer to expose and define the desired two- and three-dimensional interference patterns [99–101]. The new photo-mask would thus implement multi-beam-interference lithography without the necessity of painstakingly aligning and maintaining several laser beams while retaining the positive aspects and process options inherent with MBIL. In this new methodology, a simple single collimated laser beam would generate

the needed beams in a single step. In previously published research, only isolated individual photonic crystal structures were produced via MBIL. These include microring resonators [12–15, 102], Mach-Zehnder interferometers [103], wavelength-division multiplexing [23], waveguides [10, 11], delay lines [104], filters [15–17], waveguide couplers [18–21], directional couplers [22], antennas [24], switches [25], and sensors [26]. These individual devices can provide the functions needed in many optical-based circuits and systems previously provided by the hybrid integration of bulk optical components. By integrating these PC devices on a single wafer, the cost and size of these optical-based circuits can be drastically decreased. The physical configuration of such elementary devices and how they could possibly be designed using photonic crystal technology is illustrated in Fig. 7.1. However, there has been little effort to integrate multiple devices together, such as those in Fig. 7.1 to make a practical PC circuit or system.

The future research described here would extend previous work by introducing a photo-mask that produces a multiplicity of PC structures and devices over a large wafer-scale size area. A schematic of such a photo-mask is shown in Fig. 7.2. The photo-mask, as illustrated, incorporates both MBIL and conventional lithography by utilizing integrated diffractive optics in the top layer. Each individual diffractive optic corresponds to a customized beam used to perform MBIL. Using a commercial photopolymer such as InPhase Technology's Tapestry media, multiple diffractive elements can be multiplexed at a single location to produce the required recording beams. Retardation and absorption layers can be incorporated to control the polarization and intensity of each recording beam. Two or more diffracted beams travel through the propagation layer of the mask and the resulting interference pattern is projected onto the photosensitive material. A chrome (or similarly opaque material) layer further defines the intensity pattern by extent and, if needed, individual components. The components introduced by the photo-mask in Fig. 7.2 represents the DIPCS of an optical arbitration network used in a dense wavelength division multiplexed-based (DWDM-based) nanophotonic interconnect network for a high-performance many-core

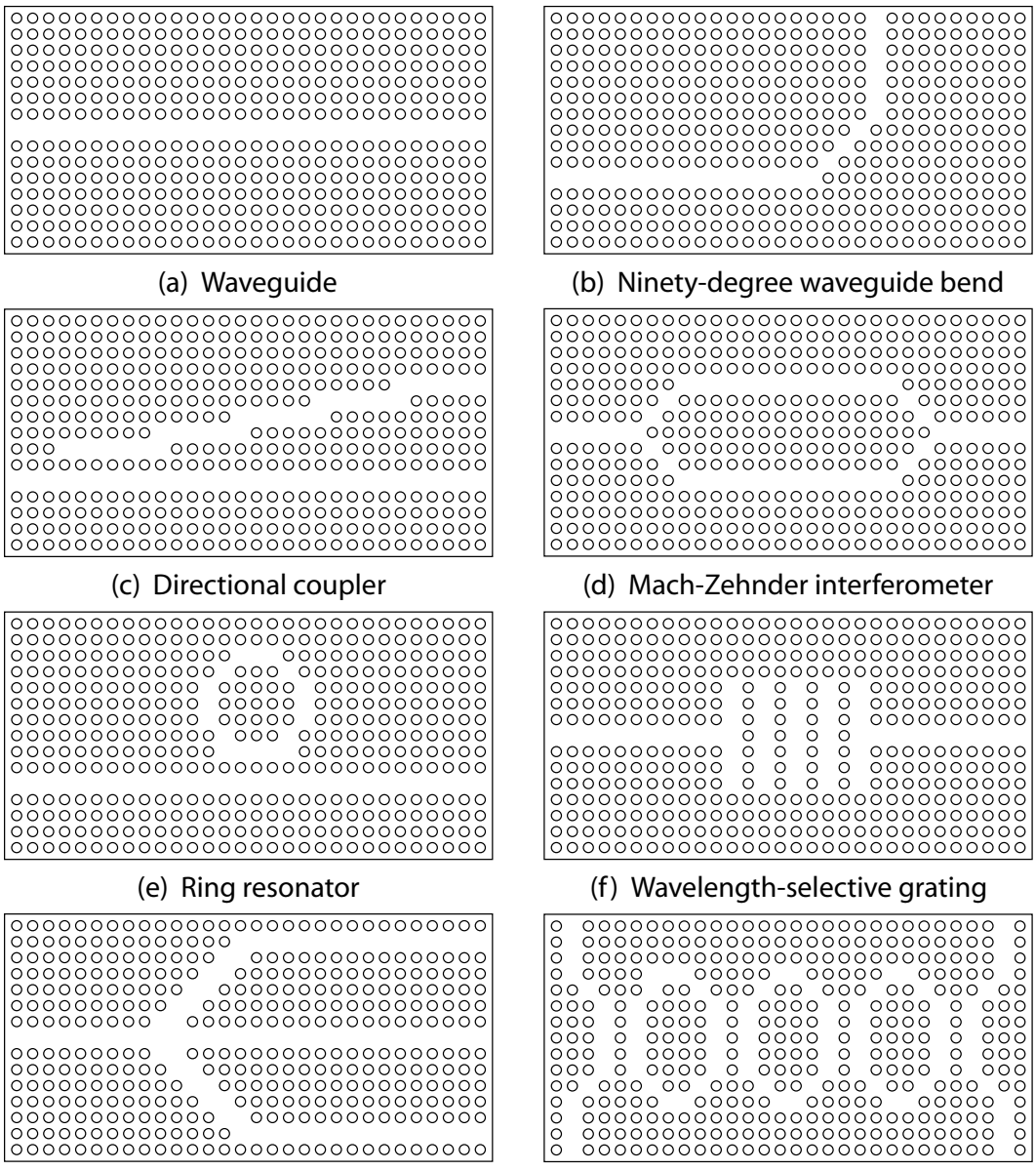

Figure 7.1: Layout configurations of photonic crystal devices

processor [105]. This particular DIPCS consists of many micro-ring resonators. Larger DIPCS can be realized with this design by incorporating more sets of diffractive elements and chrome mask areas within the same mask. Other DIPCS that could be potentially realized using photonic crystal technology and fabricated using a photo-mask include an optical network with interleaved waveband switching modulation [106], platform for wavelength-hopping time-spreading optical code division multiple access (CDMA) network [107], four-node 102-Gb/s fast frequency-hopping time-spreading optical CDMA network [108], and an all optical CDMA code drop unit for transparent ring networks [109]. As the spatial bandwidth of the diffractive layer is used, diffractive elements can be properly designed to overlap each other if needed to produce the desired recording beams. The dynamic range of most candidate recording materials is easily sufficient to accommodate the multiplexed gratings. Less complex designs would incorporate fewer and larger diffractive elements to illuminate larger areas of photosensitive material. Many more (or more complex) chrome mask areas could be illuminated by just these few diffractive elements.

The process flow of such a photo-mask needs to be carefully considered. As the pairing of light- and dark-field masks to positive- and negative-tone resists has a large impact on the process parameters, so does the design of the photo-mask and the photosensitive material. Given the design in Fig. 7.2, the bottom chrome mask layer can be considered a light-field mask (meaning that the individual components are defined by areas of low intensity). Given the discussion of the impact of the sign of the interference coefficient of the resulting interference pattern, four different process conditions need to be considered. These are defined by the type of interference pattern produced by the diffractive elements and the tone of the photoresist. Figure 7.3 summarizes the four process conditions by illustrating a waveguide introduced by the chrome mask to a two-dimensional interference pattern with *p6m* plane group symmetry (hexagonal lattice). Given this simple example, the process shown in Fig. 7.3(a), based on a positive photoresist coupled with a photo-mask capable of producing an interference pattern with a positive interference coefficient, is applicable to

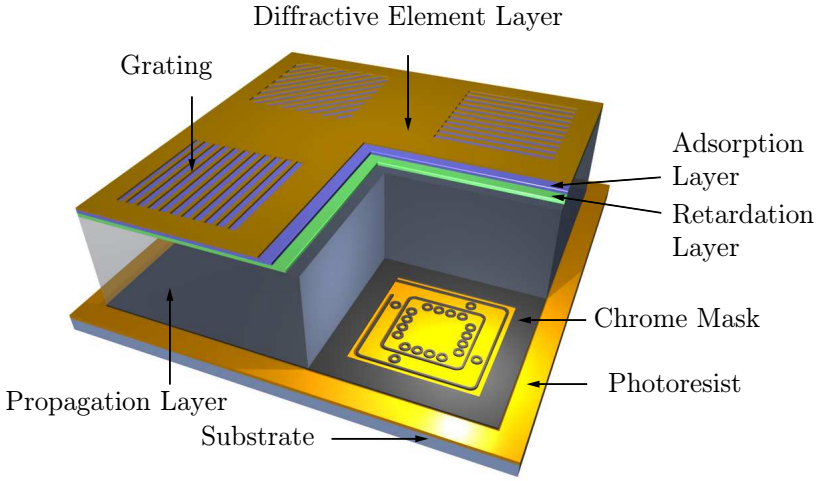

MBIL-based photo-mask

(a)

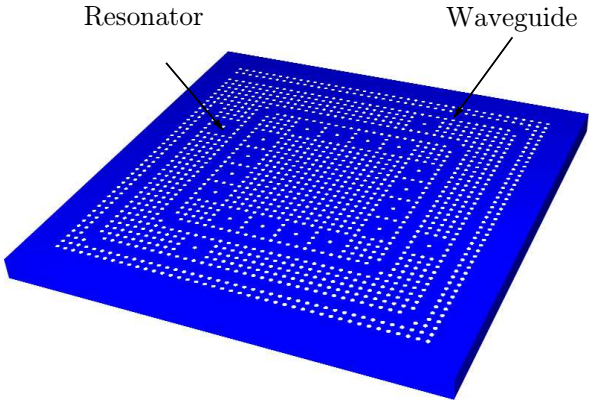

Optical network structure fabricated via MBIL-based photo-mask

(b)

Figure 7.2: (a) General structure of the MBIL-based photo-mask. Diffractive, retardation, and absorption layers control the recording beams (b) Resulting optical arbitration network structure used in a DWDM-based nanophotonic interconnect network for a high-performance many-core processor [105].

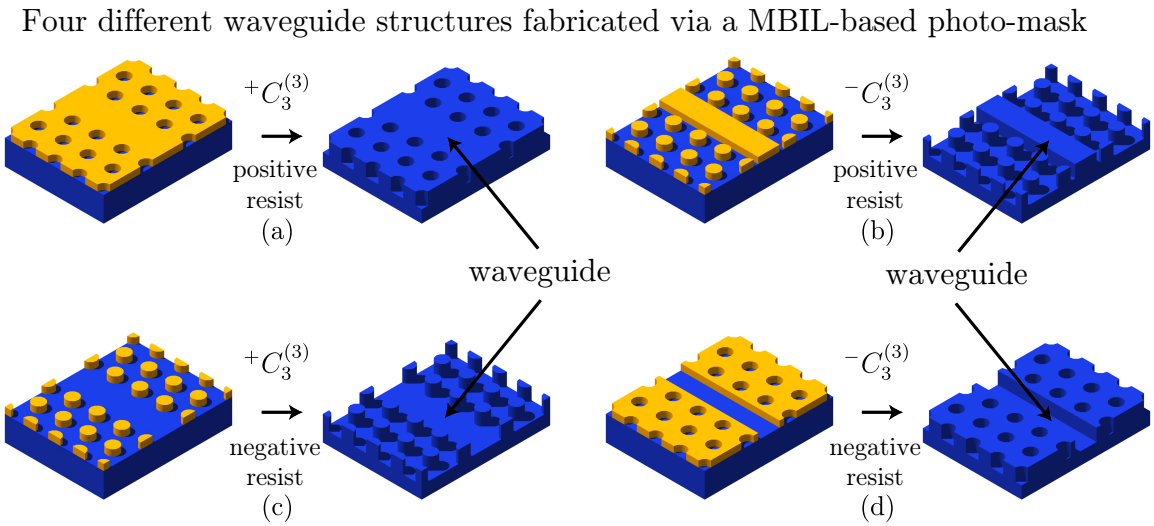

Figure 7.3: Four different process combinations of photoresist and type of interference pattern for use with photo-mask methodology for defining a waveguide in a hexagonal lattice. Each subfigure depicts the defined photoresist and resulting structure after development and etching into substrate. (a) Positive-tone photoresist exposed to a hexagonal inference pattern with a positive interference coefficient ($^{+}C_3^{(3)}$) (b) Positive-tone/negative interference coefficient ($^{-}C_3^{(3)}$) (c) Negative-tone/positive interference coefficient ($^{+}C_3^{(3)}$) (d) Negative-tone/negative interference coefficient ($^{-}C_3^{(3)}$)

most published PC devices. However, the other processes may very well hold significance in other areas. More complicated devices can be fabricated using this process and photo-masks like that illustrated in Fig. 7.2.

Three-dimensional structures can be fabricated with a minimum of four diffractive elements. Unlike the two-dimensional case, the three-dimensional structures defined in the photosensitive material cannot simply be patterned into the substrate using common etching techniques. There exists impressive processing techniques that have been invented that solve this very problem. Tetreault has demonstrated silicon single and double inversion techniques [110]. After a three-dimensional (or two-dimensional) polymer template has been fabricated, a silicon single or double inversion can be grown on the substrate. The process involves the following steps:

1. Fabrication of the polymer template.

2. Full SiO_2 infiltration by way of layer-by-layer chemical vapor deposition (CVD).

3. Anisotropic reactive-ion etching (RIE) of the top SiO_2 overlayer to uncover the polymer template.

4. Removal of the polymer template by O_2 plasma etching or calcination in air to obtain the SiO_2 inverse of the original polymer structure.

5. Re-infiltration of the SiO_2 inverse by SiO_2 CVD to fine-tune the filling fraction.

6. Si infiltration of the structure by low-pressure CVD.

7. Removal of SiO_2 inverse by chemical etching in an aqueous HF solution to obtain the Si replica.

Silicon double inversion is a CMOS compatible, versatile, and scalable method for the fabrication of high refractive index contrast replicas of three-dimensional polymer templates made by the MBIL-based photo-mask.

The photo-mask described in this thesis can be integrated into systems very much like conventional mask aligners. The mask aligner systems that will utilize the photo-mask will need illumination systems that provide light with sufficiently high coherence lengths (dependent upon the width of the propagation region). The light source can originate from a number of sources including sufficiently large-cavity-length lasers and properly filtered arc lamps. Regardless, very little will change in the mechanics and configuration of such a mask-aligner making integration into existing CMOS processes seamless.

7.2.1.1 Proposed Statement of Future Work

The work in this thesis has been partially supported by the National Science Foundation (NSF) and will continue to be supported under the same research grant in order to develop a systematic methodology for the fabrication and integration of a multiplicity of photonic crystal device structures, in parallel, across an entire wafer [111]. This will fulfill the need for an increased design space for PC structures and the need for a fabrication and integration

method to enable PC-based optoelectronic circuits to be manufactured massively in parallel over a large area. The proposed work consists of

1. Development of models describing the contrast ratios and resulting interference patterns as a function of wavevectors, polarizations, and intensities needed to produce all five 2-D Bravais lattices and all seventeen 2-D crystallographic space groups (three interfering beams).

2. Development of models describing the contrast ratios and resulting interference patterns as a function of wavevectors, polarizations, and intensities needed to produce all fourteen 3-D Bravais lattices and all 230 3-D crystallographic space groups (four interfering beams).

3. Development of photo-mask diffractive element designs for selected 2-D Bravais lattice PC's.

4. Development of photo-mask diffractive element designs for selected 3-D Bravais lattice PC's.

5. Development of material response models describing the exposure and subsequent development of candidate negative photoresist type materials.

6. Development of material response models describing the exposure and subsequent development of candidate positive photoresist type materials.

7. Development of material response models describing the "double inversion" technique of transforming photosensitive material lattice into a silicon lattice.

8. Electromagnetic optical performance analysis (band structure calculation) of the above PC structures.

9. Fabrication, testing, and demonstration of prototype photo-masks for producing 2-D photonic crystal structures.

10. Fabrication, testing, and demonstration of prototype photo-masks for producing 3-D photonic crystal structures.

11. Fabrication, testing, and demonstration of photo-masks for producing high-confinement 2-D PC waveguides.

12. Fabrication, testing, and demonstration of photo-masks for producing high-confinement 2-D PC nanoresonators.

13. Development of designs for photo-masks, including a mask spatial allocation system, for the fabrication of an integrated PC circuit (e.g. coupler, waveguide, nanoresonator).

Statement number 1 has been completed. Statement number 2 has been partially completed in terms of describing the *conditions for primitive-lattice-vector-direction equal contrasts* and providing a procedure for calculating the required recording wavevectors for all Bravais lattices. This is an important enabling step to to describe the interference patterns in terms of the crystallographic space group. Statement 8 has been partially completed. However, band structure modeling should be readdressed once material response models are developed within statements 5-7.

7.3 Concluding Remarks

Optical-based circuits will continue to be an integral part of communication [94, 106, 107, 109, 112, 113], computation [114–117], interconnection [118, 119], and sensor systems [120–134]. Traditionally these systems are built upon bulk optical components coupled together to perform these functions. These bulk components can include fiber for routing, microring resonators for optical add/drop, arrayed waveguide gratings for (de)multiplexing,

fiber coils for delay lines, and Mach-Zehnder interferometers for sensing. Integrated versions of these systems into compact optical circuits and packages would produce less expense and higher reliability. Throughout microelectronic history, smaller size and integration has always produced these advantages. Photonic-crystal-based integrated circuits have the potential to offer a platform for this integration. In fact, many of the optical circuits used in these systems have already been designed, modeled, and fabricated using photonic crystal technology. These include microring resonators [12–15, 102], Mach-Zehnder interferometers [103], wavelength-division multiplexing [23], waveguides [10, 11], delay lines [104], filters [15–17], waveguide couplers [18–21], directional couplers [22], antennas [24], switches [25], and sensors [26]. All of these components are possible because of the unique phenomena that photonic crystals possess (photonic bandgap, superprism effect, negative refraction, negative diffraction, slow light). In most cases, these result in smaller devices sizes compared to their conventional counterparts, which, in turn, translates to faster speeds. By integrating these photonic crystal-based devices into monolithically fabricated photonic circuits, the communication, computations, interconnection, and sensor systems will be less expensive and more reliable.

Utilizing a photo-mask to perform the fabrication offers a number of potential advantages over conventional fabrication. These include the reduction of the number of masks in a mask set due to the ease at which multi-beam interference can be interchanged between "light-" and "dark-field" patterns and the ability to use conventional i-line mask aligners for exposure. The proposed research increases the design space for PC structures and provides a fabrication and integration method to enable PC-based optoelectronic circuits to be manufactured massively in parallel. This will pave the way for truly dense integrated photonic circuits and systems. In turn, DIPCS offer the potential to revolutionize functions such as interconnection, communication, image acquisition, image processing, image recognition, A-to-D conversion, control, and bio/chem-sensing. Further, the resulting DIPCS would be very compact in size and could be integrated with conventional microelectronics.

7.4 Summary

The main objectives and the major contributions of the research presented in this thesis were reviewed and summarized. Potential avenues of research were highlighted for both near- and long-term efforts.

APPENDIX A

MAXIMIZATION OF CONTRAST VIA NONLINEAR OPTIMIZATION

In order to maximize the absolute contrast, an objective function must be maximized (or minimized) under constraints given by the physical problem and by each *condition for primitive-lattice-vector-direction equal contrasts*. In the most general of terms, this problem will have 9 variables and 6 constraint equations for $C_3^{(3)}$, 9 variables and 7 constraint equations for $C_3^{(2)}$, 12 variables and 10 constraint equations for $C_4^{(6)}$, $C_4^{(5)}$, and $C_4^{(4)}$, and 12 variables and 11 constraint equations for $C_4^{(3)}$. The 9 variables in three-beam interference and 12 variables in four-beam interference are the Cartesian coordinates that describe each of the polarization vectors as

$$\hat{\mathbf{e}}_i = (e_{i,x}, e_{i,y}, e_{i,z}) \, . \tag{A.1}$$

Each polarization vector must be normalized

$$|\hat{\mathbf{e}}_i| = \sqrt{e_{i,x}^2 + e_{i,y}^2 + e_{i,z}^2} = 1 \tag{A.2}$$

and be orthogonal to its corresponding wavevector. That is,

$$\hat{\mathbf{e}}_i \cdot \mathbf{k}_i = e_{i,x}k_{i,x} + e_{i,y}k_{i,y} + e_{i,z}k_{i,z} = 0 \tag{A.3}$$

where the wavevector is

$$\mathbf{k}_i = (k_{i,x}, k_{i,y}, k_{i,z}) \, . \tag{A.4}$$

Equations (A.2) and (A.3) constitute 6 of the constraint equations for three-beam interference and 8 of the constraint equations for four-beam interference (2 for each recording wavevector). The remaining constraint equations are determined by the specific *condition for primitive-lattice-vector-direction equal contrasts* in Eq. (2.44) for $C_3^{(2)}$, Eq. (3.14) for

$C_4^{(6)}$, Eqs. (3.23) and (3.24) for $C_4^{(5)}$, Eq. (3.35) for $C_4^{(4)}$, and Eq. (3.47) for $C_4^{(3)}$. The objective function is the absolute contrast. It is calculated in terms of these variables and maximized under the constraint equations.

A.1 Lagrange Multipliers

A commonly used strategy for solving constrained optimization problems is the method of Lagrange multipliers. Given the objective function to be minimized or maximized

$$f(x_1, \ldots, x_n) \tag{A.5}$$

subject to the constraint equations

$$\begin{aligned} g_1(x_1, \ldots, x_n) &= c_1 \\ &\vdots \\ g_m(x_1, \ldots, x_n) &= c_m \end{aligned} \tag{A.6}$$

the Lagrangian function is written as

$$\Lambda(x_1, \ldots, x_n, \lambda_1, \ldots, \lambda_m) = f(x_1, \ldots, x_n) + \sum_{k=1}^{m} \lambda_k \left(g_k(x_1, \ldots, x_n) - c_k\right) \tag{A.7}$$

with the introduction of m Lagrange multipliers (λ_i). A subset of the stationary points of this unconstrained function, given by

$$\nabla \Lambda = 0, \tag{A.8}$$

are the solutions to the constrained optimization problem given by Eqs. A.5 and A.6. As described above, the constrained optimization for maximizing absolute contrast results in the Lagrangian functions for each *condition for primitive-lattice-vector-direction equal contrasts* given in the next sections.

A.2 General Formulation of Lagrangian Functions for Conditions for Primitive-Lattice-Vector-Direction Equal Contrasts

The following Lagrangian functions are a function of the Cartesian coordinates of the polarization vectors $e_{i,x}$, $e_{i,y}$, and $e_{i,z}$ and the Lagrangian multipliers λ_k. For simplicity, the polarization efficiency factors e_{ij} are used to express these functions, however, the efficiency factors are functions of the polarization vectors as well, given by

$$e_{ij} = \hat{\mathbf{e}}_i \cdot \hat{\mathbf{e}}_j = e_{i,x}e_{j,x} + e_{i,y}e_{j,y} + e_{i,z}e_{j,z} \, . \tag{A.9}$$

A.2.1 $C_3^{(3)}$

The formulation of the Lagragian function for maximizing absolute contrast for $C_3^{(3)}$ consists of an objective function with 9 variables and 6 constraint equations. This yields a Lagrangian function of 15 variables (constituting 6 Lagrange multipliers). The resulting Lagrangian function, consequently, is as follows:

$$\Lambda\left(e_{1,x}, e_{1,y}, e_{1,z}, \cdots, e_{3,x}, e_{3,y}, e_{3,z}, \lambda_1, \cdots, \lambda_6\right) = \frac{2e_{12}e_{13}e_{23}}{e_{12}^2 + e_{13}^2 + e_{23}^2} + \sum_{k=1}^{3} \lambda_k(|\hat{\mathbf{e}}_i| - 1) + \sum_{k=1}^{3} \lambda_{k+3}\hat{\mathbf{e}}_i \cdot \mathbf{k}_i \tag{A.10}$$

A.2.2 $C_3^{(2)}$

The formulation of the Lagragian function for maximizing absolute contrast for $C_3^{(2)}$ consists of an objective function with 9 variables and 7 constraint equations. This yields a Lagrangian function of 16 variables (constituting 7 Lagrange multipliers). The resulting Lagrangian function, consequently, is as follows:

$$\Lambda\left(e_{1,x}, e_{1,y}, e_{1,z}, \cdots, e_{3,x}, e_{3,y}, e_{3,z}, \lambda_1, \cdots, \lambda_7\right) = \frac{2e_{12}e_{13}}{\sqrt{e_{12}^2 + e_{13}^2}} + \sum_{k=1}^{3} \lambda_k(|\hat{\mathbf{e}}_i| - 1) + \sum_{k=1}^{3} \lambda_{k+3}\hat{\mathbf{e}}_i \cdot \mathbf{k}_i + \lambda_7 e_{23} \tag{A.11}$$

A.2.3 $C_4^{(6)}$

The formulation of the Lagragian function for maximizing absolute contrast for $C_4^{(6)}$ consists of an objective function with 12 variables and 10 constraint equations. This yields a Lagrangian function of 22 variables (constituting 10 Lagrange multipliers). The resulting Lagrangian function, consequently, is as follows:

$$\Lambda\left(e_{1,x}, e_{1,y}, e_{1,z}, \cdots, e_{4,x}, e_{4,y}, e_{4,z}, \lambda_1, \cdots, \lambda_{10}\right) = \frac{2e_{12}e_{13}e_{23}}{e_{12}^2 + e_{13}^2 + e_{23}^2 + e_{13}^2 e_{23}^2/e_{34}^2} + \sum_{k=1}^{4} \lambda_k(|\hat{\mathbf{e}}_i| - 1) + \sum_{k=1}^{4} \lambda_{k+4}\hat{\mathbf{e}}_i \cdot \mathbf{k}_i + \lambda_9(e_{12}e_{34} - e_{13}e_{24}) + \lambda_{10}(e_{12}e_{34} - e_{14}e_{23}) \quad \text{(A.12)}$$

A.2.4 $C_4^{(5)}$

The formulation of the Lagragian function for maximizing absolute contrast for $C_4^{(5)}$ consists of an objective function with 12 variables and 10 constraint equations. This yields a Lagrangian function of 22 variables (constituting 10 Lagrange multipliers). The resulting Lagrangian function, consequently, is as follows:

$$\Lambda\left(e_{1,x}, e_{1,y}, e_{1,z}, \cdots, e_{4,x}, e_{4,y}, e_{4,z}, \lambda_1, \cdots, \lambda_{10}\right) = \frac{2e_{12}e_{13}e_{23}}{e_{12}^2 + e_{13}^2 + e_{23}^2 + e_{12}^2 e_{23}^2/e_{24}^2} + \sum_{k=1}^{4} \lambda_k(|\hat{\mathbf{e}}_i| - 1) + \sum_{k=1}^{4} \lambda_{k+4}\hat{\mathbf{e}}_i \cdot \mathbf{k}_i + \lambda_9(e_{13}e_{24} - e_{14}e_{23}) + \lambda_{10}e_{34} \quad \text{(A.13)}$$

A.2.5 $C_4^{(4)}$

The formulation of the Lagragian function for maximizing absolute contrast for $C_4^{(4)}$ consists of an objective function with 12 variables and 10 constraint equations. This yields a Lagrangian function of 22 variables (constituting 10 Lagrange multipliers). The resulting

Lagrangian function, consequently, is as follows:

$$\Lambda\left(e_{1,x}, e_{1,y}, e_{1,z}, \cdots, e_{4,x}, e_{4,y}, e_{4,z}, \lambda_1, \cdots, \lambda_{10}\right) = \frac{2e_{12}e_{13}e_{23}}{e_{12}^2 + e_{13}^2 + e_{23}^2 + e_{12}^2 e_{13}^2/e_{14}^2} + \sum_{k=1}^{4} \lambda_k(|\hat{\mathbf{e}}_i| - 1) + \sum_{k=1}^{4} \lambda_{k+4}\hat{\mathbf{e}}_i \cdot \mathbf{k}_i + \lambda_9 e_{24} + \lambda_{10} e_{34} \quad \text{(A.14)}$$

A.2.6 $C_4^{(3)}$

The formulation of the Lagragian function for maximizing absolute contrast for $C_4^{(3)}$ consists of an objective function with 12 variables and 11 constraint equations. This yields a Lagrangian function of 23 variables (constituting 11 Lagrange multipliers). The resulting Lagrangian function, consequently, is as follows:

$$\Lambda\left(e_{1,x}, e_{1,y}, e_{1,z}, \cdots, e_{4,x}, e_{4,y}, e_{4,z}, \lambda_1, \cdots, \lambda_{11}\right) = \frac{e_{12}e_{13}e_{14}}{\sqrt{e_{13}^2 e_{14}^2 + e_{12}^2 e_{14}^2 + e_{12}^2 e_{13}^2}} + \sum_{k=1}^{4} \lambda_k(|\hat{\mathbf{e}}_i| - 1) + \sum_{k=1}^{4} \lambda_{k+4}\hat{\mathbf{e}}_i \cdot \mathbf{k}_i + \lambda_9 e_{23} + \lambda_{10} e_{24} + \lambda_{11} e_{34} \quad \text{(A.15)}$$

A.3 Enhanced Formulation of Lagrangian Functions for Conditions for Primitive-Lattice-Vector-Direction Equal Contrasts

The present work, however, utilizes a different approach that incorporates an objective function of only 4 variables with no more than 3 constraint equations. The 4 variables are counter-clockwise angular rotations (when looking anti-parallel to the wavevector $\mathbf{k}_i$), $\psi_{z,i}$, of the vector

$$\hat{\mathbf{e}}_{z0,i} = \hat{\mathbf{z}} \times \mathbf{k}_i \quad \text{(A.16)}$$

about $\mathbf{k}_i$ which describes the polarization vector, $\hat{\mathbf{e}}_i$, for the wavevector $\mathbf{k}_i$. This is accomplished by applying 5 rotational transformations to $\hat{\mathbf{e}}_{z0,i}$. This results in the vectors

$$\hat{\mathbf{e}}_i = \mathbf{R}_z(-\phi)\mathbf{R}_y(-\theta)\mathbf{R}_z(-\psi_{z,i})\mathbf{R}_y(\theta)\mathbf{R}_z(\phi)\hat{\mathbf{e}}_{z0,i} \quad \text{(A.17)}$$

where θ and ϕ are the spherical coordinates of $\mathbf{k}_i$ given by

$$\theta_i = \cos^{-1}\left(\frac{k_{i,z}}{|\mathbf{k}_i|}\right) \tag{A.18}$$

$$\phi = \tan^{-1}\left(\frac{k_{i,y}}{k_{i,x}}\right) . \tag{A.19}$$

The rotational matrices for the counter-clockwise rotations of the x-, y-, and z-axes as $\mathbf{R}_x(\alpha)$, $\mathbf{R}_y(\beta)$, and $\mathbf{R}_z(\gamma)$, respectively, are given as

$$\mathbf{R}_x(\alpha) = \begin{pmatrix} 1 & 0 & 0 \\ 0 & \cos\alpha & \sin\alpha \\ 0 & -\sin\alpha & \cos\alpha \end{pmatrix} \tag{A.20}$$

$$\mathbf{R}_y(\beta) = \begin{pmatrix} \cos\beta & 0 & -\sin\beta \\ 0 & 1 & 0 \\ \sin\beta & 0 & \cos\beta \end{pmatrix} \tag{A.21}$$

$$\mathbf{R}_z(\gamma) = \begin{pmatrix} \cos\gamma & \sin\gamma & 0 \\ -\sin\gamma & \cos\gamma & 0 \\ 0 & 0 & 1 \end{pmatrix} . \tag{A.22}$$

By definition, $\hat{\mathbf{e}}_{z0,i}$ and $\hat{\mathbf{e}}_i$ satisfy the orthogonality and normalization conditions, eliminating the need to incorporate the 8 constraint equations given by Eqs. A.2 and A.3. The objective function is then calculated in terms of these 4 variables and maximized under no more than 3 constraint equations given by each *condition for primitive-lattice-vector-direction equal contrasts*. This results in a Lagrangian function with a significant reduction in the number of variables. This approach resulted in a quicker and more stable implementation of the nonlinear optimization.

The following Lagrangian functions are a function of the angular rotations $\psi_{z,i}$ of the polarizations and the Lagrangian multipliers λ_k. For simplicity, the polarization efficiency factors e_{ij} are used to express these functions, however, the efficiency factors are functions of the angular rotations as well. This is accomplished by applying Eq. A.17 to all four

polarization vectors in Eq. A.16 to calculate the Cartesian coordinates of the polarization vectors. The efficiency factors are then calculated in the same manner as in the general formulation of Lagrangian functions in Eq. A.9.

A.3.1 $C_3^{(3)}$

The enhanced formulation of the Lagragian function for maximizing absolute contrast for $C_3^{(3)}$ consists of an objective function with 4 variables and 0 constraint equations. This yields a Lagrangian function of 4 variables (constituting 0 Lagrange multipliers). The resulting Lagrangian function, consequently, is as follows:

$$\Lambda\left(\psi_{z,1},\cdots,\psi_{z,3}\right)=\frac{2e_{12}e_{13}e_{23}}{e_{12}^2+e_{13}^2+e_{23}^2} \tag{A.23}$$

A.3.2 $C_3^{(2)}$

The enhanced formulation of the Lagragian function for maximizing absolute contrast for $C_3^{(2)}$ consists of an objective function with 3 variables and 1 constraint equation. This yields a Lagrangian function of 4 variables (constituting 1 Lagrange multiplier). The resulting Lagrangian function, consequently, is as follows:

$$\Lambda\left(\psi_{z,1},\cdots,\psi_{z,3},\lambda_1\right)=\frac{2e_{12}e_{13}}{\sqrt{e_{12}^2+e_{13}^2}}+\lambda_1 e_{23} \tag{A.24}$$

A.3.3 $C_4^{(6)}$

The enhanced formulation of the Lagragian function for maximizing absolute contrast for $C_4^{(6)}$ consists of an objective function with 4 variables and 2 constraint equations. This yields a Lagrangian function of 6 variables (constituting 2 Lagrange multipliers). The resulting Lagrangian function, consequently, is as follows:

$$\begin{aligned}\Lambda\left(\psi_{z,1},\cdots,\psi_{z,4},\lambda_1,\lambda_2\right)=&\\ &\frac{2e_{12}e_{13}e_{23}}{e_{12}^2+e_{13}^2+e_{23}^2+e_{13}^2e_{23}^2/e_{34}^2}+\lambda_1(e_{12}e_{34}-e_{13}e_{24})+\lambda_2(e_{12}e_{34}-e_{14}e_{23})\end{aligned} \tag{A.25}$$

A.3.4 $C_4^{(5)}$

The enhanced formulation of the Lagragian function for maximizing absolute contrast for $C_4^{(5)}$ consists of an objective function with 4 variables and 2 constraint equations. This yields a Lagrangian function of 6 variables (constituting 2 Lagrange multipliers). The resulting Lagrangian function, consequently, is as follows:

$$\Lambda\left(\psi_{z,1},\cdots,\psi_{z,4},\lambda_1,\lambda_2\right)=\frac{2e_{12}e_{13}e_{23}}{e_{12}^2+e_{13}^2+e_{23}^2+e_{12}^2e_{23}^2/e_{24}^2}+\lambda_1(e_{13}e_{24}-e_{14}e_{23})+\lambda_2e_{34} \quad \text{(A.26)}$$

A.3.5 $C_4^{(4)}$

The enhanced formulation of the Lagragian function for maximizing absolute contrast for $C_4^{(4)}$ consists of an objective function with 4 variables and 2 constraint equations. This yields a Lagrangian function of 6 variables (constituting 2 Lagrange multipliers). The resulting Lagrangian function, consequently, is as follows:

$$\Lambda\left(\psi_{z,1},\cdots,\psi_{z,4},\lambda_1,\lambda_2\right)=\frac{2e_{12}e_{13}e_{23}}{e_{12}^2+e_{13}^2+e_{23}^2+e_{12}^2e_{13}^2/e_{14}^2}+\lambda_1e_{24}+\lambda_2e_{34} \quad \text{(A.27)}$$

A.3.6 $C_4^{(3)}$

The enhanced formulation of the Lagragian function for maximizing absolute contrast for $C_4^{(3)}$ consists of an objective function with 4 variables and 3 constraint equations. This yields a Lagrangian function of 7 variables (constituting 3 Lagrange multipliers). The resulting Lagrangian function, consequently, is as follows:

$$\Lambda\left(\psi_{z,1},\cdots,\psi_{z,4},\lambda_1,\cdots,\lambda_3\right)=\frac{e_{12}e_{13}e_{14}}{\sqrt{e_{13}^2e_{14}^2+e_{12}^2e_{14}^2+e_{12}^2e_{13}^2}}+\lambda_1e_{23}+\lambda_2e_{24}+\lambda_3e_{34} \quad \text{(A.28)}$$

APPENDIX B

PROGRAM LISTINGS

Fully-vectorial eigenmodes of Maxwell's equations with periodic boundary conditions were computed by preconditioned conjugate-gradient minimization of the block Rayleigh quotient in a planewave basis, using a freely available software package [89]. The MIT Photonic-Bands (MPB) package is a free program for computing the band structures (dispersion relations) and electromagnetic modes of periodic dielectric structures, on both serial and parallel computers. It incorporates a flexible, scriptable user interface based upon the GNU Guile extension and scripting language. GNU Guile is essentially an interpreter for the Scheme programming language which, as an extension language, gives access to the user-definable aspects of the MIT Photonic-Bands software such as the spatial permittivity function and the Bloch wavevector at which modes are calculated.

Within the MIT Photonic-Bands (MPB) package, all program variables are written in terms of specific units and specific bases. While all of this information is available in its entirety on the MIT Photonic-Bands website, a few notable points will be discussed here. All spatial distances are written in terms of a fundamental length scale a. In the study of photonic crystals, it is convenient to use the lattice constant as this distance. The three lattice directions of the crystal (basis1, basis2, basis3), are specified in the Cartesian basis. The lengths of these vectors are ignored; only their directions have significance. The lengths are determined by the basis-size property (given in terms of a). The resulting basis vectors (constituting these magnitudes and directions) are then used as a basis for all other spatial 3-vectors in the ctl file. The Bloch wavevectors listed in k-points are specified in the basis of the reciprocal lattice vectors of the lattice. Functions included with the software [(**lattice->cartesian** x), (**cartesian->lattice** x), (**reciprocal->cartesian** x),

(**cartesian->reciprocal** x), (**reciprocal->lattice** x), (**lattice->reciprocal** x)] are used to convert back and forth between the lattice, Cartesian, and reciprocal bases. It must be noted that when written in the Cartesian basis, spatial vectors are specified in terms of a and reciprocal vectors are specified in terms of $2\pi/a$.

The following program listings are used to calculate the dispersion relations of photonic crystals fabricated via multi-beam-interference lithography. Scripts used to model the lattices of cylindrical rods and holes in two-dimensions and spherical masses and vacancies in three-dimensions are also included. Each script can be used to model a single structure and are included as a guide. Plots (such as the bandgap maps) included in this thesis require modeling hundreds of different structures. This can be done by modifying the included Guile code or utilizing bash scripts (used by the author). This is left as an exercise to the interested reader.

B.1 Two-Dimensional Photonic Crystal Structures

The following Guile scripts model both square and hexagonal two-dimensional photonic crystals. The MBIL fabricated photonic crystal structures are modeled by the interference of three linearly-polarized plane waves. The structures are defined by the intensity contour of an interference pattern that satisfies one of two *conditions for primitive-lattice-vector-direction equal contrasts*.

B.1.1 Square Lattice Defined via MBIL

Listing B.1: Guile script for calculating band structures of a square lattice fabricated via multi-beam-interference lithography.

```
;-------------------------------------------------------------------------------;
;Control file for simulation of MBIL define 2D square lattice.
;Adjust parameters accordingly.
;Justin L. Stay
;4/8/2009
;-------------------------------------------------------------------------------;
;Primitive Lattice Vectors
(define a (vector3 1 0 0))
(define b (vector3 0 1 0))
```

```
;Specify basis vectors and lattice size of computational/primitive unit cell
;Note:  basis1,basis2,basis3 are DIRECTION ONLY, magnitudes are set in basis-size
(set! geometry-lattice
    (make lattice
        (size 1 1 no-size)
        (basis1 a)
        (basis2 b)
        (basis-size (vector3 1 1 no-size))))
;Specifies the computational grid resolution, in pixels per lattice unit
(set-param! resolution 32)
;Number of bands (eigenvectors) to compute at each k point
(set-param! num-bands 10)
;Dielectric constant is averaged over a "mesh" of points
(set! mesh-size 3)
;Number of k-points to interpolate between specified k-points
(define num-k-points 10)
;Processing Type---1-dielectric rods in air, 2-holes in dielectric
(define pr-type 1)
;Dielectric permittivity
(define eps 13)
;Normalized intensity contour defining structure (Intensity is normalized (0<I<1))
(define Ith 0.5)
;-------------------------------------------------------------------------------;
;MPB required definitions and calculations
;Required basis vector
(define z (vector3 0 0 1))
;Constant PI
(define pi (* 4 (atan 1)))
;Defines substrate material
(define substrate (make dielectric (epsilon eps)))
;Calculates reciprocal lattice vectors
(define A (vector3* 2 (vector3* pi (vector3*
    (/ 1 (vector3* a (vector3-cross b z))) (vector3-cross b z)))))
(define B (vector3* 2 (vector3* pi (vector3*
    (/ 1 (vector3* a (vector3-cross b z))) (vector3-cross z a)))))
;Calculates spatial cosine wavevectors
(define G21 A)
(define G31 B)
(define G32 (vector3- B A))
;Critical points of irreducible Brillouin Zone
;expressed in the basis of reciprocal lattice vectors!
(define k1 (vector3 0   0   0)) ;Gamma
(define k2 (vector3 0   0.5 0)) ;X
(define k3 (vector3 0.5 0.5 0)) ;M
(define k4 (vector3 0   0   0)) ;Gamma
;List of Bloch wavevectors to compute bands,
(set! k-points (interpolate num-k-points (list k1 k2 k3 k1)))
;Normalized intensity function - C^{(2)}_3
(define I-uc2 (lambda (p)
    (set! p (lattice->cartesian p))
    (/ (+ (cos (vector3* G21 p)) (cos (vector3* G31 p)) 2) 4)))
;Dielectric calculator (depends on flags)
(define eps-func (lambda (p)
    (define Ip 0)
```

```
    (set! Ip (I-uc2 p))
    (if (= Ith 0)
            (make dielectric (epsilon (+ Ip 1)))
            (if (= pr-type 1)
            (if (> Ip Ith) substrate air)
            (if (> Ip Ith) air substrate)))))
;Sets spatial permittivity function
(set! default-material
    (make material-function (material-func eps-func)))

;Run and calculate modes for each Bloch wavevector
(run-te)
(run-tm)
```

B.1.2 Hexagonal Lattice Defined via MBIL

Listing B.2: Guile script for calculating band structures of a hexagonal lattice fabricated via multi-beam-interference lithography.

```
;-------------------------------------------------------------------------------;
;Control file for simulation of MBIL define 2D hexagonal lattice.
;Adjust parameters accordingly.
;Justin L. Stay
;4/8/2009
;-------------------------------------------------------------------------------;
;Primitive Lattice Vectors
(define a (vector3  1    0              0))
(define b (vector3 -0.5 (/ (sqrt 3) 2) 0))
;Specify basis vectors and lattice size of computational/primitive unit cell
;Note:  basis1,basis2,basis3 are DIRECTION ONLY, magnitudes are set in basis-size
(set! geometry-lattice
    (make lattice
        (size 1 1 no-size)
        (basis1 a)
        (basis2 b)
        (basis-size (vector3 1 1 no-size))))
;Specifies the computational grid resolution, in pixels per lattice unit
(set-param! resolution 32)
;Number of bands (eigenvectors) to compute at each k point
(set-param! num-bands 10)
;Dielectric constant is averaged over a "mesh" of points
(set! mesh-size 3)
;Number of k-points to interpolate between specified k-points
(define num-k-points 10)
;Processing Type---1-dielectric rods in air, 2-holes in dielectric
(define pr-type 1)
;Dielectric permittivity
(define eps 13)
;Normalized intensity contour defining structure (Intensity is normalized (0<I<1))
(define Ith 0.5)
;-------------------------------------------------------------------------------;
;MPB required definitions and calculations
;Required basis vector
(define z (vector3 0 0 1))
;Constant PI
(define pi (* 4 (atan 1)))
;Defines substrate material
(define substrate (make dielectric (epsilon eps)))
;Calculates reciprocal lattice vectors
(define A (vector3* 2 (vector3* pi (vector3*
    (/ 1 (vector3* a (vector3-cross b z))) (vector3-cross b z)))))
(define B (vector3* 2 (vector3* pi (vector3*
    (/ 1 (vector3* a (vector3-cross b z))) (vector3-cross z a)))))
;Calculates spatial cosine wavevectors
(define G21 A)
(define G31 B)
(define G32 (vector3- B A))
```

```
;Critical points of irreducible Brillouin Zone
(define k1 (vector3  0       0      0)) ;Gamma
(define k2 (vector3  0       0.5    0)) ;M
(define k3 (vector3 (/ 1 3) (/ 1 3) 0)) ;K
(define k4 (vector3  0       0      0)) ;Gamma
;List of Bloch wavevectors to compute bands,
;expressed in basis of reciprocal lattice vectors!
(set! k-points (interpolate num-k-points (list k1 k2 k3 k1)))
;Normalized intensity function - C^{3}_3
(define I-uc1 (lambda (p)
    (set! p (lattice->cartesian p))
    (/ (+ (cos (vector3* G21 p))
        (cos (vector3* G31 p))
        (cos (vector3* G32 p)) 1.5) 4.5)))
;Dielectric calculator
(define eps-func (lambda (p)
    (define Ip 0)
    (set! Ip (I-uc1 p))
    (if (= Ith 0)
            (make dielectric (epsilon (+ Ip 1)))
            (if (= pr-type 1)
            (if (> Ip Ith) substrate air)
            (if (> Ip Ith) air substrate)))))
;Sets spatial permittivity function
(set! default-material
    (make material-function (material-func eps-func)))

;Run and calculate modes for each Bloch wavevector
(run-te)
(run-tm)
```

B.1.3 Square Lattice of Cylindrical Rods/Holes

Listing B.3: Guile script for calculating band structures of a square lattice of cylindrical rods/holes.

```
;-------------------------------------------------------------------------------;
;Control file for simulation of square lattice of cylindrical rods/holes.
;Adjust parameters accordingly.
;Justin L. Stay
;4/8/2009
;-------------------------------------------------------------------------------;
;Primitive Lattice Vectors
(define a (vector3 1 0 0))
(define b (vector3 0 1 0))
;Specify basis vectors and lattice size of computational/primitive unit cell
;Note:  basis1,basis2,basis3 are DIRECTION ONLY, magnitudes are set in basis-size
(set! geometry-lattice
    (make lattice
        (size 1 1 no-size)
        (basis1 a)
        (basis2 b)
        (basis-size (vector3 1 1 no-size))))
;Specifies the computational grid resolution, in pixels per lattice unit
(set-param! resolution 32)
;Number of bands (eigenvectors) to compute at each k point
(set-param! num-bands 10)
;Dielectric constant is averaged over a "mesh" of points
(set! mesh-size 3)
;Number of k-points to interpolate between specified k-points
(define num-k-points 10)
;Processing Type---1-dielectric rods in air, 2-holes in dielectric
(define pr-type 1)
;Dielectric permittivity
(define eps 13)
;Define radius of cylindrical rods/holes
(define r 0.5)
;-------------------------------------------------------------------------------;
;MPB required definitions and calculations
;Defines substrate material
(define substrate (make dielectric (epsilon eps)))
;Critical points of irreducible Brillouin Zone
(define k1 (vector3 0   0   0)) ;Gamma
(define k2 (vector3 0   0.5 0)) ;X
(define k3 (vector3 0.5 0.5 0)) ;M
(define k4 (vector3 0   0   0)) ;Gamma
;List of Bloch wavevectors to compute bands,
;expressed in basis of reciprocal lattice vectors!
(set! k-points (interpolate num-k-points (list k1 k2 k3 k1)))
;Sets spatial permittivity function
(if (= pr-type 1)
    (begin
        (set! default-material air)
        (set! geometry (list (make cylinder
```

```
            (material substrate)
            (center 0 0)
            (radius r)
            (height infinity)))))
    (begin
        (set! default-material substrate)
        (set! geometry (list (make cylinder
            (material air)
            (center 0 0)
            (radius r)
            (height infinity))))))
;Run and calculate modes for each Bloch wavevector
(run-te)
(run-tm)
```

B.1.4 Hexagonal Lattice of Cylindrical Rods/Holes

Listing B.4: Guile script for calculating band structures of a hexagonal lattice of cylindrical rods/holes.

```
;------------------------------------------------------------------------------;
;Control file for simulation of hexagonal lattice of cylindrical rods/holes.
;Adjust parameters accordingly.
;Justin L. Stay
;4/8/2009
;------------------------------------------------------------------------------;
;Primitive Lattice Vectors
(define a (vector3  1    0              0))
(define b (vector3 -0.5 (/ (sqrt 3) 2) 0))
;Specify basis vectors and lattice size of computational/primitive unit cell
;Note:  basis1,basis2,basis3 are DIRECTION ONLY, magnitudes are set in basis-size
(set! geometry-lattice
    (make lattice
        (size 1 1 no-size)
        (basis1 a)
        (basis2 b)
        (basis-size (vector3 1 1 no-size))))
;Specifies the computational grid resolution, in pixels per lattice unit
(set-param! resolution 32)
;Number of bands (eigenvectors) to compute at each k point
(set-param! num-bands 10)
;Dielectric constant is averaged over a "mesh" of points
(set! mesh-size 3)
;Number of k-points to interpolate between specified k-points
(define num-k-points 10)
;Processing Type---1-dielectric rods in air, 2-holes in dielectric
(define pr-type 1)
;Dielectric permittivity
(define eps 13)
;Define radius of cylindrical rods/holes
(define r 0.5)
;------------------------------------------------------------------------------;
;MPB required definitions and calculations
;Defines substrate material
(define substrate (make dielectric (epsilon eps)))
;Critical points of irreducible Brillouin Zone
(define k1 (vector3  0       0      0)) ;Gamma
(define k2 (vector3  0       0.5    0)) ;M
(define k3 (vector3 (/ 1 3) (/ 1 3) 0)) ;K
(define k4 (vector3  0       0      0)) ;Gamma
;List of Bloch wavevectors to compute bands,
;expressed in basis of reciprocal lattice vectors!
(set! k-points (interpolate num-k-points (list k1 k2 k3 k1)))
;Sets spatial permittivity function
(if (= pr-type 1)
    (begin
        (set! default-material air)
        (set! geometry (list (make cylinder
```

```
            (material substrate)
            (center 0 0)
            (radius r)
            (height infinity)))))
    (begin
        (set! default-material substrate)
        (set! geometry (list (make cylinder
            (material air)
            (center 0 0)
            (radius r)
            (height infinity))))))
;Run and calculate modes for each Bloch wavevector
(run-te)
(run-tm)
```

B.2 Three-Dimensional Photonic Crystal Structures

The following Guile scripts model FCC, BCC, simple cubic, and diamond three-dimensional photonic crystals. The MBIL fabricated photonic crystal structures (FCC, BCC, and simple cubic) are modeled by the interference of four linearly-polarized plane waves. The structures are defined by the intensity contour of an interference pattern that satisfies one of four *conditions for primitive-lattice-vector-direction equal contrasts*.

B.2.1 Face-Centered Cubic Lattice Defined via MBIL

Listing B.5: Guile script for calculating band structures of an BCC lattice fabricated via MBIL.

```
;-------------------------------------------------------------------------------;
;Control file for simulation of a MBIL defined BCC lattice.
;Adjust parameters accordingly.
;Justin L. Stay
;4/8/2009
;-------------------------------------------------------------------------------;
;Primitive Lattice Vectors
(define a (vector3 -1  1  1))
(define b (vector3  1 -1  1))
(define c (vector3  1  1 -1))
(define La (sqrt .75))
(define Lb (sqrt .75))
(define Lc (sqrt .75))
;Specify basis vectors and lattice size of computational/primitive unit cell
;Note:  basis1,basis2,basis3 are DIRECTION ONLY, magnitudes are set in basis-size
(set! geometry-lattice
    (make lattice
        (basis1 a)
        (basis2 b)
        (basis3 c)
        (basis-size (vector3 La Lb Lc))))
;Specifies the computational grid resolution, in pixels per lattice unit
(set-param! resolution 32)
;Number of bands (eigenvectors) to compute at each k point
(set-param! num-bands 10)
;Dielectric constant is averaged over a "mesh" of points
(set! mesh-size 3)
;Number of k-points to interpolate between specified k-points
(define num-k-points 10)
;Processing Type---1-dielectric rods in air, 2-holes in dielectric
(define pr-type 1)
;Dielectric permittivity
(define eps 13)
;Normalized intensity contour defining structure (Intensity is normalized (0<I<1))
```

```
(define Ith 0.5)
;Contrast condition type
(define uc-type 64)
;-------------------------------------------------------------------------------;
;MPB required definitions and calculations
;Constant PI
(define pi (* 4 (atan 1)))
;Defines substrate material
(define substrate (make dielectric (epsilon eps)))
;Calculates reciprocal lattice vectors
(set! a (vector3* La (vector3* a (/ 1 (vector3-norm a)))))
(set! b (vector3* La (vector3* b (/ 1 (vector3-norm b)))))
(set! c (vector3* La (vector3* c (/ 1 (vector3-norm c)))))
(define A (vector3* 2 (vector3* pi (vector3* (/ 1 (vector3* a
    (vector3-cross b c))) (vector3-cross b c)))))
(define B (vector3* 2 (vector3* pi (vector3* (/ 1 (vector3* a
    (vector3-cross b c))) (vector3-cross c a)))))
(define C (vector3* 2 (vector3* pi (vector3* (/ 1 (vector3* a
    (vector3-cross b c))) (vector3-cross a b)))))
;Calculates spatial cosine wavevectors
(define G21 A)
(define G31 B)
(define G41 C)
(define G32 (vector3- B A))
(define G42 (vector3- C A))
(define G43 (vector3- C B))
;Normalized intensity function - C^{(6)}_4
(define I-PLVEC-64 (lambda (p)
    (set! p (lattice->cartesian p))
    (/ (+
        (cos (vector3* G21 p))
        (cos (vector3* G31 p))
        (cos (vector3* G41 p))
        (cos (vector3* G32 p))
        (cos (vector3* G42 p))
        (cos (vector3* G43 p))
        2) 8)))
;Normalized intensity function - C^{(5)}_4
(define I-PLVEC-54 (lambda (p)
    (set! p (lattice->cartesian p))
    (/ (+
        (cos (vector3* G21 p))
        (cos (vector3* G31 p))
        (cos (vector3* G41 p))
        (cos (vector3* G32 p))
        (cos (vector3* G42 p))
        3) 8)))
;Normalized intensity function - C^{(4)}_4
(define I-PLVEC-44 (lambda (p)
    (set! p (lattice->cartesian p))
    (/ (+
        (cos (vector3* G21 p))
        (cos (vector3* G31 p))
        (cos (vector3* G41 p))
```

```
        (cos (vector3* G32 p))
        2.5) 6.5)))
;Normalized intensity function - C^{(3)}_4
(define I-PLVEC-34 (lambda (p)
    (set! p (lattice->cartesian p))
    (/ (+
        (cos (vector3* G21 p))
        (cos (vector3* G31 p))
        (cos (vector3* G41 p))
        3) 6)))
;Critical points of Brillouin Zone
;expressed in basis of reciprocal lattice vectors!
(define k1  (vector3  0      0      0    )) ; Gamma
(define k2  (vector3  0.25   0.25   0.25 )) ; Pabc
(define k3  (vector3  0.75  -0.25  -0.25 )) ; Pa
(define k4  (vector3 -0.25   0.75  -0.25 )) ; Pb
(define k5  (vector3 -0.25  -0.25   0.75 )) ; Pc
(define k6  (vector3  0.5    0.5   -0.5  )) ; Hab
(define k7  (vector3  0.5   -0.5    0.5  )) ; Hac
(define k8  (vector3 -0.5    0.5    0.5  )) ; Hbc
(define k9  (vector3  0.625 -0.375 -0.375)) ; Fa
(define k10 (vector3 -0.375  0.625 -0.375)) ; Fb
(define k11 (vector3 -0.375 -0.375  0.625)) ; Fc
(define k12 (vector3  0.375  0.375 -0.125)) ; Fab
(define k13 (vector3 -0.125  0.375  0.375)) ; Fbc
(define k14 (vector3  0.375 -0.125  0.375)) ; Fac
(define k15 (vector3  0.375  0.375 -0.625)) ; F_ab
(define k16 (vector3  0.375 -0.625  0.375)) ; F_ac
(define k17 (vector3 -0.625  0.375  0.375)) ; F_bc
(define k18 (vector3  0.625  0.125 -0.375)) ; Faab
(define k19 (vector3  0.625 -0.375  0.125)) ; Faac
(define k20 (vector3 -0.375  0.625  0.125)) ; Fbbc
(define k21 (vector3  0.125  0.625 -0.375)) ; Fbba
(define k22 (vector3 -0.375  0.125  0.625)) ; Fccb
(define k23 (vector3  0.125 -0.375  0.625)) ; Fcca
(define k24 (vector3  0      0      0.5  )) ; Nc
(define k25 (vector3  0.5    0      0    )) ; Na
(define k26 (vector3  0      0.5    0    )) ; Nb
(define k27 (vector3  0.5   -0.5    0    )) ; Naac
(define k28 (vector3 -0.5    0.5    0    )) ; Nbbc
(define k29 (vector3  0     -0.5    0.5  )) ; Ncca
(define k30 (vector3 -0.5    0      0.5  )) ; Nccb
(define k31 (vector3  0.5    0     -0.5  )) ; Naab
(define k32 (vector3  0      0.5   -0.5  )) ; Nbba
;List of Bloch wavevectors to compute bands,
(set! k-points (interpolate num-k-points (list k1 k2 k3 k4 k5
    k6 k7 k8 k9 k10 k11 k12 k13 k14 k15 k16 k17 k18 k19 k20
    k21 k22 k23 k24 k25 k26 k27 k28 k29 k30 k31 k32)))
;Dielectric calculator
(define eps-func (lambda (p)
    (define Ip 0)
    (cond
        ((= uc-type 64) (set! Ip (I-PLVEC-64 p)))
        ((= uc-type 54) (set! Ip (I-PLVEC-54 p)))
```

```
143         ((= uc-type 44) (set! Ip (I-PLVEC-44 p)))
            ((= uc-type 34) (set! Ip (I-PLVEC-34 p))))
            (if (= Ith 0)
                (make dielectric (epsilon (+ 1 Ip)))
                (if (= pr-type 1)
148                 (if (> Ip Ith) substrate air)
                    (if (> Ip Ith) air substrate)))))
    ;Sets spatial permittivity function
    (set! default-material
        (make material-function (material-func eps-func)))
153
    ;Run and calculate modes for each Bloch wavevector
    (run)
```

B.2.2 Body-Centered Cubic Lattice Defined via MBIL

Listing B.6: Guile script for calculating band structures of an FCC lattice fabricated via MBIL.

```
;-------------------------------------------------------------------------------;
;Control file for simulation of a MBIL defined FCC lattice.
;Adjust parameters accordingly.
;Justin L. Stay
;4/8/2009
;-------------------------------------------------------------------------------;
;Primitive Lattice Vectors
(define a (vector3 1 1 0))
(define b (vector3 0 1 1))
(define c (vector3 1 0 1))
(define La (sqrt .5))
(define Lb (sqrt .5))
(define Lc (sqrt .5))
;Specify basis vectors and lattice size of computational/primitive unit cell
;Note:  basis1,basis2,basis3 are DIRECTION ONLY, magnitudes are set in basis-size
(set! geometry-lattice
    (make lattice
        (basis1 a)
        (basis2 b)
        (basis3 c)
        (basis-size (vector3 La Lb Lc))))
;Specifies the computational grid resolution, in pixels per lattice unit
(set-param! resolution 16)
;Number of bands (eigenvectors) to compute at each k point
(set-param! num-bands 10)
;Dielectric constant is averaged over a "mesh" of points
(set! mesh-size 3)
;Number of k-points to interpolate between specified k-points
(define num-k-points 10)
;Processing Type---1-dielectric rods in air, 2-holes in dielectric
(define pr-type 1)
;Dielectric permittivity
(define eps 13)
;Normalized intensity contour defining structure (Intensity is normalized (0<I<1))
(define Ith 0.5)
;Contrast condition type
(define uc-type 64)
;-------------------------------------------------------------------------------;
;MPB required definitions and calculations
;Constant PI
(define pi (* 4 (atan 1)))
;Defines substrate material
(define substrate (make dielectric (epsilon eps)))
;Calculates reciprocal lattice vectors
(set! a (vector3* La (vector3* a (/ 1 (vector3-norm a)))))
(set! b (vector3* La (vector3* b (/ 1 (vector3-norm b)))))
(set! c (vector3* La (vector3* c (/ 1 (vector3-norm c)))))
(define A (vector3* 2 (vector3* pi (vector3* (/ 1 (vector3* a
```

```
    (vector3-cross b c))) (vector3-cross b c)))))
(define B (vector3* 2 (vector3* pi (vector3* (/ 1 (vector3* a
    (vector3-cross b c))) (vector3-cross c a)))))
(define C (vector3* 2 (vector3* pi (vector3* (/ 1 (vector3* a
    (vector3-cross b c))) (vector3-cross a b)))))
;Calculates spatial cosine wavevectors
(define G21 A)
(define G31 B)
(define G41 C)
(define G32 (vector3- B A))
(define G42 (vector3- C A))
(define G43 (vector3- C B))
;Normalized intensity function - C^{(6)}_4
(define I-PLVEC-64 (lambda (p)
    (set! p (lattice->cartesian p))
    (/ (+
        (cos (vector3* G21 p))
        (cos (vector3* G31 p))
        (cos (vector3* G41 p))
        (cos (vector3* G32 p))
        (cos (vector3* G42 p))
        (cos (vector3* G43 p))
        2) 8)))
;Normalized intensity function - C^{(5)}_4
(define I-PLVEC-54 (lambda (p)
    (set! p (lattice->cartesian p))
    (/ (+
        (cos (vector3* G21 p))
        (cos (vector3* G31 p))
        (cos (vector3* G41 p))
        (cos (vector3* G32 p))
        (cos (vector3* G42 p))
        3) 8)))
;Normalized intensity function - C^{(4)}_4
(define I-PLVEC-44 (lambda (p)
    (set! p (lattice->cartesian p))
    (/ (+
        (cos (vector3* G21 p))
        (cos (vector3* G31 p))
        (cos (vector3* G41 p))
        (cos (vector3* G32 p))
        2.5) 6.5)))
;Normalized intensity function - C^{(3)}_4
(define I-PLVEC-34 (lambda (p)
    (set! p (lattice->cartesian p))
    (/ (+
        (cos (vector3* G21 p))
        (cos (vector3* G31 p))
        (cos (vector3* G41 p))
        3) 6)))
;Critical points of Brillouin Zone
;expressed in basis of reciprocal lattice vectors!
(define k1  (vector3  0      0      0    )) ; Gamma
(define k2  (vector3  0.5    0.5    0    )) ; Xab
```

```
(define k3  (vector3  0      0.5    0.5  )) ; Xbc
(define k4  (vector3  0.5    0      0.5  )) ; Xac
(define k5  (vector3  0.25  -0.375 -0.375)) ; Ua
(define k6  (vector3 -0.375  0.25  -0.375)) ; Ub
(define k7  (vector3 -0.375 -0.375  0.25 )) ; Uc
(define k8  (vector3  0.625  0.625  0.25 )) ; Uab
(define k9  (vector3  0.25   0.625  0.625)) ; Ubc
(define k10 (vector3  0.625  0.25   0.625)) ; Uac
(define k11 (vector3  0.375  0.375 -0.25 )) ; U_ab
(define k12 (vector3 -0.25   0.375  0.375)) ; U_bc
(define k13 (vector3  0.375 -0.25   0.375)) ; U_ac
(define k14 (vector3  0.625  0.375  0    )) ; Uaab
(define k15 (vector3  0.375  0.625  0    )) ; Ubba
(define k16 (vector3  0      0.625  0.375)) ; Ubbc
(define k17 (vector3  0      0.375  0.625)) ; Ubcc
(define k18 (vector3  0.375  0      0.625)) ; Ucca
(define k19 (vector3  0.625  0      0.375)) ; Uaac
(define k20 (vector3  0.5    0.5    0.5  )) ; Labc
(define k21 (vector3  0.5    0      0    )) ; La
(define k22 (vector3  0      0.5    0    )) ; Lb
(define k23 (vector3  0      0      0.5  )) ; Lc
(define k24 (vector3  0.75   0.5    0.25 )) ; Waab
(define k25 (vector3  0.5    0.75   0.25 )) ; Wbba
(define k26 (vector3  0.25   0.75   0.5  )) ; Wbbc
(define k27 (vector3  0.25   0.5    0.75 )) ; Wccb
(define k28 (vector3  0.75   0.25   0.5  )) ; Waac
(define k29 (vector3  0.5    0.25   0.75 )) ; Wcca
(define k30 (vector3  0.5    0.25  -0.25 )) ; W_aab
(define k31 (vector3  0.25   0.5   -0.25 )) ; W_bba
(define k32 (vector3  0.25  -0.25   0.5  )) ; W_cca
(define k33 (vector3  0.5   -0.25   0.25 )) ; W_aac
(define k34 (vector3 -0.25   0.25   0.5  )) ; W_ccb
(define k35 (vector3 -0.25   0.5    0.25 )) ; W_bbc
(define k36 (vector3  0.75   0.375  0.375)) ; Ka
(define k37 (vector3  0.375  0.75   0.375)) ; Kb
(define k38 (vector3  0.375  0.375  0.75 )) ; Kc
(define k39 (vector3  0.375  0     -0.375)) ; Kaab
(define k40 (vector3  0      0.375 -0.375)) ; Kbba
(define k41 (vector3 -0.375  0.375  0    )) ; Kbbc
(define k42 (vector3 -0.375  0      0.375)) ; Kccb
(define k43 (vector3  0     -0.375  0.375)) ; Kcca
(define k44 (vector3  0.375 -0.375  0    )) ; Kaac
;List of Bloch wavevectors to compute bands,
(set! k-points (interpolate num-k-points (list k1 k2 k3 k4 k5
    k6 k7 k8 k9 k10 k11 k12 k13 k14 k15 k16 k17 k18 k19 k20
    k21 k22 k23 k24 k25 k26 k27 k28 k29 k30 k31 k32 k33 k34
    k35 k36 k37 k38 k39 k40 k41 k42 k43 k44)))
;Dielectric calculator
(define eps-func (lambda (p)
    (define Ip 0)
    (cond
        ((= uc-type 64) (set! Ip (I-PLVEC-64 p)))
        ((= uc-type 54) (set! Ip (I-PLVEC-54 p)))
        ((= uc-type 44) (set! Ip (I-PLVEC-44 p)))
```

```
        ((= uc-type 34) (set! Ip (I-PLVEC-34 p))))
        (if (= Ith 0)
            (make dielectric (epsilon (+ 1 Ip)))
            (if (= pr-type 1)
                (if (> Ip Ith) substrate air)
                (if (> Ip Ith) air substrate)))))
;Sets spatial permittivity function
(set! default-material
    (make material-function (material-func eps-func)))

;Run and calculate modes for each Bloch wavevector
(run)
```

B.2.3 Simple Cubic Lattice Defined via MBIL

Listing B.7: Guile script for calculating band structures of a simple cubic lattice fabricated via MBIL.

```
;-------------------------------------------------------------------------------;
;Control file for simulation of a MBIL defined simple cubic lattice.
;Adjust parameters accordingly.
;Justin L. Stay
;4/8/2009
;-------------------------------------------------------------------------------;
;Primitive Lattice Vectors
(define a (vector3 1 0 0))
(define b (vector3 0 1 0))
(define c (vector3 0 0 1))
(define La 1)
(define Lb 1)
(define Lc 1)
;Specify basis vectors and lattice size of computational/primitive unit cell
;Note:  basis1,basis2,basis3 are DIRECTION ONLY, magnitudes are set in basis-size
(set! geometry-lattice
    (make lattice
        (basis1 a)
        (basis2 b)
        (basis3 c)
        (basis-size (vector3 La Lb Lc))))
;Specifies the computational grid resolution, in pixels per lattice unit
(set-param! resolution 32)
;Number of bands (eigenvectors) to compute at each k point
(set-param! num-bands 10)
;Dielectric constant is averaged over a "mesh" of points
(set! mesh-size 3)
;Number of k-points to interpolate between specified k-points
(define num-k-points 10)
;Processing Type---1-dielectric rods in air, 2-holes in dielectric
(define pr-type 1)
;Dielectric permittivity
(define eps 13)
;Normalized intensity contour defining structure (Intensity is normalized (0<I<1))
(define Ith 0.5)
;Contrast condition type
(define uc-type 64)
;-------------------------------------------------------------------------------;
;MPB required definitions and calculations
;Constant PI
(define pi (* 4 (atan 1)))
;Defines substrate material
(define substrate (make dielectric (epsilon eps)))
;Calculates reciprocal lattice vectors
(set! a (vector3* La (vector3* a (/ 1 (vector3-norm a)))))
(set! b (vector3* La (vector3* b (/ 1 (vector3-norm b)))))
(set! c (vector3* La (vector3* c (/ 1 (vector3-norm c)))))
(define A (vector3* 2 (vector3* pi (vector3* (/ 1 (vector3* a
```

```
    (vector3-cross b c))) (vector3-cross b c)))))
(define B (vector3* 2 (vector3* pi (vector3* (/ 1 (vector3* a
    (vector3-cross b c))) (vector3-cross c a)))))
(define C (vector3* 2 (vector3* pi (vector3* (/ 1 (vector3* a
    (vector3-cross b c))) (vector3-cross a b)))))
;Calculates spatial cosine wavevectors
(define G21 A)
(define G31 B)
(define G41 C)
(define G32 (vector3- B A))
(define G42 (vector3- C A))
(define G43 (vector3- C B))
;Normalized intensity function - C^{(6)}_4
(define I-PLVEC-64 (lambda (p)
    (set! p (lattice->cartesian p))
    (/ (+
        (cos (vector3* G21 p))
        (cos (vector3* G31 p))
        (cos (vector3* G41 p))
        (cos (vector3* G32 p))
        (cos (vector3* G42 p))
        (cos (vector3* G43 p))
        2) 8)))
;Normalized intensity function - C^{(5)}_4
(define I-PLVEC-54 (lambda (p)
    (set! p (lattice->cartesian p))
    (/ (+
        (cos (vector3* G21 p))
        (cos (vector3* G31 p))
        (cos (vector3* G41 p))
        (cos (vector3* G32 p))
        (cos (vector3* G42 p))
        3) 8)))
;Normalized intensity function - C^{(4)}_4
(define I-PLVEC-44 (lambda (p)
    (set! p (lattice->cartesian p))
    (/ (+
        (cos (vector3* G21 p))
        (cos (vector3* G31 p))
        (cos (vector3* G41 p))
        (cos (vector3* G32 p))
        2.5) 6.5)))
;Normalized intensity function - C^{(3)}_4
(define I-PLVEC-34 (lambda (p)
    (set! p (lattice->cartesian p))
    (/ (+
        (cos (vector3* G21 p))
        (cos (vector3* G31 p))
        (cos (vector3* G41 p))
        3) 6)))
;Critical points of Brillouin Zone
(define k1  (vector3  0    0    0  ))    ; Gamma
(define k2  (vector3  0.5  0    0  ))    ; Xa
(define k3  (vector3  0    0.5  0  ))    ; Xb
```

```
(define k4  (vector3  0    0    0.5))   ; Xc
(define k5  (vector3  0.5 -0.5 -0.5))   ; Ra
(define k6  (vector3 -0.5  0.5 -0.5))   ; Rb
(define k7  (vector3 -0.5 -0.5  0.5))   ; Rc
(define k8  (vector3  0.5  0.5 -0.5))   ; Rab
(define k9  (vector3 -0.5  0.5  0.5))   ; Rbc
(define k10 (vector3  0.5 -0.5  0.5))   ; Rac
(define k11 (vector3  0.5  0.5  0.5))   ; Rabc
(define k12 (vector3  0.5  0.5  0  ))   ; Mab
(define k13 (vector3  0.5  0    0.5))   ; Mca
(define k14 (vector3  0    0.5  0.5))   ; Mbc
(define k15 (vector3  0.5  0   -0.5))   ; Maab
(define k16 (vector3  0.5 -0.5  0  ))   ; Maac
(define k17 (vector3  0    0.5 -0.5))   ; Mbba
(define k18 (vector3 -0.5  0.5  0  ))   ; Mbbc
(define k19 (vector3 -0.5  0    0.5))   ; Mccb
(define k20 (vector3  0   -0.5  0.5))   ; Mcca
;List of Bloch wavevectors to compute bands,
;expressed in basis of reciprocal lattice vectors!
(set! k-points (interpolate num-k-points (list k1 k2 k3 k4 k5
    k6 k7 k8 k9 k10 k11 k12 k13 k14 k15 k16 k17 k18 k19 k20)))
;Dielectric calculator
(define eps-func (lambda (p)
    (define Ip 0)
    (cond
        ((= uc-type 64) (set! Ip (I-PLVEC-64 p)))
        ((= uc-type 54) (set! Ip (I-PLVEC-54 p)))
        ((= uc-type 44) (set! Ip (I-PLVEC-44 p)))
        ((= uc-type 34) (set! Ip (I-PLVEC-34 p))))
        (if (= Ith 0)
            (make dielectric (epsilon (+ 1 Ip)))
            (if (= pr-type 1)
                (if (> Ip Ith) substrate air)
                (if (> Ip Ith) air substrate)))))
;Sets spatial permittivity function
(set! default-material
    (make material-function (material-func eps-func)))

;Run and calculate modes for each Bloch wavevector
(run)
```

B.2.4 Face-Centered Cubic Lattice of Spherical Masses/Vacancies

Listing B.8: Guile script for calculating band structures of a FCC lattice of spherical rods/holes.

```
;------------------------------------------------------------------------------;
;Control file for simulation of FCC lattice of spherical balls/holes.
;Adjust parameters accordingly.
;Justin L. Stay
;4/8/2009
;------------------------------------------------------------------------------;
;Primitive Lattice Vectors
(define a (vector3 0 1 1))
(define b (vector3 1 0 1))
(define c (vector3 1 1 0))
(define La (sqrt 0.5))
(define Lb (sqrt 0.5))
(define Lc (sqrt 0.5))
;Specify basis vectors and lattice size of computational/primitive unit cell
;Note:  basis1,basis2,basis3 are DIRECTION ONLY, magnitudes are set in basis-size
(set! geometry-lattice (make lattice
                         (basis-size La Lb Lc)
                         (basis1 a)
                         (basis2 b)
                         (basis3 c)))
;Specifies the computational grid resolution, in pixels per lattice unit
(set-param! resolution 16)
;Number of bands (eigenvectors) to compute at each k point
(set-param! num-bands 10)
;Dielectric constant is averaged over a "mesh" of points
(set! mesh-size 3)
;Number of k-points to interpolate between specified k-points
(define num-k-points 10)
;Processing Type---1-dielectric rods in air, 2-holes in dielectric
(define pr-type 1)
;Dielectric permittivity
(define eps 13)
;Define radius of cylindrical rods/holes
(define r 0.5)
;------------------------------------------------------------------------------;
;MPB required definitions and calculations
;Defines substrate material
(define substrate (make dielectric (epsilon eps)))
;Critical points of irreducible Brillouin Zone
;expressed in basis of reciprocal lattice vectors!
(define k1 (vector3 0     0.5   0.5  )) ; X
(define k2 (vector3 0     0.625 0.375)) ; U
(define k3 (vector3 0     0.5   0    )) ; L
(define k4 (vector3 0     0     0    )) ; Gamma
(define k5 (vector3 0     0.5   0.5  )) ; X
(define k6 (vector3 0.25  0.75  0.5  )) ; W
(define k7 (vector3 0.375 0.75  0.375)) ; K
;List of Bloch wavevectors to compute bands,
```

```
(set! k-points
    (interpolate num-k-points (list k1 k2 k3 k4 k5 k6 k7)))
(define substrate (make dielectric (epsilon eps)))
;Sets spatial permittivity function
(if (= pr-type 1)
    (begin
        (set! default-material air)
        (set! geometry (list (make sphere
            (center 0 0 0) (radius r) (material substrate)))))
    (begin
        (set! default-material substrate)
        (set! geometry (list (make sphere
            (center 0 0 0) (radius r) (material air))))))
;Run and calculate modes for each Bloch wavevector
(run)
```

B.2.5 Body-Centered Cubic Lattice of Spherical Masses/Vacancies

Listing B.9: Guile script for calculating band structures of a BCC lattice of spherical rods/holes.

```
;-------------------------------------------------------------------------------;
;Control file for simulation of BCC lattice of spherical balls/holes.
;Adjust parameters accordingly.
;Justin L. Stay
;4/8/2009
;-------------------------------------------------------------------------------;
;Primitive Lattice Vectors
(define a (vector3 -1 1 1))
(define b (vector3 1 -1 1))
(define c (vector3 1 1 -1))
(define La (sqrt 0.75))
(define Lb (sqrt 0.75))
(define Lc (sqrt 0.75))
;Specify basis vectors and lattice size of computational/primitive unit cell
;Note:  basis1,basis2,basis3 are DIRECTION ONLY, magnitudes are set in basis-size
(set! geometry-lattice (make lattice
    (basis-size La Lb Lc)
    (basis1 a)
    (basis2 b)
    (basis3 c)))
;Specifies the computational grid resolution, in pixels per lattice unit
(set-param! resolution 16)
;Number of bands (eigenvectors) to compute at each k point
(set-param! num-bands 10)
;Dielectric constant is averaged over a "mesh" of points
(set! mesh-size 3)
;Number of k-points to interpolate between specified k-points
(define num-k-points 10)
;Processing Type---1-dielectric rods in air, 2-holes in dielectric
(define pr-type 1)
;Dielectric permittivity
(define eps 13)
;Define radius of cylindrical rods/holes
(define r 0.5)
;-------------------------------------------------------------------------------;
;MPB required definitions and calculations
;Defines substrate material
(define substrate (make dielectric (epsilon eps)))
;Critical points of irreducible Brillouin Zone
;expressed in basis of reciprocal lattice vectors!
(define k1 (vector3 0    0    0.5 ))    ;N
(define k2 (vector3 0.25 0.25 0.25))    ;P
(define k3 (vector3 0    0    0   ))    ;Gamma
(define k4 (vector3 0    0    0.5 ))    ;N
(define k5 (vector3 0.5 -0.5  0.5 ))    ;H
(define k6 (vector3 0.25 0.25 0.25))    ;P
(define k7 (vector3 0    0    0   ))    ;Gamma
(define k8 (vector3 0.5 -0.5  0.5 ))    ;H
```

```
;List of Bloch wavevectors to compute bands,
(set! k-points
    (interpolate num-k-points (list k1 k2 k3 k4 k5 k6 k7 k8)))
(define substrate (make dielectric (epsilon eps)))
;Sets spatial permittivity function
(if (= pr-type 1)
    (begin
        (set! default-material air)
        (set! geometry (list (make sphere
            (center 0 0 0) (radius r) (material substrate)))))
    (begin
        (set! default-material substrate)
        (set! geometry (list (make sphere
            (center 0 0 0) (radius r) (material air))))))
;Run and calculate modes for each Bloch wavevector
(run)
```

B.2.6 Simple Cubic Lattice of Spherical Masses/Vacancies

Listing B.10: Guile script for calculating band structures of a simple cubic lattice of spherical rods/holes.

```
;------------------------------------------------------------------------------;
;Control file for simulation of simple cubic lattice of spherical balls/holes.
;Adjust parameters accordingly.
;Justin L. Stay
;4/8/2009
;------------------------------------------------------------------------------;
;Primitive Lattice Vectors
(define a (vector3 1 0 0))
(define b (vector3 0 1 0))
(define c (vector3 0 0 1))
;Specify basis vectors and lattice size of computational/primitive unit cell
;Note:  basis1,basis2,basis3 are DIRECTION ONLY, magnitudes are set in basis-size
(set! geometry-lattice (make lattice
    (basis-size 1 1 1)
    (basis1 a)
    (basis2 b)
    (basis3 c)))
;Specifies the computational grid resolution, in pixels per lattice unit
(set-param! resolution 16)
;Number of bands (eigenvectors) to compute at each k point
(set-param! num-bands 10)
;Dielectric constant is averaged over a "mesh" of points
(set! mesh-size 3)
;Number of k-points to interpolate between specified k-points
(define num-k-points 10)
;Processing Type---1-dielectric rods in air, 2-holes in dielectric
(define pr-type 1)
;Dielectric permittivity
(define eps 13)
;Define radius of cylindrical rods/holes
(define r 0.5)
;------------------------------------------------------------------------------;
;MPB required definitions and calculations
;Defines substrate material
(define substrate (make dielectric (epsilon eps)))
;Critical points of irreducible Brillouin Zone
(define k1 (vector3 0.5 0   0  ))    ; X
(define k2 (vector3 0.5 0.5 0  ))    ; M
(define k3 (vector3 0   0   0  ))    ; Gamma
(define k4 (vector3 0.5 0.5 0.5))    ; R
;List of Bloch wavevectors to compute bands,
;expressed in basis of reciprocal lattice vectors!
(set! k-points (interpolate num-k-points (list k1 k2 k3 k4)))
(define substrate (make dielectric (epsilon eps)))
;Sets spatial permittivity function
(if (= pr-type 1)
    (begin
        (set! default-material air)
```

```
        (set! geometry (list (make sphere
            (center 0 0 0) (radius r) (material substrate)))))
    (begin
        (set! default-material substrate)
        (set! geometry (list (make sphere
            (center 0 0 0) (radius r) (material air))))))
;Run and calculate modes for each Bloch wavevector
(run)
```

B.2.7 Diamond Lattice of Spherical Masses/Vacancies

Listing B.11: Guile script for calculating band structures of a diamond lattice of spherical rods/holes.

```
;------------------------------------------------------------------------------;
;Control file for simulation of diamond lattice of spherical balls/holes.
;Adjust parameters accordingly.
;Justin L. Stay
;4/8/2009
;------------------------------------------------------------------------------;
;Primitive Lattice Vectors
(define a (vector3 0 1 1))
(define b (vector3 1 0 1))
(define c (vector3 1 1 0))
(define La (sqrt 0.5))
(define Lb (sqrt 0.5))
(define Lc (sqrt 0.5))
;Specify basis vectors and lattice size of computational/primitive unit cell
;Note:  basis1,basis2,basis3 are DIRECTION ONLY, magnitudes are set in basis-size
(set! geometry-lattice (make lattice
                         (basis-size La Lb Lc)
                         (basis1 a)
                         (basis2 b)
                         (basis3 c)))
;Specifies the computational grid resolution, in pixels per lattice unit
(set-param! resolution 16)
;Number of bands (eigenvectors) to compute at each k point
(set-param! num-bands 10)
;Dielectric constant is averaged over a "mesh" of points
(set! mesh-size 3)
;Number of k-points to interpolate between specified k-points
(define num-k-points 10)
;Processing Type---1-dielectric rods in air, 2-holes in dielectric
(define pr-type 1)
;Dielectric permittivity
(define eps 13)
;Define radius of cylindrical rods/holes
(define r 0.5)
;------------------------------------------------------------------------------;
;MPB required definitions and calculations
;Defines substrate material
(define substrate (make dielectric (epsilon eps)))
;Critical points of irreducible Brillouin Zone
(define k1 (vector3 0     0.5   0.5  )) ; X
(define k2 (vector3 0     0.625 0.375)) ; U
(define k3 (vector3 0     0.5   0    )) ; L
(define k4 (vector3 0     0     0    )) ; Gamma
(define k5 (vector3 0     0.5   0.5  )) ; X
(define k6 (vector3 0.25  0.75  0.5  )) ; W
(define k7 (vector3 0.375 0.75  0.375)) ; K
;List of Bloch wavevectors to compute bands,
;expressed in basis of reciprocal lattice vectors!
```

```
(set! k-points
    (interpolate num-k-points (list k1 k2 k3 k4 k5 k6 k7)))
(define substrate (make dielectric (epsilon eps)))
;Sets spatial permittivity function
(if (= pr-type 1)
    (begin
        (set! default-material air)
        (set! geometry (list
            (make sphere (center 0.125 0.125 0.125)
                (radius r) (material substrate))
            (make sphere (center -0.125 -0.125 -0.125)
                (radius r) (material substrate)))))
    (begin
        (set! default-material substrate)
        (set! geometry (list
            (make sphere (center 0.125 0.125 0.125)
                (radius r) (material air))
            (make sphere (center -0.125 -0.125 -0.125)
                (radius r) (material air))))))
;Run and calculate modes for each Bloch wavevector
(run)
```

APPENDIX C

THREE DIMENSIONAL BAND GAP MAPS

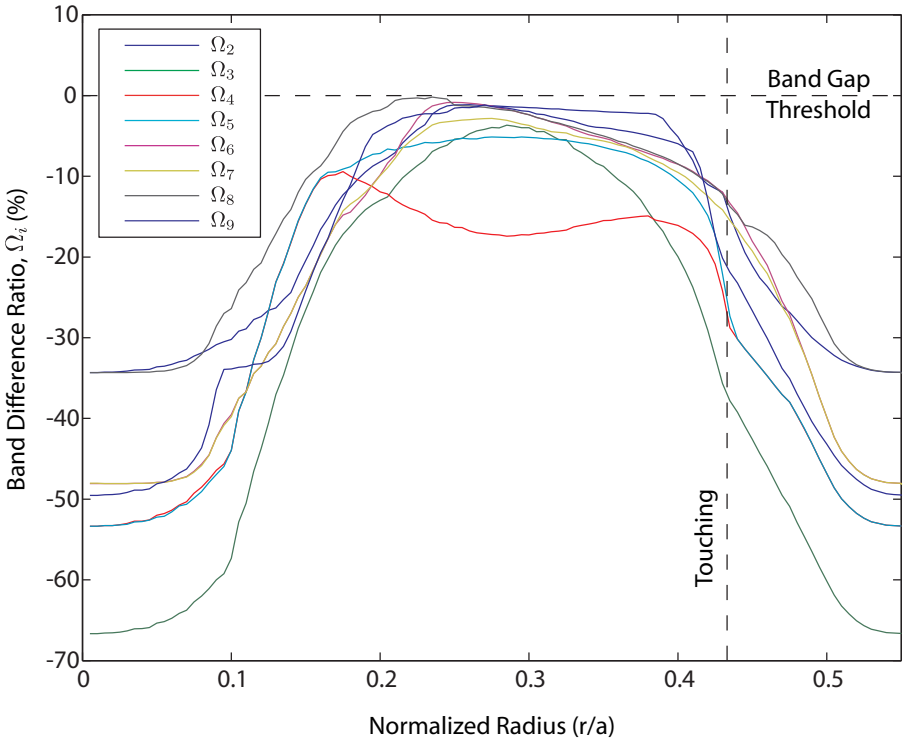

Figure C.1: Band gap map for BCC lattice of spherical masses.

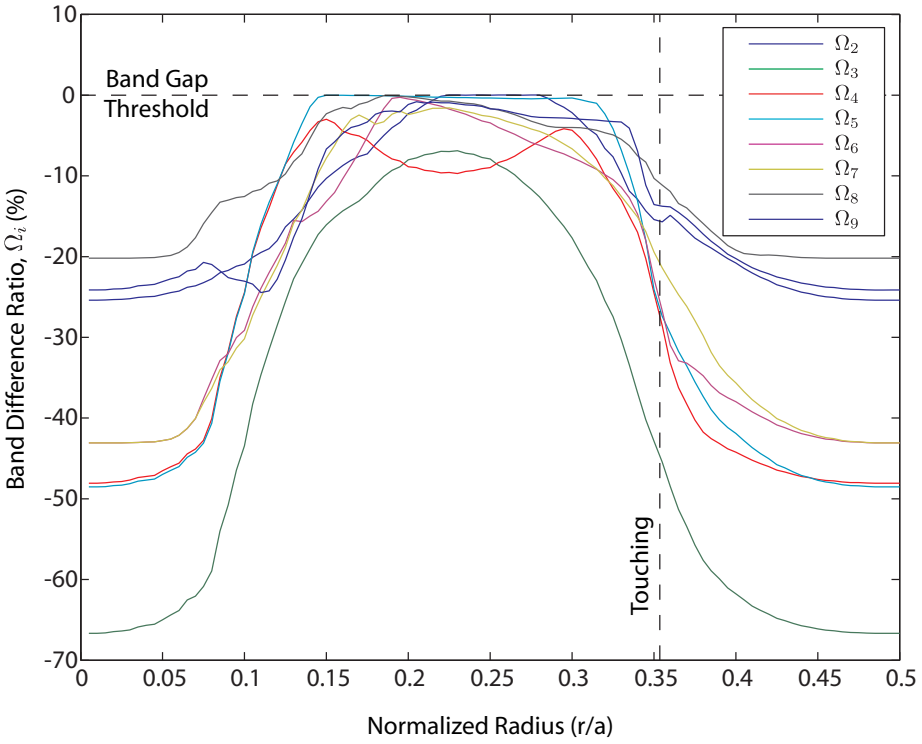

Figure C.2: Band gap map for FCC lattice of spherical masses.

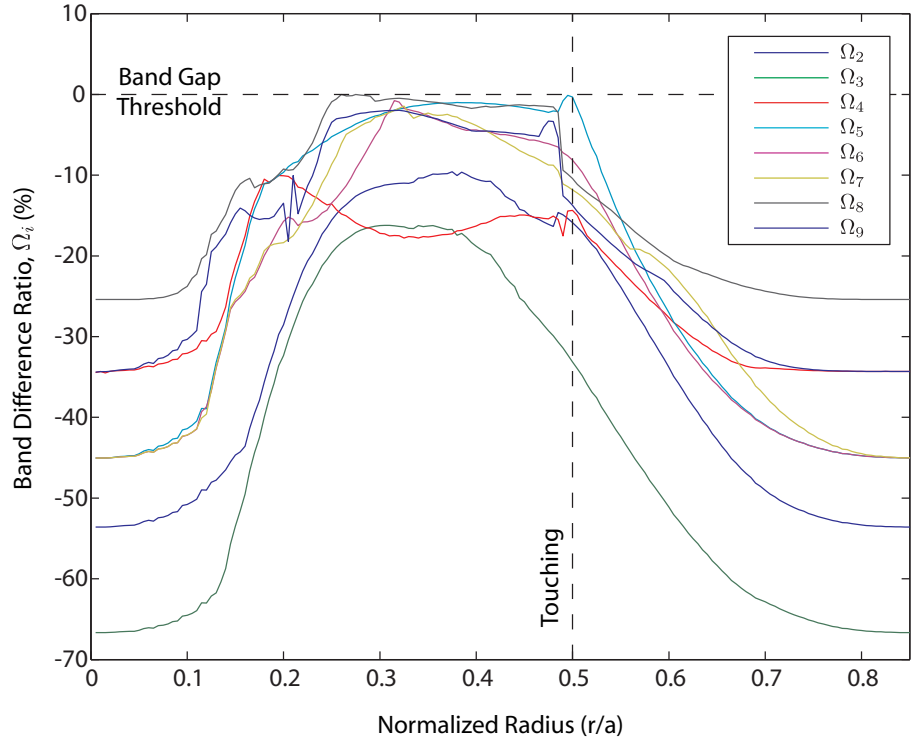

Figure C.3: Band gap map for cubic lattice of spherical masses.

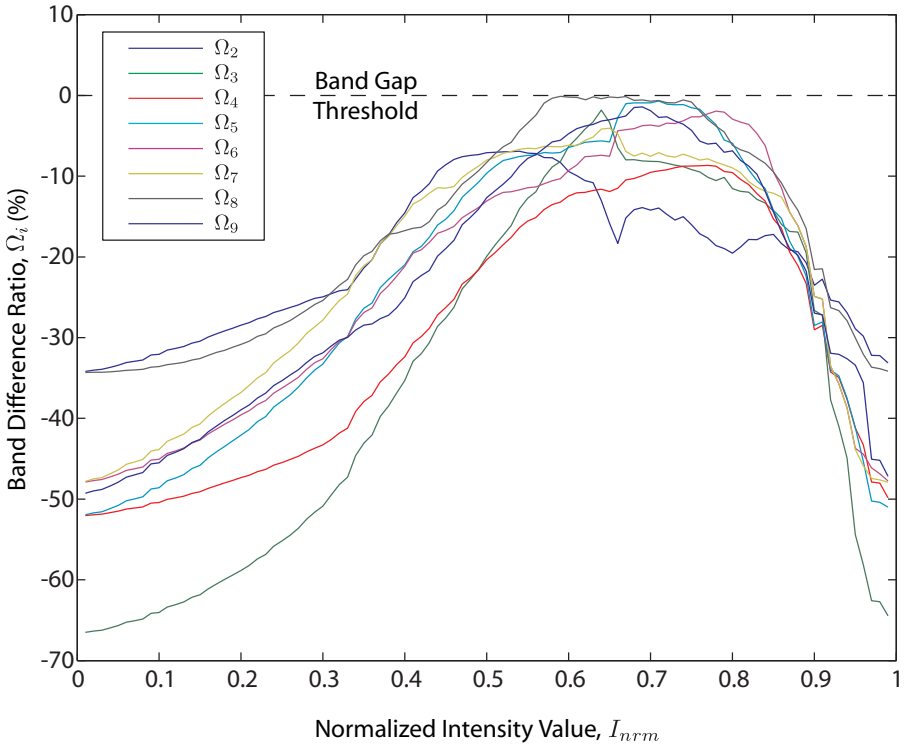

Figure C.4: Band gap map for BCC lattice of masses defined via MBIL satisfying $C_4^{(3)}$.

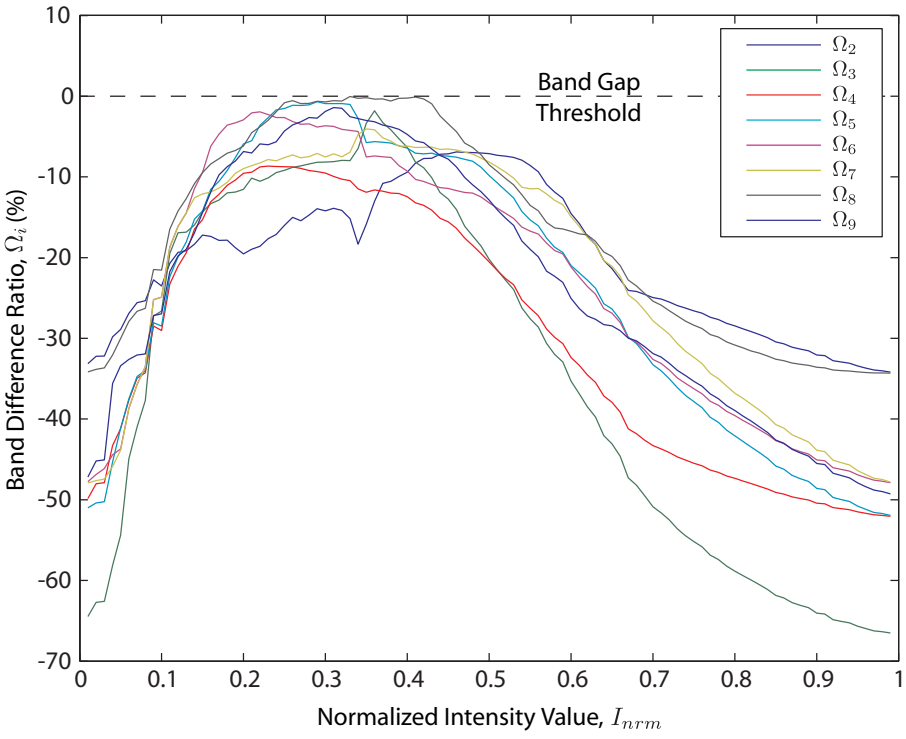

Figure C.5: Band gap map for BCC lattice of vacancies defined via MBIL satisfying $C_4^{(3)}$.

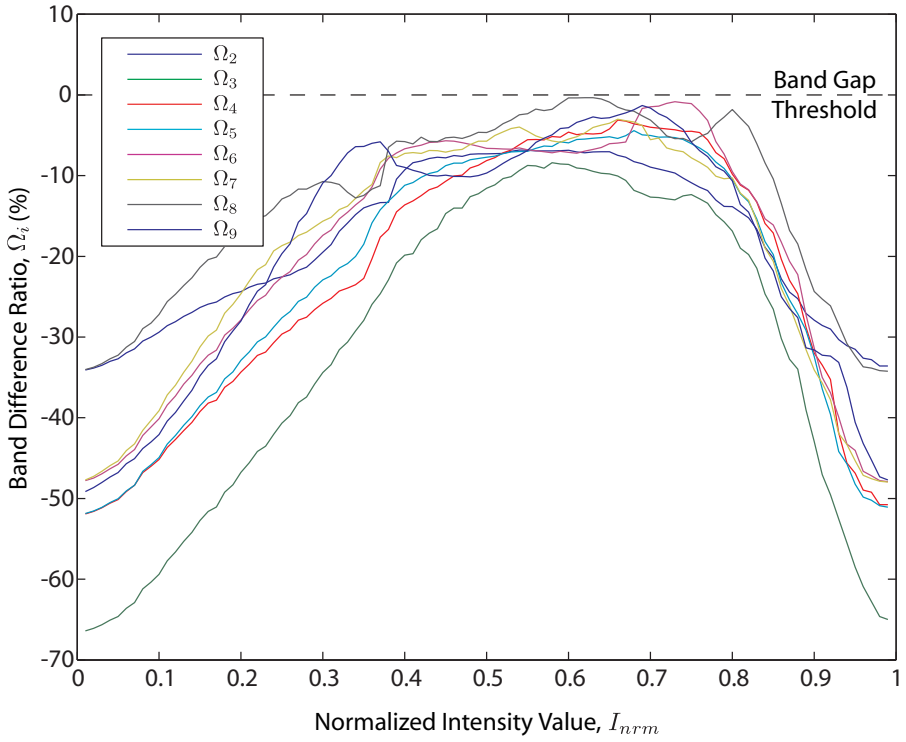

Figure C.6: Band gap map for BCC lattice of masses defined via MBIL satisfying $C_4^{(4)}$.

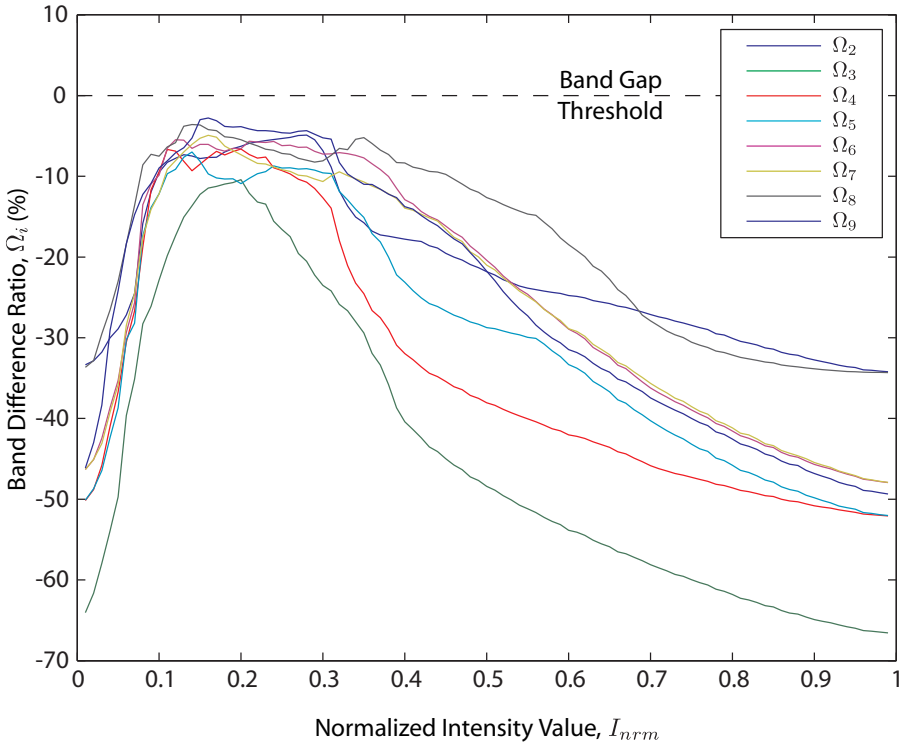

Figure C.7: Band gap map for BCC lattice of vacancies defined via MBIL satisfying $C_4^{(4)}$.

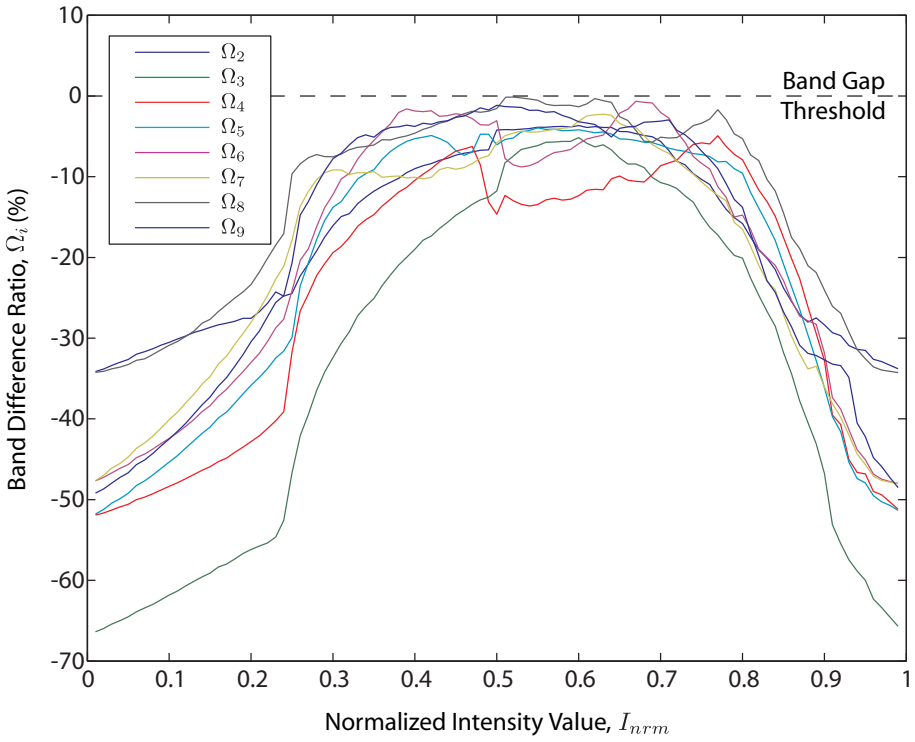

Figure C.8: Band gap map for BCC lattice of masses defined via MBIL satisfying $C_4^{(5)}$.

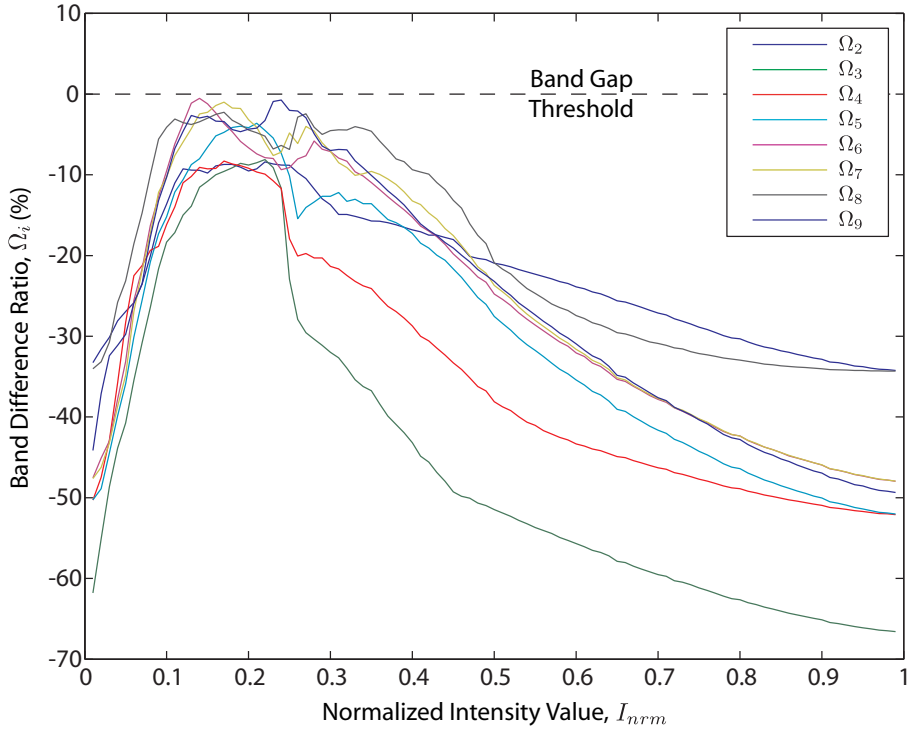

Figure C.9: Band gap map for BCC lattice of vacancies defined via MBIL satisfying $C_4^{(5)}$.

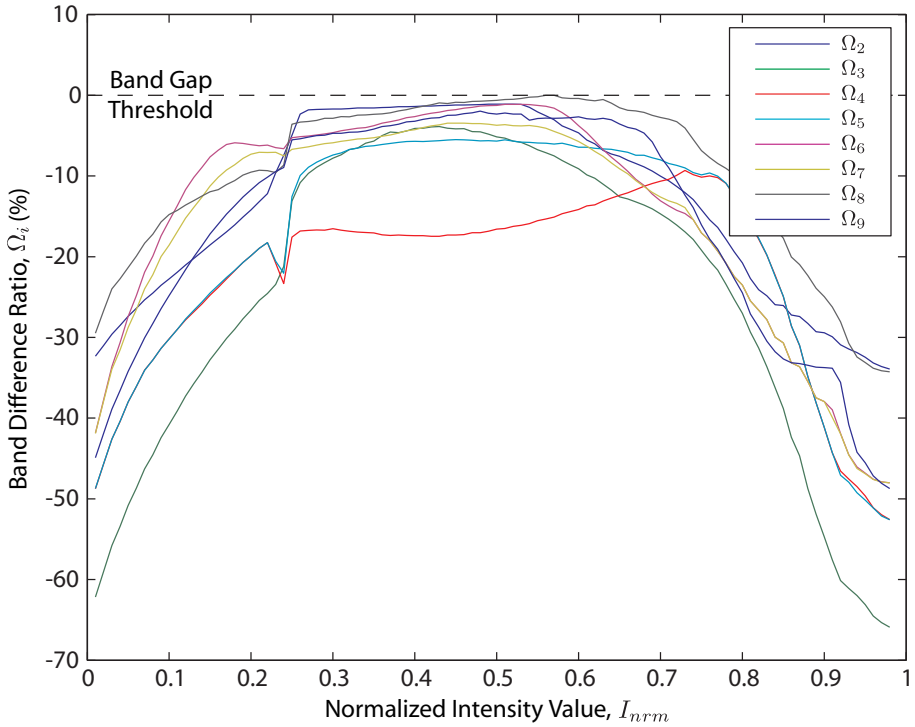

Figure C.10: Band gap map for BCC lattice of masses defined via MBIL satisfying $C_4^{(6)}$.

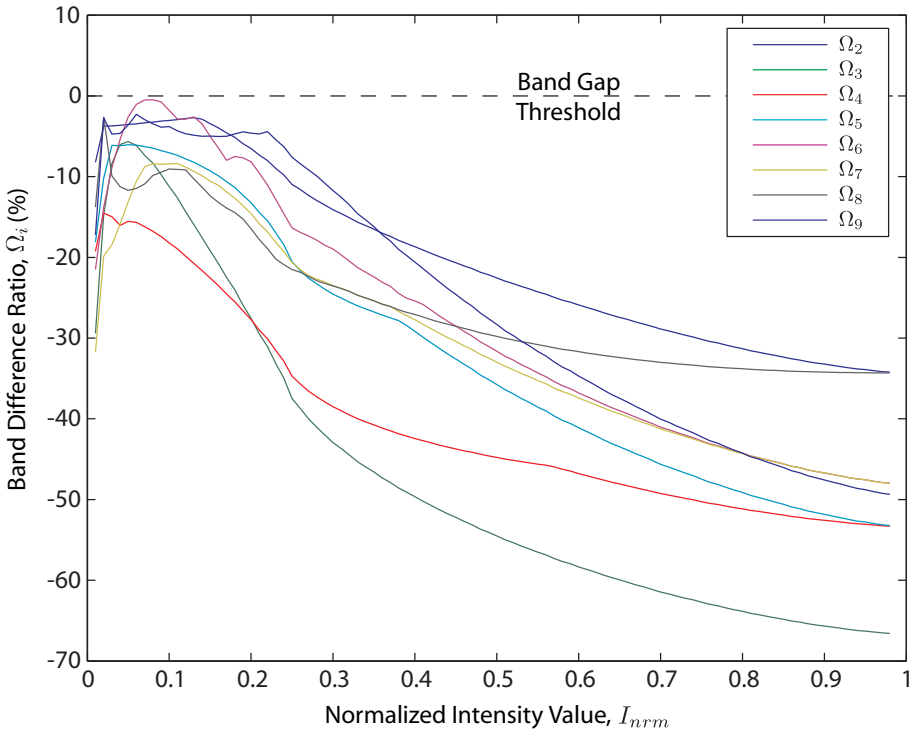

Figure C.11: Band gap map for BCC lattice of vacancies defined via MBIL satisfying $C_4^{(6)}$.

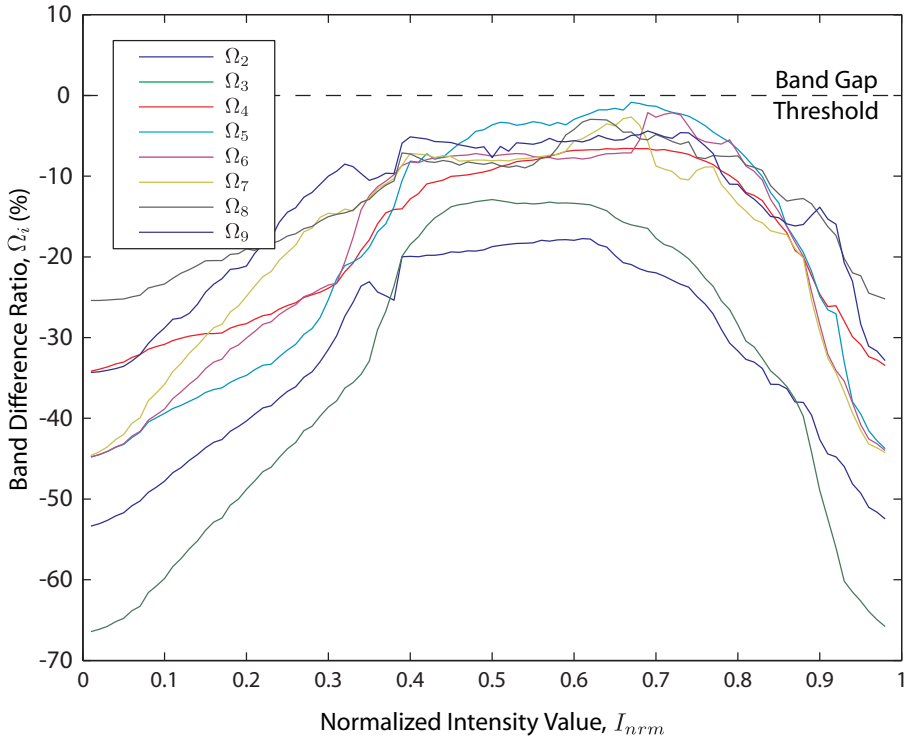

Figure C.12: Band gap map for cubic lattice of masses defined via MBIL satisfying $C_4^{(4)}$.

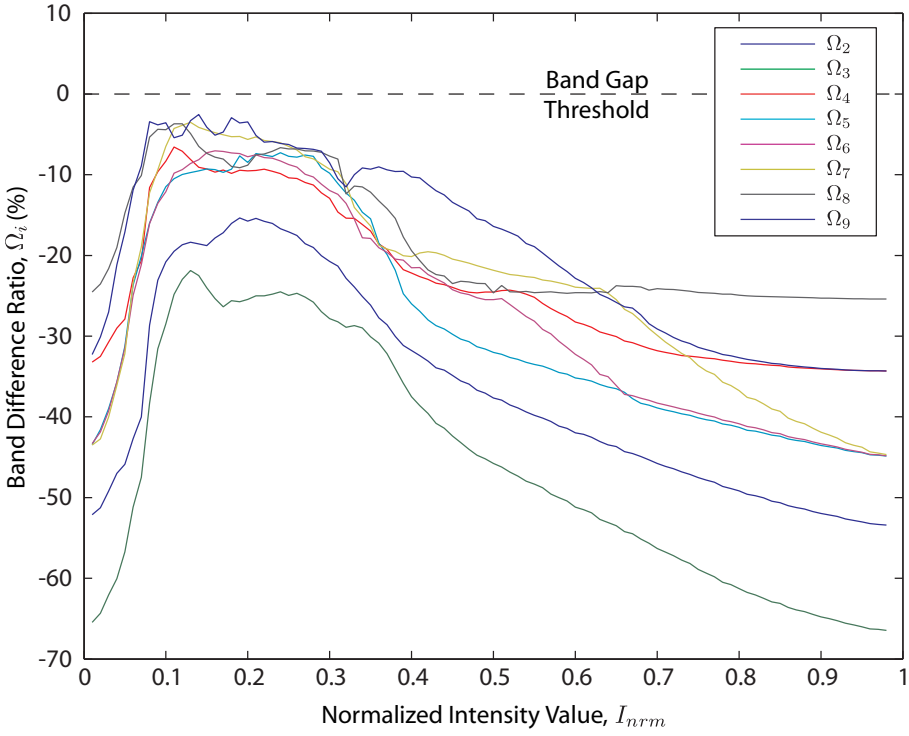

Figure C.13: Band gap map for cubic lattice of vacancies defined via MBIL satisfying $C_4^{(4)}$.

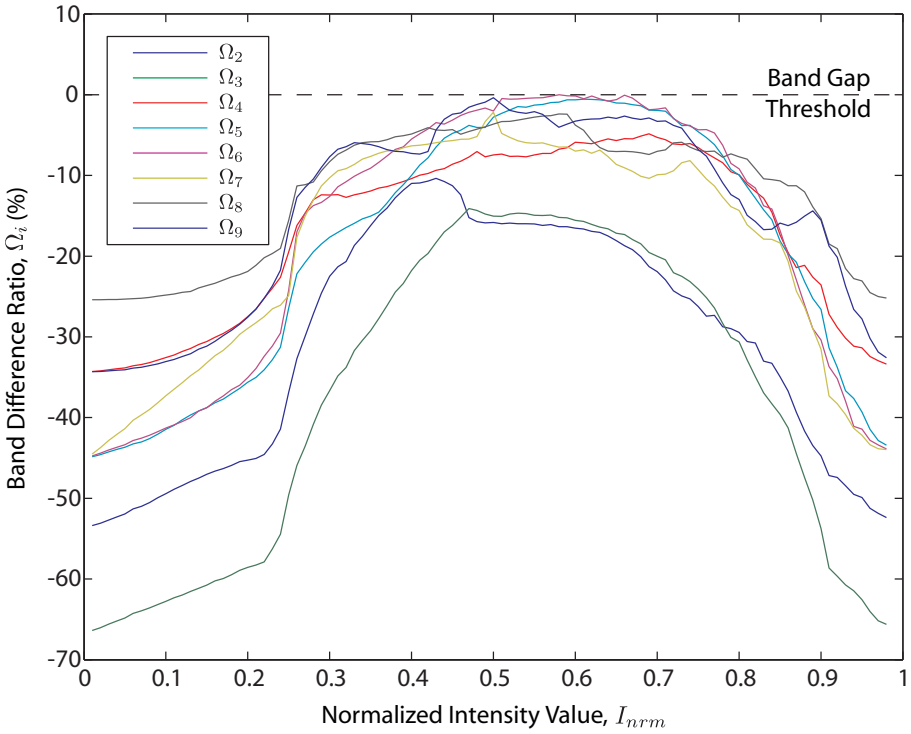

Figure C.14: Band gap map for cubic lattice of masses defined via MBIL satisfying $C_4^{(5)}$.

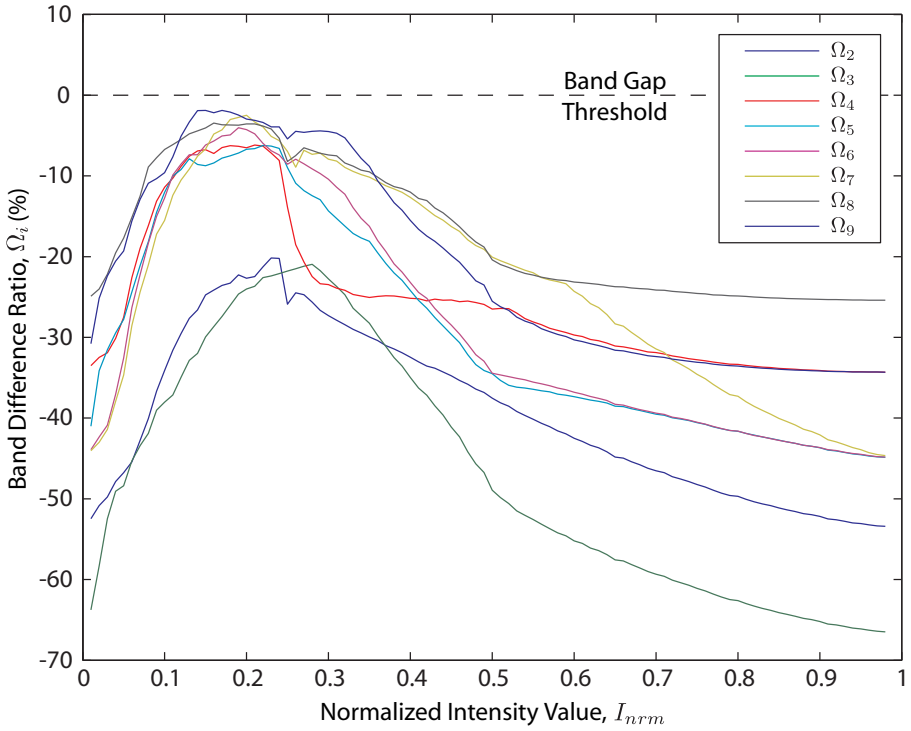

Figure C.15: Band gap map for cubic lattice of vacancies defined via MBIL satisfying $C_4^{(5)}$.

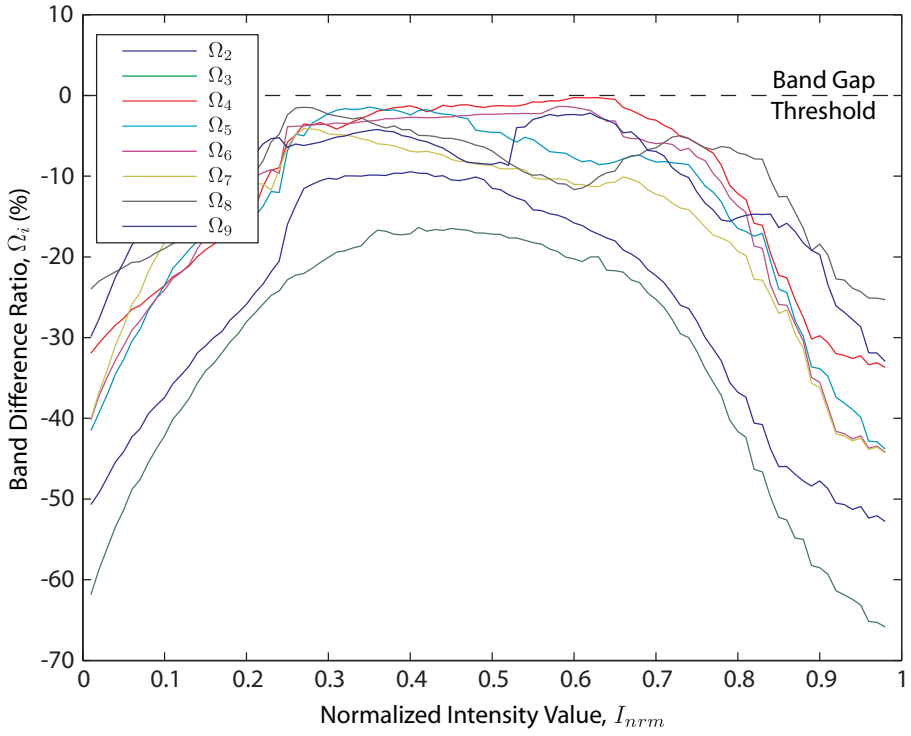

Figure C.16: Band gap map for cubic lattice of masses defined via MBIL satisfying $C_4^{(6)}$.

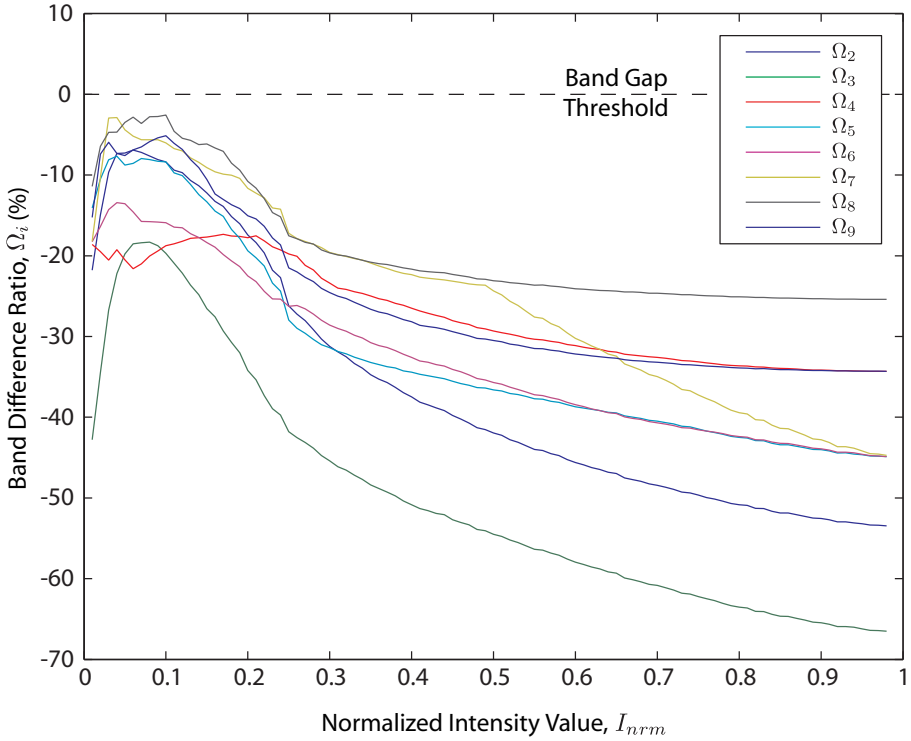

Figure C.17: Band gap map for cubic lattice of vacancies defined via MBIL satisfying $C_4^{(6)}$.

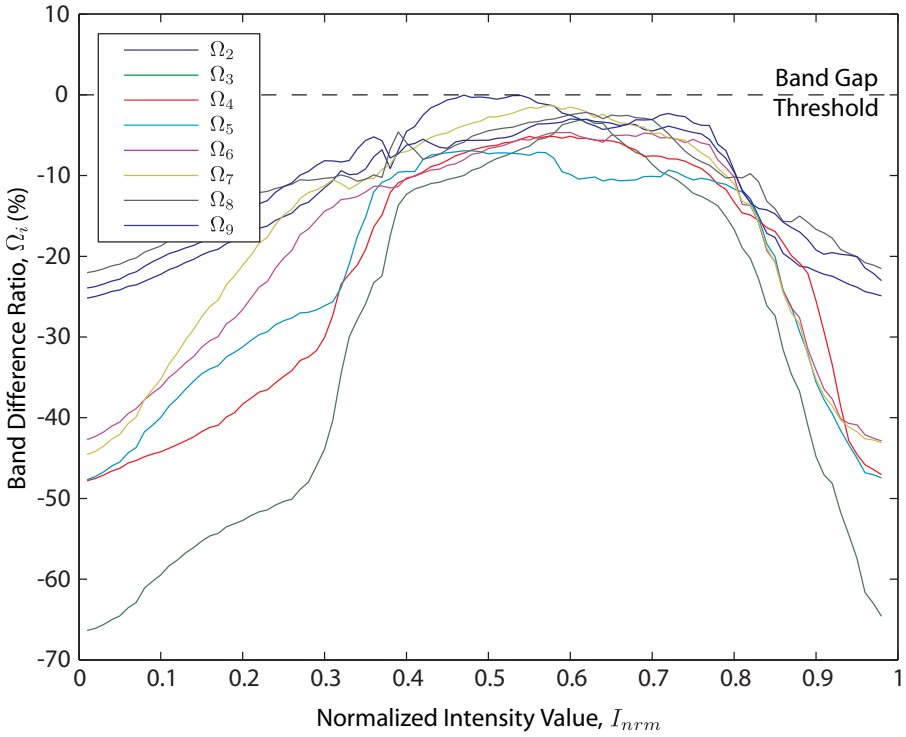

Figure C.18: Band gap map for FCC lattice of masses defined via MBIL satisfying $C_4^{(4)}$.

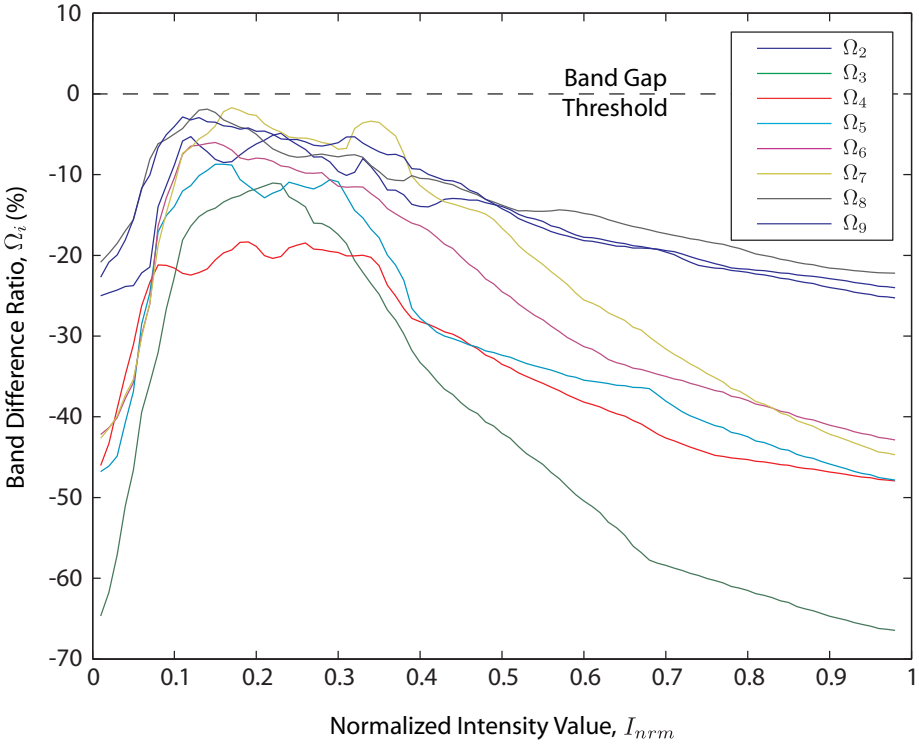

Figure C.19: Band gap map for FCC lattice of vacancies defined via MBIL satisfying $C_4^{(4)}$.

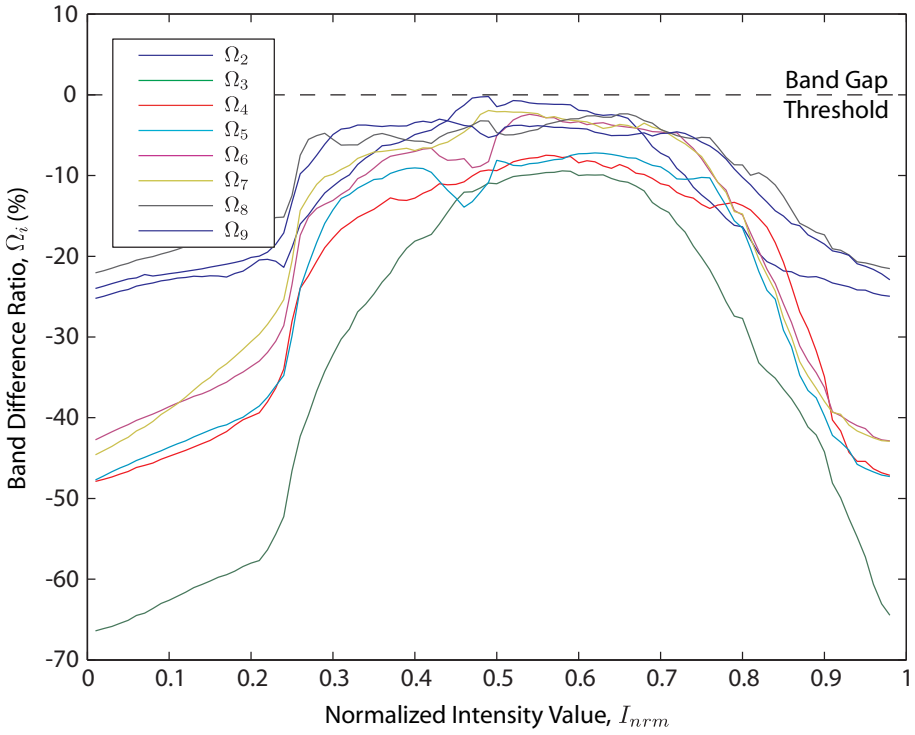

Figure C.20: Band gap map for FCC lattice of masses defined via MBIL satisfying $C_4^{(5)}$.

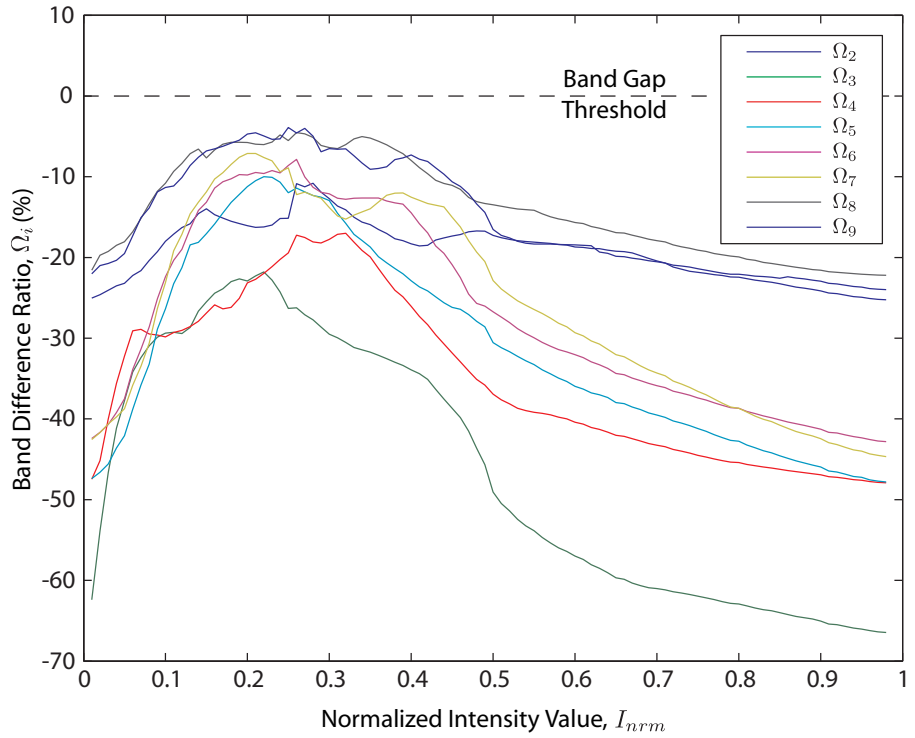

Figure C.21: Band gap map for FCC lattice of vacancies defined via MBIL satisfying $C_4^{(5)}$.

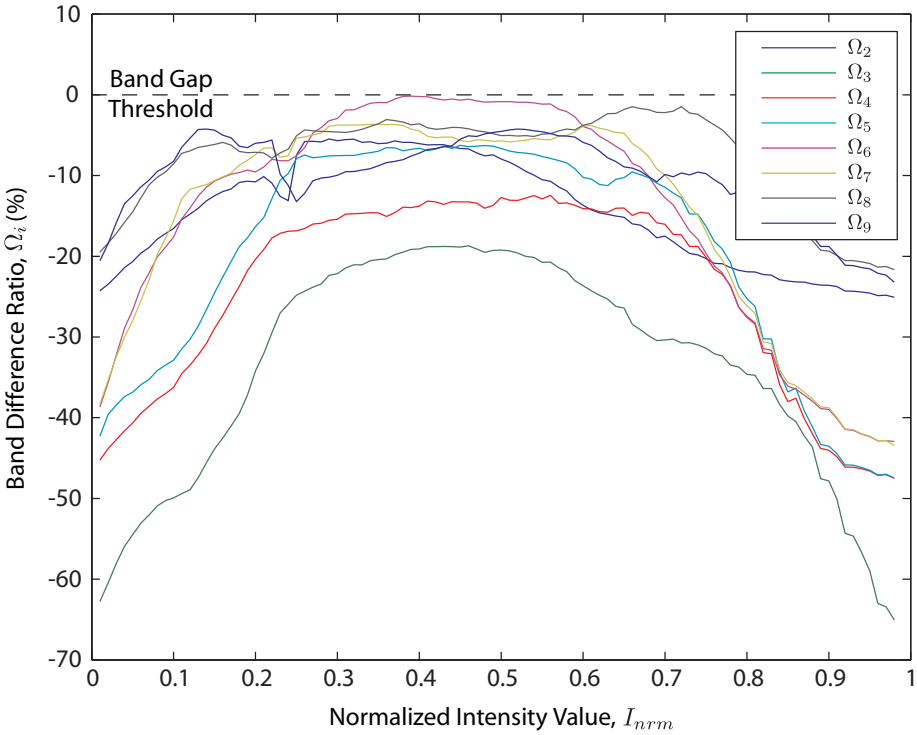

Figure C.22: Band gap map for FCC lattice of masses defined via MBIL satisfying $C_4^{(6)}$.

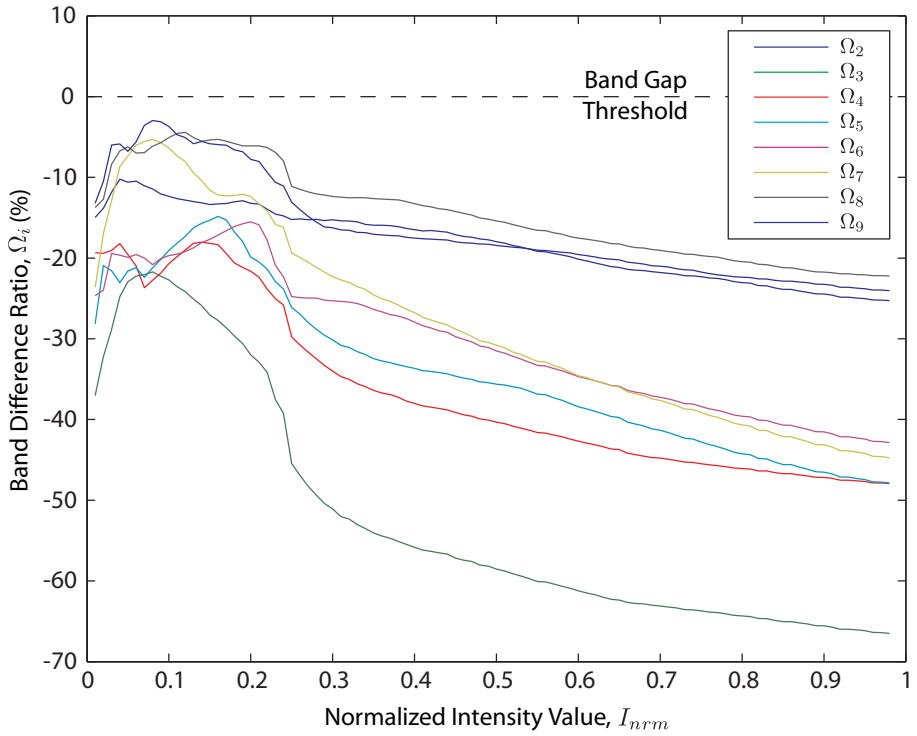

Figure C.23: Band gap map for FCC lattice of vacancies defined via MBIL satisfying $C_4^{(6)}$.

APPENDIX D

IRREDUCIBLE BRILLOUIN ZONES

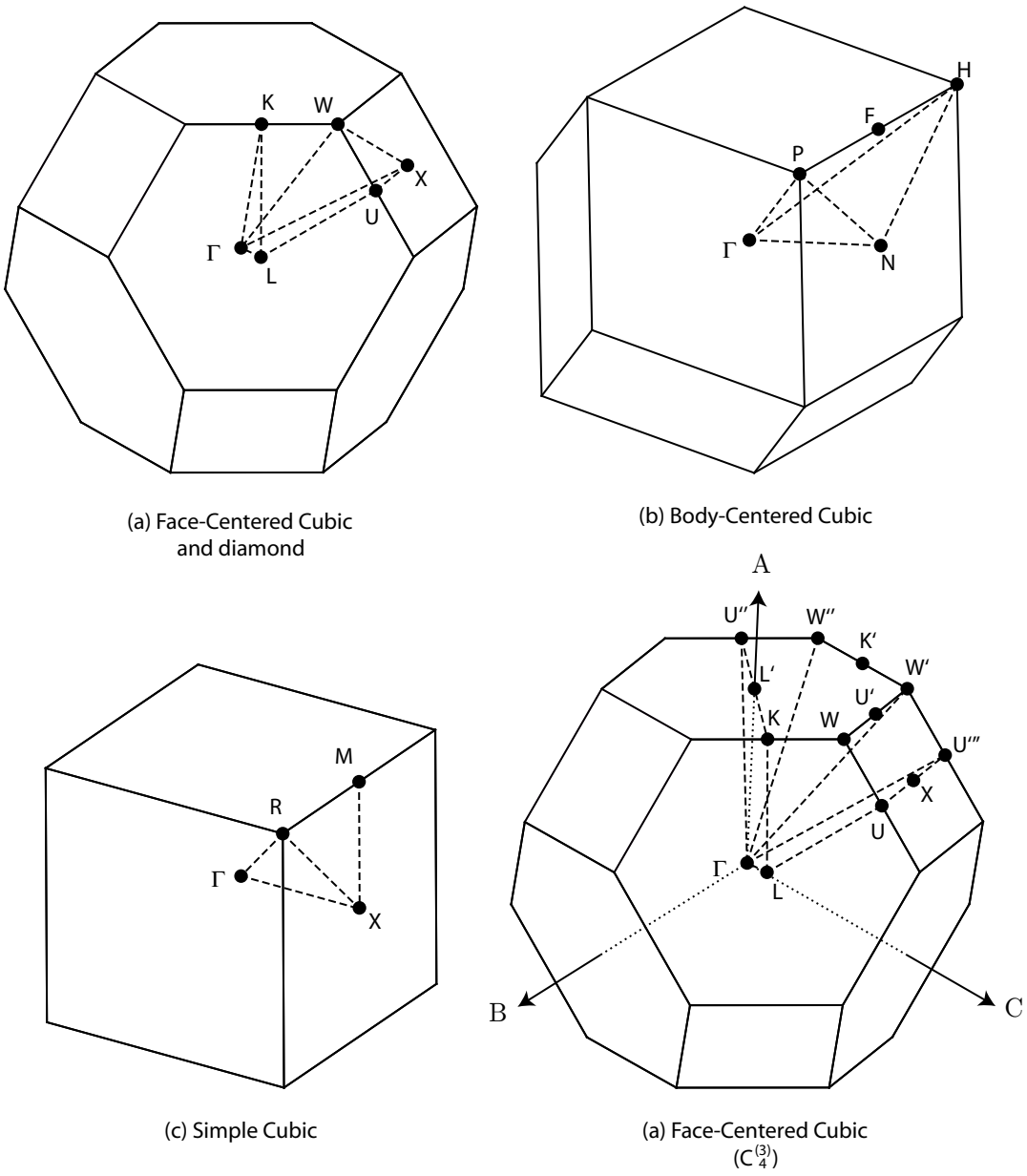

(a) Face-Centered Cubic and diamond

(b) Body-Centered Cubic

(c) Simple Cubic

(a) Face-Centered Cubic ($C_4^{(3)}$)

Figure D.1: Irreducible first Brillouin zones for the (a) face-centered cubic and diamond lattices, (b) body-centered cubic lattice, (c) cubic lattice and (d) face-centered cubic lattice defined by a $C_4^{(3)}$ interference pattern.

REFERENCES

[1] J. D. Joannopoulos, S. G. Johnson, J. N. Winn, and R. D. Meade, *Photonic Crystals: Molding the Flow of Light*. Princeton: Princeton University Press, 2nd ed., 2008.

[2] A. Di Falco, C. Conti, and G. Assanto, "Three-dimensional superprism effect in photonic-crystal slabs," *J. Lightwave Technol.*, vol. 22, pp. 1748–1753, July 2004.

[3] H. Kosaka, T. Kawashima, A. Tomita, M. Notomi, T. Tamamura, T. Sato, and S. Kawakami, "Superprism phenomena in photonic crystals: Toward microscale lightwave circuits," *J. Lightwave Technol.*, vol. 17, pp. 2032–2038, Nov. 1999.

[4] T. Matsumoto and T. Baba, "Photonic crystal k-vector superprism," *J. Lightwave Technol.*, vol. 22, pp. 917–922, Mar. 2004.

[5] A. Locatelli, M. Conforti, D. Modotto, and C. De Angelis, "Discrete negative refraction in photonic crystal waveguide arrays," *Opt. Lett.*, vol. 31, pp. 1343–1345, May 1, 2006.

[6] M. Qiu, L. Thylen, M. Swillo, and B. Jaskorzynska, "Wave propagation through a photonic crystal in a negative phase refractive-index region," *IEEE J. Sel. Top. Quantum Electron.*, vol. 9, pp. 106–110, Jan./Feb. 2003.

[7] J. Witzens, T. Baehr-Jones, and A. Scherer, "Hybrid superprism with low insertion losses and suppressed cross-talk," *Phys. Rev. E*, vol. 71, pp. 026604-1–026604-9, Mar. 10, 2005.

[8] T. Matsumoto, S. Fujita, and T. Baba, "Wavelength demultiplexer consisting of photonic crystal superprism and superlens," *Opt. Express*, vol. 13, pp. 10768–10783, Dec. 26, 2005.

[9] B. Momeni, J. Huang, M. Soltani, M. Askari, S. Mohammadi, M. Rakhshandehroo, and A. Adibi, "Compact wavelength demultiplexing using focusing negative index photonic crystal superprisms," *Opt. Express*, vol. 14, pp. 2413–2422, Mar. 20, 2006.

[10] A. Adibi, Y. Xu, R. K. Lee, A. Yariv, and A. Scherer, "Properties of the slab modes in photonic crystal optical waveguides," *J. Lightwave Technol.*, vol. 18, pp. 1554–1564, Nov. 2000.

[11] A. Jafarpour, E. Chow, C. M. Reinke, J. Huang, A. Adibi, A. Grot, L. W. Mirkarimi, G. Girolami, R. K. Lee, and Y. Xu, "Large-bandwidth ultra-low-loss guiding in bi-periodic photonic crystal waveguides," *Appl. Phys. B*, vol. 79, pp. 409–414, July 20, 2004.

[12] M. M. Beaky, J. B. Burk, H. O. Everitt, M. A. Haider, and S. Venakides, "Two-dimensional photonic crystal Fabry-Perot resonators with lossy dielectrics," *IEEE Trans. Microwave Theory Technol.*, vol. 47, pp. 2085–2091, Nov. 1999.

[13] P. Kramper, A. Birner, M. Agio, C. M. Soukoulis, F. Muller, U. Gosele, J. Mlynek, and V. Sandoghdar, "Direct spectroscopy of a deep two-dimensional photonic crystal microresonator," *Phys. Rev. B*, vol. 64, pp. 233102-1–233102-4, Nov. 8, 2001.

[14] P. Kramper, M. Kafesaki, C. M. Soukoulis, A. Birner, F. Muller, U. Gosele, R. B. Wehrspohn, J. Mlynek, and V. Sandoghdar, "Near-field visualization of light confinement in a photonic crystal microresonator," *Opt. Lett.*, vol. 29, pp. 174–176, Jan. 15, 2004.

[15] T. Kim and C. Seo, "A novel photonic bandgap structure for low-pass filter of wide stopband," *IEEE Microwave Guided Wave Lett.*, vol. 10, pp. 13–15, Jan. 2000.

[16] R. C. Rumpf, A. Mehta, P. Srinivasan, and E. G. Johnson, "Design and optimization of space-variant photonic crystal filters," *Appl. Opt.*, vol. 46, pp. 5755–5761, Aug. 10, 2007.

[17] B. Z. Steinberg, A. Boag, and R. Lisitsin, "Sensitivity analysis of narrowband photonic crystal filters and waveguides to structure variations and inaccuracy," *J. Opt. Soc. Am. A*, vol. 20, pp. 138–146, Jan. 2003.

[18] T. Kamalakis and T. Sphicopoulos, "Numerical study of the implications of size nonuniformities in the performance of photonic crystal couplers using coupled mode theory," *IEEE J. Quantum Electron.*, vol. 41, pp. 863–871, June 2005.

[19] C.-Y. Liu and L.-W. Chen, "Tunable photonic crystal waveguide coupler with nematic liquid crystals," *IEEE Photonics Technol. Lett.*, vol. 16, pp. 1849–1851, Aug. 2004.

[20] A. Mekis and J. D. Joannopoulos, "Tapered couplers for efficient interfacing between dielectric and photonic crystal waveguides," *J. Lightwave Technol.*, vol. 19, pp. 861–865, June 2001.

[21] Y. Tanaka, H. Nakamura, Y. Sugimoto, N. Ikeda, K. Asakawa, and K. Inoue, "Coupling properties in a 2-D photonic crystal slab directional coupler with a triangular lattice of air holes," *IEEE J. Quantum Electron.*, vol. 41, pp. 76–84, Jan. 2005.

[22] M. Thorhauge, L. H. Frandsen, and P. I. Borel, "Efficient photonic crystal directional couplers," *Opt. Lett.*, vol. 28, pp. 1525–1527, Sept. 1, 2003.

[23] B. Momeni and A. Adibi, "Demultiplexers harness photonic-crystal dispersion properties," *Laser Focus World*, vol. 42, pp. 125–128, June 2006.

[24] C. Caloz, A. K. Skrivervik, and F. E. Gardiol, "An efficient method to determine Green's functions of a two-dimensional photonic crystal excited by a line source - the phased-array method," *IEEE Trans. Microwave Theory Technol.*, vol. 50, pp. 1380–1391, May 2002.

[25] T. Tanabe, M. Notomi, S. Mitsugi, A. Shinya, and E. Kuramochi, "All-optical switches on a silicon chip realized using photonic crystal nanocavities," *Appl. Phys. Lett.*, vol. 87, pp. 151112-1–151112-3, Oct. 5, 2005.

[26] S. Chakravarty, J. Topol'ancik, P. Bhattacharya, S. Chakrabarti, Y. Kang, and M. E. Meyerhoff, "Ion detection with photonic crystal microcavities," *Opt. Lett.*, vol. 30, pp. 2578–2580, Oct. 1, 2005.

[27] W. M. Robertson, G. Arjavalingam, R. D. Meade, K. D. Brommer, A. M. Rappe, and J. D. Joannopoulos, "Measurement of photonic band structure in a two-dimensional periodic dielectric array," *Phys. Rev. Lett.*, vol. 68, pp. 2023–2026, Mar. 30, 1992.

[28] E. Yablonovitch, "Photonic band-gap structures," *J. Opt. Soc. Am. B*, vol. 10, pp. 283–295, Feb. 1993.

[29] E. Ozbay, E. Michel, G. Tuttle, R. Biswas, M. Sigalas, and K. M. Ho, "Micromachined millimeter-wave photonic band-gap crystals," *Appl. Phys. Lett.*, vol. 64, pp. 2059–2061, Apr. 18, 1994.

[30] S.-Y. Lin, E. Chow, V. Hietala, P. R. Villeneuve, and J. D. Joannopoulos, "Experimental demonstration of guiding and bending of electromagnetic waves in a photonic crystal," *Science*, vol. 282, pp. 274–276, Oct. 9, 1998.

[31] A. De Lustrac, F. Gadot, S. Cabaret, J. M. Lourtioz, T. Brillat, A. Priou, and E. Akmansoy, "Experimental demonstration of electrically controllable photonic crystals at centimeter wavelengths," *Appl. Phys. Lett.*, vol. 75, pp. 1625–1627, Sept. 13, 1999.

[32] J. M. Lourtioz, A. de Lustrac, F. Gadot, S. Rowson, A. Chelnokov, T. Brillat, A. Ammouche, J. Danglot, O. Vanbesien, and D. Lippens, "Toward controllable photonic crystals for centimeter- and millimeter-wave devices," *J. Lightwave Technol.*, vol. 17, pp. 2025–2031, Nov. 1999.

[33] C.-Y. Chang and W.-C. Hsu, "Photonic bandgap dielectric waveguide filter," *IEEE Microwave Compon. Lett.*, vol. 12, pp. 137–139, Apr. 2002.

[34] J. M. Hickmann, D. Solli, C. F. McCormick, R. Plambeck, and R. Y. Chiao, "Microwave measurements of the photonic band gap in a two-dimensional photonic crystal slab," *J. Appl. Phys.*, vol. 92, pp. 6918–6920, Dec. 1, 2002.

[35] M. M. Sigalas and C. A. Flory, "Microwave measurements of stub tuners in two-dimensional photonic crystal waveguides," *Phys. Rev. B*, vol. 65, pp. 125209-1–125209-5, Mar. 13, 2002.

[36] F. Cuesta, A. Griol, A. Martinez, and J. Marti, "Experimental demonstration of photonic crystal directional coupler at microwave frequencies," *Electron. Lett*, vol. 39, pp. 455–456, Mar. 6, 2003.

[37] P. V. Parimi, W. T. Lu, P. Vodo, J. Sokoloff, J. S. Derov, and S. Sridhar, "Negative refraction and left-handed electromagnetism in microwave photonic crystals," *Phys. Rev. Lett.*, vol. 92, pp. 127401-1–127401-4, Mar. 26, 2004.

[38] U. Gruning, V. Lehmann, and C. M. Engelhardt, "Two-dimensional infrared photonic band gap structure based on porous silicon," *Appl. Phys. Lett.*, vol. 66, pp. 3254–3256, June 12, 1995.

[39] S. Rowson, A. Chelnokov, J. M. Lourtioz, and F. Carcenac, "Reflection and transmission characterization of a hexagonal photonic crystal in the mid infrared," *J. Appl. Phys.*, vol. 83, pp. 5061–5064, May 15, 1998.

[40] S. Rowson, A. Chelnokov, and J. M. Lourtioz, "Two-dimensional photonic crystals in macroporous silicon: From mid-infrared (10 μm) to telecommunication wavelengths (1.3-1.5 μm)," *J. Lightwave Technol.*, vol. 17, pp. 1989–1995, Nov. 1999.

[41] G. R. Kilby, *Infrared Methods Applied to Photonic Crystal Device Development*. PhD thesis, Georgia Institute of Technology, 2005.

[42] J. Witzens, T. Baehr-Jones, and A. Scherer, "Erratum: Publisher's note: Hybrid superprism with low insertion losses and suppressed cross-talk (Physical Review E (2005) 71 (026604))," *Phys. Rev. E*, vol. 71, p. 039904, Mar. 22, 2005.

[43] E. Yablonovitch, T. J. Gmitter, and K. M. Leung, "Photonic band structure: The face-centered-cubic case employing nonspherical atoms," *Phys. Rev. Lett.*, vol. 67, pp. 2295–2298, Oct. 21, 1991.

[44] D. Schurig, J. J. Mock, B. J. Justice, S. A. Cummer, J. B. Pendry, A. F. Starr, and D. R. Smith, "Metamaterial electromagnetic cloak at microwave frequencies," *Science*, vol. 314, pp. 977–980, Nov. 10, 2006.

[45] W. J. Padilla, D. N. Basov, and D. R. Smith, "Negative refractive index metamaterials," *Mater. Today*, vol. 9, pp. 28–35, July/Aug. 2006.

[46] J. Serbin, A. Ovsianikov, and B. Chichkov, "Fabrication of woodpile structures by two-photon polymerization and investigation of their optical properties," *Opt. Express*, vol. 12, pp. 5221–5228, Oct. 18, 2004.

[47] S. Kawata, H.-B. Sun, T. Tanaka, and K. Takada, "Finer features for functional microdevices," *Nature*, vol. 412, pp. 697–698, Aug. 16, 2001.

[48] S. Cabrini, L. Businaro, M. Prasciolu, A. Carpentiro, D. Gerace, M. Galli, L. C. Andreani, F. Riboli, L. Pavesi, and E. Di Fabrizio, "Focused ion beam fabrication of one-dimensional photonic crystals on Si_3N_4/SiO_2 channel waveguides," *J. Opt. A: Pure Appl. Opt.*, vol. 8, pp. 550–553, June 12, 2006.

[49] A. P. Hynninen, J. H. J. Thijssen, E. C. M. Vermolen, M. Dijkstra, and A. Van Blaaderen, "Self-assembly route for photonic crystals with a bandgap in the visible region," *Nature Mater.*, vol. 6, pp. 202–205, Feb. 11, 2007.

[50] A. J. Danner, B. Wang, S.-J. Chua, and J.-K. Hwang, "Fabrication of efficient light-emitting diodes with a self-assembled photonic crystal array of polystyrene nanoparticles," *IEEE Photonics Technol. Lett.*, vol. 20, pp. 48–50, Jan. 1, 2008.

[51] T. Prasad, R. Rengarajan, D. M. Mittleman, and V. L. Colvin, "Advanced photonic crystal architectures from colloidal self-assembly techniques," *Opt. Mater.*, vol. 27, pp. 1250–1254, Jan. 22, 2005.

[52] Z. Zheng, X. Liu, Y. Luo, B. Cheng, D. Zhang, Q. Meng, and Y. Wang, "Pressure controlled self-assembly of high quality three-dimensional colloidal photonic crystals," *Appl. Phys. Lett.*, vol. 90, pp. 51910-1–51910-3, Jan. 31, 2007.

[53] X. Checoury, S. Enoch, C. Lopez, and A. Blanco, "Stacking patterns in self-assembly opal photonic crystals," *Appl. Phys. Lett.*, vol. 90, pp. 161131-1–161131-3, Apr. 20, 2007.

[54] R. Xie, T. Sekiguchi, D. Li, D. Yang, and M. Jiang, "Precise fabrication of point defects in self-assembled three-dimensional macroporous photonic crystals," *J. Phys. Chem. B*, vol. 110, pp. 1107–1110, Jan. 4, 2006.

[55] N. Tetreault, H. Miguez, and G. A. Ozin, "Silicon inverse opal - a platform for photonic bandgap research," *Adv. Mater.*, vol. 16, pp. 1471–1476, Aug. 18, 2004.

[56] A. Birner, A. P. Li, F. Mueller, U. Goesele, P. Kramper, V. Sandoghdar, J. Mlynek, K. Busch, and V. Lehmann, "Transmission of a microcavity structure in a two-dimensional photonic crystal based on macroporous silicon," *Mater. Sci. Semicond. Process.*, vol. 3, no. 5-6, pp. 487–491, 2000.

[57] T. Zijlstra, E. Van Der Drift, M. J. A. De Dood, E. Snoeks, and A. Polman, "Fabrication of two-dimensional photonic crystal waveguides for 1.5 μm in silicon by deep anisotropic dry etching," *J. Vac. Sci. Technol., B*, vol. 17, pp. 2734–2739, Nov./Dec. 1999.

[58] M. Loncar, T. Doll, J. Vuckovic, and A. Scherer, "Design and fabrication of silicon photonic crystal optical waveguides," *J. Lightwave Technol.*, vol. 18, pp. 1402–1411, Oct. 2000.

[59] A. Chelnokov, S. David, K. Wang, F. Marty, and J. M. Lourtioz, "Fabrication of 2-D and 3-D silicon photonic crystals by deep etching," *IEEE J. Sel. Top. Quantum Electron.*, vol. 8, pp. 919–927, July/Aug. 2002.

[60] S. Venkataraman, G. J. Schneider, J. Murakowski, S. Shi, and D. W. Prather, "Fabrication of three-dimensional photonic crystals using silicon micromachining," *Appl. Phys. Lett.*, vol. 85, pp. 2125–2127, Sept. 13, 2004.

[61] J. K. Bhardwaj and H. Ashraf, "Advanced silicon etching using high density plasmas," *Proc. SPIE*, vol. 2639, pp. 224–233, 1995.

[62] R. C. Rumpf and E. G. Johnson, "Fully three-dimensional modeling of the fabrication and behavior of photonic crystals formed by holographic lithography," *J. Opt. Soc. Am. A*, vol. 21, pp. 1703–1713, Sept. 2004.

[63] V. Berger, O. Gauthier-Lafaye, and E. Costard, "Photonic band gaps and holography," *J. Appl. Phys.*, vol. 82, pp. 60–64, July 1, 1997.

[64] V. Berger, O. Gauthier-Lafaye, and E. Costard, "Fabrication of a 2D photonic bandgap by a holographic method," *Electron. Lett*, vol. 33, pp. 425–426, Feb. 27, 1997.

[65] M. Campbell, D. N. Sharp, M. T. Harrison, R. G. Denning, and A. J. Turberfield, "Fabrication of photonic crystals for the visible spectrum by holographic lithography," *Nature*, vol. 404, pp. 53–56, Mar. 2, 2000.

[66] D. N. Sharp, M. Campbell, E. R. Dedman, M. T. Harrison, R. G. Denning, and A. J. Turberfield, "Photonic crystals for the visible spectrum by holographic lithography," *Opt. Quantum Electron.*, vol. 34, pp. 3–12, 2002.

[67] S. Yang, M. Megens, J. Aizenberg, P. Wiltzius, P. M. Chaikin, and W. B. Russel, "Creating periodic three-dimensional structures by multibeam interference of visible laser," *Chem. Mater.*, vol. 14, pp. 2831–2833, July 2002.

[68] Y. V. Miklyaev, D. C. Meisel, A. Blanco, G. von Freymann, K. Busch, W. Koch, C. Enkrich, M. Deubel, and M. Wegener, "Three-dimensional face-centered-cubic photonic crystal templates by laser holography: Fabrication, optical characterization, and band-structure calculations," *Appl. Phys. Lett.*, vol. 82, pp. 1284–1286, Feb. 24, 2003.

[69] L. Z. Cai, X. L. Yang, and Y. R. Wang, "Formation of a microfiber bundle by interference of three noncoplanar beams," *Opt. Lett.*, vol. 26, pp. 1858–1860, Dec. 1, 2001.

[70] L. Z. Cai, X. L. Yang, and Y. R. Wang, "All fourteen Bravais lattices can be formed by interference of four noncoplanar beams," *Opt. Lett.*, vol. 27, pp. 900–902, June 1, 2002.

[71] L. Z. Cai, X. L. Yang, and Y. R. Wang, "Formation of three-dimensional periodic microstructures by interference of four noncoplanar beams," *J. Opt. Soc. Am. A*, vol. 19, pp. 2238–2244, Nov. 2002.

[72] W. Mao, Y. Zhong, J. Dong, and H. Wang, "Crystallography of two-dimensional photonic lattices formed by holography of three noncoplanar beams," *J. Opt. Soc. Am. B*, vol. 22, pp. 1085–1091, May 2005.

[73] Y. Lin, D. Rivera, Z. Poole, and K. Chen, "Five-beam interference pattern controlled through phases and wave vectors for diamondlike photonic crystals," *Appl. Opt.*, vol. 45, pp. 7971–7976, Nov. 1, 2006.

[74] W. D. Mao, J. W. Dong, Y. C. Zhong, G. Q. Liang, and H. Z. Wang, "Formation principles of two-dimensional compound photonic lattices by one-step holographic lithography," *Opt. Express*, vol. 13, Apr. 18, 2005.

[75] C. Chang, T.-M. Yan, and H.-K. Liu, "Creation of line defects in holographic photonic crystals by a double-exposure thresholding method," *Appl. Opt.*, vol. 44, pp. 2580–2591, May 1, 2005.

[76] N. D. Lai, J. H. Lin, and C. C. Hsu, "Fabrication of highly rotational symmetric quasi-periodic structures by multiexposure of a three-beam interference technique," *Appl. Opt.*, vol. 46, pp. 5645–5648, Aug. 10, 2007.

[77] L. Wu, Y. Zhong, C. T. Chan, K. S. Wong, and G. P. Wang, "Fabrication of large area two- and three-dimensional polymer photonic crystals using single refracting prism holographic lithography," *Appl. Phys. Lett.*, vol. 86, pp. 241102-1–241102-3, June 7, 2005.

[78] I. Divliansky, T. S. Mayer, K. S. Holliday, and V. H. Crespi, "Fabrication of three-dimensional polymer photonic crystal structures using single diffraction element interference lithography," *Appl. Phys. Lett.*, vol. 82, pp. 1667–1669, Mar. 17, 2003.

[79] S. Jeon, J. Park, R. Cirelli, S. Yang, C. Heitzman, P. Braun, P. Kenis, and J. Rogers, "Fabricating complex three-dimensional nanostructures with high-resolution conformable phase masks," *Proc. Nat. Acad. Sci. U.S.A.*, vol. 101, pp. 12428–12433, Aug. 24, 2004.

[80] Y. Lin, P. R. Herman, and E. L. Abolghasemi, "Proposed single-exposure holographic fabrication of microsphere-type photonic crystals through phase-mask techniques," *J. Appl. Phys.*, vol. 97, pp. 096102-1–096102-3, Apr. 14, 2005.

[81] Y. Lin, P. R. Herman, and K. Darmawikarta, "Design and holographic fabrication of tetragonal and cubic photonic crystals with phase mask: Toward the mass-production of three-dimensional photonic crystals," *Appl. Phys. Lett.*, vol. 86, pp. 071117-1–071117-3, Feb. 10, 2005.

[82] T. Y. M. Chan, O. Toader, and S. John, "Photonic band-gap formation by optical-phase-mask lithography," *Phys. Rev. E*, vol. 73, pp. 46610–46611, Apr. 26, 2006.

[83] G. Zhou and F. S. Chau, "Three-dimensional photonic crystal by holographic contact lithography using a single diffraction mask," *Appl. Phys. Lett.*, vol. 90, pp. 181106-1–181106-3, Apr. 30, 2007.

[84] J. L. Stay and T. K. Gaylord, "Three-beam-interference lithography: Contrast and crystallography," *Appl. Opt.*, vol. 47, pp. 3221–3230, June 20, 2008.

[85] J. L. Stay, A. T. Heidt, and T. K. Gaylord, "Contrast in multi-beam-interference lithography for the fabrication of photonic crystal structures," Frontiers in Optics 2008, Rochester, NY, JSuA5, Oct. 19, 2008.

[86] *International Tables for Crystallography*, vol. A. Dordrecht: Kluwer, 5th ed., 2002.

[87] J. L. Stay and T. K. Gaylord, "Contrast in four-beam-interference lithography," *Opt. Lett.*, vol. 33, pp. 1434–1436, July 1, 2008.

[88] J. L. Stay and T. K. Gaylord, "Conditions for primitive-lattice-vector-direction equal contrasts in four-beam-interference lithography," *Appl. Opt.*, vol. 48, pp. 4801–4813, Aug. 20, 2009.

[89] S. G. Johnson and J. D. Joannopoulos, "Block-iterative frequency-domain methods for maxwell's equations in a planewave basis," *Opt. Express*, vol. 8, Jan. 29, 2001.

[90] R. D. Group, "Bandsolve 1.0," 2002.

[91] J. L. Stay and T. K. Gaylord, "Band structure calculation of photonic crystal structures fabricated via multi-beam-interference lithography," Frontiers in Optics 2009, San Jose, CA, FTuX5, Oct. 13, 2009.

[92] K. M. Ho, C. T. Chan, and C. M. Soukoulis, "Existence of a photonic gap in periodic dielectric structures," *Phys. Rev. Lett.*, vol. 65, pp. 3152–3155, Dec. 17, 1990.

[93] E. Yablonovitch, T. J. Gmitter, and K. M. Leung, "Photonic band structure: The face-centered-cubic case employing nonspherical atoms," *Phys. Rev. Lett.*, vol. 67, no. 17, pp. 2295–2298, Oct. 21, 1991.

[94] K. M. Ho, C. T. Chan, C. M. Soukoulis, R. Biswas, and M. Sigalas, "Photonic band gaps in three dimensions: New layer-by-layer periodic structures," *Solid State Commun.*, vol. 89, no. 5, pp. 413–416, 1994.

[95] H. S. Sozuer and J. P. Dowling, "Photonic band calculations for woodpile structures," *J. Mod. Optics*, vol. 41, no. 2, pp. 231–239, 1994.

[96] S. Y. Lin, J. G. Fleming, D. L. Hetherington, B. K. Smith, R. Biswas, K. M. Ho, M. M. Sigalas, W. Zubrzycki, S. R. Kurtz, and J. Bur, "A three-dimensional photonic crystal operating at infrared wavelengths," *Nature*, vol. 394, pp. 251–253, July 16, 1998.

[97] S. Nojima and Y. Kamakura, "Irreducible first Brillouin-zone for two-dimensional binary-compound photonic crystals," *J. Phys. Soc. Jpn.*, vol. 77, no. 3, pp. 034403-1–034403-6, Mar. 2008.

[98] J. L. Stay and T. K. Gaylord, "Three-beam-interference lithography configuration," *Rev. Sci. Instrum.*, 2009. (submitted)

[99] J. L. Stay and T. K. Gaylord, "Photo-mask for wafer-scale fabrication of two- and three-dimensional photonic crystal structures," Frontiers in Optics 2006, Rochester, NY, FThC5, Oct. 12, 2006.

[100] T. K. Gaylord, J. L. Stay, and J. D. Meindl, "Photo-masks and methods for fabricating periodic optical structures," U. S. Utility Patent Application no. 11/970,502 assigned to Georgia Tech Research Corporation, filed Jan. 7, 2008.

[101] T. K. Gaylord, J. L. Stay, and J. D. Meindl, "Photo-masks for wafer-scale fabrication of one-, two-, and three-dimensional photonic crystal devices," U. S. Utility Patent Application no. 11/871,834 assigned to Georgia Tech Research Corporation, filed October 12, 2007.

[102] F. Monifi, A. Ghaffari, M. Djavid, and M. S. Abrishamian, "Three output port channel-drop filter based on photonic crystals," *Appl. Opt.*, vol. 48, pp. 804–809, Feb. 1, 2009.

[103] M. A. Mansouri-Birjandi, M. K. Moravvej-Farshi, and A. Rostami, "Ultrafast low-threshold all-optical switch implemented by arrays of ring resonators coupled to a Mach-Zehnder interferometer arm: Based on 2D photonic crystals," *Appl. Opt.*, vol. 47, pp. 5041–5050, Sept. 20, 2008.

[104] J. He, Y. Jin, Z. Hong, and S. He, "Slow light in a dielectric waveguide with negative-refractive-index photonic crystal cladding," *Opt. Express*, vol. 16, pp. 11077–11082, July 21, 2008.

[105] R. G. Beausoleil, J. Ahn, N. Binkert, A. Davis, D. Fattal, M. Fiorentino, N. P. Jouppi, M. McLaren, C. M. Santori, R. S. Schreiber, S. M. Spillane, D. Vantrease, and Q. Xu1, "A nanophotonic interconnect for high-performance many-core computation," *IEEE LEOS Newsletter*, pp. 15–22, June 2008.

[106] M. P. Fok and P. R. Prucnal, "All-optical encryption based on interleaved waveband switching modulation for optical network security," *Opt. Lett.*, vol. 34, pp. 1315–1317, May 1, 2009.

[107] Y.-K. Huang, V. Baby, I. Glesk, C. S. Bres, C. M. Greiner, D. Iazikov, T. W. Mossberg, and P. R. Prucnal, "Novel multicode-processing platform for wavelength-hopping time-spreading optical CDMA: A path to device miniaturization and enhanced network functionality," *IEEE J. Sel. Top. Quantum Electron.*, vol. 13, pp. 1471–1479, Sept./Oct. 2007.

[108] V. Baby, I. Glesk, R. J. Runser, R. Fischer, Y.-K. Huang, C. S. Bres, W. C. Kwong, T. H. Curtis, and P. R. Prucnal, "Experimental demonstration and scalability analysis of a four-node 102-Gchip/s fast frequency-hopping time-spreading optical CDMA network," *IEEE Photonics Technol. Lett.*, vol. 17, pp. 253–255, Jan. 2005.

[109] C. S. Bres, I. Glesk, R. J. Runser, and P. R. Prucnal, "All-optical OCDMA code-drop unit for transparent ring networks," *IEEE Photonics Technol. Lett.*, vol. 17, pp. 1088–1090, May 2005.

[110] N. Tetreault, G. Von Freymann, M. Deubel, M. Hermatschweiler, F. Perez-Willard, S. John, M. Wegener, and G. A. Ozin, "New route to three-dimensional photonic

bandgap materials: Silicon double inversion of polymer templates," *Adv. Mater.*, vol. 18, pp. 457–460, Oct. 11, 2006.

[111] "Photo-mask-based multi-beam-interference lithography for wafer-scale-integration of photonic crystal devices," National Science Foundation grant no. ECCS 0925119, July 2009.

[112] K. Kravtsov, Y. Deng, and P. R. Prucnal, "Self-clocked all-optical add/drop multiplexer for asynchronous CDMA ring networks," *IEEE J. Quantum Electron.*, vol. 45, pp. 396–401, Apr. 2009.

[113] P. Toliver, I. Glesk, and P. R. Prucnal, "All-optical clock and data separation technique for asynchronous packet-switched optical time-division-multiplexed networks," *Opt. Commun.*, vol. 173, pp. 101–106, Jan. 1, 2000.

[114] Q. Wu, H. Zhang, Y. Peng, X. Fu, and M. Yao, "40GS/s optical analog-to-digital conversion system and its improvement," *Opt. Express*, vol. 17, pp. 9252–9257, May 25, 2009.

[115] M. Gehl, C. Dapkus, S. Granieri, and A. Siahmakoun, "2-GB/s all-optical serial digital-to-analog converter," *Microwave Opt. Technol. Let.*, vol. 51, pp. 1561–1565, June 2009.

[116] W. Li, H. Zhang, Q. Wu, Z. Zhang, and M. Yao, "All-optical analog-to-digital conversion based on polarization-differential interference and phase modulation," *IEEE Photonics Technol. Lett.*, vol. 19, pp. 625–627, Apr. 15, 2007.

[117] Q. Wu, H. Zhang, M. Yao, and W. Zhou, "All-optical analog-to-digital conversion using inherent multiwavelength phase shift in $LiNbO_3$ phase modulator," *IEEE Photonics Technol. Lett.*, vol. 20, pp. 1036–1038, June 15, 2008.

[118] L. Zhou, S. S. Djordjevic, R. Proietti, D. Ding, S. J. B. Yoo, R. Amirtharajah, and V. Akella, "Design and evaluation of an arbitration-free passive optical crossbar for on-chip interconnection networks," *Appl. Phys. A*, vol. 95, pp. 1111–1118, Sept. 5, 2009.

[119] K. Ohashi, K. Nishi, T. Shimizu, M. Nakada, J. Fujikata, J. Ushida, S. Torii, K. Nose, M. Mizuno, H. Yukawa, M. Kinoshita, N. Suzuki, A. Gomyo, T. Ishi, D. Okamoto, K. Furue, T. Ueno, T. Tsuchizawa, T. Watanabe, K. Yamada, S.-I. Itabashi, and J. Akedo, "On-chip optical interconnect," *Proc. IEEE*, vol. 97, pp. 1186–1196, July 2009.

[120] S. Abad, M. Lopez-Amo, J. M. Lopez-Higuera, D. Benito, A. Unanua, and E. Achaerandio, "Single and double distributed optical amplifier fiber bus networks with wavelength-division multiplexing for photonic sensors," *Opt. Lett.*, vol. 24, pp. 805–807, June 15, 1999.

[121] E. Achaerandio, S. Jarabo, S. Abad, and M. Lopez-Amo, "New WDM amplified network for optical sensor multiplexing," *IEEE Photonics Technol. Lett.*, vol. 11, pp. 1644–1646, Dec. 1999.

[122] N. Dietz and F. L. Madarasz, "Chemical and biological sensors based on optically confined birefringent chalcopyrite heterostructures," *Mat. Sci. Eng. B-Solid*, vol. B97, no. 2, pp. 182–195, 2003.

[123] H. Helmers, P. Greco, R. Rustad, R. Kherrat, G. Bouvier, and P. Benech, "Performance of a compact, hybrid optical evanescent-wave sensor for chemical and biological applications," *Appl. Opt.*, vol. 35, pp. 676–680, Feb. 1, 1996.

[124] O. Hugon, P. Benech, and H. Gagnaire, "Surface plasmon chemical/biological sensor in integrated optics," *Sens. Actuators B, Chem.*, vol. B51, pp. 316–320, 1998.

[125] M. Lopez-Amo, L. T. Blair, and P. Urquhart, "Wavelength-division-multiplexed distributed optical fiber amplifier bus network for data and sensors," *Opt. Lett.*, vol. 18, pp. 1159–1161, July 15, 1993.

[126] S. J. Pember, C. M. France, and B. E. Jones, "A multiplexed network of optically powered, addressed and interrogated hybrid resonant sensors," *Sens. Actuators A, Phys.*, vol. A47, pp. 474–477, 1995.

[127] M. Fernandez Vallejo, R. A. Perez-Herrera, C. Elosua, S. Diaz, P. Urquhart, C. Bariain, and M. Lopez-Amo, "Resilient amplified double-ring optical networks to multiplex optical fiber sensors," *J. Lightwave Technol.*, vol. 27, pp. 1301–1306, May 15, 2009.

[128] Y. Libo and Y. Jun, "Two-loop-based low-coherence multiplexing fiber-optic sensor network with a Michelson optical path demodulator," *Opt. Lett.*, vol. 30, pp. 601–603, Mar. 15, 2005.

[129] N. A. Yebo, D. Taillaert, J. Roels, D. Lahem, M. Debliquy, D. Van Thourhout, and R. Baets, "Silicon-on-insulator (SOI) ring resonator-based integrated optical hydrogen sensor," *IEEE Photonics Technol. Lett.*, vol. 21, pp. 960–962, July 15, 2009.

[130] B. Bhola, P. Nosovitskiy, H. Mahalingam, and W. H. Steier, "Sol-gel-based integrated optical microring resonator humidity sensor," *IEEE Sens. J.*, vol. 9, pp. 740–747, July 2009.

[131] C. Ciminelli, C. E. Campanella, and M. N. Armenise, "Optimized design of integrated optical angular velocity sensors based on a passive ring resonator," *J. Lightwave Technol.*, vol. 27, pp. 2658–2666, July 15, 2009.

[132] R. Martin, A. Sharkawy, J. Humphrey, E. J. Kelmelis, and D. W. Prather, "Integrated optical sensor using a dispersion guided photonic crystal structure," *Proc. SPIE*, vol. 6322, 2006.

[133] N. Pelletier, B. Beche, E. Gaviot, L. Camberlein, N. Grossard, F. Polet, and J. Zyss, "Single-mode rib optical waveguides on SOG/SU-8 polymer and integrated Mach-Zehnder for designing thermal sensors," *IEEE Sens. J.*, vol. 6, pp. 565–570, June 2006.

[134] B. Sepulveda, G. Armelles, and L. M. Lechuga, "Magneto-optical phase modulation in integrated Mach-Zehnder interferometric sensors," *Sensor Actuat. A-Phys.*, vol. 134, no. 2, pp. 339–347, 2007.

VITA

Justin L. Stay was born in 1980 in Philadelphia, PA. He entered the Georgia Institute of Technology in 1999 and received his Bachelor of Science and Masters of Science from the School of Electrical Engineering in 2003 and 2005 respectively. Justin has been the recipient of the Szlam Fellowship. He is a member of the Institute of Electrical and Electronics Engineers and the Optical Society of America.